

PHYSICS-BASED SIMULATION AND RELIABILITY MODELING  
FOR MULTI-OBJECTIVE OPTIMIZATION OF ADVANCED CUTTING  
TOOLS IN MACHINING TITANIUM ALLOYS

By

MOHAMMAD SIMA

A Dissertation submitted to the  
Graduate School-New Brunswick  
Rutgers, The State University of New Jersey

In partial fulfillment of the requirements

for the degree of

Doctor of Philosophy

Graduate Program in Industrial and Systems Engineering

Written under direction of

Professor Tugrul Özel

Professor David W. Coit

and approved by

\_\_\_\_\_  
\_\_\_\_\_  
\_\_\_\_\_  
\_\_\_\_\_  
\_\_\_\_\_

New Brunswick, New Jersey

May, 2015

## ABSTRACT OF THE DISSERTATION

# Physics-Based Simulation and Reliability Modeling for Multi-Objective Optimization of Advanced Cutting Tools in Machining Titanium Alloys

By MOHAMMAD SIMA

Dissertation Directors:

Dr. Tugrul Özel

Dr. David W. Coit

Titanium alloys are widely used in various industries due to their superior characteristics such as high strength-to-weight ratio, toughness, corrosion resistance and biocompatibility. Ti-6Al-4V is the most commonly used titanium alloy and considered as difficult-to-cut because of its low thermal conductivity, high chemical reactivity with cutting tool materials at elevated temperatures, and low modulus of elasticity. Therefore, rapid tool wear and poor surface quality are the issues in machining of this alloy. Hence, selecting appropriate cutting conditions (cutting speed, uncut chip thickness, depth of cut, etc.), tool materials, coatings, and geometry are essential not only to increase productivity and decrease the costs, but also to obtain a desirable surface integrity.

Initially, a modified constitutive model was proposed for Ti-6Al-4V which is able to predict the behavior under high strains and temperatures. Since workpiece experiences high

strain, strain rate at elevated temperatures during machining, it is important to develop a material model that captures material behavior at these conditions. Using this material model, two dimensional finite element simulations were designed to predict machining forces and serrated chip geometry and results were validated with experiments. This verified material model was used in three dimensional finite element simulations to predict tool wear, temperature, stress and strain distributions. Effects of different cutting tool materials, coatings (TiAlN and cBN), geometry and machining process parameters were investigated. A reliability model for different types of cutting tools is created with experimental and physics-based data. Furthermore, using genetic algorithms, a multi-objective optimization problem was designed and solved to find the optimal process parameters (cutting speed and feed) and cutting tool selection in order to maximize reliability and machining efficiency. Finally, validation experiments were conducted to measure tool wear on uncoated and TiAlN coated inserts under the optimum cutting conditions with expected reliability rating. The results indicate that there is an adequate agreement and the discrepancy may be related to model uncertainty and stochastic nature of the tool wear.

## ACKNOWLEDGEMENTS

First and foremost I would like to express my deepest gratitude to my PhD co-advisors, Dr. Tugrul Özel and Dr. David W. Coit for their enthusiastic endless scientific support, insightful guidance and patience throughout the course of this research. Working with them has been a constant learning experience for me.

I appreciate the sound advice and constructive suggestions I received from my PhD committee members, Dr. Richard Riman and Dr. James Luxhoj. I sincerely would like to thank Dr. Melike Baykal-Gursoy, the ISE department's graduate advisor, for all her supports.

I would like to take this opportunity to express my deepest appreciation to these super supportive friends and family: Ms. Sahar Ghasemi, Ms. Nadereh Abolghasemi, and Dr. Iman Soltani. Without their love and support this dream would never come true.

I cannot thank enough my very close friends and colleagues, Dr. Mostafa Aboui-Ardakan, Dr. Thanongsak Thepsonthi and, Dr. Saltuk Bugra Selcuklu. Their kind help was really significant throughout my research.

I would also like to thank the National Science Foundation for funding my research via graduate research assistantships and Rutgers University Industrial and Systems Engineering Department for offering teaching assistantships and fellowships. I am also grateful to Reliasoft Company for generously providing me with their ALTA software.

I cannot thank enough the administrative and technical support I received from Ms. Cindy Ielmini, and Mr. Joe Lippencott.

Finally, I want to thank my family for having faith in me and motivating me in pursuing my degree.

## **DEDICATION**

*To my parents,  
for their endless love all these years from long distance*

# TABLE OF CONTENTS

ABSTRACT OF THE DISSERTATION .....	ii
ACKNOWLEDGEMENTS .....	iv
DEDICATION .....	v
TABLE OF CONTENTS .....	vi
LIST OF TABLES .....	x
LIST OF FIGURES.....	xi
LIST OF SYMBOLS .....	xvii
<b>1. Introduction.....</b>	<b>1</b>
1.1. Introduction .....	2
1.2. Titanium Alloy Manufacturing .....	5
1.3. New Material Constitutive Model for Ti-6Al-4V .....	6
1.3.1. The Johnson–Cook material model.....	7
1.3.2. The Nemat-Nasser micromechanical model .....	10
1.3.3. Dynamic material behavior of titanium alloy .....	12
1.3.4. Strain rate and temperature sensitivity .....	15
1.4. Physics Based Simulation Modeling.....	17
1.5. Advance Cutting Tools and Limitations .....	19
1.5.1. Wear-based degradation mechanisms .....	22
1.5.2. Tool wear models.....	26
1.6. Physics-Based Reliability Analysis.....	31
1.7. Statistics-Based Reliability Modeling of Cutting Tool Wear .....	35
1.8. Motivation .....	40
1.9. Objectives.....	43
1.10. Summary of the Dissertation.....	44

<b>2. FINITE-ELEMENT BASED PROCESS SIMULATIONS .....</b>	<b>47</b>
2.1. Introduction .....	48
2.2. Constitutive Material Models for Ti-6Al-4V Titanium Alloy .....	50
2.2.1. Modified material model with non-temperature-dependent parameters ( <i>Model 1</i> ) ....	51
2.2.2. Modified material model with temperature-dependent parameters ( <i>Model 2</i> ) .....	53
2.2.3. Modified material model with temperature-dependent parameters and strain softening ( <i>Model 3</i> ).....	54
2.3. 2-D Finite Element Process Simulations.....	61
2.3.1. Temperature-dependent mechanical and thermo-physical properties.....	62
2.3.2. Chip–tool interfacial friction model.....	63
2.3.3. Simulation experiments for constitutive material model validation .....	64
2.4. 3-D Finite Element Process Simulations.....	71
2.5. 2-D FE Simulations Results on Chip Geometry and Morphology.....	79
2.6. Results and Discussions .....	83
<b>3. MACHINING EXPERIMENTS.....</b>	<b>86</b>
3.1. Introduction .....	87
3.2. Experimental Analysis .....	89
3.2.1. 2-D Orthogonal Machining Experiments.....	89
3.2.2. Straight bar turning (Three-dimensional) experiments .....	91
3.3. Results and Discussion.....	92
3.3.1. Orthogonal cutting experiments.....	92
3.3.2. Straight bar turning experiments.....	96
3.4. Conclusions .....	103

<b>4. RELIABILITY MODELING OF ADVANCED CUTTING TOOLS IN MACHINING TI-6AL-4V.....</b>	<b>108</b>
4.1. Introduction .....	109
4.2. Reliability Modeling of Cutting Tools.....	111
4.3. Experimental-Based Reliability Evaluation.....	115
4.4. Physics-based Reliability Evaluation.....	129
4.5. Usui’s Wear Model Coefficient Determination .....	139
4.6. Results and Discussions .....	149
4.7. Conclusion.....	151
<b>5. MULTI-OBJECTIVE OPTIMIZATION.....</b>	<b>153</b>
5.1. Introduction .....	154
5.2. Multi-Objective Optimization Problem Formulation.....	155
5.3. Fast Non-dominated Sorting Genetic Algorithm (NSGA-II).....	159
5.3.1. Chromosome definition .....	162
5.3.2. Fitness function.....	162
5.3.3. Initial population.....	163
5.3.4. Selection.....	163
5.3.5. Crossover breeding operator .....	163
5.3.6. Mutation operator.....	166
5.3.7. Stopping condition .....	167
5.4. Optimization Results .....	167
5.5. Validation of Results.....	172
5.6. Conclusion.....	177
<b>6. CONTRIBUTIONS AND FUTURE WORK .....</b>	<b>179</b>
<b>References.....</b>	<b>187</b>

<b>Appendix.....</b>	<b>197</b>
Appendix 1 .....	197
Appendix 2 .....	221
Appendix 3 .....	245
Appendix 4 .....	248
Appendix 5 .....	253

## LIST OF TABLES

Table 1.1. Constants of J-C model suggested for Ti-6Al-4V (Sima & Özel, 2010).....	7
Table 2.1. Mechanical and thermo-physical properties of work and tool materials used in FE simulations (Özel et al., 2010b) .....	62
Table 2.2. Benchmark FE simulations to identify modified material model parameters (Sima & Özel, 2010).....	65
Table 2.3. Summary of 3D FE Simulation Force Predictions (mean value and range of the predicted forces) (Özel et al., 2010b) .....	73
Table 2.4. Summary of 3D FE Simulation Predictions.....	74
Table 2.5. Comparison of predicted chip thickness and serrated pitch with experiments (Sima & Özel, 2010).....	80
Table 3.1. Chemical composition of Ti-6Al-4V titanium-based alloy (Ulutan, 2013).....	88
Table 3.2. Mechanical and thermal properties of Ti-6Al-4V titanium-based alloy (Ulutan, 2013) .....	88
Table 3.3. Serrated chip dimensions under certain orthogonal cutting conditions (Sima & Özel, 2010) .....	96
Table 4.1. FE simulations utilized in physics-based reliability modeling .....	110
Table 4.2. FE Experimental setup for machining test for the purpose of tool wear measurement and reliability modeling.....	116
Table 4.3. Weibull wear rate distribution parameters obtained from experimental results for different tool types at each wear zone.....	123
Table 4.4. Experimental-based reliability models of cutting tools at crater wear sub-regions....	126
Table 4.5. Weibull wear rate distribution parameters for physics-based FE simulation results for different tools types at each wear region .....	133
Table 4.6. Physics-based reliability models of cutting tools at crater wear sub-regions .....	137
Table 4.7. Experimental crater wear amounts vs. predicted worn geometry and anticipated wear amount for cutting edge region (Zone 3) using non-calibrated Usui's wear model coefficients. ....	140

## LIST OF FIGURES

Figure 1.1. Flow stress data obtained from SHPB tests (Lee and Lin, 1998b).....	13
Figure 1.2. The relationship between strain rate sensitivity and true strain (at 700 °C). (Sima & Özel, 2010).....	16
Figure 1.3. The relationship between temperature sensitivity and true strain. (Sima & Özel, 2010).....	16
Figure 1.4. Illustration of simulation models for a: 2D and b: 3D machining processes.....	18
Figure 1.5. Schematic diagram of the tool wear mechanisms appearing at different cutting temperatures corresponding to cutting speed and feed (König 1984).....	23
Figure 1.6. a) Flank and crater wear in machining of Ti-6Al-4V with WC/Co tool with coolant, b) Flank and crater wear in dry machining of Ti-6Al-4V with WC/Co tool (Muthukrishnan & Davim, 2011), c) schematic three views of a worn tool, and d) three dimensional schematic view of a worn tool (Kalpakjian and Schmid 2010).....	26
Figure 1.7. Summary of selected empirical tool life models and tool wear rate models (Yen et al., 2004).....	29
Figure 1.8. Predicted results of the wear rate distribution when orthogonal cutting AISI 1045 using uncoated carbide tool (Schmidt et al. 2003).....	31
Figure 2.1. Mesh for the workpiece and the tool (a) and the boundary conditions (b) (Özel and Zeren, 2007).....	50
Figure 2.2. Flow stress data obtained from SHPB tests (Lee & Lin, 1998b).....	52
Figure 2.3. Flow stress curves using modified material model, <i>Model 1</i> ( $M = 0.7, S = 7, p = 0, r = 1$ ).....	53
Figure 2.4. Flow stress curves using modified material model, <i>Model 2</i> ( $r = 1, d = 0.5, b = 1, S = 5$ ) (Sima & Özel, 2010).....	54
Figure 2.5. Flow stress curves using modified material model, <i>Model 3</i> ( $a = 2, r = 1, d = 0.5, b = 1, S = 5$ ) (Sima & Özel, 2010).....	56
Figure 2.6. Flow stress curves depicting the effects of parameter “ <i>a</i> ” at 700 °C (Sima & Özel, 2010).....	58

Figure 2.7. Flow stress curves depicting the effects of parameter “ <i>b</i> ” at 500 °C (Sima & Özel, 2010)	59
Figure 2.8. Flow stress curves depicting the effects of parameter “ <i>d</i> ” at 300 °C (Sima & Özel, 2010)	60
Figure 2.9. Flow stress curves depicting the effects of parameter “ <i>S</i> ” at 700 °C (Sima & Özel, 2010)	61
Figure 2.10. Velocity field and friction regions defined in FE models.....	64
Figure 2.11. Serrated chip formation with adiabatic shearing using <i>Model 1</i> (uncoated WC/Co tool, $V_c = 121.9$ m/min, $t_u = 0.1$ mm/rev, $0^\circ$ rake angle, $r_\beta = 5$ $\mu$ m) (Özel et al., 2010a).....	66
Figure 2.12. Comparison of forces predicted ( $V_c = 120$ m/min, $t_u = 0.1$ mm/rev, $\gamma = 0^\circ$ , $r_\beta = 5$ $\mu$ m) (Sima & Özel, 2010).....	67
Figure 2.13. Comparison of forces predicted with <i>Model 3</i> ( $V_c = 120$ m/min, $\gamma = 0^\circ$ , $r_\beta = 5$ $\mu$ m) (Sima & Özel, 2010).....	68
Figure 2.14. Comparison of modified material models on serrated chip formation with adiabatic shearing ( $V_c = 120$ m/min, $t_u = 0.1$ mm/rev, $\gamma = 0^\circ$ , $r_\beta = 5$ $\mu$ m) (Sima & Özel, 2010).....	69
Figure 2.15. Effective strain values along a path into the segmented chip with adiabatic shearing (Sima & Özel, 2010).....	70
Figure 2.16. Effective strain values along a path into the segmented chip (Sima & Özel, 2010)..	71
Figure 2.17. Mesh for the workpiece and the tool in 3D simulations (Sima et al., 2010) .....	72
Figure 2.18. Predicted Temperature Distributions in °C (Özel et al., 2010b).....	76
[Figure 2.19. Simulated Chip Formation with Effective Strain Distributions (Özel et al., 2010b)77	
Figure 2.20. Experimental and Predicted Wear Rate Distributions in [mm/s] (Özel et al., 2010b)	78
Figure 2.21. Comparison of measured and simulated cutting forces (Sima & Özel, 2010) .....	79
Figure 2.22. Comparison of simulated serrated chip formation and captured chip images (Sima & Özel, 2010).....	81
Figure 2.23. Temperature distribution in simulated serrated chip formation (Sima & Özel, 2010)	82
Figure 3.1. Illustration of orthogonal cutting.....	89

Figure 3.2. Orthogonal cutting of Ti-6Al-4V workpiece specimens (Özel et al. 2009) .....	90
Figure 3.3. Straight bar turning of Ti-6Al-4V Titanium Alloy (Özel et al. 2010).....	91
Figure 3.4. Cutting and thrust forces in orthogonal cutting test of Ti-6Al-4V (Sima & Özel, 2010) .....	94
Figure 3.5. Images of serrated chips at different cutting conditions (Sima & Özel, 2010) .....	95
Figure 3.6. Forces in straight turning of Ti-6Al-4V titanium alloy using uncoated, TiAlN and cBN coated inserts ( $a_p = 2$ mm, $f = 0.1$ mm/rev) (Özel et al., 2010).....	97
Figure 3.7. Measured forces in turning of Ti-6Al-4V titanium alloy using TiAlN coated and variable micro-geometry inserts ( $a_p = 2$ mm, $f = 0.1$ mm/rev) (Özel et al., 2010).....	98
Figure 3.8. Measured forces in turning of Ti-6Al-4V titanium alloy using TiAlN coated and variable micro-geometry inserts ( $a_p = 2$ mm, $f = 0.2$ mm/rev) (Özel et al., 2010).....	98
Figure 3.9. a) Schematic drawing of wear patterns (Özel et al., 2010) b) typical tool wear features in titanium machining (Antoniali et al., 2012), c) crater wear indexes (Wikipedia) .....	99
Figure 3.10. Measured tool wear of uncoated, TiAlN and cBN Coated inserts in turning of Ti-6Al- 4V titanium alloy ( $a_p = 2$ mm, $f = 0.1$ mm/rev) (Sima et al., 2011).....	100
Figure 3.11. Measured tool wear of uniform and variable micro-geometry WC/Co, TiAlN coated inserts in turning of Ti-6Al-4V titanium alloy ( $a_p = 2$ mm, $f = 0.1$ mm/rev) (Sima et al., 2011)	100
Figure 3.12. Measured tool wear of uniform and variable micro-geometry WC/Co, TiAlN coated inserts in turning of Ti-6Al-4V titanium alloy ( $a_p = 2$ mm, $f = 0.2$ mm/rev) (Sima et al., 2011)	101
Figure 3.13. Experimental crater wear zones in cutting tools.....	103
Figure 4.1. Illustration of proposed regions on rake face of cutting tool. (Region 1: Tool tip trailing, Region 2: Tool nose radius, and Region 3: Tool cutting edge) .....	114
Figure 4.2. Sample images of worn tools from machining tests with measurement lines for the purpose of quantifying crater wear .....	117
Figure 4.3. Schematic view of uncut chip thickness in turning and its relation with crater wear region classification .....	119
Figure 4.4. Classification of three regions on tool crater face a) tool tip, b) tool radius and, c) tool cutting edge.....	120

Figure 4.5. Probability distributions and distribution fits of experimental-based wear rate values .....	125
Figure 4.6. Experimental -based reliability of TiAlN coated WC/Co at tool cutting edge region (Region 3) for two levels of feed $f = 0.1$ mm/rev and $0.2$ mm/rev, cutting speed $V_c = 100$ m/min, and wear threshold $H_3 = 0.2$ mm .....	128
Figure 4.7. Experimental -based reliability of TiAlN coated WC/Co at tool cutting edge region (Region 3) for two levels of cutting speed $V_c = 100$ m/min and $50$ m/min, feed $f = 0.1$ mm/rev, and wear threshold $H_3 = 0.2$ mm .....	128
Figure 4.8. Experimental -based reliability of TiAlN coated WC/Co at tool cutting edge region (Region 3) for two levels of wear threshold $H_3 = 0.2$ mm and $H_3 = 0.1$ mm, cutting speed $V_c = 100$ m/min, and feed $f = 0.1$ mm/rev .....	129
Figure 4.9. Extraction of tool wear rate values from tool rake surfaces for different tool types and cutting conditions in FE simulations of machining Ti-6Al-4V .....	130
Figure 4.10. Classification of three regions on tool rake face a) tool tip trailing (Region 1), b) tool radius (Region 2) and, c) tool cutting edge (Region 3) in FE simulations.....	131
Figure 4.11. Experimentally measured wear amounts vs. FE simulation predictions for uncoated WC/Co cutting tools .....	132
Figure 4.12. Experimentally measured wear amounts vs. FE simulation predictions for TiAlN coated WC/Co cutting tools.....	132
Figure 4.13. Experimentally measured wear amounts vs. FE simulation predictions for cBN coated WC/Co cutting tools .....	133
Figure 4.14. Experimentally measured wear amounts vs. FE simulation predictions for multi-layered coated WC/Co cutting tools .....	133
Figure 4.15. Probability distributions and distribution fits of physics-based wear rate values....	136
Figure 4.16. Physics-based reliability of uncoated WC/Co tool at tool tip trailing region for two levels of feed ( $f = 0.1$ mm/rev and $0.2$ mm/rev), cutting speed ( $V_c = 100$ m/min), wear threshold ( $H_1 = 0.2$ mm).....	138
Figure 4.17. Physics-based reliability of uncoated WC/Co tool at tool tip trailing region for two levels of cutting speed ( $V_c = 100$ m/min and $V_c = 50$ m/min), feed ( $f = 0.1$ mm/rev), wear threshold ( $H_1 = 0.2$ mm).....	138

Figure 4.18. Physics-based reliability of uncoated WC/Co tool at tool tip trailing region for two levels of wear threshold ( $H_1 = 0.2\text{mm}$ and $H_1 = 0.1\text{mm}$ ), cutting speed ( $V_c = 100\text{ m/min}$ ), feed ( $f = 0.1\text{ mm/rev}$ ).....	139
Figure 4.19. Column graph presentation of Table 4.7, cutting edge (region 3) crater wear values, experimental tests, FE worn geometries and FE anticipated wear values using non-calibrated Usui's wear coefficients for uncoated WC/Co and TiAlN coated WC/Co at different cutting conditions .....	142
Figure 4.20. Crater wear rate extraction from cutting edge zone (Uncoated WC/Co, $V_c = 100\text{ m/min}$ and $f = 0.2\text{ mm/rev}$ ).....	143
Figure 4.21. FE predicted worn geometry illustration with non-calibrated Usui's wear model coefficients for uncoated WC/Co, $V_c = 50\text{ m/min}$ , $f = 0.2\text{ mm/rev}$ and cutting time of $t = 216\text{s}$ .	143
Figure 4.22. Column graph presentation of cutting edge (region 3) crater wear values, experimental tests, FE worn geometries and FE anticipated wear values using calibrated Usui's wear coefficients for uncoated WC/Co and TiAlN coated WC/Co at different cutting conditions .....	145
Figure 4.23. FE predicted cratered worn geometries at cutting edge regions for two tool types, uncoated WC/Co and TiAlN coated WC/Co using calibrated Usui's wear model coefficients (Cutting condition 1&2).....	147
Figure 4.24. FE predicted cratered worn geometries at cutting edge regions for two tool types, uncoated WC/Co and TiAlN coated WC/Co using calibrated Usui's wear model coefficients (Cutting condition 3&4).....	148
Figure 4.25. Physics-based reliability of cutting tools at $V_c = 100\text{ m/min}$ and two levels of feed $f = 0.1$ and $0.2\text{ mm/rev}$ in machining of Ti6Al4V titanium alloy .....	150
Figure 4.26. Experimental-based reliability of cutting tools at $V_c = 100\text{ m/min}$ and two levels of feed $f = 0.1$ and $0.2\text{ mm/rev}$ .....	150
Figure 5.1. Dependency of physics-based reliability of tip trailing region of uncoated WC/Co on failure threshold $H_1$ at $t = 100\text{ s}$ .....	157
Figure 5.2. Dependency of physics-based reliability of tip trailing region of uncoated WC/Co on cutting time at failure threshold $H_1 = 100\text{ mm}$ .....	157
Figure 5.3. Illustration of dependency of physics-based reliability of cutting tool to values of thresholds $H_j$ (Uncoated WC/Co, cutting time $t = 50\text{ s}$ ) .....	158

Figure 5.4. Illustration of dependency of physics-based reliability of cutting tool to cutting time (Uncoated WC/Co, $H_1 = 0.05$ mm, $H_2 = 0.15$ mm and $H_3 = 0.2$ mm).....	158
Figure 5.5. NSGA-II algorithm flowchart (Ardakan et al., 2014) .....	161
Figure 5.6. Sample shape of NSGA-II chromosome used in this research.....	162
Figure 5.7. Double point crossover on a 3x14 matrix.....	164
Figure 5.8. Sample representation of a crossover operation on two parent chromosomes and achieved children chromosomes .....	164
Figure 5.9. Sample single point crossover operation with a left-handed genes exchange .....	165
Figure 5.10. Example of Mask Operator.....	167
Figure 5.11. Illustration of dependency of physics-based reliability of cutting tool to cutting time (Uncoated WC/Co, $H_1 = 0.05$ mm, $H_2 = 0.15$ mm and $H_3 = 0.2$ mm).....	168
Figure 5.12. Solution space in different generations and how Pareto frontier forms .....	170
Figure 5.13. Optimum solution space in different views.....	171
Figure 5.14. Pareto frontier considering only uncoated WC/Co tool type for cutting time $t = 60$ s .....	173
Figure 5.15. Pareto frontiers considering only TiAlN coated WC/Co tool type for cuttings time $t = 30$ s, 40s, 50s and 60s.....	173
Figure 5.16. Wear conditions of 9 uncoated WC/Co inserts replication of condition #37 in Appendix 4.....	174
Figure 5.17. Wear conditions of 9 uncoated WC/Co inserts replication of condition #25 in Appendix 5.....	176

## LIST OF SYMBOLS

$\psi(x)$	Tool wear function in Hitomi equation
$\varepsilon_c$	Critical strain (mm/mm)
$(\sigma_f)_{rec}, (\sigma_f)_{def}$	Andrade-Meyers modified Johnson-Cook material model coefficients
$\dot{\varepsilon}_0$	Reference true strain rate (1/sec)
$N_f(x\%)$	number of cycles (fatigue life) that corresponds to $x\%$ failures
$\dot{\varepsilon}$	True strain rate (1/sec)
$\hat{\sigma}$	Stress term in Nemat-Nasser micromechanical model (MPa)
$\Delta T_e$	the effective thermal cycling range
$\Delta\alpha$	factor of difference in thermal expansion coefficient of substrate and component
$\mu$	Coulomb friction coefficient
$A, B, C, n, m$	Original Johnson-Cook material model parameters
$a, c, b, d, r, p$	Modified Johnson-Cook material model parameters
$a_p$	Depth of cut (mm)
$C, \lambda$	Characteristics constants in Kitigawa wear model
$C_0$	Tool wear equation coefficient
$c_1, c_2$	Usui's model material coefficients
$c_p$	heat capacity
$D, S, M$	Modified Johnson-Cook material model parameters
$E$	Young's modulus (GPa)
$f$	feed (rev/mm)
$F_c$	Cutting force (N/mm in 2D) (N in 3D)
$F_t$	Thrust force (N/mm in 2D) (N in 3D)
$F_z$	Feed force

$G_0$	Total energy barrier (J/mol)
$h$	heat conduction coefficient ( $\text{kWm}^{-2}\text{K}^{-1}$ )
$h(t)$	Hazard rate
$h, L_D$	Dimensions of solder attachment
hcp	Hexagonal closed pack
$H_e$	Tool cutting edge region wear threshold
$H_j$	Failure threshold in zone $j$
$H_r$	Tool nose radius region wear threshold
$H_t$	Tool trailing tip region wear threshold
$k$	Boltzmann constant
$k$	shear flow stress ( $\text{N/mm}^2$ )
$K_B$	Crater wear amount (mm)
$m$	Shear friction coefficient
$n_a$	Temperature sensitivity
$p$	Chip segment pitch (mm)
$p, q$	Constants in Nemat-Nasser micromechanical model
$p_m$	Percentage of genes subject to change in mutation of a chromosome (%)
$PoP$	Number of population in genetic algorithm
Q	Corrosion kinetics factor
$Q(t)$	Tool wear cumulative distribution function
$q(t)$	Tool wear probability density function
R	Reliability
$r_c$	Crossover rate
RH	Relative humidity (%)
$R_M$	Mutation rate
$r_\beta$	Tool edge radius (mm)

$r_\varepsilon$	Tool nose radius (mm)
$t$	Time (sec)
$T$	Temperature ( $^{\circ}\text{C}$ )
$t_{c\_max}$	Maximum chip thickness (mm)
$t_{c\_min}$	Minimum chip thickness (mm)
$T_m$	Melting temperature ( $^{\circ}\text{C}$ )
$T_r$	Ambient temperature ( $^{\circ}\text{C}$ )
$t_u$	Uncut chip thickness or feed (mm/rev)
$V_B$	Flank wear (mm)
$V_B^*$	Flank wear threshold (mm)
$V_c$	Cutting speed (m/min)
$V_s$	Sliding velocity (m/min)
$W$	Wear amount (mm)
$\alpha$	Thermal expansion (mm/mm $^{\circ}\text{C}$ )
$\alpha$	Relief angle (deg.)
$\beta$	Shape parameter in Weibull distribution
$\beta_1, \beta_2, \beta_3, \beta_4$	Tool wear and machining variables coefficients in Hitomi equation
$\gamma$	Tool rake angle(deg.)
$\gamma$	Shape factor of Weibull distribution
$\Gamma(x)$	Gamma function
$\delta$	Strain rate sensitivity
$\varepsilon$	True strain (mm/mm)
$\eta$	Scale parameter in Weibull distribution
$\theta$	Scale factor of Weibull distribution
$\lambda$	thermal conductivity (W.m $^{-1}$ . $^{\circ}\text{C}^{-1}$ )
$\mu$	Mean of normal distribution

$\sigma$	Flow stress (N/mm <sup>2</sup> )
$\sigma^*$	Thermally activated stress term in Nemat-Nasser micromechanical model (N/mm <sup>2</sup> )
$\sigma_0$	Reference stress in Nemat-Nasser micromechanical model (N/mm <sup>2</sup> )
$\sigma_a$	Athermal stress in Nemat-Nasser micromechanical model (N/mm <sup>2</sup> )
$\sigma_n$	Normal stress (N/mm <sup>2</sup> )
$\tau$	Frictional shear stress (N/mm <sup>2</sup> )

# 1. Introduction

## 1.1. Introduction

Titanium alloys are widely used in aerospace, biomedical, food, automotive and many other industries. Ti-6Al-4V is the most suitable and commonly used Titanium alloy, because of its favorable properties such as high strength-to-weight ratio, good heat treatment capability, low density, good bio-compatibility and superb resistance to corrosion. But on the other hand, manufacturing, specially machining of these alloys is an important issue since they are hard to machine materials due to low thermal conductivity, diffusivity and modulus of elasticity, and high rigidity and chemical reactivity with tool materials at elevated temperatures (Byrne et al. 2003). These difficulties in machining not only result in shorter tool life but also in undesirable dimensions of the machined products with respect to accuracy and tolerances, or quality problems of final product such as lower lifespan, reliability and surface integrity issues. Generally, product surface quality is very dependent on the final manufacturing processes such as finish machining and grinding, therefore in order to reach to a desirable level of product accuracy and quality and longer lifetime, machining process should be well-controlled and optimized.

Increasing the life time of cutting tools is another critical issue in machining Titanium alloys in productive regimes in order to decrease the production downtime and costs. Cutting tools tend to wear out pretty fast during machining of Titanium alloys. Due to their low thermal conductivity; heat does not dissipate easily from tool cutting edges, resulting in excessive stress and heat built-up, hence rapid tool wear. Titanium alloy machining performance can be increased by improving cutting tool materials, micro-geometry and coatings. In order to reduce the costs of tool replacement, an appropriate maintenance/replacement policy should be determined and optimized inspection periods should be selected. To have maintenance policy, Reliability of cutting tools can be studied by modeling the degradation/wear of cutting tools during machining process. Tools fail because of three main reasons; a) stress activated wear b) temperature activated wear and c) chemical activated wear. These failure mechanisms are competing against each other, meaning that

whichever reaches to the threshold, leads the tool to fail. Studying Physics-based reliability of cutting tools based on these failure mechanisms and deriving empirical equations is one of the purposes of this research.

Therefore, many objectives are of great importance in machining process of Titanium alloys, such as minimizing production time, maximizing tool life and achieving the best possible mechanical and metallurgical properties of the end product. In order to obtain these multiple objectives, the only variables which can be changed are machining input process parameters such as the cutting speed, feed rate, depth of cut, cutting tool geometry and material, or tool coating. However, it would be highly impractical if not impossible to conduct experiments for every possible combination of these parameters (as well as many others). Hence, in order to determine the possible outcome, some representative combinations of these input variables need to be experimented. Based on experimental results, in the computational domain, process simulations are designed to replace the experiments, and once the simulations are validated, then these simulations are utilized to forecast the effects of each input parameter on each output parameter. Since the physics of such processes like machining is very complicated to be solved by analytical methods, process simulations have to be physics-based.

Finite Element Analysis (FEA) was found to be easier and more accurate among all different methods to simulate the machining processes. In FEA, the object/s is divided into smaller elements. Each element possesses the physical and mechanical properties of the material which is assigned to and the interactions within these elements follow physics, statics and dynamics rules. Moreover, if two or more different are in contact with each other, such as machining process in which workpiece and tool are moving against each other, the interactions between their elements are also investigated separately and simultaneously. For a few seconds long simulation of machining process, the simulation divides it to some steps in the order of microseconds. The simulation updates interactions between elements after completion of each step. After successful completion

of adequate number of steps of simulation of machining process, extraction of output parameters and validation with experimental tests can be started.

Two dimensional machining simulations and experiments are the easiest mean of understanding the physics of the process, since the effects of third dimension would be eliminated theoretically, and could be neglected practically. Even though it is possible to convert these two dimensional finding into three dimensional mechanics by implementing the appropriate angles of 3D process, not only conversion of some of these 2D simulations and experiments to 3D counterparts is not possible, but also are not representative enough. Therefore, for the purpose of more accurate understanding of the process, in most of cases, 2D process studies are followed by 3D simulations and experimental validations. However, with current level of technology, designing and running 3D simulations have some obstacles and drawbacks comparing with 2D simulations such as, considerable longer run-time and constraint on implementing elastic-viscoplastic workpiece assumption in 3D simulations of machining process for titanium alloys such as Ti-6Al-4V, which captures both elastic and plastic behavior of the material and of course is more accurate since it is more similar to the actual material behavior. Hence, the best solution to this technological obstacle is to run 2D simulations with elasto-viscoplastic workpiece assumption and then calibrate the 3D simulations with plastic workpiece results according to the predicted outputs of the 2D simulations.

In finite element models, a constitutive material model is required to relate the flow stress to strain, strain rate and temperature. The experimental flow stress data are obtained by using the Split-Hopkinson pressure bar (SHPB) tests performed under various strain rates and temperatures. The experimental data obtained from these tests are used to calculate the unknown parameters of material constitutive models. Commonly used material models include: the Johnson–Cook (J–C) material model (Johnson & Cook, 1983); the Bammann–Chiesa–Johnson (BCJ) model (Bammann et al. 1996); the Maekawa model (Maekawa et al. 1983); the micromechanical models (Nemat-

Naser & Isaacs 1997, Guo et al. 2006). Some of these models are discussed as they are pertinent to the temperature-dependent flow softening in Ti-6Al-4V alloy.

In summary, it is important to study the machining processes of titanium alloys, for the purpose of higher quality and reliability of end product and validation of experimental tests findings with finite element simulations, it is possible to simulate the effects of input parameters of the machining processes and select the optimal machining and tool parameters (tool material, coating, tool angles, edge micro-geometry, etc.). Determining a comprehensive material constitutive model which captures material behavior in elevated conditions is the first step to start the validation, and then determining the coefficients of friction between the cutting tool and the machined workpiece would be the next step of validation, and after these validations are done, it is possible to reproduce the simulations to achieve a mean and standard deviation for the simulation results and optimize the simulation findings.

## **1.2. Titanium Alloy Manufacturing**

Titanium-based alloys (e.g. Ti-6Al-4V (alpha beta), Ti-13V-11Cr-3Al (beta) or Ti-5Al-2.55Nb (alpha)) offer high strength-to-weight ratio, high toughness, superb corrosion and creep resistance, and bio-compatibility and are used mainly in aerospace, gas turbine, rocket, vessels and considerably in biomedical applications (Wu 2007, Guo et al. 2009, M'Saoubi et al. 2008). Recent technological developments made the usage of titanium alloys more possible and that is mainly because of improved manufacturability of these alloys. The major challenge against the machining of titanium-based alloys besides low machinability is tool wear. Most widely-used and hence studied titanium-based alloy has been Ti-6Al-4V, or Ti-64 in short, because of its increasingly utilization in the aerospace industry (Thomas et al. 2010, Sun & Guo 2009, Sun et al. 2009, Nurul-Amin et al. 2007, Wang et al. 2005, Che-Haron & Jawaid 2005, Chen et al. 2004). It is predicted that in near future utilization of titanium alloys will be even higher especially in manufacturing of

carbon fiber compounds of aircrafts in which titanium alloys are being used, and that will not happen only if decent amount of studies are dedicated to improving the productivity and machinability of these alloys.

Due to high toughness and work hardening behavior of these alloys, machining is generally extremely difficult. Several research studies have been reported in literature addressing the issues related to machining of titanium alloys such as rapid tool wear. The low thermal conductivity of such alloys often leads to increased temperatures at the tool cutting edge and results in adhesion of workpiece material to the cutting edge and presence of hard abrasive particles in alloys structure creating accelerated tool wear. The high localized heat, increased temperatures, temperature gradients and high pressure induced stresses also cause microstructural changes creating surface integrity problems within the material in-depth direction and may cause detrimental effects on the performance of the machined part (Ulutan & Özel, 2011).

### **1.3. New Material Constitutive Model for Ti-6Al-4V**

In FE models, a constitutive material model is required to relate the flow stress to strain, strain rate and temperature, which often obtained from Split-Hopkinson pressure bar (SHPB) tests performed under various strain rates and temperatures. Dynamic material behavior of Ti-6Al-4V titanium alloy has been widely published in literature. Nemat-Nasser (Nemat-Nasser et al. 2001) reported that a phenomenon known as strain (flow) softening is observed which is responsible for adiabatic shearing in titanium alloys. Localized softening is described as offering less resistance to local deformations due to rearrangement of dislocations caused by subsequent cycling in hard materials. This phenomenon is usually seen during an increase in strain beyond a critical strain value. Specifically, Lee and Lin (Lee & Lin, 1998) investigated temperature and strain-rate sensitivity of Ti-6Al-4V and presented flow stress data at temperatures from 20 to 1100 °C and strain rates ranging from 800 up to 3300 s<sup>-1</sup>. They used The Johnson-Cook (JC) material model to represent

their flow stress data. However, their model did not include temperature-dependent strain softening effect.

### 1.3.1. The Johnson–Cook material model

The Johnson–Cook (JC) material model (Johnson and Cook, 1983) (Equation 1.1) is widely used for analysis of material flow stress, especially for those materials which their flow stress is highly influenced by temperature and strain rate; the influence of strain, strain rate and temperature on the flow stress is defined by three multiplicative yet distinctive terms:

$$\sigma = (A + B\varepsilon^n) \left(1 + C \ln \frac{\dot{\varepsilon}}{\dot{\varepsilon}_0}\right) \left[1 - \left(\frac{T - T_r}{T_m - T_r}\right)^m\right] \quad (1.1)$$

where  $\sigma$  is the equivalent flow stress,  $\varepsilon$  is the equivalent plastic strain,  $\dot{\varepsilon}$  is the equivalent plastic strain rate,  $\dot{\varepsilon}_0$  is the reference equivalent plastic strain,  $T$  is the workpiece temperature,  $T_m$  is the material melting temperature and,  $T_r$  is the room temperature. However, based on the experimental works done by researchers, different values for these constants were offered which are given in Table 1.1:

Table 1.1. Constants of J-C model suggested for Ti-6Al-4V (Sima & Özel, 2010)

Reference	A	B	C	n	m
Lee-Lin(a) (1998)	782.7	498.4	0.028	0.28	1
Lee-Lin(b) (1998)	724.7	683.1	0.035	0.47	1
Meyer-Kleponis (2001)	862.5	331.2	0.012	0.34	0.8
Kay (2003)	1098	1092	0.014	0.93	1.1
Seo et al. (2005)	997.9	653.1	0.0198	0.45	0.7

The J–C model constants shown in Table 1.1 are obtained at different testing conditions. Lee & Lin (Lee & Lin, 1998a) obtained them at a constant strain rate of  $2000 \text{ s}^{-1}$  and a maximum true strain of  $0.3 \text{ mm/mm}$ , later they reported another set of parameters that were obtained at strain rates of  $500\text{--}3000 \text{ s}^{-1}$  and maximum strain as  $0.35$  with temperatures up to  $1100 \text{ }^\circ\text{C}$  (Lee and Lin, 1998b). Meyer & Kleponis (Meyer & Kleponis, 2001) used strain rate levels of  $0.0001$ ,  $0.1$  and  $2150 \text{ s}^{-1}$  and a maximum plastic strain of  $0.57 \text{ mm/mm}$ . Kay (Kay, 2003) tested Ti–6Al–4V alloy under strains up to  $0.6 \text{ mm/mm}$  and strain rates up to  $10^4 \text{ s}^{-1}$ . Seo et al. (Seo et al., 2005) tested the same material at temperatures up to  $1000 \text{ }^\circ\text{C}$  and strain rates of  $1400 \text{ s}^{-1}$  and strains up to  $0.25 \text{ mm/mm}$ . The J–C constitutive material model can be represented as a combination of three functions as

$$\sigma = f(\varepsilon)g(\dot{\varepsilon})h(T) \quad (1.2)$$

Where

$$f(\varepsilon) = (A + B\varepsilon^n) \quad (1.3)$$

$$g(\dot{\varepsilon}) = \left(1 + C \ln \frac{\dot{\varepsilon}}{\dot{\varepsilon}_0}\right) \quad (1.4)$$

$$h(T) = \left[1 - \left(\frac{T - T_r}{T_m - T_r}\right)^m\right] \quad (1.5)$$

In this form, functions  $f(\varepsilon)$ ,  $g(\dot{\varepsilon})$  and  $h(T)$  represent strain hardening, strain rate sensitivity and thermal softening behaviors of the work material, respectively. Often the SHPB test data fitted to those functions separately (one by one). Despite the abilities of this constitutive model to represent material behavior by taking into account of strain and strain rate hardening as well as thermal softening phenomenon; it still has some weak points as it can be summarized as follows: (a) the model is not applicable for all materials since some materials exhibit different behavior, (b) the

model is meaningful in certain ranges of strain and strain rate but fails to capture high strain behavior e.g. flow softening, (c) fails to take into account the coupling effects of strain, strain rate and temperature e.g.,  $g(\varepsilon, \dot{\varepsilon})$  and  $h(\varepsilon, T)$ . Because of these known deficiencies, some of the researchers suggested modifications to the J–C constitutive model.

### 1.3.1.1 The Andrade–Meyers modified Johnson–Cook material model

Andrade et al. (Andrade et al. 1994) suggested a modification term to the J–C model in order to describe the material response above recrystallization temperature in which, the flow stress is affected by phase transformations:

$$\sigma = f(\varepsilon)g(\dot{\varepsilon})H(T) \quad (1.6)$$

This modification term for the material flow stress behavior above the recrystallization/recovery temperature is

$$H(T) = \frac{1}{1 - \left[1 - \left(\frac{(\sigma_f)_{rec}}{(\sigma_f)_{def}}\right)\right] u(T)} \quad (1.7)$$

Where

$$\begin{cases} u(T) = 0 & \text{if } T < T_c \\ u(T) = 1 & \text{if } T > T_c \end{cases}$$

### 1.3.1.2 The Calamaz modified Johnson–Cook material model

Another modification to the J–C model is suggested by Calamaz et al. (Calamaz et al., 2008) for Finite Element simulations. These modifications included flow softening at elevated strains and temperatures. In the Calamaz model (Calamaz, 2008), flow softening is defined as a decreasing behavior in flow stress with increasing strain beyond a critical strain value. Nonetheless, below that

critical strain, the material still exhibits strain hardening. The flow softening modifiers suggested to be included in the modified J–C flow stress model are as follows:

- a) modified strain hardening function of the original J–C model by including flow softening at higher strain values as

$$f(\varepsilon) = A + B\varepsilon^n \left( \frac{1}{\exp(\varepsilon^a)} \right) \quad (1.8)$$

- b) modified thermal softening function of the original J–C model by including temperature-dependent flow softening as

$$h(T) = \left[ 1 - \left( \frac{T - T_r}{T_m - T_r} \right)^m \right] \left[ D + (1 - D) \tanh \left( \frac{1}{(\varepsilon + S)^c} \right) \right] \quad (1.9)$$

where  $D = 1 - (T/T_m)^d$  and  $S = (T/T_m)^b$ .

Hence the Calamaz modified J–C material model developed by Calamaz et al. (Calamaz et al., 2008) is given as

$$\sigma = \left( A + B\varepsilon^n \left( \frac{1}{\exp(\varepsilon^a)} \right) \right) \left( 1 + C \ln \frac{\dot{\varepsilon}}{\dot{\varepsilon}_0} \right) \left[ 1 - \left( \frac{T - T_r}{T_m - T_r} \right)^m \right] \left( D + (1 - D) \tanh \left( \frac{1}{(\varepsilon + S)^c} \right) \right) \quad (1.10)$$

### 1.3.2. The Nemat-Nasser micromechanical model

Nemat-Nasser and co-workers have studied high strain rate dynamic material behavior of metals extensively (Nemat-Nasser et al., 2001) and (Nemat-Nasser & Isacs, 1997). They observed that at relatively high temperatures, flow stress, while monotonically decreasing as a function of temperature, exhibits sudden increase at a critical temperature and begins to decrease with further increase in temperature. This phenomenon is known as dynamic strain-aging. However, many

constitutive models developed for Ti–6Al–4V alloy do not include the effect of dynamic strain aging. Moreover, Nemat-Nasser et al. (Nemat-Nasser et al., 2001) studied the dependence of the flow stress on the temperature and strain rate at different strains on workpieces which due to different ways of preparation had various microstructures, and the result was that this dependence is related to the material microstructure. Besides, based on the experiments they have found that adiabatic shear bands and the related fracture are developed at high strain rates (any temperature) and at high temperatures (any strain rate). The shear bands are initiated once the magnitude of strain reaches to a certain level depending on the material temperature. Anurag & Guo (Anurag & Guo, 2007) proposed a micromechanical constitutive model to predict the material behavior of Ti–6Al–4V titanium alloy based on the work of Nemat-Nasser and his co-workers (Nemat-Nasser et al., 2001). In their model, the effect of strain rate and temperature on the flow stress is considered with a thermally activated stress,  $\sigma^*$ , term and the effect of microstructure (i.e. dislocation density, resistance of the lattice to dislocation motion, slip system, sub-granular slip, or grain boundary glide) is represented with an athermal stress,  $\sigma_a$ , term as

$$\sigma = \sigma_a + \sigma^* \quad (1.11)$$

Where  $\sigma_a = \sigma_0 \varepsilon^n$  and

$$\sigma^* = g(T, \dot{\varepsilon}) = \hat{\sigma} \left\{ 1 - \left[ -\frac{k}{G_0} T \left( \ln \frac{\dot{\varepsilon}}{\dot{\varepsilon}_0} \right) \right]^{1/q} \right\}^{1/p} \quad (1.12)$$

In thermally activated stress term,  $k$  is Boltzmann constant and  $G_0$  is the total energy barrier,  $p$  and  $q$  are constants,  $0 < p < 1$  and  $1 < q < 2$ . It is found that specimen's microstructure only affects the athermal part of the flow stress, but not the thermally activated part which is dependent on temperature and strain rate (Nemat-Nasser et al. 2001). Anurag & Guo (Anurag & Guo, 2007) used the SHPB test results reported in Lee & Lin (Lee & Lin, 1998b) and calculated the athermal part

of the flow stress by considering the critical temperature at which flow stress becomes insensitive to temperature changes. They identified the critical temperature at which dynamic strain aging occurs from the stress vs. temperature plots obtained using the SHPB test results at a given strain rate. The athermal stress representation was obtained by a curve fitting approach from the strain vs. flow stress data at the identified critical temperature. The thermal stress below the critical temperature can be calculated by subtracting the athermal stress from the total stress at different strains. In order to predict flow stress above the critical temperature, they multiplied the athermal stress with a temperature coefficient and obtained a good fit to experimental flow stress data.

In summary, the effects of strain hardening, thermal softening, dynamic strain aging, etc. are considered in these models. The levels of strain and strain rate observed at shear zones during machining are much higher than those attained by using the SHPB tests. As a result, the flow stress at high strains beyond the experimental range is calculated by extrapolation using constitutive models. The need to modify these material models is related to the material behavior at strains higher than strain ranges achievable with the Split-Hopkinson Pressure Bar tests. In machining, the strains are much higher in the deformation zones ( $\epsilon > 1$ ).

### **1.3.3. Dynamic material behavior of titanium alloy**

In room temperature, titanium (an allotropic element) has hcp crystalline structure known as  $\alpha$ -Ti but forms bcc crystalline structure around 900 °C known as  $\beta$ -Ti. Aluminum and Vanadium are used as phase stabilizers to obtain  $\alpha+\beta$  alloy phase (Nemat-Nasser & Isaacs, 1997). As given in Table 1, dynamic material behavior data for Ti–6Al–4V titanium alloy have been widely published in literature. Lee & Lin (Lee & Lin, 1998b) investigated temperature and strain rate sensitivity of Ti–6Al–4V alloy and presented some SHPB test results at temperatures from 20 to 1100 °C, with strain rates from 800 up to 3300 s<sup>-1</sup> as shown in Figure 1.1.

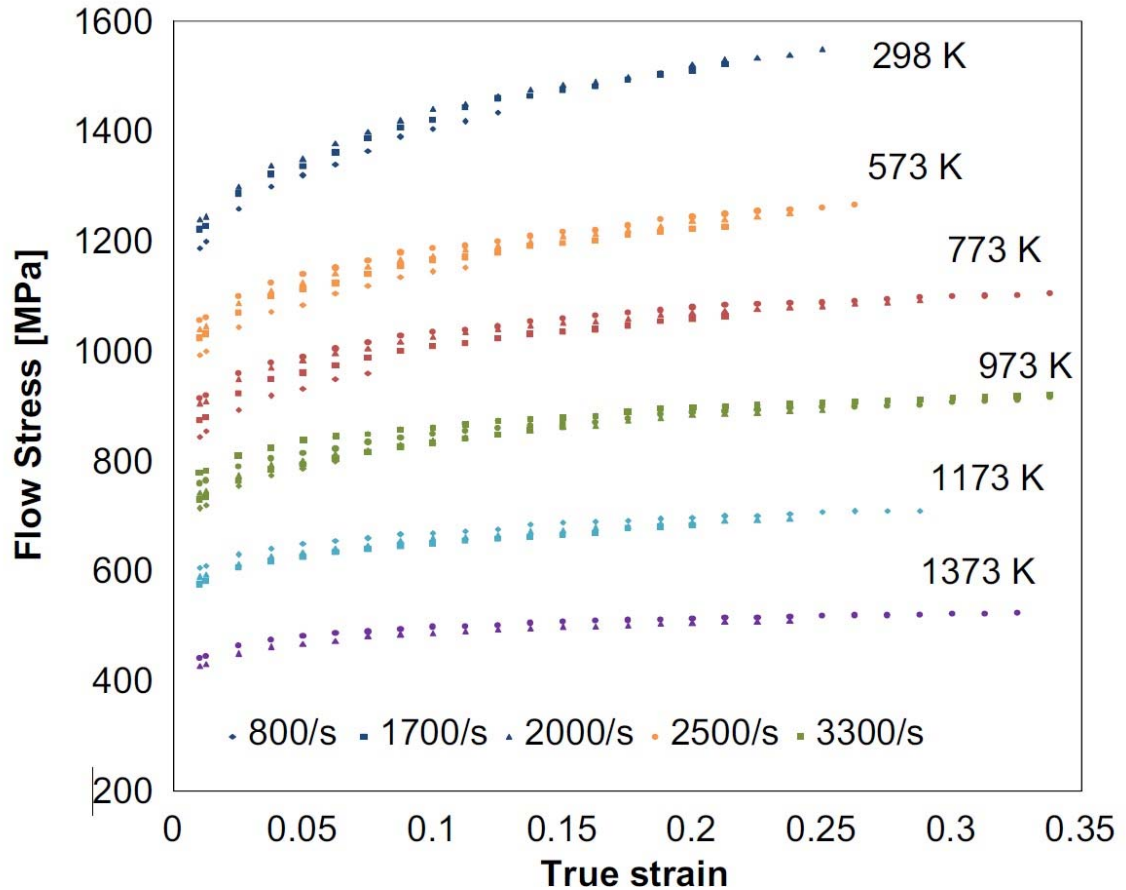


Figure 1.1. Flow stress data obtained from SHPB tests (Lee and Lin, 1998b)

Several years later, Nemat-Nasser et al. (Nemat-Nasser et al., 2001) have studied the dynamic behavior of Ti-6Al-4V alloy with different microstructures using the SHPB compression tests at strain rates ranging from 1000 to 7000  $s^{-1}$ , and initial temperatures ranging from 77 up to 1000 K. The dependence of the flow stress on the temperature and the strain rate at various strains was related to the material microstructure. Their results indicated that adiabatic shear bands develop at high strain rates as well as at low strain rates and high temperatures and flow stress is more sensitive to temperature than to the strain rate. They claimed that thermally activated dislocation motion mechanisms are responsible for adiabatic shear bands. One of the revealing results of that study was the flow softening behavior of the flow stress curve at strain rate of 1  $s^{-1}$  and temperature of 980 °C above the strain value of 0.3. Since there was no flow stress data presented below 960 °C,

it was not possible to discuss possible dynamic strain aging behavior of Ti–6Al–4V. In summary, it was concluded that flow stress of Ti–6Al–4V alloy is more sensitive to the temperature than to the strain rate (Nemat-Nasser et al., 2001).

### **1.3.3.1 Adiabatic shearing and flow softening phenomenon**

In machining titanium alloys, it is commonly known that plastic instability and adiabatic shearing related chip serration occurs. Work material often goes to secondary shearing after primary shearing zone and saw-tooth shape regular chip segments form. The underlying cause of chip serration is often associated with adiabatic shearing (Komanduri & Hou, 2002). Recent studies have considered the effects of flow softening and adiabatic shearing effect on the behavior of titanium Ti–6Al–4V alloy at high strains (Calamaz et al., 2008) and (Sun & Guo, 2009). The flow softening is believed to be related to dynamic recovery and/or recrystallization occurring after a critical value of strain. The effect of flow softening is more pronounced at low temperatures, and as temperatures increase, both strain hardening and flow softening effects are reduced. Recently, Calamaz et al. (Calamaz et al., 2008) modified the J–C material constitutive model by multiplying it with a function in order to include flow softening in their simulations. They were able to simulate serrated chip formation resembling experimental chips. They did not study the influence of different flow softening parameters on the simulations. Sun & Guo (Sun & Guo, 2009) pointed out the difference between machining and compression tests and considered the adiabatic effect on the flow stress. They calculated shear flow stress during machining by using an orthogonal machining model and showed that flow stress values obtained at high strains are much lower than flow stress values obtained under isothermal conditions with compression tests. In this study, the strain-rate and temperature sensitivity as well as interrelationship between strain–strain rate and softening at high strains in dynamic behavior of Ti–6Al–4V alloy is also investigated.

### 1.3.4. Strain rate and temperature sensitivity

The influence of increasing strain rate on the flow stress is represented with strain rate sensitivity parameter  $\delta$ , defined as

$$\delta = \frac{(\sigma_2 - \sigma_1)}{\ln(\dot{\epsilon}_2/\dot{\epsilon}_1)} \quad (1.13)$$

Strain rate sensitivity is calculated by considering the difference in flow stress values at two different strain rate levels at each strain using Equation 1.13 and it is found that strain rate sensitivity decreases with increasing strain (Lee & Lin, 1998b). The influence of increasing temperature on the flow stress, i.e. temperature sensitivity, is represented with a parameter  $n_a$  defined as

$$n_a = \frac{\{\ln(\sigma_2/\sigma_1)\}}{\{\ln(T_2/T_1)\}} \quad (1.14)$$

where  $T_2 > T_1$ , and  $T_l = 25$  °C. Using Equation 1.14, temperature sensitivity is calculated similarly. The resultant strain rate sensitivity and temperature sensitivity are shown in Figure 1.2 and Figure 1.3 by using the flow stress data given in Figure 1.1. During deformation, the rate of thermal softening caused by increasing temperatures is found greater than that of strain hardening induced by plastic deformation, and thus it can be seen that strain rate sensitivity decreases rapidly with increasing strain for all the strain rate ranges.

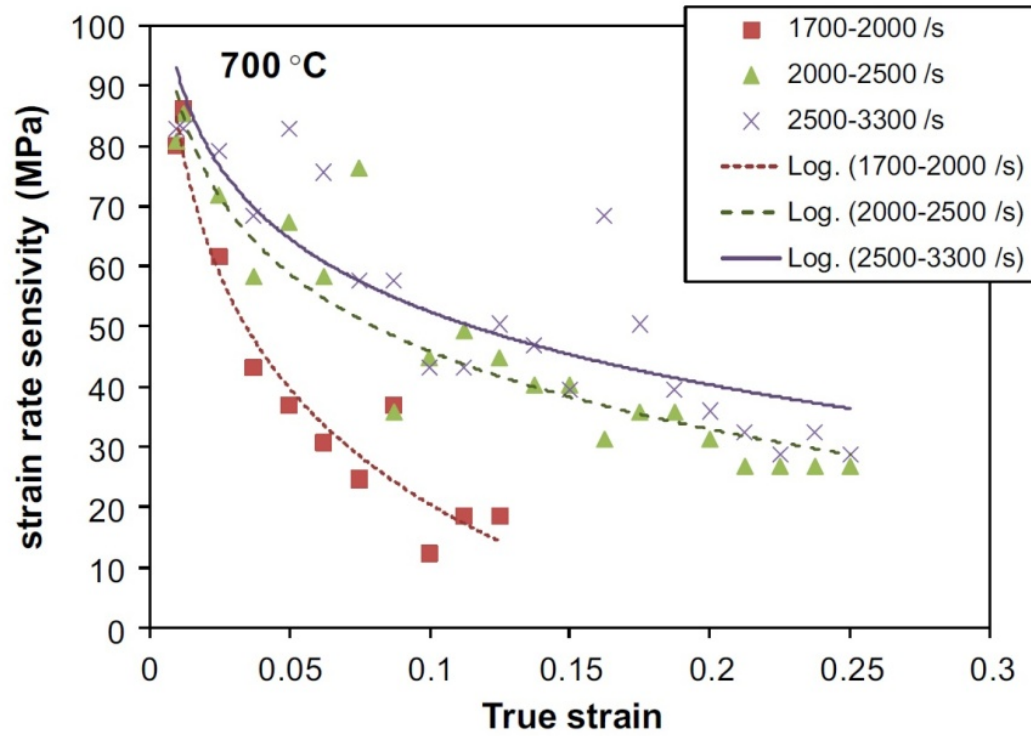


Figure 1.2. The relationship between strain rate sensitivity and true strain (at 700 °C). (Sima & Özel, 2010)

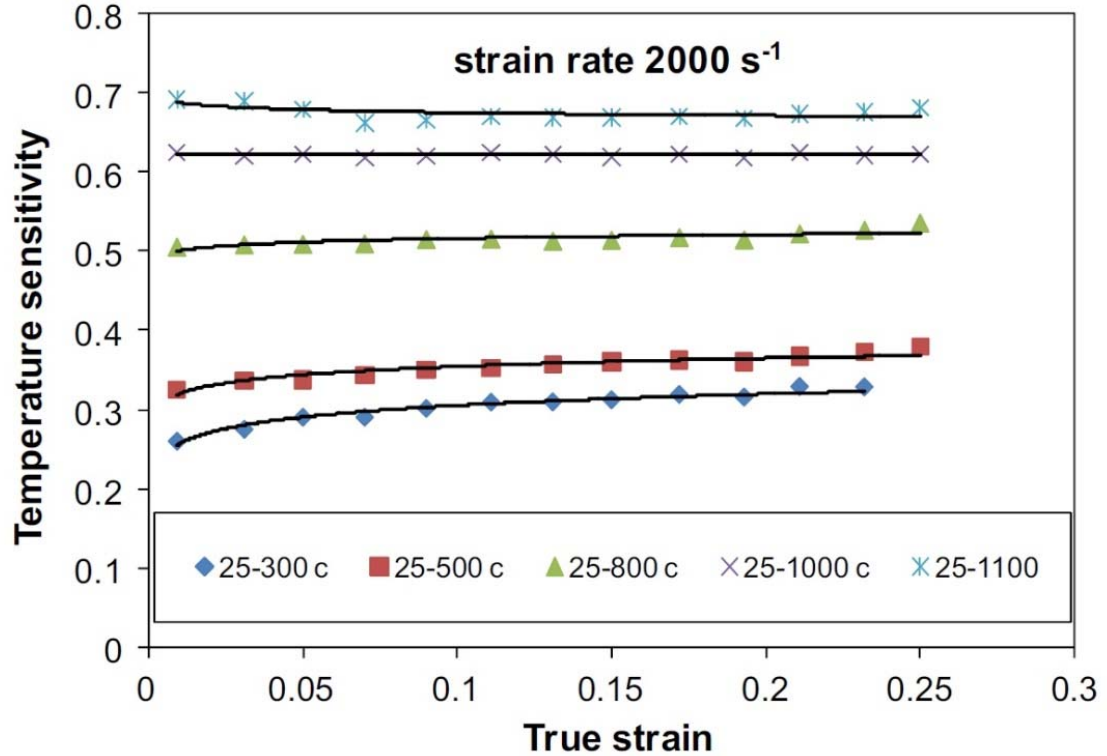


Figure 1.3. The relationship between temperature sensitivity and true strain. (Sima & Özel, 2010)

## 1.4. Physics Based Simulation Modeling

Although experimental tests are considered as the most useful and reliable procedure for research purposes, they are costly to design and sometimes hard to conduct; considering the fact that sufficient number of experiments are needed to achieve reasonable conclusion due to high sensitivity and dependency of output parameters to input parameters. Taking these limitations into account, simulation models play a significant role as a replacement for experimentation. Technically, it is necessary for the initial models to be verified and calibrated by experimental results in order to be validated properly for further use in predicting output parameters relevant to those experimental conditions. Importantly, these models should be physics-based which provide rich data about fundamental process variables (i.e., temperature, forces, stresses, etc.) empowering supplementary analysis on process performance (i.e., tool wear and life, etc.).

(2D) and (3D) FE-Modeling-based mechanics of machining processes are shown in Figure 1.4 in which the cutting tool and workpiece positioned against each other. Gradual movement of workpiece towards cutting tool models cutting motion. Assuming plain strain, vertical location of the cutting tool in 2D simulation signifies the feed rate. The behavior of the elements and their interactions during the simulation of the machining process, ascertains the field output parameters, such as temperature, stress, forces and strain, etc. Having satisfactory progress in simulation and appropriate quantities of reliable outputs, the FE-Modeling results will be compared to experiments results for validation purposes.

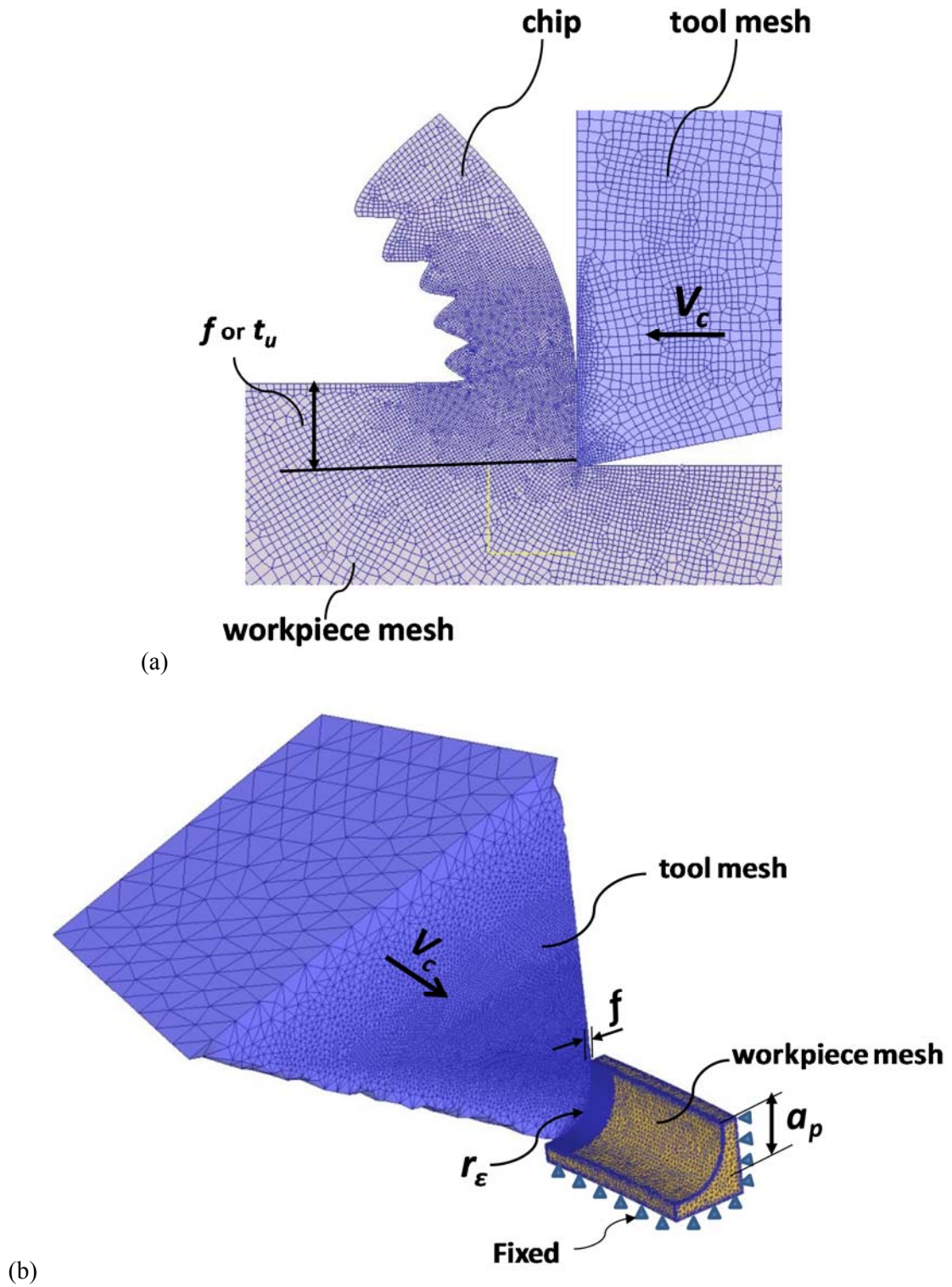


Figure 1.4. Illustration of simulation models for a: 2D and b: 3D machining processes

Preliminary simulation consists of two dimensional orthogonal cutting configurations. Changing the input machining parameters such as workpiece and tool material, tool micro-geometry and tool rake angle, feed, depth of cut and cutting speed, provides the path to diverse simulation analysis. However, there are couples of restrictions with 2D simulation such as plain strain deformation and symmetric mechanical setup assumption and also neglecting the third dimension, which rarely happens in real-life machining operations while could be considered as a good guide for researchers. Having successful and satisfactory results from 2D simulation make it possible to move to 3D simulations, in order to model the real and practical machining operation and take the third dimensions into account.

By this fashion, researchers would be able to design and conduct many simulations to study all aspects of the problem, for which, if they wanted to run experimental tests, it would be much more time consuming and costly.

Finite Element Analysis software DEFORM will be utilized for finite element-based simulation modeling, for both two-dimensional and three-dimensional, in this study. Using the results of the friction determination method, the hybrid friction models will be built. Besides, modified Johnson-cook temperature-dependent flow softening constitutive material models is taken into consideration for better representing the experimental results.

## **1.5. Advance Cutting Tools and Limitations**

Titanium alloy machining performance can be increased by improving cutting tool materials and coatings (Corduan et al., 2003) and (Bouzakis et al., 2009). Cubic boron nitride (cBN) material offers outstanding properties such as high hardness and wear resistance. However, cBN material has lower toughness and is not suitable for forming inserts into complex shapes. Recently, cBN coatings have been explored by applying several deposition techniques. Among these, physical vapor deposition (PVD) has been preferred since thinner coatings can be deposited and sharp edges

and complex shapes can be easily coated at lower temperatures. On the other hand, coating applied affects the edge radius of the inserts (typically causes an increase) and must be taken into consideration during tool performance analysis (Bouzakis et al., 2009).

In this dissertation research, single and multi-layer TiAlN and cBN coatings are experimented on tungsten carbide tool inserts (WC/Co) for possible improvements on tool wear during machining of Ti-6Al-4V titanium alloy. Positive tool geometry WC/Co inserts are coated by cBN using a PVD system; Magnetron Sputtering at BOREN institute of Turkey (Özel et al., 2010) and with collaboration in Atilim University. Machining performance of multi-layered coated inserts is examined in longitudinal turning of titanium alloy (Ti-6Al-4V) without using coolant (Özel et al., 2010). The performance of uncoated, TiAlN coated, cBN coated and multi-layer cBN + TiAlN coated tungsten carbide inserts is compared in terms of cutting forces and tool wear (Özel et al., 2010).

In addition, finite element (FE) simulations are utilized in investigating the tool temperatures and wear development (Özel et al., 2010). Two dimensional (2D) and three dimensional (3D) FE simulations have been designed and conducted to predict forces, temperatures and tool wear to investigate the advantages of coatings in machining of Ti-6Al-4V. In 3D FE simulations, updated Lagrangian FE modelling software DEFORM3D was used. The workpiece is modelled as plastic material where the material constitutive model of this deformable body is represented with the proposed modified J-C material model (Sima & Özel, 2010). The workpiece is represented by a curved model with 87 mm diameter which is consistent with the experimental conditions. Only a segment ( $3^\circ$ ) of the workpiece was modelled in order to keep the size of mesh elements small. Workpiece model includes 90,000 elements. The bottom surface of the workpiece is fixed in all directions. The cutting tool is modelled as a rigid body which moves at the specified cutting speed by using 180,000 elements. A very fine mesh density is defined at the tip of the tool and at the cutting zone to obtain fine process output distributions. The minimum element size for the

workpiece and tool mesh was set to 0.008 and 0.024 mm respectively. A tool edge radius of 5, 10 and 15 mm are designed for uncoated, single layer and multi-layer coated tools respectively for each simulation, since added layers in multi-coating design is increasing the edge radius of the inserts. All simulations were run at the same experimental cutting conditions. In 3D FE modelling, constant shear friction factor ( $m = 0.9-0.95$ ) was used to represent friction between tool and workpiece. 3D FE simulations are also utilized to predict tool wear. The tool wear rate models describe the rate of volume loss on the tool rake and flank faces per unit area per unit time. A tool wear rate model based on the adhesive wear proposed by Usui et al. (Usui et al., 1978) was employed. This model uses interface temperature ( $T$ ), normal stress ( $\sigma_n$ ), and sliding velocity ( $V_s$ ) at the contact surfaces as inputs and yields tool wear rate ( $dW/dt$ ) for a given location on the tool surface. FE simulation procedure is explained in detail in Chapter 2.

Despite several research studies performed on the development of new advanced coated cutting tools for machining of titanium alloys, unexpected tool failure or rapid tool wear development is still a major problem seen in titanium machining. Therefore, it is required to study factors affecting tool life such as machining process parameters (cutting speed, feed, depth of cut, etc.), tool coating materials and use of coolant or lubricant. It is also very important to study tool failure mechanisms and wear modes, meaning that whether tool is for example failed because of the tool sudden fracture, chipping off and/or gradual wear on flank and rake surfaces. Overall, it is critical to study reliability of these new and advanced uncoated and coated cutting tools at different machining conditions to find out which one of these cutting tools is less prone to failure comparing to others at the same conditions. Reliability of a cutting tool can be defined as the probability of not failing by certain amount of time. The failure can occur because of different wear modes and failure mechanisms. This research is focused on tool failure based on gradual wear during machining process. Once the magnitude of tool wear on either flank and/or rake surfaces reach to a pre-determined threshold level, tool is considered as failed.

Hitomi et al. (1979) and Lin (2008) analyzed the reliability of cutting tools based on the tool wear values obtained from metal cutting experiments data. They mainly tried to investigate this from a statistical point of view. They first selected an appropriate statistical distribution of tool wear, which in Hitomi case, they found the log-normal distribution to be the best fit, and in Lin's case, it was normal, and then based on distribution of tool life and reliability function of cutting tool. Lin also found that cutting speed has a direct relationship with tool flank wear and an inverse one with tool life and reliability of the cutting tool.

### **1.5.1. Wear-based degradation mechanisms**

Wear can be defined as loss of material from the body of the tool and is a result of fundamental process variables acting on the tool-workpiece interface due to relative sticking/sliding motion and cutting conditions. There are various mechanisms and modes of tool wear that have been observed in metal cutting. Tool wear mechanisms can be listed as adhesive wear, abrasive wear, delamination wear, wear due to chemical instability, and flaking wear based on physical and chemical nature of wear phenomenon and tool wear modes can be listed as flank wear, crater wear, chipping, and notch wear based on their location on the tool surfaces and edges (Holmberg & Matthews, 1998). The investigation of wear in machining due to cutting speed and temperature reveals that resultant tool wear is due to a complex combination of wear mechanisms and is highly sensitive to cutting conditions. For example, Figure 1.5 is showing the effect of increasing temperature due to changes in cutting conditions on tool wear indicating that different wear mechanisms become effective at different temperatures.

In general, cutting tools are generally subject to three basic modes of failure: a) Mechanical breakage or brittle fracture, b) Thermal failure or quick dulling, and c) Gradual wear.

- a) Mechanical breakage or brittle fracture: This type of failure happens when cutting force is excessively higher than cutting tool material strength.

- b) Thermal failure or quick dulling: Reaching to very high and elevated temperature leads the tool to undergo plastic deformation.
- c) Gradual wear: Gradual wear of cutting tools at their flank and rake face, as shown in Figure 1.6.

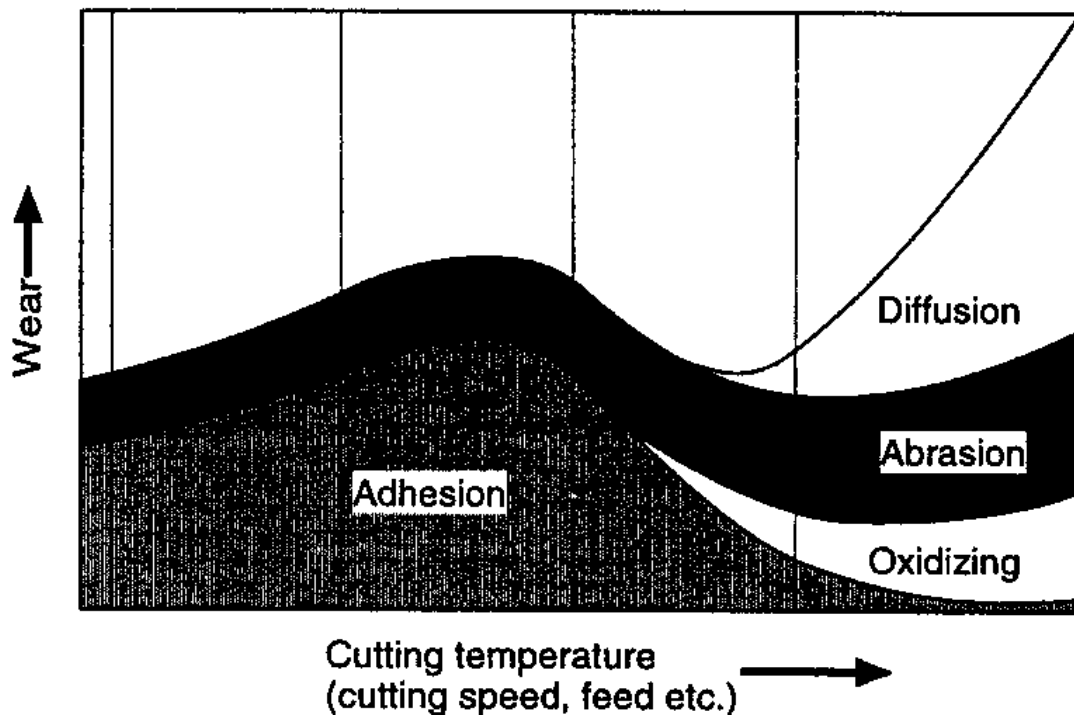


Figure 1.5. Schematic diagram of the tool wear mechanisms appearing at different cutting temperatures corresponding to cutting speed and feed (König 1984)

Despite the fact that first two aforementioned premature failure mechanisms are very harmful and detrimental for both workpiece and machine tool, it is possible to prevent them by selecting proper tool materials and geometry depending upon the workpiece material and cutting condition.

On the other hand, failure by gradual wear, which is inevitable, cannot be prevented but can be slowed down only to enhance the service life of the tool.

Cutting tool wear itself is classified to three main categories:

*Mechanical wear:* (a) thermally insensitive types: such as abrasion, delamination, and chipping, (b) thermally sensitive types: such as adhesion, flaking, fracturing etc. Abrasion usually happens when workpiece material contains very hard particles such as carbides; in this case microscopic variations on the bottom surface of the chips rub against the tool surface and break away a fraction of tool with them. While in adhesion, fragments of the workpiece get welded to the tool surface at high temperatures; eventually, they break off, tearing small parts of the tool with them.

*Thermomechanical wear:* (a) macro-diffusion by mass dissolution, (b) micro-diffusion by atomic migration (König 1984). In diffusion wear the material from the tool at its rubbing surfaces, particularly at the rake surface gradually diffuses into the flowing chips either in bulk or atom by atom when the tool material has chemical affinity or solid solubility towards the work material. Rate of such tool wear increases with the increase in temperature at the cutting zone. Diffusion wear becomes predominant when the cutting temperature becomes very high due to high cutting velocity and high strength of the work material.

On the other hand, chemical wear, leading to damages like grooving wear may occur if the tool material is not enough chemically stable against the work material and/or the atmospheric gases.

These tool wear mechanisms can be active on the tool faces at different rates due to chip-tool contact conditions, sliding velocity and interaction of surfaces at tool-chip and tool-workpiece interfaces. For this reason, tool wear modes can be classified due to their occurrence on the tool faces and geometry. These are; a) flank wear, b) crater wear, and c) notch wear as can be seen in Figure 1.6.

Flank wear at the front edge of the tool flank and crater wear at the tool rake face, as shown in Figure 1.6(a), are the most typical modes of tool wear in metal cutting. Flank wear is believed to be caused mainly by abrasion of the tool by hard particles, but there may be adhesive effects as well. It is the dominating wear mode at low cutting speeds. Crater wear is the formation of a groove or a crater on the tool rake face where the chip rubs the tool surface, as shown in Figure 1.6(b).

Cutting tools may experience different wear mechanisms in each of the flank and crater surfaces. Crater wear is mainly result of thermal-mechanical contact interaction at the tool-chip interface. This type of wear is predominant at high speeds and is caused by resultant very high temperatures. In modern machining applications, carbide and ceramic tools use metals or other types of binding materials as binder for the hard particles like carbides and cBN, these types of binding tend to weaken at elevated temperatures and promote rapid growth of crater wear (Byrne et al 2003). Therefore, temperature plays the key role in crater wear; hence crater wear is dominantly resulting of thermomechanical type of wear and/or mechanical wear sensitive to temperature. On the other hand, flank wear which is a result of tool and workpiece interface occurs during lower cutting speeds. The dominant mechanism causing flank wear is mechanical wear which is insensitive to temperature like abrasion.

In WC/Co cutting tools, tungsten carbide (WC) grains are bounded together with cobalt (Co) binders. At elevated temperatures, cobalt binder tends to soften faster and WC grains dislodge from tool surface during machining process which causes rapid tool wear. Researchers (Kagnaya et al., 2009, Jianxin et al., 2008, and Wang & Kwon, 2014) studied wear pattern of WC/Co cutting tools during machining process. Wang and Kwon (Wang & Kwon, 2014) reported that during machining of commercially pure Aluminum, flank wear was the main mode of wear, and increasing cutting speed causes increase in wear, while increase in WC grain size results in decrease in wear amount. Adhesion wear mechanism reported to be dominant wear mechanism on the crater wear mode and abrasion wear mechanism and hence dislodging of WC grains on the flank wear mode. Reduction of cobalt binder concentration in the worn area was observed as well which causes the WC grains to loosen easier and dislodge. Jianxin et al. (Jianxin et al., 2008) investigated WC/Co tool wear in dry machining of Ti-6Al-4V, finding that diffusion of elements from cutting tool to workpiece and vice versa happens during machining process. It is reported that diffusion rate is very dependent to temperature, while no diffusion is observed at 400°C, W and Co diffused long way into Ti-6Al-4V

at 600°C and 800°C. They also reported that titanium elements are diffused into WC/Co tool through tool-chip interface in machining process at 400°C which leads to change in cutting tool substrate composition and as a result, this both way diffusion accelerates the tool wear. In the research work by Kagnaya et al. (Kagnaya et al, 2009), it has been reported that in lower sliding speeds, the wear mechanisms of the WC/Co pin deal with plastic deformation and micro-cracking of WC grains, fragmentation and deboning of WC grains and polishing of the pin contact surface where at high sliding speeds, a supplementary wear mechanism is observed.

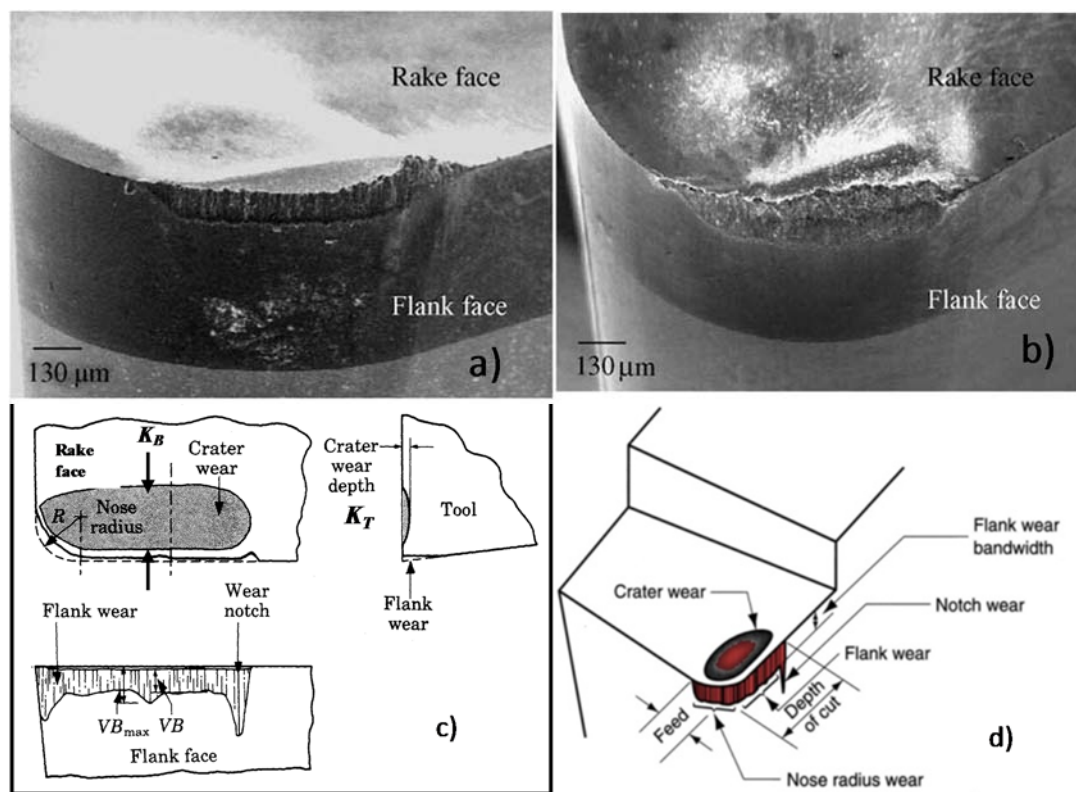


Figure 1.6. a) Flank and crater wear in machining of Ti-6Al-4V with WC/Co tool with coolant, b) Flank and crater wear in dry machining of Ti-6Al-4V with WC/Co tool (Muthukrishnan & Davim, 2011), c) schematic three views of a worn tool, and d) three dimensional schematic view of a worn tool (Kalpakjian and Schmid 2010)

### 1.5.2. Tool wear models

Many researchers have contributed on developing models for abrasive wear (Rabinowicz 1964, Shaw 1989 & Yamaguchi 1990), adhesive wear (Shaw 1989, Gahr 1987, Rhee 1970, Peterson et

al. 1974 & Jain and Bahadur 1979) and delamination wear (Gahr 1987, Suh 1973 & Jahanmir et al. 1974). These wear models are for the sliding wear mechanisms and given in terms of different parameters, such as the size and the shape of the abrasive particles, hardness of surfaces in contact, sliding distance and many others. Some of those models reveal that the amount of wear due to sliding wear mechanisms is directly proportional to the coefficient of friction, normal stress on the tool surface, sliding distance/velocity and inversely proportional to the hardness of the wearing surface. Models are also developed for non-sliding wear mechanisms and given in terms of different atomic and molecular properties as well as hardness and velocity. Research on solution and diffusion wear (Loladze 1981, Strenkowski et al. 1991 & Kramer and Judd 1985), and oxidation wear (Lim et al. 1993) concludes that the amount of wear is directly proportional to the temperature of the wearing surface. Therefore, for both categories of models, the amount of wear is related in one way or another to the physical process variables such as stress, temperature and velocity.

### 1.5.2.1 Flank and crater wear modeling

Location dependent, i.e. flank and crater, wear models that are expressed in terms of physical process variables such as stress, temperature and velocity are developed in (Kitigawa et al. 1988 & Maekawa et al. 1989). A characteristic equation based on sliding wear mechanism was formulated in (Kitigawa et al. 1988) from empirical results and given as,

$$\frac{dw}{dt} = C\sigma V_c \exp\left(\frac{-\lambda}{T}\right) \quad (1.15)$$

In Equation 1.15,  $\frac{dw}{dt}$  is depth of wear per unit time,  $\sigma$  is normal stress on the rake face,  $V_s$  is chip sliding velocity,  $T$  is temperature on the rake face,  $C$  and  $\lambda$  are the characteristic constants dependent on material combinations. This equation was formulated for sliding wear mechanisms and used for both flank and crater wear of carbide tools with different values of the constants  $C$  and  $\lambda$ . The

validity of the wear model was proven for dry machining of carbon steels (Maekawa et al. 1989). Later, a FEM code was generated to incorporate this particular wear model (Maekawa et al. 1996). In these simulations, chip shape was previously assumed and matched with the actual chip shape at every stage of simulation with trial and error. Crater wear depth for cutting high manganese steel and leaded Cr-Mo steel was calculated at the steady state using similar wear equations (Maekawa et al. 1993 & Maekawa et al. 1996).

Those FEM simulations were successful in predicting tool wear for given cutting conditions and workpiece/tool material pair but chip shape needed to be determined from the experiments for each cutting condition. It was claimed that conducting experiments is a rather expensive option and can be eliminated by using well proven FEM based simulations of deformation processes.

The review of the technical literature indicates that there is no predictive tool wear model independent of any empirical constants. Prior attempts to estimate tool wear illustrate that to reduce the amount of experimentation necessary to predict tool wear, a FEM-based approach may be useful. This approach, however, requires an additional programming tool that can interact with the FEM calculations and allow investigating various tool wear models in terms of various process parameters.

Several researchers attempted to correlate the results of tool life with the machining parameters (cutting speed, feed rate, etc.). The well-known Taylor's tool life relationship and its various extended equations are of this type (Oxley 1989 & Takeyama and Murata 1963), Figure 1.7. These empirical tool life equations include several constants that must be experimentally determined for the given combination of tool and workpiece materials. Tool wear rate models (the right column of Figure 1.7-left) describe the rate of local volume loss on the tool contact face (rake or flank face) per unit area per unit time. The derivations of this type of tool wear rate models require the knowledge of wear mechanisms associated with the tool and workpiece materials and the range of cutting conditions used. It is generally accepted that for carbide tools under practical cutting

conditions the wear rate is dominated by a temperature-sensitive diffusion process, in particular at higher cutting speeds (Mathew 1989, Molinari and Nourai 2002 & Usui et al. 1978).

Takeyama and Murata derived a fundamental wear rate equation by considering abrasive wear (Takeyama and Murata 1963). Mathew (Mathew 1989) analyzed the tool wear of carbide tools when machining carbon steels. At cutting temperatures higher than 800 °C, the first abrasive term  $G(V, f)$ , Figure 1.7, can be neglected (Mathew 1989). Molinari and Nouari (Molinari and Nourai 2002) proposed a new diffusion wear model by considering the contact temperature to be the main parameter controlling the rate of diffusion in the normal direction to the tool-chip interface.

Empirical Tool Life Models	Tool Wear Rate Models	Kanmately-Asibu's model
Taylor's basic equation: $VL^n = C_1$ ( $n, C_1 = \text{constants}$ )	Takeyama & Murata's wear model (considering abrasive wear and diffusive wear): $dW/dt = G(V, f) + D \exp(-E/RT)$ ( $G, D = \text{constants}$ )	$\frac{dh}{dt} = \frac{F_t P_0 K_0}{b L H_w} \left( \frac{n}{L b} \right)^{\frac{1}{2}} V \frac{T^a}{H_{r0} T_0} + 2 \frac{m}{L f \rho_t} C_0 \sqrt{\frac{D_0 V}{\pi}} e^{-\left(\frac{Q}{2RT}\right)} \frac{1}{L^{\frac{1}{2}}}$
Taylor's extended equation: $L = \frac{C_2}{V^p f^q d^r}$ ( $p, q, r, C_2 = \text{constants}$ )	Usui's wear model (considering adhesive wear): $dW/dt = A \sigma_n V_s \exp(-B/T)$ ( $A, B = \text{constants}$ )	where $h$ =height of welded joint torn off in shear, $V$ =cutting velocity, $F_t$ =thrust Force, $P_0$ =probability that a wear particle of the harder material be formed, $b$ =width of cut, $L$ =wear land length, $H_w$ =workpiece hardness, $n/Lb$ =number of welded asperity joints per unit area, $T$ =temperature, $H_{r0}$ =tool hardness at room temperature $T_0$ , $m$ =atomic weight of the diffusing species, $f$ =weight percentage of diffusing species in the tool material, $\rho_t$ =tool density, $C_0$ =concentration of diffusing species at the tool-work interface, $D_0$ =diffusion coefficient, $Q$ =activation energy for diffusion, $R$ =universal gas constant
Taylor's extended equation: $V = \frac{C_3}{L^m f^p d^q (BHN/200)^r}$ ( $m, p, q, r, C_3 = \text{constants}$ )		
Temperature-based equation: $TL^n = C_4$ ( $n, C_4 = \text{constants}$ )		
$L$ = tool life $T$ = cutting temperature $E$ = process activation energy $R$ = universal gas constant $dW/dt$ = wear rate (volume loss per unit contact area per unit time)	$\sigma_n$ = Normal stress $V$ = cutting speed $V_s$ = sliding velocity $BHN$ = workpiece hardness	
	$f$ = feed rate $d$ = depth of cut	

Figure 1.7. Summary of selected empirical tool life models and tool wear rate models (Yen et al., 2004)

For carbide tools (Usui et al. 1978, Kitigawa et al. 1988 & Maekawa et al. 1989) derived a wear rate model based on the equation of adhesive wear, which involves temperature, normal stress, and sliding velocity at the contact surface. Similar to the tool life models, the wear rate models involve unknown wear constants that depend on the given workpiece and tool materials and need to be determined by conducting some calibration cutting tests.

Smithey et al. (Smithey et al. 2000) developed a worn tool force model for 3D cutting operations. Jawahir et al. (Jawahir et al. 1995) analyzed the tool wear mechanisms in grooved tool inserts based on the associated chip flow patterns through high-speed filming and scanning electron microscopy (SEM). Chou et al. (Chou et al. 2002) experimentally investigated the effects of tool and workpiece microstructures on the wear of cubic boron nitride (cBN) tool in finish hard turning. A review of typical wear behaviors of soft and hard film coatings, metallic alloys, composites, and ceramics in relation to their frictional characteristics was summarized by Kato in (Kato 2000). Kannatey-Asibu (Kannatey-Asibu 1985) proposed a wear model for predicting the tool flank wear in hard turning. Kannatey-Asibu's model takes account both adhesion wear and diffusion wear (see Figure 1.7, right).

Shatla et al. (Shatla et al. 2000) have attempted to relate the experimental flank wear data in cutting 0.2% carbon steel, given by Mathew (Mathew, 1989), to the values of tool temperature, stress and sliding velocity predicted by cutting simulations, based on the Usui's wear model. A similar approach was also taken in analyzing different carbide tools by using a computer program (OXCUT) based on Oxley's analytical machining theory (Shatla, 1999). Further improvements that considered geometric changes have been summarized in (Yen et al. 2002). Recently, the tool wear model for an uncoated WC-Co carbide tool (Kennametal, K68) when orthogonal cutting AISI 1045 was developed and implemented on a 2D FEM, DEFORM-2D® (Schmidt et al. 2003 & Yen et al. 2002). The measurements of tool wear in cutting were performed in accordance with the ISO Standard 3685-1977 adopted by NIST (National Institute of Standards and Technology). The cutting tests were conducted at three different cutting speeds ( $V_c = 112, 208 \text{ \& } 300 \text{ m/min}$ ) with a constant feed rate of 0.145 mm/rev and width of cut of 2 mm. Figure 1.8 illustrates predicted results of the wear rate distribution with updated geometries of crater wear and flank wear for an uncoated carbide tool with an initial flank wear land of 0.06 mm when cutting AISI-1045 workpiece at cutting speed ( $V_c$ ) of 300 m/min, feed rate ( $f$ ) of 0.145 mm/rev.

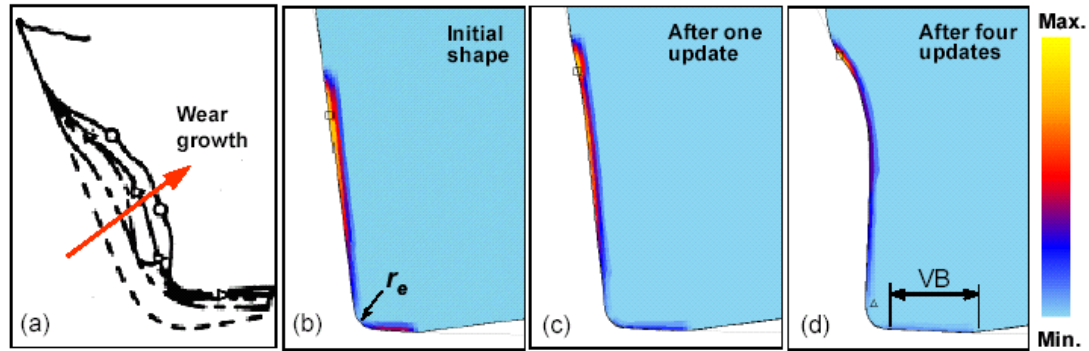


Figure 1.8. Predicted results of the wear rate distribution when orthogonal cutting AISI 1045 using uncoated carbide tool (Schmidt et al. 2003)

As mentioned earlier in this chapter several wear models are proposed by researchers. In this research, Usui's wear model (Usui et al., 1978) has been used in 3D finite element simulation models to predict tool wear. Usui's wear model, cutting tool wear rate is dependent on other physical output attributes of the machining process, i.e. temperature ( $T$ ), sliding velocity ( $V_s$ ), and normal stress ( $\sigma_n$ ). Due to the fact that cutting tool fails once the wear amount exceeds failure criteria or wear threshold, it is possible to build a reliability model for cutting tools based on physics-based wear models such as Usui's wear model. These physics-based reliability models are widely used in reliability engineering where failure of the component has some direct dependency to some physical and/or environmental inputs, such as temperature, humidity, voltage, etc. In section 1.6 some examples of reliability models that are based on physical phenomena are presented.

## 1.6. Physics-Based Reliability Analysis

Generally reliability modeling and analysis of parts, components and systems are based on statistically analyzing previously acquired failure data or predicting failure time again by assistance of statistical techniques. However, studying physics of the failure mechanisms of parts is another method of reliability analysis. Physics-based reliability analysis is either based on development of

theoretical formulations for the failure mechanisms or based on experiments which are conducted at different levels of stress parameters to find out time to failure accordingly. Therefore, it is essential to study reliability physics (kinetics) of the parts potential failure mechanisms and then develop the proper reliability model in order to either prevent or minimize the occurrence of device failure.

Reliability physics is basically about understanding the kinetics (temperature and stress dependence) of failure mechanisms. Device failure is usually associated with the degradation of a given material under certain amount of stress. This “stress” term varies with respect to application of the device. Electronic components can fail in result of high electric field stress, high current density stress and/or high voltage/field stress and etc. While mechanical components may fail due to fatigue because of cyclical mechanical stresses, frictional shear stresses and least but not last, can rupture in the result of crack propagation because of thermomechanical stress caused by temperature cycling (McPherson 2013).

To illustrate, some of the famous physical reliability models are listed as follows:

a) Electromigration Model:

Electromigration is the transport of microcircuit current conductor metal atoms due to electron wind effects. In case of very high density of electron current in an aluminum conductor, electron wind effect takes place. In a result of collision of enough numbers of electrons with the aluminum atom, the aluminum atom will move, causing gradual depletion at the negative end of the conductor. This will lead to hillocks or voids in the conductor, causing a catastrophic failure. The median time to failure as a result of electromigration is given by (Black 1969):

$$MTF = AJ^{-n}e^{E_a/kT} \quad (1.16)$$

where  $A$ ,  $n$  are constants,  $J$  is the current density,  $K$  is Boltzmann's constant.  $T$  is the absolute temperature, and  $E_a$  is the activation energy in Equation (1.16). The electromigration exponent  $n$  ranges from 1 to 6.

b) Corrosion Induced Failures:

Metal elements have a great tendency to oxidize/corrode naturally, therefore it is hard to find pure metallic element in nature comparing to its oxidized form. Significant amount of time, energy and budget is being spent for corrosion prevention and corroded parts replacement (McPherson 2013).

Researchers categorized Corrosion to two main classes, Dry Corrosion and Wet Corrosion. There are at least three oxidation models for dry oxidation: linear growth rate, parabolic growth rate and logarithmic growth rate. Assuming the initial growth rate for a period of time  $t_0$  remains erratic up to the point that some minimum oxide thickness  $x_0$  is reached. Afterwards, the growth rate follows one of the given regimes on top of the initial thickness and time conditions  $(x_0, t_0)$ .

As an illustration, linear growth model is explained here in Equation (1.17). In linear growth rate, it is assumed that the oxidized region thickness  $x$  grows constantly by the rate of  $k_1$  which depends on temperature.

$$\frac{dx}{dt} = k_1 \quad (1.17)$$

Where

$$k_1 = k_{10} \exp\left(-\frac{Q}{K_B T_{temp}}\right) \quad (1.18)$$

Assuming that oxidation thickness threshold for failure is  $(\Delta x)_{crit} = (x_{crit} - x_0)$  then  $T$ , time to failure is given by:

$$T = t_0 + \frac{(\Delta x)_{crit}}{k_{10}} \exp\left(\frac{Q}{K_B T_{temp}}\right) \quad (1.19)$$

Humidity induced oxidation is a form of wet corrosion. This happens when as a result of metal oxidation; it gives up its conduction electrons at the anode region of the metal. Hence, that ion must diffuse away from the corroded region in order to corrosion process to continue; otherwise increase in local electric potential will cause offsetting the chemical potential for oxidation. Time to failure equation for metal corrosion subject to humid condition is given as:

$$T = A_0 \exp\left[-a(\%RH) + \frac{Q}{K_B T_{temp}}\right] \quad (1.20)$$

where  $a$  and  $Q$  are the corrosion time to failure kinetics,  $RH$  is relative humidity, and pre-factor  $A_0$  can be a strong function of concentration of any corrosive contaminants in the water and a function of water acidity level (PH level).

c) Fatigue Failures:

Fatigue is a result of repetitive cyclic tensile and compressive stress on a material. As a result of this accumulation of damage caused by fatigue, the material fails at a lower stress level than its ultimate strength. Stresses which cause fatigue may be as a result of cyclic temperature or voltage. As an illustration, thermal expansion strains, or creep fatigue originated by thermal cycling is the main reason of breakage in surface mount technology (SMT) solder attachment of printed circuits (Flaherty 1994).

The reliability of components subject to fatigue failure is usually expressed as a number of stress cycles corresponding to a given cumulative failure probability. Following equation is a typical fatigue-induced failure of a solder attachment (Engelmaier, 1993)

$$N_f(x\%) = \frac{1}{2} \left[ \frac{2\varepsilon}{F} \frac{h}{L_D \Delta\alpha \Delta T_e} \right]^{\frac{-1}{c}} \left[ \frac{\ln(1 - 0.01x)}{\ln(0.5)} \right]^{\frac{1}{\beta}} \quad (1.21)$$

where

$N_f(x\%)$  = number of cycles (fatigue life) that corresponds to  $x\%$  failures;

$\varepsilon$  = the solder ductility;

$F$  = an experimental factor (Engelmaier, 1993);

$h$  and  $L_D$  = dimensions of solder attachment;

$\Delta\alpha$  = a factor of difference in thermal expansion coefficient of substrate and component;

$\Delta T_e$  = the effective thermal cycling range; and

$c$  = a constant related to average temperature of the solder joint and time of stress relaxation.

## 1.7. Statistics-Based Reliability Modeling of Cutting Tool Wear

There has been a number of research work published on reliability modeling of cutting tool wear and failure. According to the work done by Wager and Barash (Wager and Barash 1971), Hitomi et al. (Hitomi et al., 1979) and Lin (Lin 2008), it is commonly assumed that the flank wear land,  $V_B$ , is distributed as lognormal random variable. In this research not only we will demonstrate a statistics-based reliability model for the flank wear which has been extensively studied, but a separate model for the crater wear, assuming crater wear width,  $K_B$ , is distributed as Weibull random variable. Giving the flank wear and crater wear probability distribution functions as follows:

$$f_{V_B}(v_B) = \frac{1}{\sqrt{2\pi}\sigma v_B} \exp\left(-\frac{(\ln v_B - \mu_{v_B})^2}{2\sigma^2}\right) \quad (1.22)$$

$$f_{K_B}(k_B) = \frac{\gamma}{\theta} \left(\frac{k_B}{\theta}\right)^{\gamma-1} e^{-\left(\frac{k_B}{\theta}\right)^\gamma} \quad (1.23)$$

where  $\mu_{V_B}$  and  $\sigma$  in Equation (1.22) represent the mean and standard deviation of the logarithm of tool flank wear, and  $V_B$  is the random tool wear;  $\gamma$  and  $\theta$  in Equation (1.23) are the shape and scale parameters of the Weibull distribution respectively.

To illustrate, the reliability model of cutting tool and failure that is only based on experimental data and statistical point of view considering only the flank wear  $V_B$  would be explained in detail below. Similar methodology will be performed to derive reliability model of cutting tools based on crater wear  $K_B$  failure criterion.

Let the cumulative distribution function for tool life and its density function be denoted by  $Q(t)$  and  $q(t)$ , respectively. The end of tool life (failure) is defined by the limit of tool wear ( $V_B^*$ ), called the tool flank wear threshold.

Suppose that a cutting tool begins to function at the time period of  $t = 0$ , and that its failure occurs at  $t = T$ . Then, the probability that the cutting tool wears out prior to the time period of  $t$ , is given by:

$$\Pr\{T < t\} = Q(t) = \int_0^t q(u) du \quad (1.24)$$

Let the probability of tool flank wear and its density function is denoted by  $F(V_B)$  and  $f(V_B)$ , respectively, at time  $t$ . The probability that the tool wear reaches its life limit at time  $t = T$ , is given by:

$$\Pr\{V_B \geq V_B^*\} = 1 - \Pr\{V_B < V_B^*\} = 1 - F(V_B^*) = 1 - \int_0^{V_B^*} f(v_B) dv_B \quad (1.25)$$

Reaching to the conclusion of:

$$\int_0^t q(u) du = 1 - \int_0^{V_B^*} f(v_B) dv_B \quad (1.26)$$

Considering that the mean tool wear,  $\mu_{V_B}$  can be expressed as a function  $\psi(x_1, x_2, \dots, x_n)$ , of the independent variables,  $x_1, x_2, \dots, x_n$ . Introducing an error term  $\delta$ , tool life can be expressed as

$$V_B = \psi(x_1, x_2, \dots, x_n)(\delta) \quad (1.27)$$

Taking logarithm from both sides of the equation leads to:

$$\ln V_B = \ln \psi(x_1, x_2, \dots, x_n) + \varepsilon \quad (1.28)$$

where  $\varepsilon = \ln(\delta)$ .

Therefore the mean and standard deviation of the logarithm of tool flank wear can be obtained as:

$$\mu_{V_B} = E[\ln V_B] = E[\ln \psi(x_1, x_2, \dots, x_n) + \varepsilon] = \ln \psi(x_1, x_2, \dots, x_n) \quad (1.29)$$

$$Var[\ln V_B] = E[\varepsilon^2] = \sigma^2 \quad (1.30)$$

Assuming the logarithmic normal distribution for the tool wear distribution, as given by Equation (1.22), the following relation is obtained from equation (1.26).

$$\int_0^t q(u) du = 1 - \int_{-\infty}^{(\ln V_B^* - \ln \psi)/\sigma} \frac{1}{\sqrt{2\pi}} e^{-v_B^2/2} dv_B \quad (1.31)$$

Now, by assuming that the basic function of  $\psi$  is given by:

$$\psi(x_1, x_2, \dots, x_n) = \psi(a_p, v_c, t_u, t) \quad (1.32)$$

where  $a_p$  : depth of cut (mm),  $V_c$ : cutting speed (m/min),  $t_u$ : feed (mm/rev), and  $t$ : cutting time (min). In case that the relationship between the tool wear and machining variables are exponential (Hitomi et al. 1979), this relation can be expressed as,

$$\psi(a_p, v_c, t_u, t) = C_0 a_p^{\beta_1} v_c^{\beta_2} t_u^{\beta_3} t^{\beta_4} \quad (1.33)$$

where  $C_0, \beta_1, \beta_2, \beta_3$  and  $\beta_4$  are constants, which are determined from experimental results.

Basically the physical meaning of  $\psi(a_p, v_c, t_u, t)$  at time  $t$  is the mean of tool wear at that time:

$$\mu_{V_B} = \psi(a_p, v_c, t_u, t) \quad (1.34)$$

Now by differentiating Equation (1.31) with respect to  $t$ ,  $q(t)$  is obtained as follows:

$$q(t) = V_B^* \frac{\psi'}{\psi} \frac{1}{\sqrt{2\pi}\sigma V_B^*} e^{-\frac{(\ln V_B^* - \ln \psi)^2}{2\sigma^2}} = V_B^* \frac{\psi'}{\psi} f(V_B^*) \quad (1.35)$$

Substituting equation (1.33) into equation (1.35), tool life probability density function becomes,

$$q(t) = \frac{1}{\sqrt{2\pi}(\sigma/\beta_4)t} e^{-\frac{(\ln \hat{\mu}_T - \ln t)^2}{2(\sigma/\beta_4)^2}} = \phi\left(\frac{\ln \hat{\mu}_T - \ln t}{\sigma/\beta_4}\right) \quad (1.36)$$

where  $\hat{\mu}_T$  is estimate of mean tool life and can be calculated from the following equations. Since,

$$\mu_{V_B} = C_0 a_p^{\beta_1} v_c^{\beta_2} t_u^{\beta_3} t^{\beta_4} \quad (1.37)$$

The estimate of tool life,  $\hat{\mu}_T$ , when tool flank wear volume reaches to its failure threshold,  $V_B \geq V_B^*$ , would be

$$\hat{\mu}_T = \left( \mu_{V_B} / C_0 a_p^{\beta_1} v_c^{\beta_2} t_u^{\beta_3} \right)^{1/\beta_4} \quad (1.38)$$

Thus, the tool-life distribution which is determined from the tool-wear distribution, also obeys the logarithmic normal distribution. It has been assumed that the life length of a cutting tool,  $T$ , is a random variable with distribution function of  $Q(t)$ , which completely determines the reliability of the cutting tool. With this function, the reliability function,  $R(t)$ , i.e., the probability of failure-free operation of the cutting tool during the time  $t$ , is given by:

$$\begin{aligned} R(t) &= 1 - Q(t) = \Pr\{T > t\} \\ &= \int_t^\infty \frac{1}{\sqrt{2\pi}(\sigma/\beta_4)u} e^{-\frac{(\ln \hat{\mu}_T - \ln u)^2}{2(\sigma/\beta_4)^2}} du \\ &= \Phi\left(\frac{\ln \hat{\mu}_T - \ln t}{\sigma/\beta_4}\right) \end{aligned} \quad (1.39)$$

Using the above function, the reliability measures of the tool is as follows:

1. Mean time to failure:

$$\mu_T = E[T] = \int_0^\infty t q(t) dt = \int_0^\infty R(t) dt = \hat{\mu}_T e^{(\sigma/\beta_4)^2/2} \quad (1.40)$$

2. Variance of tool life:

$$\begin{aligned} Var[T] &= E(T - \mu_T)^2 = \int_0^\infty t^2 q(t) dt - \mu_T^2 \\ &= 2 \int_0^\infty t R(t) dt - \mu_T^2 \\ &= \mu_T^2 \left[ e^{(\sigma/\beta_4)^2/2} - 1 \right] \end{aligned} \quad (1.41)$$

3. Hazard rate of the cutting tool;

$$\begin{aligned}
h(t) &= \frac{q(t)}{1-Q(t)} \\
&= \frac{1}{(\sigma/\beta_4)t} \left\{ \phi\left(\frac{\ln \hat{\mu}_T - \ln t}{\sigma/\beta_4}\right) / \Phi\left(\frac{\ln \hat{\mu}_T - \ln t}{\sigma/\beta_4}\right) \right\}
\end{aligned} \tag{1.42}$$

## 1.8. Motivation

In order to summarize, this research is mainly focused on development of physics-based simulation and modeling of machining process of titanium alloy Ti-6Al-4V in order to reduce the number of costly and time-consuming experimental machining tests. However, for the purpose of validation of simulation models, some experimental tests have been designed and conducted initially. The initial inputs of this research work are machining conditions, cutting tool material and coating properties and micro-geometry, and workpiece material properties, then the study utilizes FEM-based simulations to predict the forces, serrated chip morphology, tool wear, temperatures, and stresses. Furthermore, these predictions are validated with experimental results (mainly cutting forces, chip geometry and tool wear), and the deterministic property models such as material constitutive model will be achieved. Tool wear and effect of tool material, coating materials and multi layered coating under different cutting conditions are experimentally tested and then validated using the 2D and 3D FE simulations. Among these outputs, cutting forces, chip morphology and tool wear will be validated with experimental findings, and the input parameters will be optimized based on these findings. These results will be further used to establish cutting tool experimental and physics based reliability models knowing the failure mechanisms following with multi-objective optimization of reliability of cutting tools and machining efficiency. The major methodologies that will be used to establish these relationships are explained below.

1. **Experimental modeling:** Even though it is possible to find out the relationships between inputs and outputs by experimentation and the results are more accurate and reliable;

extensive number of experimentation need to be designed and conducted which takes very long time to reach to certain level of significance. Two-dimensional (orthogonal) and three-dimensional cutting tests using different cutting tools and coating types are designed and conducted under some specific cutting conditions. Forces, chip morphologies and tool wear are measured, for the purpose of model validation, since performing extensive experimental study is very costly and time-consuming, a better method that is less costly and faster is required.

2. **Finite element modeling:** Cutting tool and workpiece are modeled from small element building blocks in Finite Element Analysis-based techniques by employing the principles of continuum mechanics. If the inputs and the sub-routines and sub-models of the finite element model are well-defined, these techniques offer the optimal results based on reliability, quickness, and cost-effectiveness, with the advantage of involving not too many assumptions. Moreover, finite element analysis based methodologies provide researchers with a thorough set of output parameters and cutting forces with respect to time, strain, stress, geometries such as chip morphology, tool wear, and temperature distribution fields in tool and workpiece. By using these finite element simulations, modifications to the Johnson-Cook material model is proposed and tested with FE models, and further validated with the experimentally generated cutting forces and chip morphology. The main problems with these models are concerned with meshing of the workpiece and the viscoplastic deformation assumption that needs to be done with three-dimensional simulations. Unlike 2D finite element simulations that are designed using elasto-viscoplastic workpiece material assumption, the software failed to run simulations of machining process by this type of material assumption. Therefore, plastic workpiece material assumption, the closest to real flow stress model of material, is considered for 3D simulations. This model assumption overlooks the material behavior in elastic region and therefore the simulation

loses the accuracy in prediction of force, stress, temperature, etc. to some extent. Therefore, it should be noted that 3D FE simulation of machining with plastic workpiece material assumption is not able to generate serrated chip.

3. **Reliability analysis of coated and uncoated cutting tools:** Based on experimental results and finite element simulation results of different cutting tools (uncoated, coated, multi layered coatings), reliability models of these cutting tools are derived. Wear condition in different cutting zones (tool tip trailing, tool nose radius and tool cutting edge) are investigated and a reliability model associated to each of these regions is generated based on both experimental and physics-based finite element results. Failure of each of these regions results in failure of the tool, meaning that once tool wear magnitude reaches to the specified failure criteria (threshold) associated to that specific wear region, tool is considered as failed; hence a competing risk reliability model for each tool is developed afterwards.

It is important to note that failure of a cutting tool is often considered fracture or loss of tool material at cutting edge so that cutting tool loses geometrically defined edge geometry. This loss could happen by different mechanisms, such as gradual wear, sudden chip-off, and chemical reaction, etc. this research is only focused on failures caused by gradual wear.

4. **Multi-objective optimization:** Physics-based reliability models of each tool type have been utilized to construct a multi-objective optimization problem in which one objective is to maximize the reliability, and the other is to maximize the Material Removal Rate (MRR) which is a good measure for machining efficiency. To solve this problem Fast Non-dominated Sorting Genetic Algorithm (NSGA II) is being utilized. Feed, cutting speed and tool type are considered as the decision variables in which selection of their optimum values leads to optimum values of these two objective functions.

In this study, a combination of experimental modeling and finite element modeling was used, while also some reliability modeling is employed for evaluation of different types of cutting tools in terms of reliability and then constructing multi-objective optimization problem. A new constitutive material model is proposed for titanium alloy Ti-6Al-4V in this research as well.

## 1.9. Objectives

The main research objectives of this study is to first develop a meaningful material constitutive model to use as a precise input for the process simulation for further predictions of temperature, stress and therefore, tool wear under different cutting conditions. Hence based on these predictions, and by utilizing deterministic and probabilistic modeling approaches to find out the reliability of the cutting tools and optimization of machining parameters and tool selection (material, coatings and geometry), manufacturing of titanium alloys would be more sustainable and less costly for the industrial sections. The following specific objectives of the research present the overall achievements of the study:

**Objective 1:** Comprehensive understanding of the physics and mechanics of the machining process, mechanical and thermal properties of titanium Ti-6Al-4V, including temperature-dependent flow softening, dynamic recrystallization, adiabatic shearing and in general, material constitutive model. Employing this knowledge may result in building accurate physics-based simulation models and more accurate prediction of process outputs such as cutting forces, tool wear, temperatures, and stresses.

**Objective 2:** FE based process models link inputs such as machining parameters (cutting speed, feed, depth of cut), tool parameters (material, coating material, coating thickness, multi or single layer coating, rake angle), and workpiece parameters (material) to outputs (force, temperature, tool wear rate, worn geometry). These models will be extended to establish a physics-based reliability modeling system that can be better utilized in the industry.

**Objective 3:** Input set of parameters such as cutting speed, feed rate, depth of cut, tool cutting edge radius, rake angle, tool material and coatings, and workpiece material all have different influences on the force, temperature, tool wear and stress outputs. In the end, this result in different level of tool wear, mechanisms of tool failure, and these different conclusions will be investigated using the reliability modeling of cutting tools.

**Objective 4:** Reliability of different types of cutting tools are modeled and investigated using both experimental and physics-based simulation results and effects of input parameters, such as cutting speed, feed and type of tool on the reliability is studied. In this research, the main concentration is on the crater wear failure which is the main failure mode of carbide tools in machining of titanium alloys.

**Objective 5:** After investigating the influences of different parameters and generating of competing risk reliability models for cutting tools, the input parameter set selection (i.e feed, cutting speed and tool type) will be optimized. In this optimization process, multiple objectives are achieved and satisfied as much as it is possible. These objectives include but may not be limited to maximizing reliability of cutting tool and material removal rate. Decision variables of this multi-objective optimization problem are feed ( $f$ ), cutting speed ( $V_c$ ) and, selection of tool type. The results of reliability models are further validated with special tool wear experiments that are run at calculated cutting conditions and for expected failure threshold and failure time.

## **1.10. Summary of the Dissertation**

The detailed organization of this dissertation is as follows:

Chapter 2 will be focused on physics based simulation of titanium machining process. First, the procedure and the reason of having a detailed material constitutive model which is able to capture the material behavior in very high strain rates and elevated temperatures will be presented. Many different models have been studied and tested and the best one that has been developed is with

temperature-dependent parameters and captures the unique phenomenon of strain softening which happens in some specific alloys such as Ti-6Al-4V. Then, necessity of 2D and 3D finite element simulation is going to be discussed. The proposed material constitutive model will be verified by utilizing the 2D simulation results and experimental studies using cutting force measurements and serrated chip morphology. The best material constitutive model will be incorporated in 3D FE simulation models yielding accurate prediction and estimation of the cutting tool wear mechanisms and effect of coatings, tool material and tool micro-geometry.

In Chapter 3, experimental set-up, selected process parameters (uncut chip thickness, cutting speed, feed rate, etc.), different types of cutting tools (uncoated vs. coated, tool tip design, tool base and coating material) will be introduced and discussed. After conducting 3D cutting tests, cutting forces are measured and recorded during experiments using a force dynamometer attached to the machine. Chips are collected for every run in order to measure the chip geometry using optical microscopy. Furthermore, worn regions of the cutting inserts are closely studied and evaluated.

In Chapter 4, derivation of physics-based and experimental-based reliability of cutting tools used during the course of research will be studied. The cutting tools under the study are used to machine Ti-6Al-4V titanium alloy, therefore both experimental data and simulation results will be used to conduct the reliability evaluation of the cutting tools. Reliability estimation of coated cutting tools will be the next step. Since the main reason of tool failure in machining process is tool wear and fracture, in order to perform such a study, mechanisms of tool wear should be carefully understood. In this research, the main concentration is on crater tool wear rather tool flank wear because of two reasons; first, tool crater wear seems to be dominant factor in failure of carbide tools in machining of titanium alloys and second, because of the complexity of crater worn surface, very few researchers studied crater wear-based failure. The new concept of dividing the crater wear zone to three sub-regions (tip trailing, nose radius, and cutting edge) is introduced in this chapter followed by modeling reliability of these individual zones respectively.

Chapter 5 is dedicated to multi-objective optimization of machining process for titanium alloy Ti-6Al-4V. Objectives of interests in this research were maximization of physics-based reliability of cutting tools modeled in Chapter 4 and maximization of material removal rate as an indication of process efficiency. Fast Non-dominated Sorting Genetic Algorithm (NSGA-II) is utilized to solve multi-objective optimization problem. Machining input parameters are decision variables needed to be optimized include feed, cutting speed and selection of type of tool out of four choices.

## **2. FINITE-ELEMENT BASED PROCESS SIMULATIONS**

## 2.1. Introduction

In order to understand mechanics of machining processes, the best and most accurate solution is conducting a set of experiments and run a thorough experimental analysis as is the only complete physics-based method. However, since there are large numbers of input parameters under the study and some of these parameters tend to have combined effects as well, conducting comprehensive study of machining process all experimentally would be very timely, long, and in some cases almost impossible. These parameters could be categorized as:

- Machining parameters: Feed rate, depth of cut, width of cut, cutting speed, lubricant use, etc.
- Cutting tool parameters: Tool material, rake, flank, and other tool angles, coating material, single or multiple layers of coating, coating thickness, method of coating, tool nose radius, edge radius, etc.
- Workpiece parameters: physical, thermal, and mechanical properties, material hardness, chemical composition, pre-processing history, etc.

Therefore, it is clear that there is critical demand for a method to simulate the machining process, preferably physics-based analytical methods which take the physics of phenomenon into account and are based on the proven computational methods such as finite element methods. Using these physics-based simulation methods, several important measures of the process can be analyzed, compared, and validated with experimental results (such as stress, strain, strain rate, and temperature fields, etc.).

In Finite Element Analysis (FEA) based methods, simulation of the process is relatively fast with high accuracy and a comprehensive set of process output variables (chip morphology, stress, and strain and temperature fields) can be achieved for validation purposes. Once the validation is completed, these process outputs can be used in predicting other types of physics-based parameters

such as tool wear and therefore requirement of further experimental tests would be eliminated after validation of physics-based simulations via experimental machining tests by measurements of chip morphology, cutting forces, and temperatures. Analytical simulation modeling is a powerful tool for optimizing the machining parameters such as tool material, tool edge geometry, and cutting conditions. Simulation modeling empowers the researchers to reduce or optimize the costly experimental analysis. In order for us to model the specimens analytically, updated Lagrangian software DEFORM-2D and DEFORM-3D is utilized in this research which is explained in this chapter, further. This research covers both 2D and 3D simulation modeling which are presented in chapters two and three, respectively. Also, the differences between the two types of modeling and analyzing are shown in chapter three. These differences are mainly coming from the complicated nature of 3D analysis as compared to 2D analysis in running, controlling, and obtaining output data. The output results from both analyses are presented in chapter four. The last chapter includes the conclusions for both 2D and 3D sections.

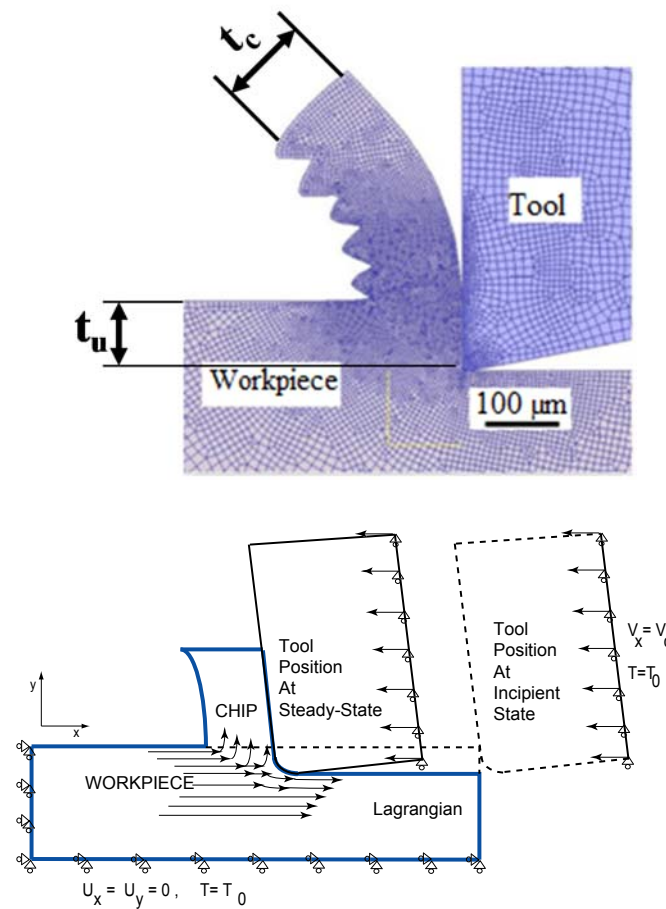


Figure 2.1. Mesh for the workpiece and the tool (a) and the boundary conditions (b) (Özel and Zeren, 2007)

## 2.2. Constitutive Material Models for Ti-6Al-4V Titanium Alloy

In thermal-mechanical processing of workpiece material during machining process, localized flow softening phenomenon can occur which can be described as offering less resistance to local plastic deformations due to rearrangement of dislocations caused by subsequent cycling or dynamic recrystallization in the material. This phenomenon is usually observed during an increase in strain beyond a critical strain value together with a rapid rise in material's temperature. Flow softening is believed to cause adiabatic shearing within the primary shear zone. Thus, chip segmentation with shear bands are formed as the deformed material leaves this zone.

For this reason, modified material constitutive models with flow softening resulting from strain softening and temperature softening are sought in literature. By developing such a modified constitutive model and implementing it into Finite Element software Forge-2D, Calamaz et al. (Calamaz et al. 2008) were able to simulate serrated chip formation in machining of titanium alloy Ti-6Al-4V.

### 2.2.1. Modified material model with non-temperature-dependent parameters (*Model I*)

During flow softening, flow stress begins to decrease with increasing strain beyond a critical strain value and resumes strain hardening behavior with further increase in strain. Below that critical strain, the material exhibits strain hardening. Therefore, a flow softening modification should be included in the modified Johnson-Cook (J-C) (Johnson and Cook 1983) constitutive material model.

In order to include the effect of flow softening at high strains, another term is integrated into flow stress as shown in Equation (2.1). The purpose of using tanh function is to leave flow stress at low (experimental) strains unchanged and introduce different levels of softening at higher strains through parameters  $p$ ,  $r$ ,  $S$ , and  $M$ :

$$g(\varepsilon) = M + (1 - M) \left[ \tanh \left( \frac{1}{(\varepsilon + p)^r} \right) \right]^S \quad (2.1)$$

Thus, this modified J-C model with an overarching flow softening modifier becomes

$$\sigma = (A + B\varepsilon^n) \left( 1 + C \ln \frac{\dot{\varepsilon}}{\dot{\varepsilon}_0} \right) \left[ 1 - \left( \frac{T - T_r}{T_m - T_r} \right)^m \right] \left[ M + (1 - M) \left[ \tanh \left( \frac{1}{(\varepsilon + p)^r} \right) \right]^S \right] \quad (2.2)$$

In this modified J–C material model, the SHPB test data obtained at high strain rates and high temperatures by Lee and Lin (Lee and Lin, 1998b) as given in Figure 2.2 is employed.

Hence, a modified J–C model (*Model 1*) using an overarching modifier that includes flow softening effect can be introduced. The flow stress curves depicting flow softening effect in *Model 1* are presented in Figure 2.3. The parameter  $M$  substantially modifies the flow stress after a critical value of strain ( $\epsilon_c$ ) around 0.5 mm/mm. However, it should be noted that flow softening is equally applied to flow stress at all temperatures.

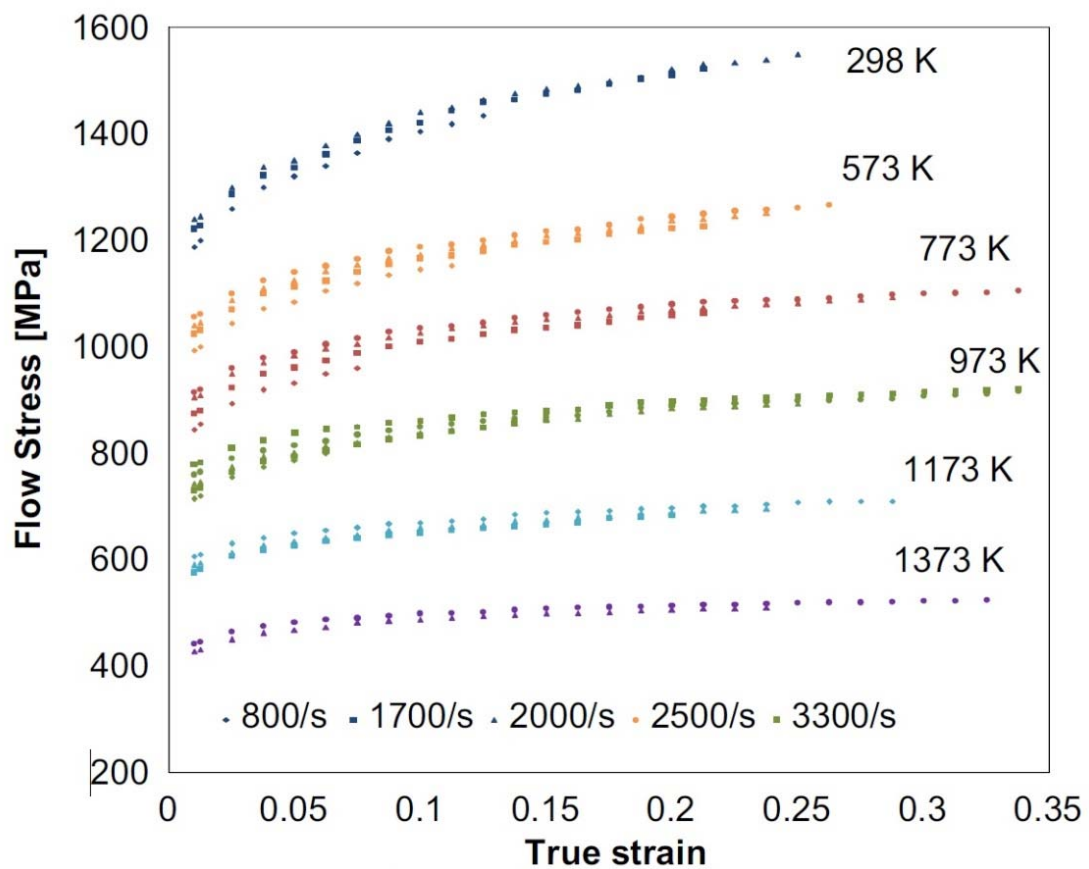


Figure 2.2. Flow stress data obtained from SHPB tests (Lee & Lin, 1998b)

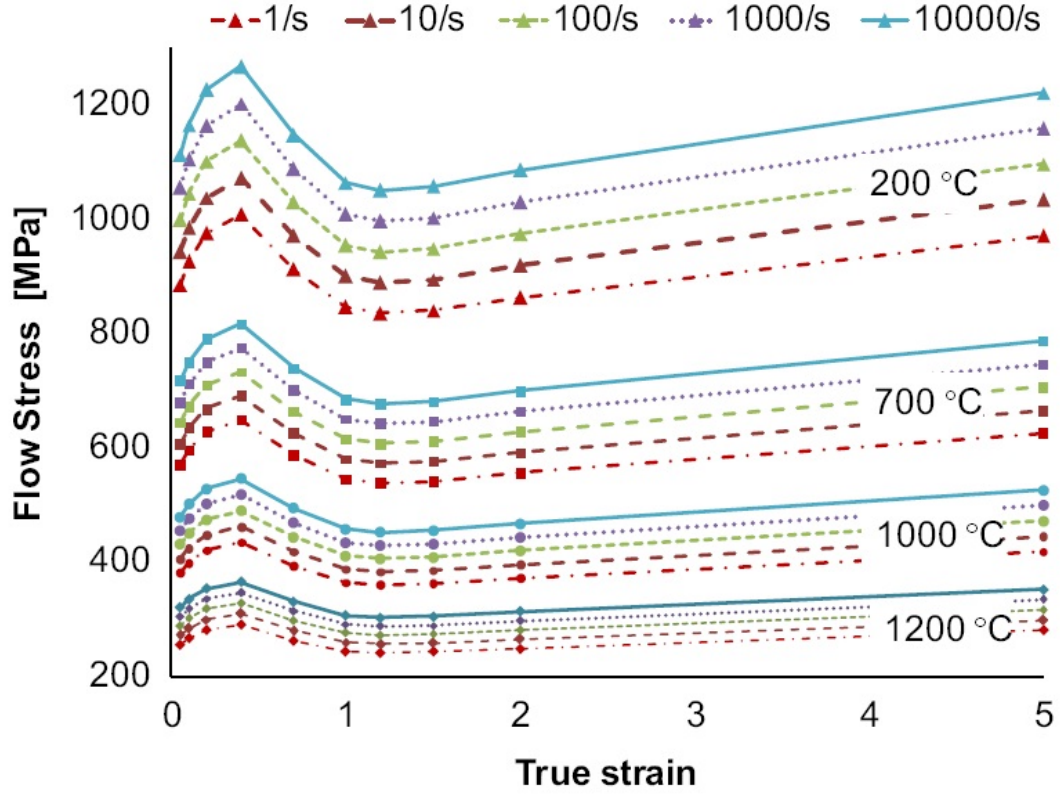


Figure 2.3. Flow stress curves using modified material model, *Model 1* ( $M = 0.7$ ,  $S = 7$ ,  $p = 0$ ,  $r = 1$ )

### 2.2.2. Modified material model with temperature-dependent parameters (*Model 2*)

Modifications to the thermal softening part of the J–C model by including temperature-dependent flow softening parameters are proposed and the model is given in Equation (2.3)

$$\sigma = (A + B\varepsilon^n) \left( 1 + C \ln \frac{\dot{\varepsilon}}{\dot{\varepsilon}_0} \right) \left[ 1 - \left( \frac{T - T_r}{T_m - T_r} \right)^m \right] \left[ M + (1 - M) \left[ \tanh \left( \frac{1}{(\varepsilon + p)r} \right) \right] \right] \quad (2.3)$$

where in this model, the parameters  $D$  and  $p$  are dependent on the workpiece temperature,  $T$ , as following:

$$D = 1 - \left( \frac{T}{T_m} \right)^d \quad \text{and} \quad S = \left( \frac{T}{T_m} \right)^b \frac{\gamma}{T_m}$$

Temperature dependency of the overarching modifier is governed by the exponents  $d$  and  $b$  which enhances the softening behavior of the flow stress at elevated temperatures (see Figure 2.4), since this phenomenon may be related to phase transformation and recrystallization of the material which may occur at a certain temperature range. This dependency on temperature and its effect on the flow stress model appear to be more reasonable than *Model 1* as shown in Figure 2.4. Flow softening gradually occurs with increasing temperature.

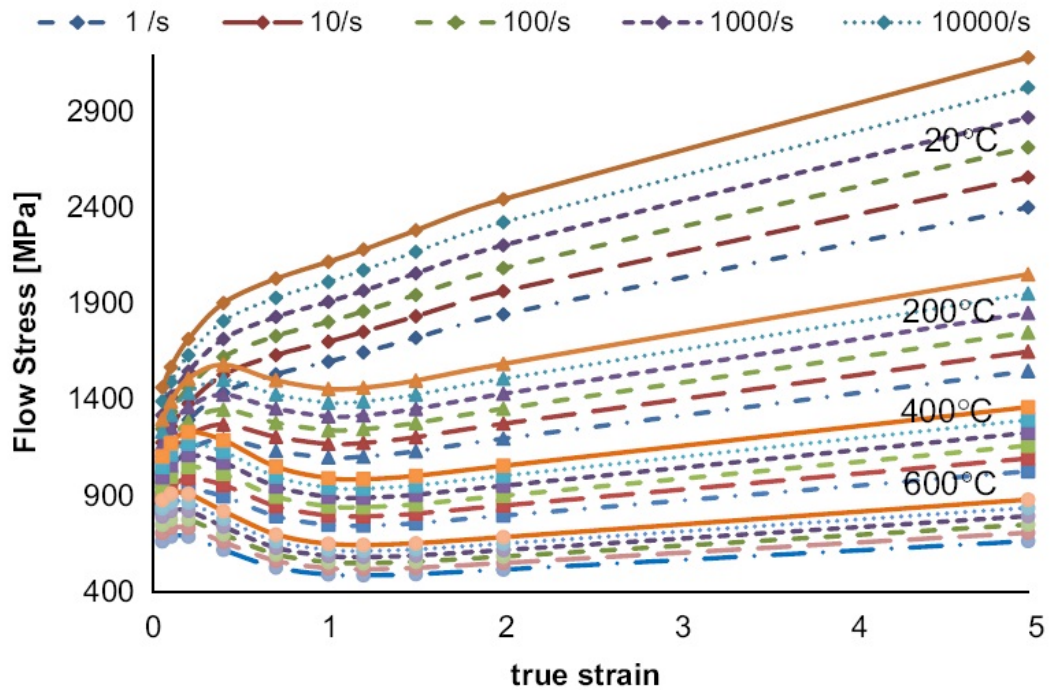


Figure 2.4. Flow stress curves using modified material model, *Model 2* ( $r = 1$ ,  $d = 0.5$ ,  $b = 1$ ,  $S = 5$ ) (Sima & Özel, 2010)

### 2.2.3. Modified material model with temperature-dependent parameters and strain softening (*Model 3*)

Further modifications to the strain hardening part of the J–C model by including flow softening at higher strain values are proposed and the model is given in Equation (2.4). This model is almost

identical to the Calamaz modified J–C (Calamaz et al. 2008) material model. Here an exponent  $S$  is introduced to further control tanh function for thermal softening.

$$\sigma = \left[ A + B \varepsilon^n \left( \frac{1}{\exp(\varepsilon^a)} \right) \right] \left[ 1 + C \ln \frac{\dot{\varepsilon}}{\dot{\varepsilon}_0} \right] \left[ 1 - \left( \frac{T - T_r}{T_m - T_r} \right)^m \right] \left[ D + (1 - D) \left[ \tanh \left( \frac{1}{(\varepsilon + p)^r} \right) \right]^S \right] \quad (2.4)$$

where  $D = 1 - (T/T_m)^d$  and  $p = (T/T_m)^b$

Again, the experimental flow stress curves obtained by Lee and Lin (Lee & Lin, 1998b) have been taken as the base for this Calamaz modified J–C model (Calamaz et al., 2008). In this modified model (*Model 3*), a multiplicative term is added to the strain hardening part, causes dependency of flow softening phenomenon not only upon temperature, but also on strain, as it can be seen in Figure 2.5. This additional term affects the softening behavior of flow stress at a controlled range of strain.

In order to identify the model parameters in *Model 3*, the effects of parameters,  $a$ ,  $b$ ,  $d$ ,  $r$  and  $S$  on the flow stress curves at high strain ranges and high temperatures are studied, while maintaining a good agreement between the model generated flow stress curves and the SHPB test data obtained from Lee and Lin (Lee & Lin, 1998b).

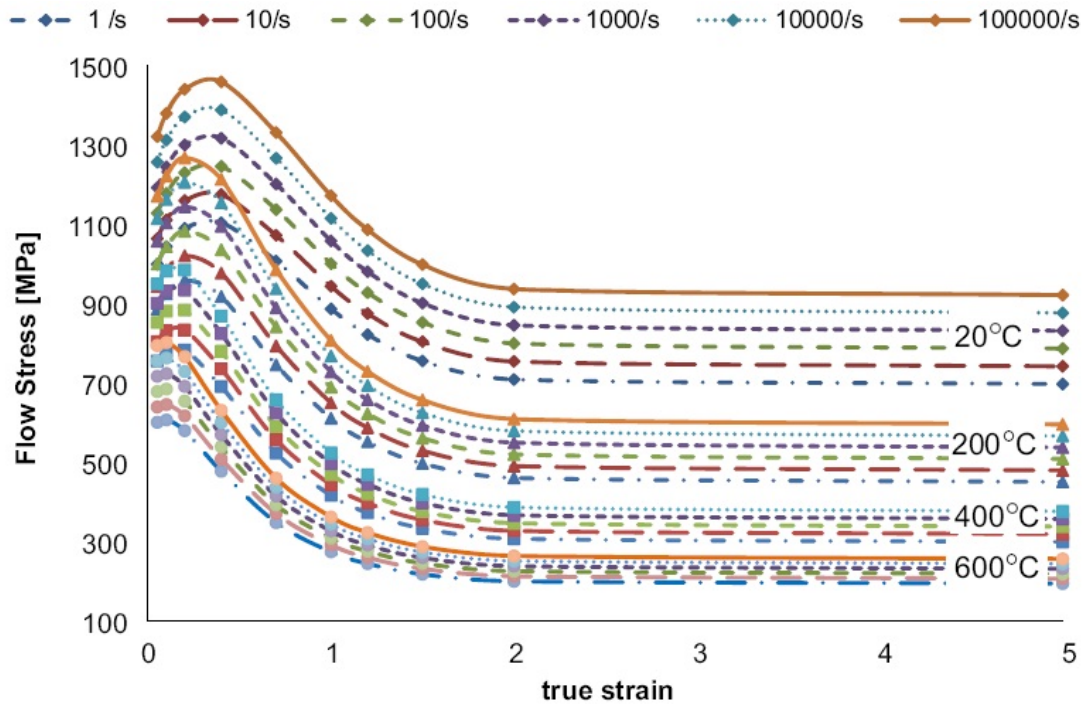


Figure 2.5. Flow stress curves using modified material model, *Model 3* ( $a = 2$ ,  $r = 1$ ,  $d = 0.5$ ,  $b = 1$ ,  $S = 5$ ) (Sima & Özel, 2010)

In order to study the effects of the parameters used in the flow softening terms (either the ones added to thermal softening part or strain hardening part), one parameter is varied while other parameters are held constant.

In Figures 2.6–2.9, SHPB experimental data obtained by Lee and Lin (Lee & Lin, 1998b) in the range of strains below 0.3 mm/mm which was the limitation of the apparatus, and the flow stress curves generated by the model (dotted lines) are compared for a range of model parameters at temperatures of 300, 500 and 700 °C. While proposed material flow stress model is compared with experimental data at lower strains, its behavior at higher strain ranges which are typical in cutting process ( $0.5 \text{ mm/mm} < \varepsilon < 5 \text{ mm/mm}$ ) is investigated. The best fitting parameters are identified by using a factor screening method that resulted in good agreement of the model generated flow stress curves with the SHPB test data. In factor screening, a wide range of values for each factor (model

parameter) is initially utilized and the ranges of each factor significantly affecting the flow softening behavior are identified. This method is repeated until a suitable parameter range is obtained.

As shown in Figure 2.6, parameter  $a$  controls the strain hardening part by decreasing flow stress after a critical strain value ( $\epsilon_c$ ). It should be noted that a low value of parameter  $a$  results in a mismatch to the SHPB test data. Increasing the parameter “ $a$ ” from a value of 1–5 creates a sharper decline in flow stress curve and a larger drop at higher strain regions. The parameter “ $b$ ” in the tanh function (see Equation (2.4)) controls the temperature dependent flow softening effect and where (i.e. in which strain) peak or maximum flow stress would take place. The lower the value of parameter “ $b$ ”, the lower the strain value of the peak flow stress occurs. A higher value of parameter “ $b$ ” also increases the value of the peak flow stress as shown in Figure 2.7.

The parameter “ $d$ ” which is an exponent for the temperature controls the degree of temperature dependency of parameter “ $D$ ” as given in Equation (2.4). The parameter  $d$  has a strong impact on the value of flow softening and determines the minimum flow stress value as shown in Figure 2.8. It does not affect the corresponding strain value for peak flow stress.

The parameter “ $S$ ”, which controls the tanh function in thermal softening at elevated strains and temperatures together with parameters “ $b$ ,  $d$ ” and “ $r$ ”, also controls the softening trend. A higher value of the parameter “ $S$ ” leads to a faster entrance to the softening regime with respect to increasing strain and decreases the slope of the softening part of the flow stress curves without changing the value of the minimum flow stress as shown in Figure 2.9. A lower value of the parameter “ $S$ ” causes minimum flow stress to take place at a higher strain. Parameters “ $r$ ” and “ $S$ ” have interacting but similar effects on the flow stress.

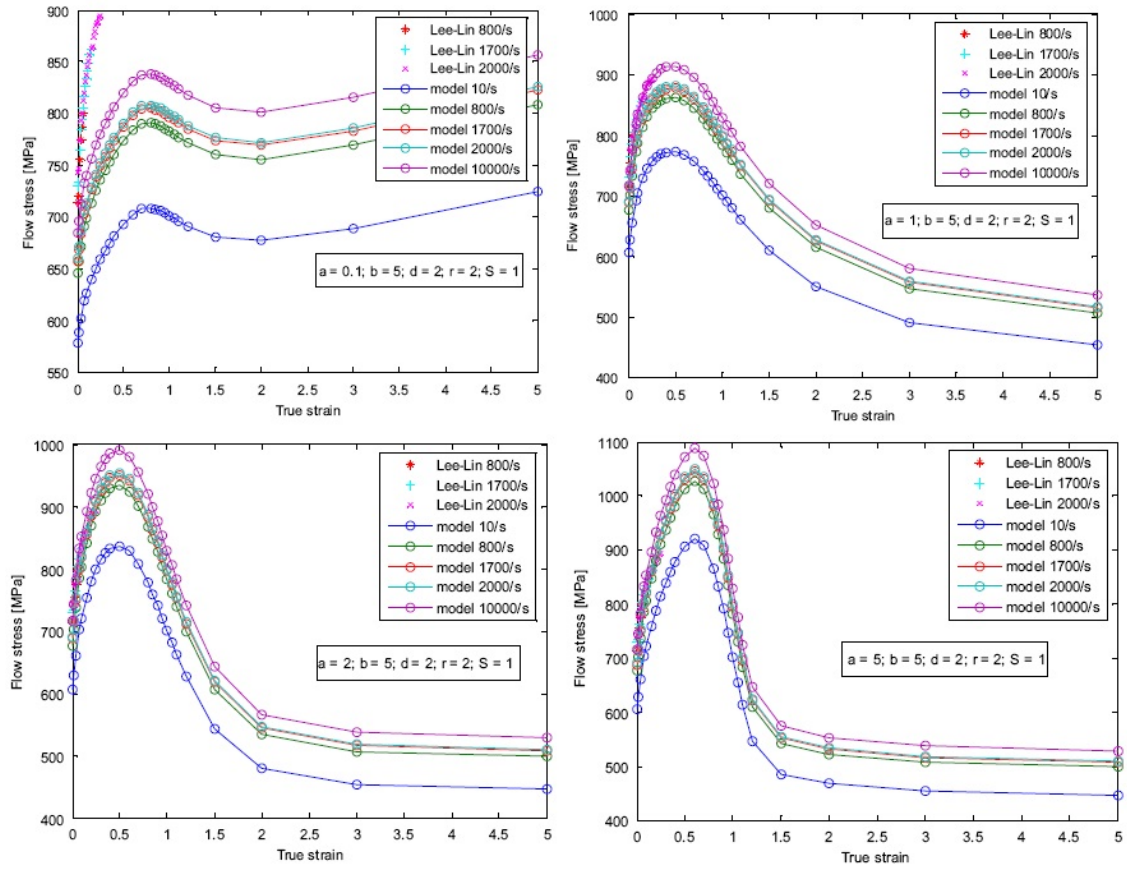


Figure 2.6. Flow stress curves depicting the effects of parameter “ $a$ ” at 700 °C (Sima & Özel, 2010)

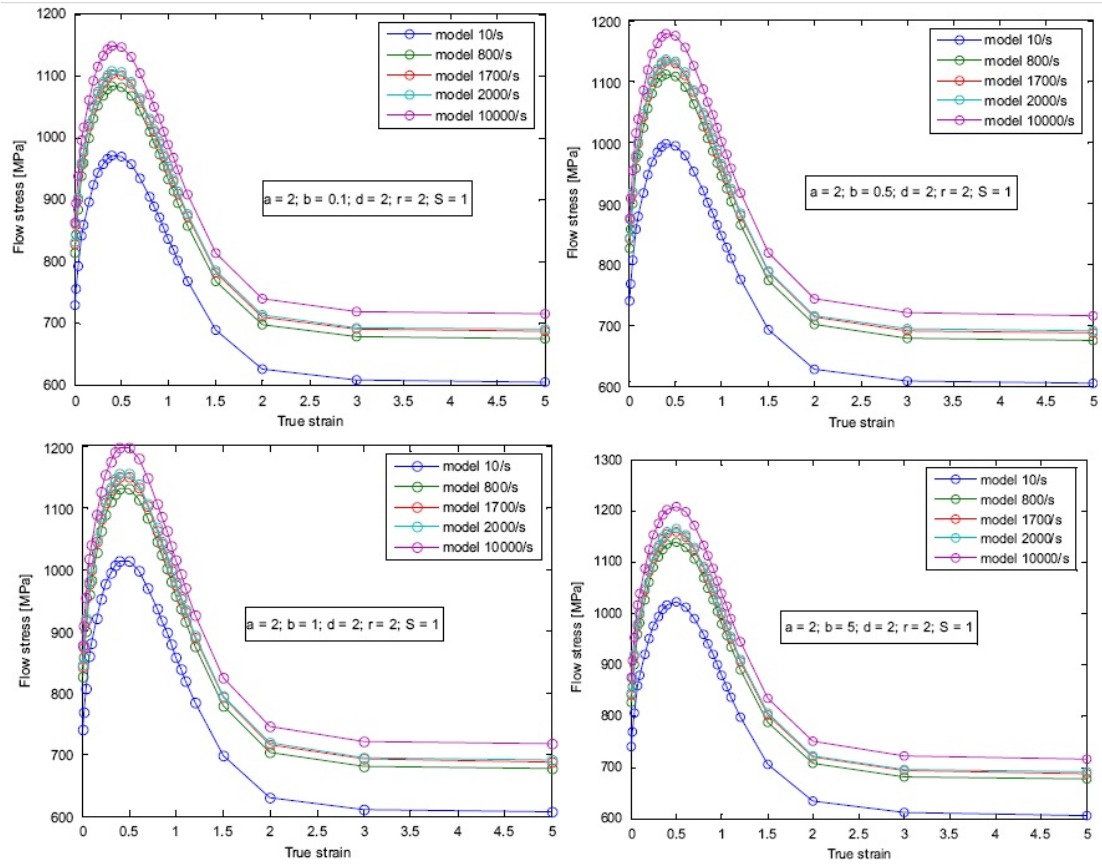


Figure 2.7. Flow stress curves depicting the effects of parameter “ $b$ ” at  $500\text{ °C}$  (Sima & Özel, 2010)

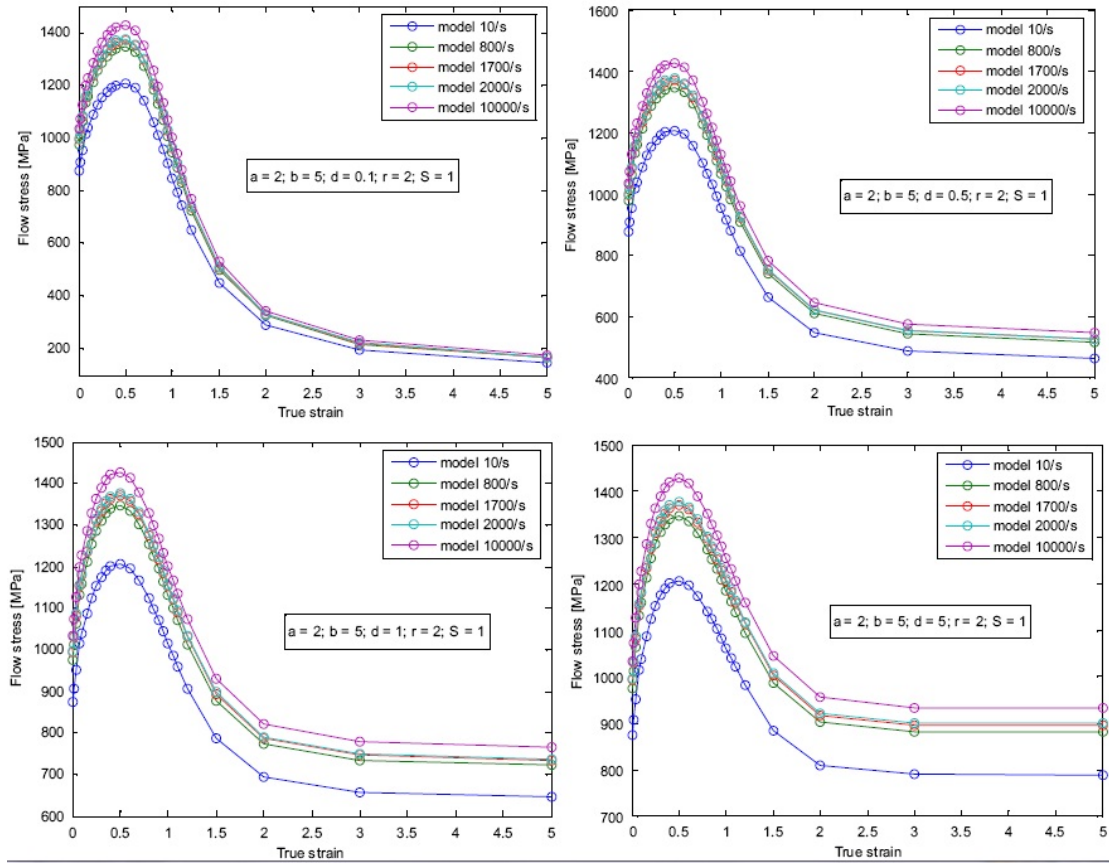


Figure 2.8. Flow stress curves depicting the effects of parameter “ $d$ ” at 300 °C (Sima & Özel, 2010)

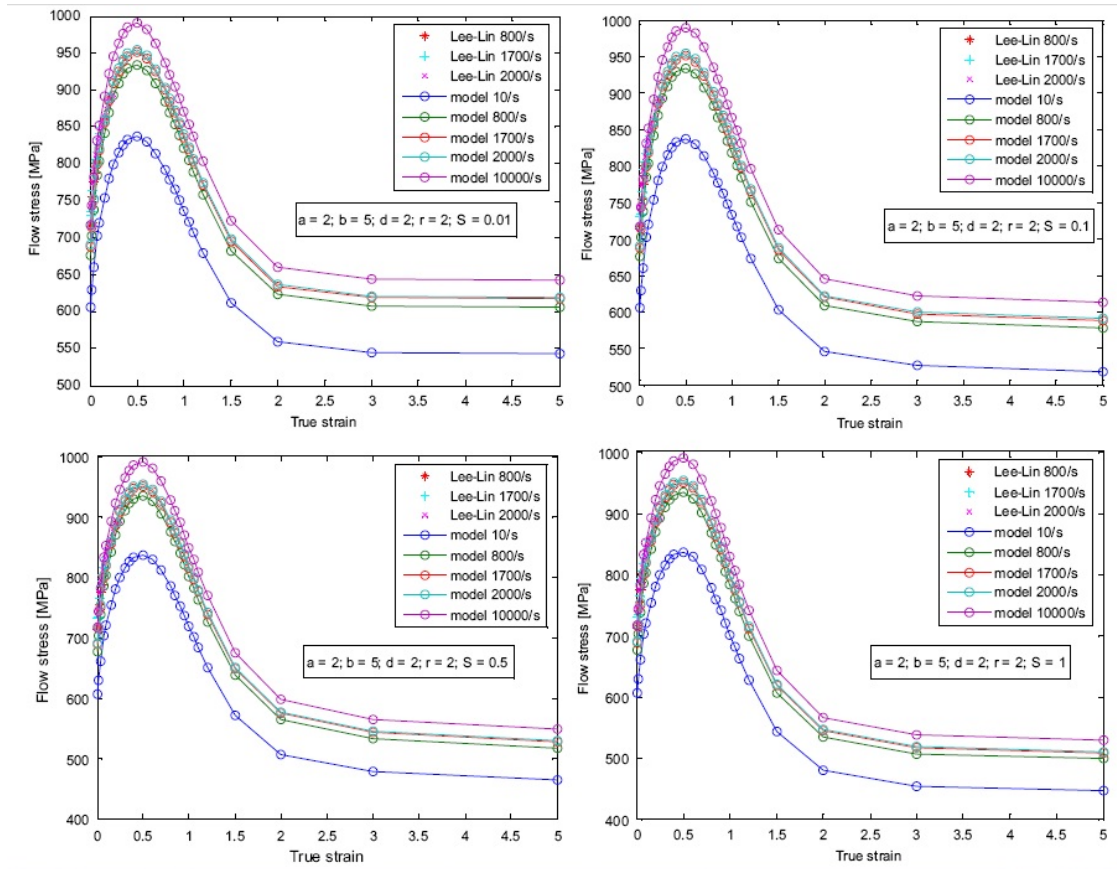


Figure 2.9. Flow stress curves depicting the effects of parameter “S” at 700 °C (Sima & Özel, 2010)

### 2.3. 2-D Finite Element Process Simulations

In this study, finite element (FE) simulations are developed using updated Lagrangian software (DEFORM-2D) in which chip separation from workpiece is achieved with continuous remeshing. Throughout this study, only coupled thermo elasto-viscoplastic finite element simulations are considered. These elasto-viscoplastic simulations included a workpiece as elasto-viscoplastic with a mesh containing 10,000 quadrilateral elements with element size ranging from 2 to 60  $\mu\text{m}$ . Tool is modeled as rigid with a mesh containing into 2500 elements. A high density mesh in the primary deformation zone was applied. A sensitivity analysis is conducted so that the number of elements in the mesh is large enough and the workpiece mesh does not influence the predictions obtained

with the FE simulations. A tool edge radius of  $r_\beta = 5 \mu\text{m}$  for uncoated carbide (WC/Co) and  $r_\beta = 10 \mu\text{m}$  for TiAlN coated carbide (WC/Co) are employed in the tool geometry. A thin layer of coating ( $5 \mu\text{m}$  thickness) is applied and meshed with elements ranging from 2 to  $4 \mu\text{m}$  in size by using “coating” feature provided in the FE software. These simulation models are compared with experimental results obtained in this study.

### 2.3.1. Temperature-dependent mechanical and thermo-physical properties

A plane-strain coupled thermo-mechanical analysis was performed using orthogonal cutting assumption. Thermal boundary conditions are defined accordingly in order to allow heat transfer from workpiece to cutting tool. The heat conduction coefficient ( $h$ ) is taken as  $1000 \text{ kWm}^{-2}\text{K}^{-1}$  to allow rapid temperature rise in the tool. Mechanical and thermo-physical properties of titanium Ti-6Al-4V alloy are defined as temperature dependent. Temperature-dependent ( $T$  in  $^\circ\text{C}$ ) Young's modulus ( $E$ ), thermal expansion ( $\alpha$ ), thermal conductivity ( $\lambda$ ), and heat capacity ( $c_p$ ) are given for Ti-6Al-4V alloy, and tool material and coating in Table 2.1.

Table 2.1. Mechanical and thermo-physical properties of work and tool materials used in FE simulations (Özel et al., 2010b)

Property	Unit	WC/Co	Ti-6Al-4V	TiAlN	cBN
$E(T)$	[MPa]	$5.6 \times 10^5$	$0.7412 \times T + 113375$	$6.0 \times 10^5$	$6.52 \times 10^5$
$\alpha(T)$	[mm/mm $^\circ\text{C}$ ]	$4.7 \times 10^{-6}$	$3 \times 10^{-9} \times T + 7 \times 10^{-6}$	$9.4 \times 10^{-6}$	$5.2 \times 10^{-6}$
$\lambda(T)$	[W/m $^\circ\text{C}$ ]	55	$7.039 \times e^{0.0011 \times T}$	$0.0081 \times T + 11.95$	100
$c_p(T)$	[N/mm $^2$ $^\circ\text{C}$ ]	$0.0005 \times T + 2.07$	$2.24 \times e^{0.0007 \times T}$	$0.0003 \times T + 0.57$	3.26

### 2.3.2. Chip–tool interfacial friction model

The friction in machining is indeed complex and requires use of variable friction along the edge radius and rake face of the insert (Özel, 2006). Friction factor, which is defined as  $m = \tau/k$  where  $\tau$  is frictional shear stress and  $k$  is the work material shear flow stress, is commonly used at severe contact conditions whereas a Coulomb friction coefficient is applied to mild contact conditions. Friction along the tool rake face when curvilinear edge inserts are employed is more sophisticated. At the rake face, friction factor decreases with increasing ratio of uncut chip thickness,  $t_u$ , to edge radius,  $r_\beta$ , and increasing cutting speed (Karpas & Özel, 2008).

In this work similar to the previous work by the authors (Özel et al. 2010a, Özel et al. 2010b), three contact and friction regions are considered at the tool–chip interface: (i) a sticking region from the tool tip point to the end of the round edge curvature ( $\tau = k$  or  $m = 1$ ), (ii) a shear friction region ( $m = 0.85$  for uncoated WC/Co and  $m = 0.9$  for TiAlN coated WC/Co) from the end of the curvature to the uncut chip thickness boundary, (iii) a sliding region along the rest of the rake face ( a friction coefficient  $\mu = 0.5$ ) as shown in Figure 2.10.

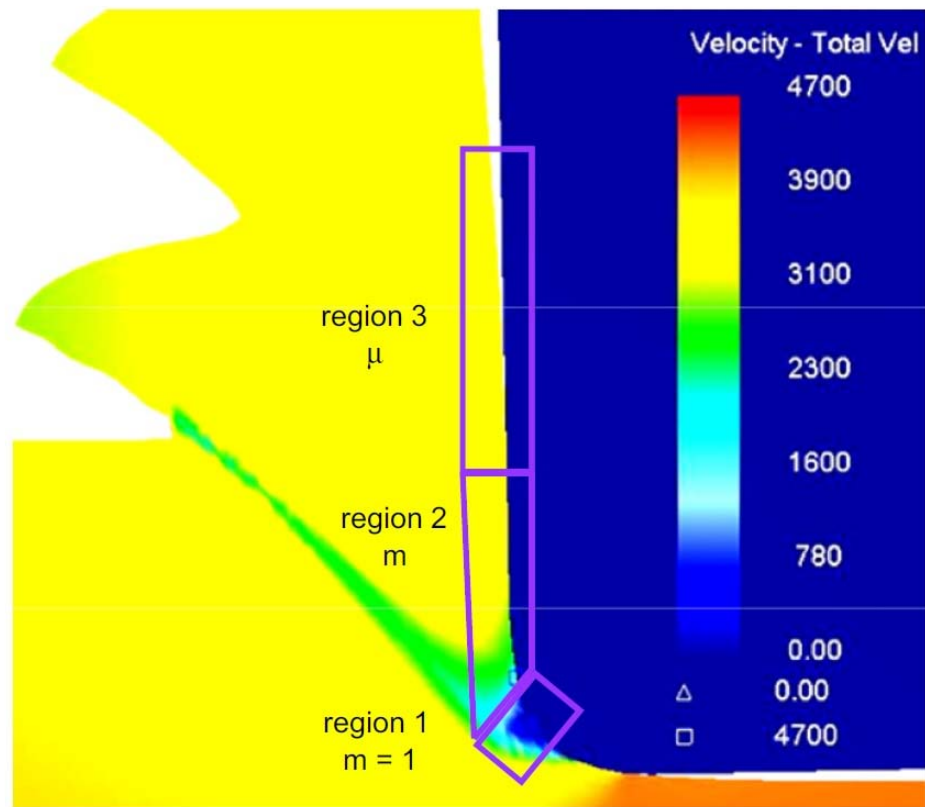


Figure 2.10. Velocity field and friction regions defined in FE models

### 2.3.3. Simulation experiments for constitutive material model validation

In these 2-D FE process simulations, serrated chip formation process is simulated from the incipient to the steady-state by using adiabatic shearing based on flow softening elasto-viscoplastic work material assumption. A set of simulations for benchmarking the modified J–C models (*Model 1*, *Model 2* and *Model 3*) is conducted. Several modified model parameters have been tested against each other at the same cutting condition (uncoated WC/Co tool,  $V_c = 121.9$  m/min,  $t_u = 0.1$  mm/rev,  $\gamma = 0^\circ$ ,  $r_\beta = 5$   $\mu$ m). The resultant force and chip geometry predictions (average minimum segmented chip thickness,  $t_{c\_min}$ , average maximum segmented chip thickness  $t_{c\_max}$  and pitch between two chip segment crests,  $p$ , are compared with experimental ones as shown in Table 2.2.

Table 2.2. Benchmark FE simulations to identify modified material model parameters (Sima &amp; Özel, 2010)

Experimental		$F_{c\_exp} =$ 189 N/mm	$F_{t\_exp} =$ 90 N/mm	$t_{c\_min} =$ 0.13 mm	$t_{c\_max} =$ 0.192 mm	$p_{exp} =$ 0.08 mm
Simulation		$ave. F_c$ [range]	$ave. F_t$ [range]	$t_{c\_min}$ [mm]	$t_{c\_min}$ [mm]	$p$ [mm]
<i>Model 1</i>	$M = 0.7, S = 4$	144 [120-160]	55 [37-66]	0.107	0.155	0.06
	$M = 0.6, S = 5$	152 [110-185]	41 [57-26]	0.106	0.130	0.04
	$M = 0.7, S = 20$	165 [140-190]	52 [42-65]	0.106	0.146	0.08
	$M = 0.7, S = 7$	177 [154-196]	54 [45-64]	0.12	0.135	0.04
<i>Model 2</i>	$S = 5, r = 1, d = 1, b = 1$	168 [138-187]	51 [40-70]	0.11	0.139	0.065
	$S = 1.5, r = 5, d = 0.5, b = 2$	172 [120-200]	47 [26-64]	0.118	0.15	0.04
	$S = 1.5, r = 2, d = 1, b = 2$	181 [148-194]	52 [44-75]	0.127	0.14	0.03
<i>Model 3</i>	$a = 2.5, S = 0.01, r = 1, d = 1, b = 2$	200 [170-240]	60 [50-70]	0.103	0.14	0.05
	$a = 2.5, S = 0.5, r = 0.1, d = 1, b = 5$	195 [163-216]	51 [41-69]	0.1	0.125	0.07
	$a = 2, S = 0.05, r = 2, d = 1, b = 5$	195 [175-230]	62 [50-72]	0.108	0.135	0.055

For example, the influence of modified J–C model (*Model 1*) parameters on the serrated chip formation can be seen in Figure 2.11. After several iterations, the model parameters highlighted in Table 2.2 are chosen as the most suitable parameters to modify J–C material model without changing the Lee and Lin (Lee & Lin, 1998b) SHPB test data which are mostly obtained at lower strains.

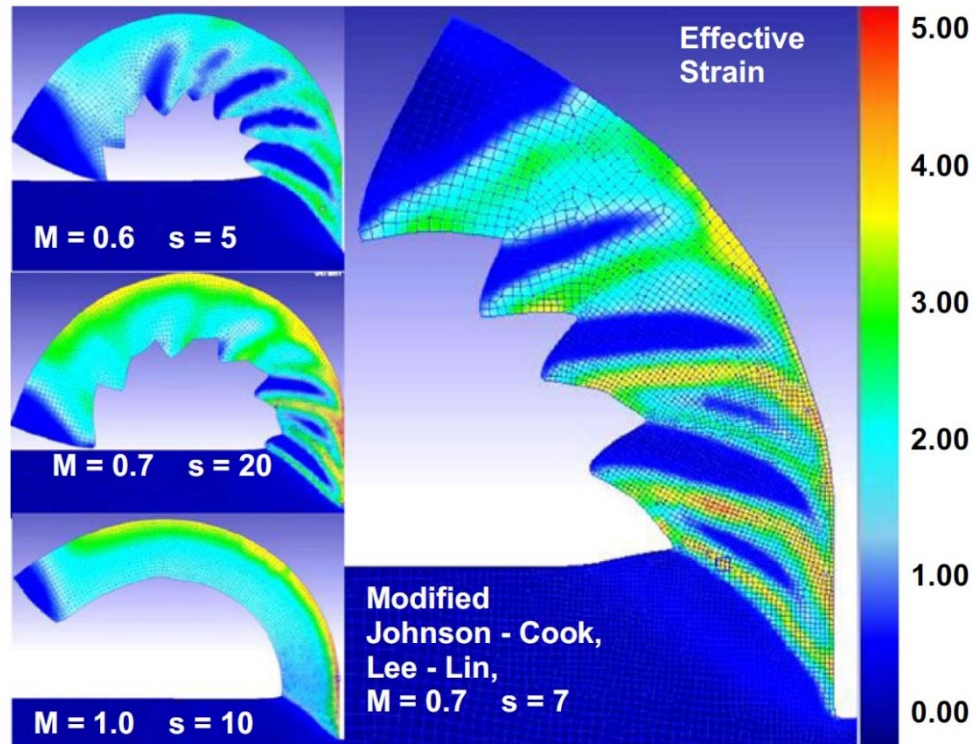


Figure 2.11. Serrated chip formation with adiabatic shearing using *Model 1* (uncoated WC/Co tool,  $V_c = 121.9$  m/min,  $t_u = 0.1$  mm/rev,  $0^\circ$  rake angle,  $r_\beta = 5$   $\mu$ m) (Özel et al., 2010a)

In order to compare modified material models for force predictions, force generations in FE simulations with respect to cutting time are also compared with the experimentally measured cutting ( $F_c$ ) and thrust ( $F_t$ ) forces as shown in Figures 2.13 and 2.14. Predictions obtained with simulations using *Model 3* have resulted in the closest matches to the experimental forces. This modified material model has also resulted in close agreement in cutting and thrust forces for the two other uncut chip thickness conditions as shown in Figure 2.14. The force predictions can further be improved by adjusting the friction parameters implemented in variable friction definition with three distinct regions (sticking and slipping).

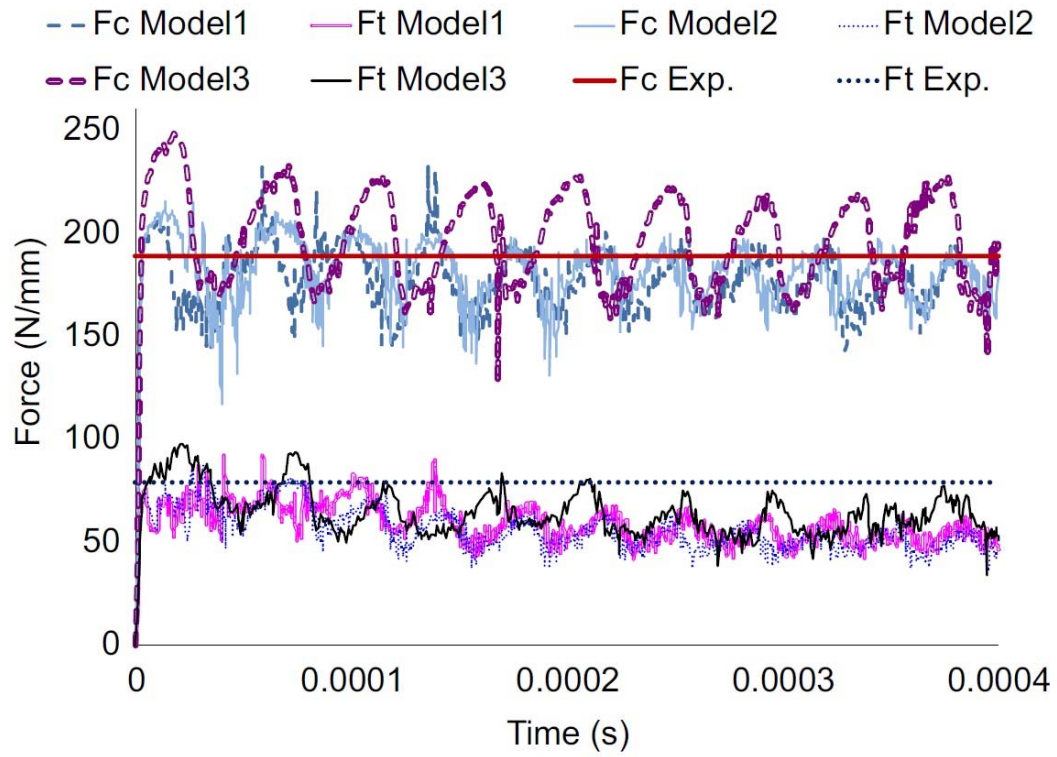


Figure 2.12. Comparison of forces predicted ( $V_c = 120$  m/min,  $t_u = 0.1$  mm/rev,  $\gamma = 0^\circ$ ,  $r_\beta = 5$   $\mu\text{m}$ ) (Sima & Özel, 2010)

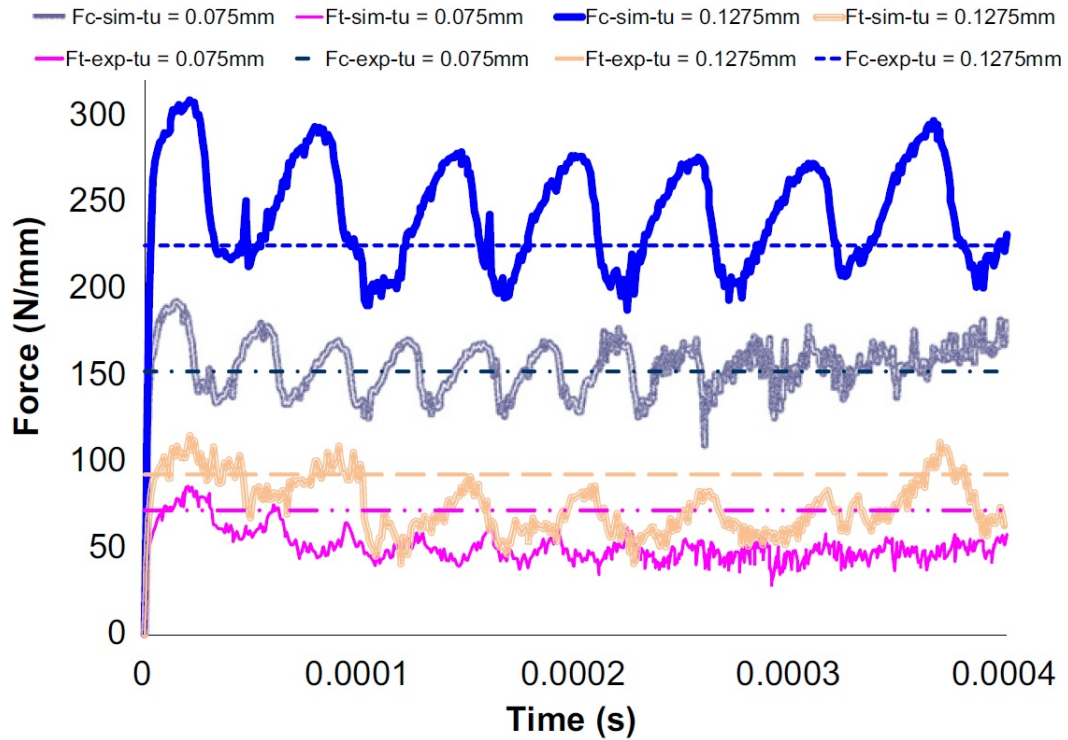


Figure 2.13. Comparison of forces predicted with *Model 3* ( $V_c = 120$  m/min,  $\gamma = 0^\circ$ ,  $r_\beta = 5$   $\mu\text{m}$ ) (Sima & Özel, 2010)

The effective strain distributions that are given in Figure 2.14 show the adiabatic shear bands very clearly. In these simulations no damage criterion was used at all. Figure 2.14 also shows the chip morphology for three different uncut chip thickness ( $t_u = 0.075$ ,  $0.100$ , and  $0.125$  mm) using *Model 3* and comparison against *Model 1* and *Model 2* predictions. As it can be seen from the predicted serrated chips with finite element simulations, a large chip segment (tooth) is followed by a smaller one in almost all models similar to the observations reported by Calamaz et al. (Calamaz et al. 2008). However, the difference is more visible in elasto-viscoplastic simulations using *Model 3* in Figure 2.14.

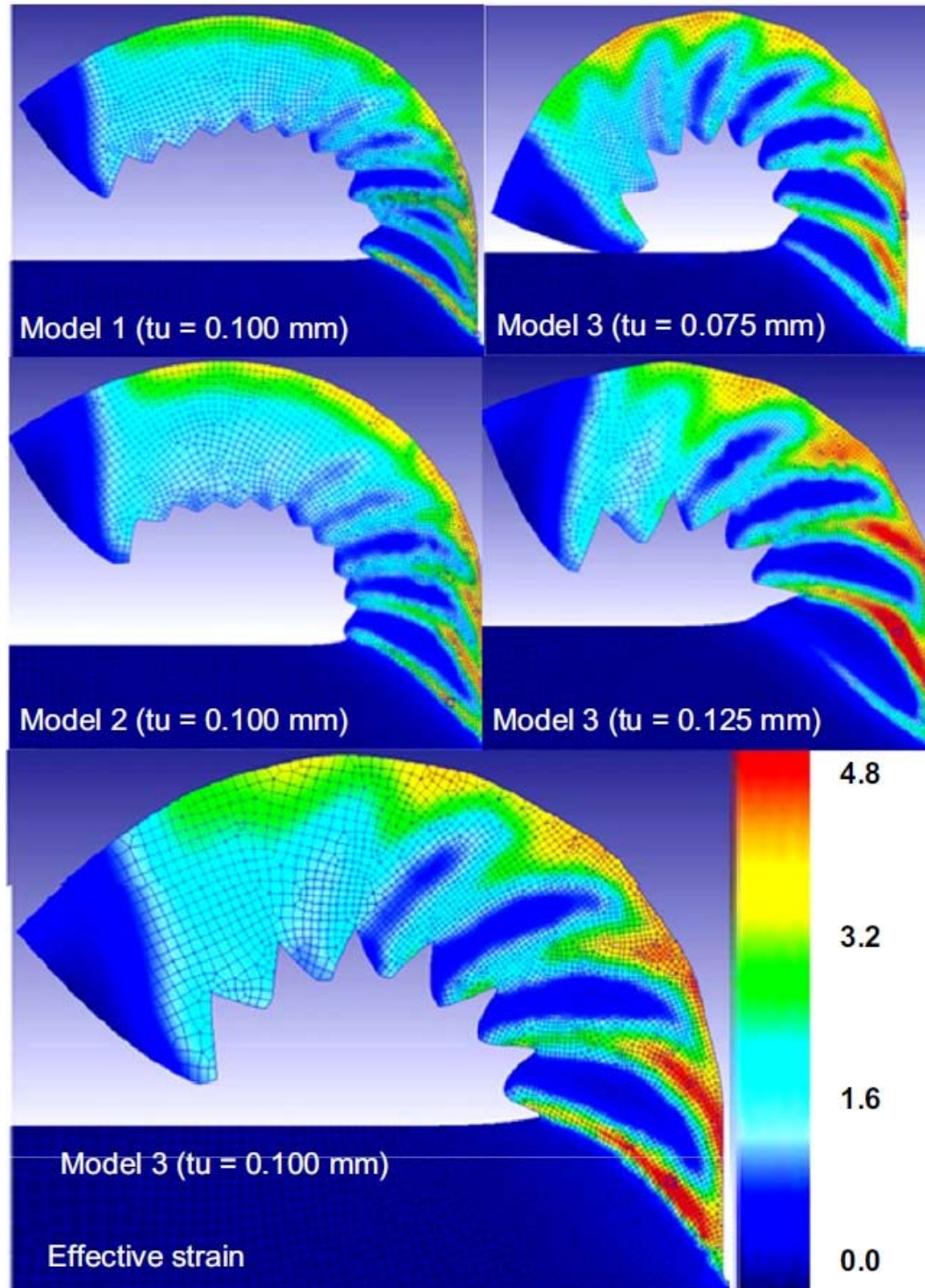


Figure 2.14. Comparison of modified material models on serrated chip formation with adiabatic shearing ( $V_c = 120$  m/min,  $t_u = 0.1$  mm/rev,  $\gamma = 0^\circ$ ,  $r_\beta = 5$   $\mu$ m) (Sima & Özel, 2010)

Therefore, the temperature-dependent flow softening modified J–C material model (*Model 3*) which is very similar to the Calamaz modified material model is adapted as the flow stress for the simulation of machining Ti–6Al–4V alloy. Thus experimental data reported in this study have been used to validate the elasto-viscoplastic finite element simulations. Since influence of friction conditions on the simulation results is not the focus of this study, same friction parameters given have been applied to simulations with different modified J–C models.

Strain and stress values at 80 nodes along the path from P1 to P80 are plotted to investigate the flow softening in adiabatic shearing. In Figure 2.15 by using temperature dependent flow softening material model *Model 3*, strain path obtained from FE simulation outputs exhibit increasing strain in the adiabatic shear bands and decreasing within the chip segments. Effective stress along the same path is also plotted as shown in Figure 2.16. Flow softening (lower effective stress) of the material leaving the primary shear zone and forming a chip segment is also observed in this plot. It should be noted that effective stress remains low within the chip segments due to high temperatures.

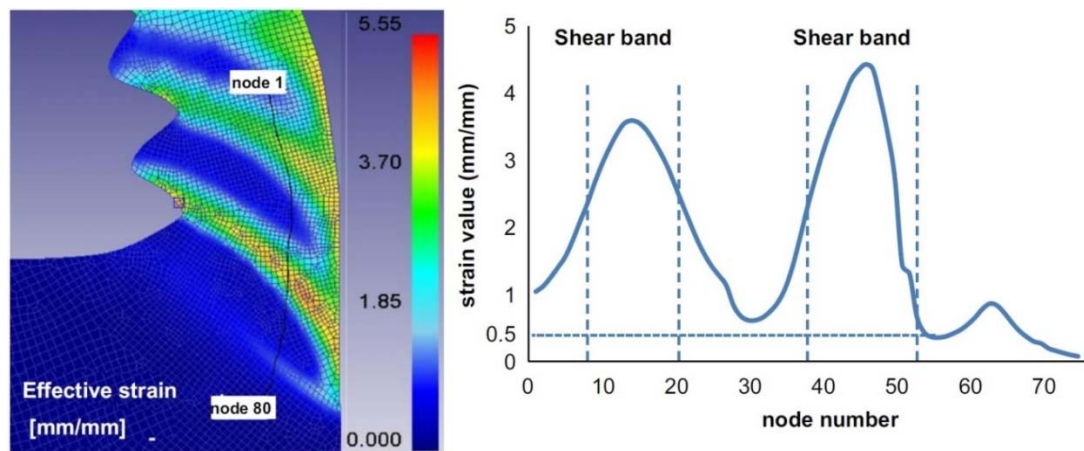


Figure 2.15. Effective strain values along a path into the segmented chip with adiabatic shearing (Sima & Özel, 2010)

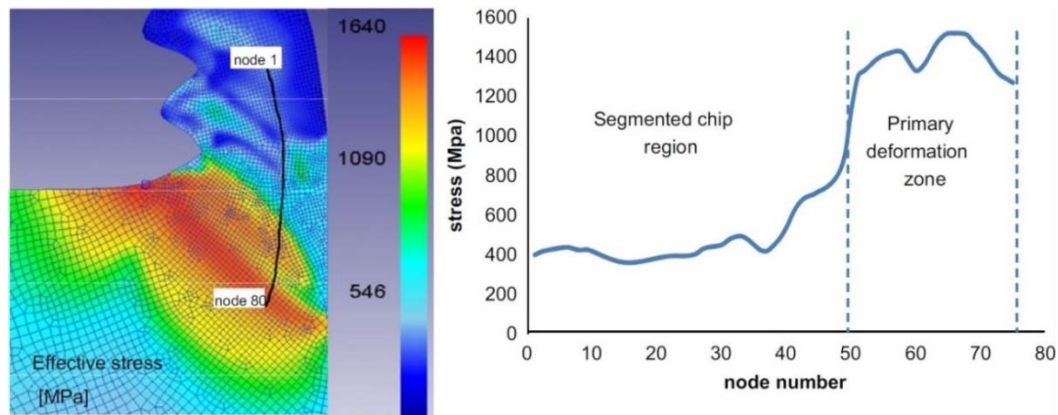


Figure 2.16. Effective strain values along a path into the segmented chip (Sima & Özel, 2010)

## 2.4. 3-D Finite Element Process Simulations

Several FE studies on 3D turning are presented in the past such as the work by Aurich and (Aurich & Bil, 2006) for segmented chip formation. In this study, updated Lagrangian FE modelling software (DEFORM-3D) was used.

In this work, the workpiece is represented by a curved model with 87 mm diameter which is consistent with the experimental conditions. Only a segment (3 degrees) of the workpiece was modeled in order to keep the size of mesh elements small. Workpiece model includes 90,000 elements. The bottom surface of the workpiece is fixed in all directions. The cutting tool ( $r_c = 0.8$  mm with  $11^\circ$  relief angle) is modeled as a rigid body which moves at the specified cutting speed by using 180,000 elements.

A very fine mesh density is defined at the tip of the tool and at the cutting zone to obtain fine process output distributions (see Figure 2.17). The minimum element size for the workpiece and tool mesh was set to 0.008 mm and 0.024 mm respectively. A tool edge radius of  $r_\beta = 5 \mu\text{m}$ ,  $r_\beta = 10 \mu\text{m}$  and  $r_\beta = 15 \mu\text{m}$  are designed for uncoated, single layer and multi-layer coated tools respectively for each simulation, since added layers in multi-coating design is increasing the edge radius of the inserts (Bouzakis et al. 2009).

Thermal boundary conditions are defined accordingly in order to allow heat transfer from workpiece to the cutting tool. The heat conduction coefficient ( $h$ ) is taken as  $1.0e5 \text{ kWm}^{-2}\text{K}^{-1}$  to allow rapid temperature rise in the tool.

Mechanical and thermo-physical properties of titanium Ti-6Al-4V alloy are defined as temperature ( $T$ ) dependent. Temperature-dependent ( $T$  in  $^{\circ}\text{C}$ ) modulus of elasticity ( $E$  in MPa), thermal expansion ( $\alpha$  in  $\text{mm.mm}^{-1}.\text{^{\circ}C}^{-1}$ ), thermal conductivity ( $\lambda$  in  $\text{W.m}^{-1}.\text{^{\circ}C}^{-1}$ ), and heat capacity ( $c_p$  in  $\text{N.mm}^{-2}.\text{^{\circ}C}^{-1}$ ) are given in Table 2.1.

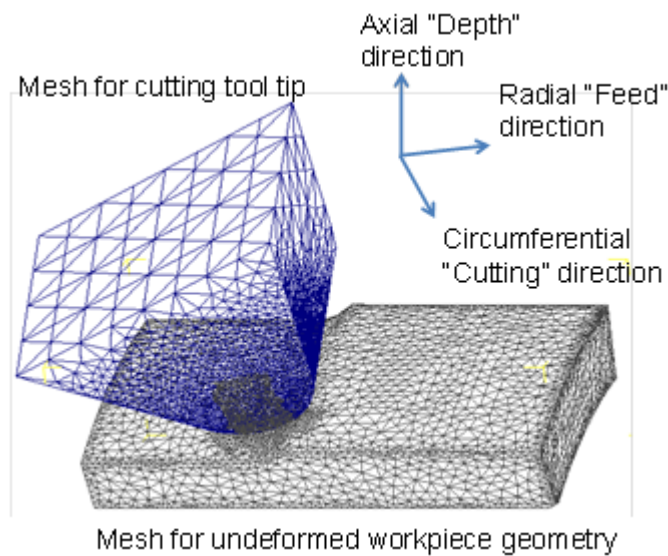


Figure 2.17. Mesh for the workpiece and the tool in 3D simulations (Sima et al., 2010)

All simulations were run at the same experimental cutting condition ( $V_c = 100 \text{ m/min}$ ,  $f = 0.1 \text{ mm/rev}$ ,  $a_p = 2 \text{ mm}$ ). In 3D FE modeling, constant shear friction factor ( $m = 0.9-0.95$ ) was used to represent friction between tool and workpiece. The averages, minimum and maximum of the simulated forces ( $F_c$ , cutting force,  $F_t$ , thrust force and  $F_z$ , feed force) are given in Table 2.3. The simulated cutting forces are found to be in close agreements with the experimental ones as summarized in Table 2.3.

Predicted temperature distributions (see Figure 2.18) depict that the lowest temperature rise in the tool is observed with cBN coated WC/Co tool due to the highest effective thermal conductivity and contact friction. Predicted chip formation is shown in Figure 2.19.

Table 2.3. Summary of 3D FE Simulation Force Predictions (mean value and range of the predicted forces) (Özel et al., 2010b)

Tool type	F <sub>c</sub> [N] (range)	F <sub>t</sub> [N] (range)	F <sub>z</sub> [N] (range)
Uncoated WC/Co	590 (485-615)	93 (69-106)	229 (137-244)
cBN coated WC/Co	602 (490-612)	99 (86-100)	236 (145-280)
TiAlN coated WC/Co	571 (490-593)	98 (77-103)	228 (135-250)
cBN+TiAlN coated WC/Co	575 (481-606)	97 (81-115)	243 (166-286)

3D FE simulations are also utilized to predict tool wear. The tool wear rate models describe the rate of volume loss on the tool rake and flank faces per unit area per unit time. A tool wear rate model based on the adhesive and chemical wear (Usui et al. 1978) was employed. This model uses interface temperature ( $T$ ), normal stress ( $\sigma_n$ ), and sliding velocity ( $V_s$ ) at the contact surfaces as inputs and yields tool wear rate ( $dW/dt$ ) for a given location on the tool surface as shown in Equation (2.5).

$$\frac{dW}{dt} = c_1 \sigma_n v_s \exp\left(\frac{-c_2}{T}\right) \quad (2.5)$$

The constants of this equation are set to  $c_1 = 7.8 \times 10^{-9}$  and  $c_2 = 2.5 \times 10^3$  in the FE simulations. Determining these constants could be extensive work so they are kept same initially. Chiefly crater wear was observed on all of the tools under these cutting conditions. A summary of maximum tool and chip temperatures along with the predicted wear rate is given in Table 2.4. Figure 2.21 shows the comparison of measured and simulated tool wear zones.

Table 2.4. Summary of 3D FE Simulation Predictions

Tool type	Max. Tool Temp. [°C]	Max. Chip Temp. [°C]	Wear Rate $dW/dt$ [mm/s]
Uncoated WC/Co	785	791	0.0024
cBN coated WC/Co	762	778	0.0019
TiAlN coated WC/Co	811	810	0.0038
cBN+TiAlN coated WC/Co	773	774	0.0025

As presented in Figure 2.18, highest temperature is predicted for TiAlN coated tools, that is why high tool wear rates are predicted for this cutting tool type in Figure 2.20. On the other hand, lowest temperature rise is predicted in cBN coated WC/Co tools because of its high thermal conductivity. Because of the temperature term in the Usui's model, lower wear rate is predicted for cBN cutting tools as well. On the right hand side of the Figure 2.20 experimental images of worn cutting tools after machining of Ti6Al4V is presented. It is visible that TiAlN coated tool is worn severely whereas Uncoated WC/Co and cBN coated tools experienced less crater wear amounts. Multi-layered cutting tools wear condition is somewhere in between TiAlN coated tools and the other two types of tools. Figure 2.19 represents effective strain distribution on formed chip and machined part of workpiece. It can be seen that no serration is predicted in these simulations because of plastic assumption of material model for workpiece material.

In Figure 2.20 as it is shown in TiAlN and multi-layered coated tools, at many places on the rake face of the cutting tool, wear rate contours show high amounts of wear rate where in uncoated WC/Co and cBN coated tools, even though at some elements high wear rates are predicted, at majority of places mild wear rate amounts are predicted. These results correlate with the images of the worn cutting tools in Figure 2.20.

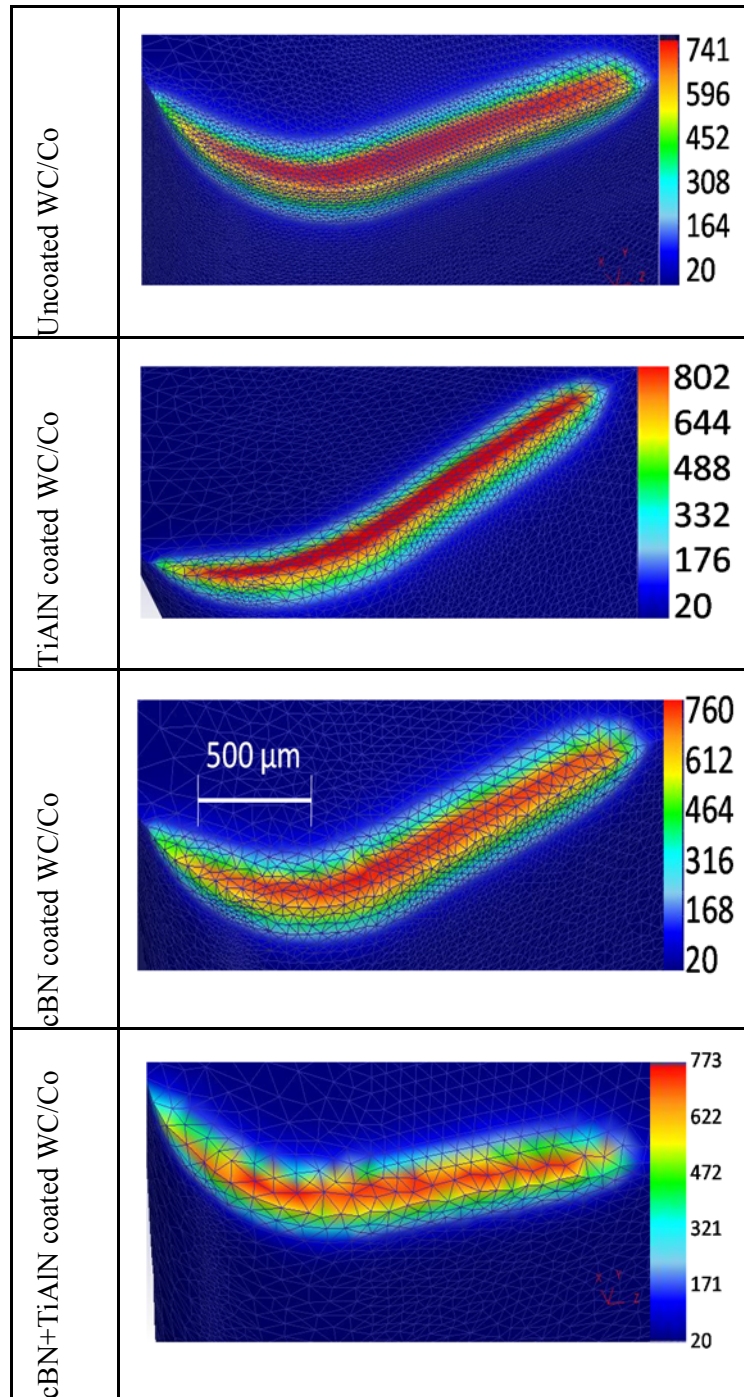


Figure 2.18. Predicted Temperature Distributions in °C (Özel et al., 2010b)

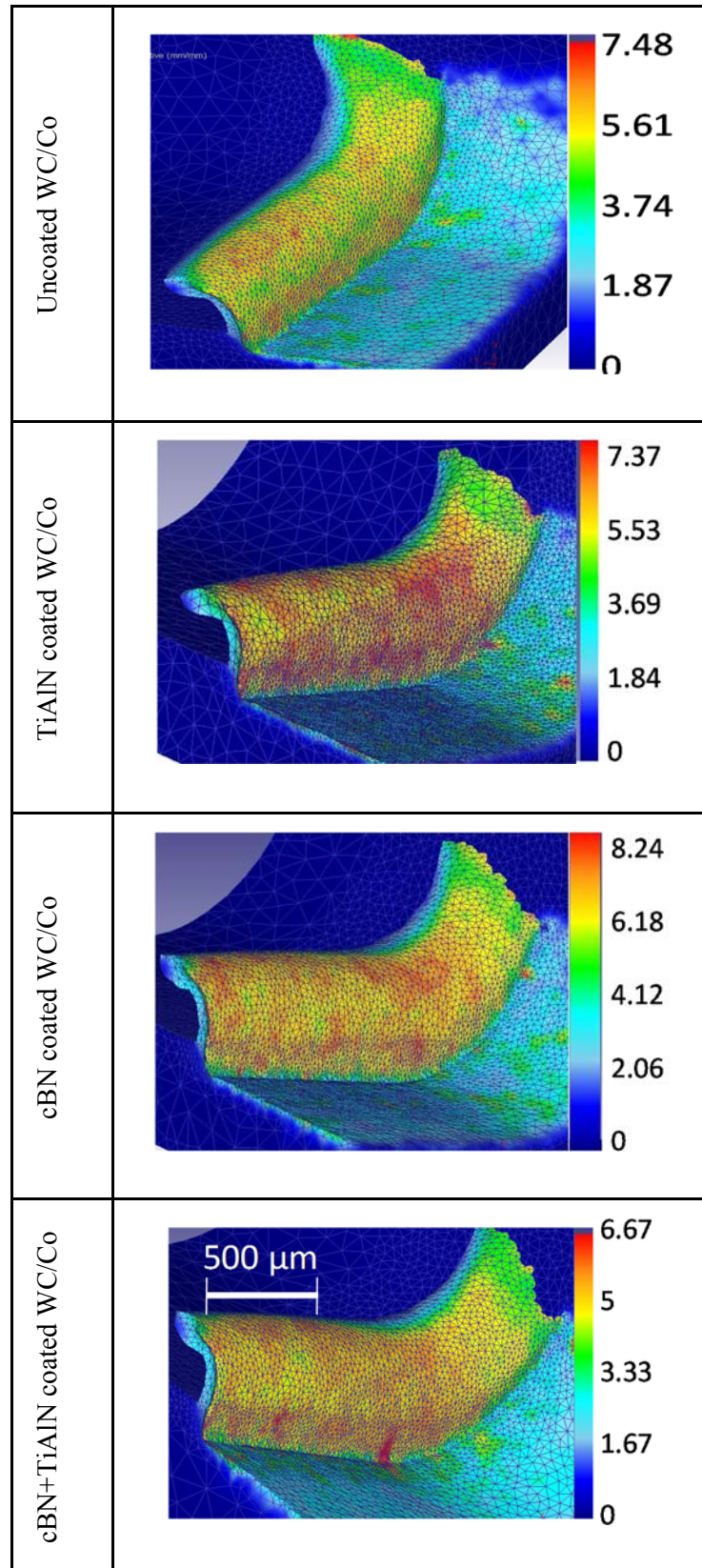


Figure 2.19. Simulated Chip Formation with Effective Strain Distributions (Özel et al., 2010b)

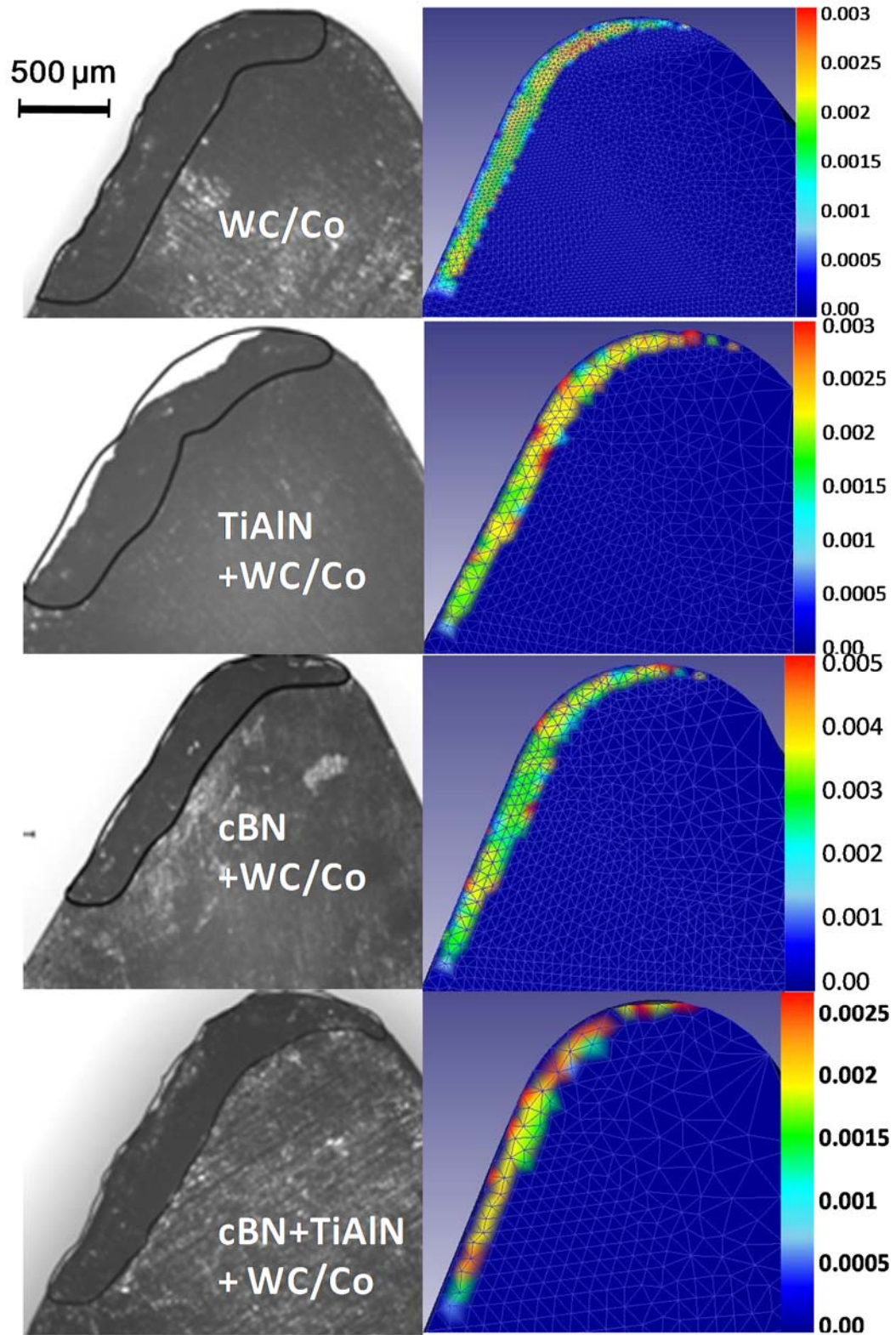


Figure 2.20. Experimental and Predicted Wear Rate Distributions in  $[\text{mm/s}]$  (Özel et al., 2010b)

## 2.5. 2-D FE Simulations Results on Chip Geometry and Morphology

After selecting the *Model 3* with best fit parameters ( $S = 0.05$ ,  $a = 2$ ,  $r = 1$ ,  $d = 1$ ,  $b = 5$ ) for the specific cutting condition ( $V_c = 120$  m/min,  $t_u = 0.1$  mm/rev,  $0^\circ$  rake angle,  $r_\beta = 5$  mm), other cutting conditions also have been simulated by using this model. All FE simulations are run for 0.1 s cutting time. Predicted forces from simulations are compared with measured forces in orthogonal cutting tests of Ti-6Al-4V alloy tubes as shown in Figure 2.21. Especially, cutting forces are in close agreements with 5% prediction error. Thrust force predictions which show 10–15% prediction error can be further improved with finer adjustments of friction regions and their values.

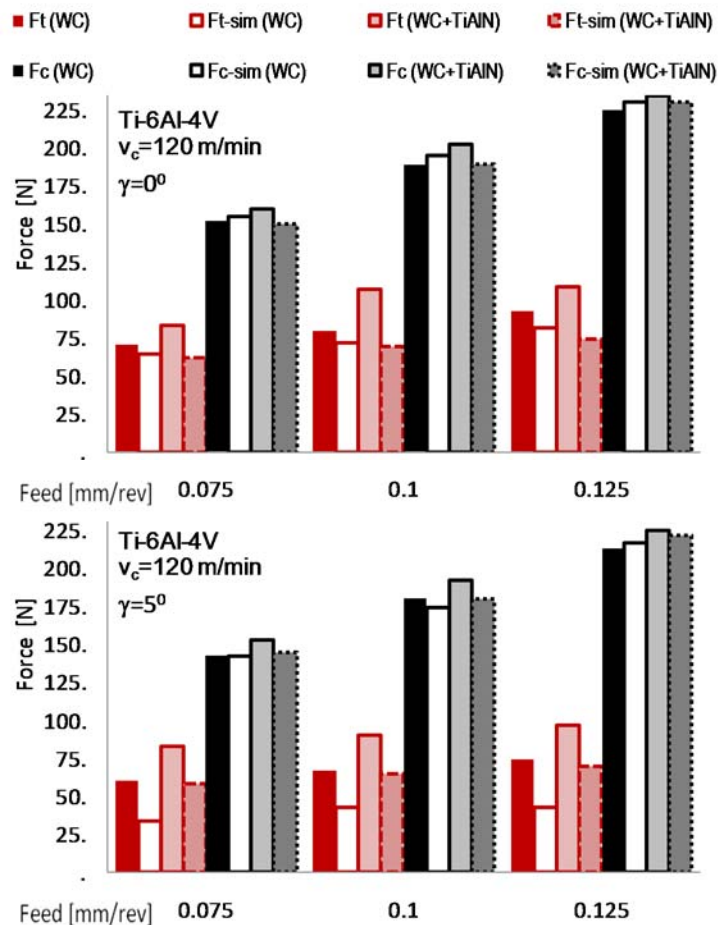


Figure 2.21. Comparison of measured and simulated cutting forces (Sima & Özel, 2010)

In Table 2.5, a comparison of simulated minimum and maximum serrated chip thickness and serration pitch with measurements is given. In addition, detailed comparisons of simulated effective strain distributions of the serrated chips with captures chip images are shown in Figure 2.22 in which close agreements are observed.

Table 2.5. Comparison of predicted chip thickness and serrated pitch with experiments (Sima & Özel, 2010)

Tool	Rake angle, $\gamma$ [°]	$V_c$ [m/min]	$t_u$ [mm]	Experimental			Simulation		
				$t_{c\_min}$	$t_{c\_max}$	$p$	$t_{c\_min}$	$t_{c\_max}$	$p$
Uncoated WC/Co	0	121.9	0.075	0.095	0.133	0.05	0.081	0.101	0.025
Uncoated WC/Co	0	121.9	0.1	0.13	0.192	0.07	0.108	0.135	0.045
Uncoated WC/Co	0	121.9	0.127	0.104	0.177	0.9	0.12	0.163	0.75
Uncoated WC/Co	0	240.8	0.1	0.087	0.16	0.08	0.107	0.137	0.035
Uncoated WC/Co	0	240.8	0.127	0.102	0.186	0.095	0.128	0.17	0.04
TiAlN coated WC/Co	0	121.9	0.1	0.137	0.182	0.075	0.107	0.135	0.035
TiAlN coated WC/Co	0	121.9	0.127	0.14	0.216	0.1	0.133	0.172	0.043
TiAlN coated WC/Co	5	121.9	0.1	0.102	0.158	0.073	0.107	0.134	0.034
TiAlN coated WC/Co	5	121.9	0.127	0.12	0.208	0.080	0.135	0.172	0.04
Uncoated WC/Co	5	121.9	0.127	0.156	0.23	0.089	0.135	0.171	0.039

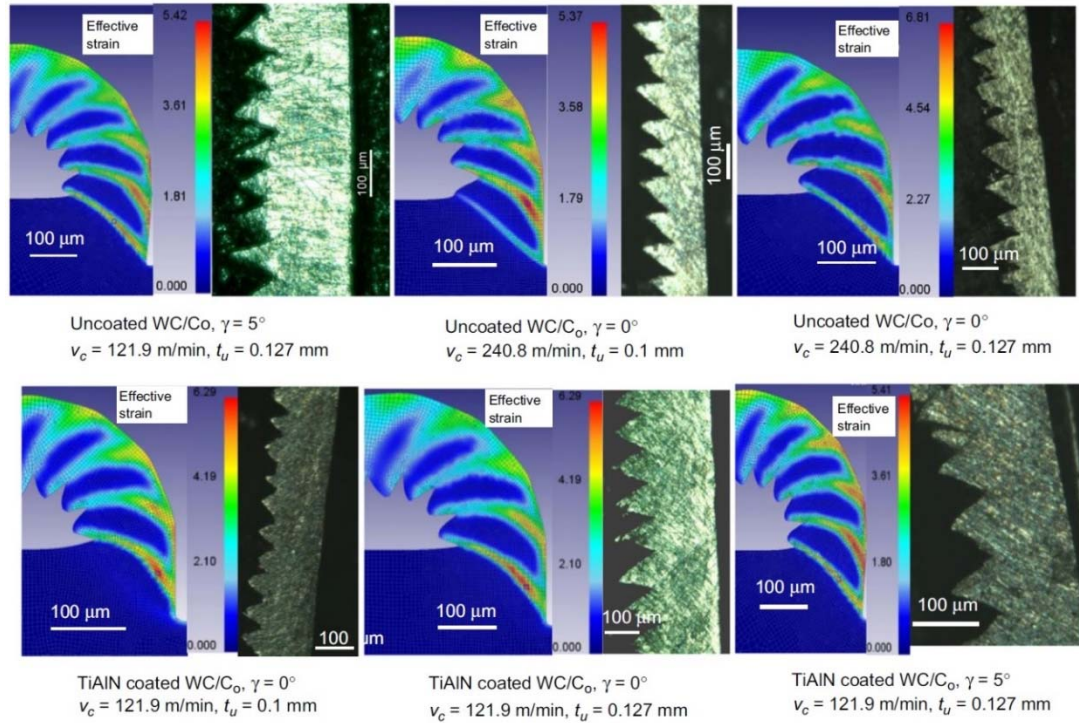


Figure 2.22. Comparison of simulated serrated chip formation and captured chip images (Sima & Özel, 2010)

In Figure 2.23, temperature distributions for various cutting conditions are given. The maximum temperatures are also indicated in each distribution. The temperatures predicted are usually higher with uncoated WC/Co tools. Temperatures increase as undeformed chip thickness increases, or cutting speed increases and decreases as rake angle decreases.

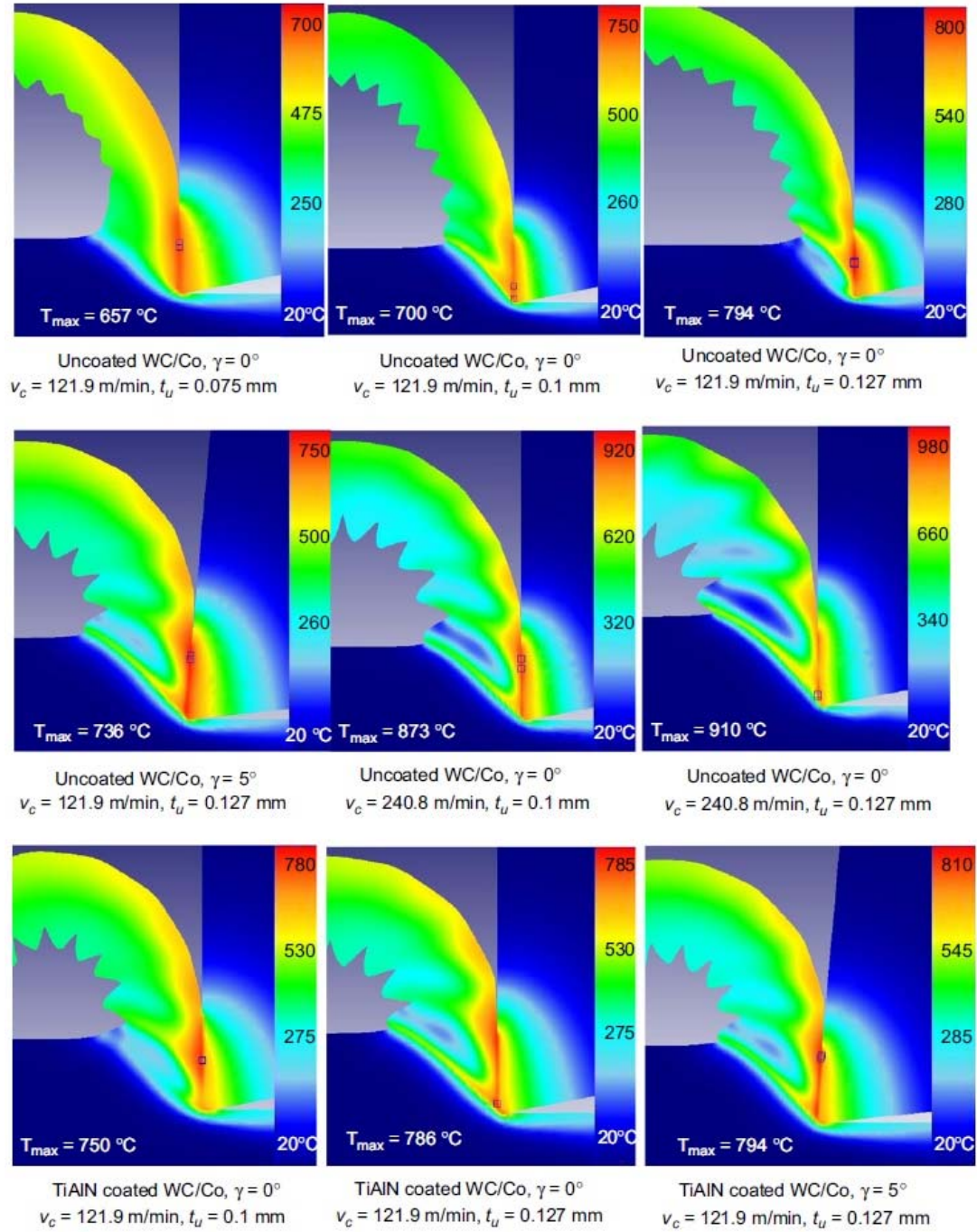


Figure 2.23. Temperature distribution in simulated serrated chip formation (Sima & Özel, 2010)

## 2.6. Results and Discussions

Finite element modeling and simulations of chip formation process in titanium alloy Ti6Al4V machining present significant challenges due to the nature of complicated dynamic material behavior of these alloys at elevated temperatures, strain and strain rates. In general, adiabatic shearing is considered as responsible for serrated chip formation. Increasing temperatures in the primary shear zone due to shear deformation weaken the material by thermal softening; therefore, the deformation is concentrated in shear bands, leading to serrated chip formation. Although it is also possible to simulate serrated chip formation by using damage models, in this work, it is assumed that serration is caused by adiabatic shearing.

In Chapter 2, FE based process simulations for machining of Ti-6Al-4V titanium alloy using uncoated carbide (WC/Co) and TiAlN coated carbide cutting tools have been presented. FE simulations are utilized in investigating the tool temperatures and wear development. Two dimensional and three dimensional FE simulations have been designed and conducted to predict forces, temperatures and tool wear to investigate the advantages of coatings in machining of Ti-6Al-4V.

Specifically, influence of material constitutive models and elastic-viscoplastic finite element formulation on serrated chip formation for modeling of machining Ti-6Al-4V titanium alloy is investigated. Temperature-dependent flow softening based modified material models are proposed where flow softening phenomenon, strain hardening and thermal softening effects and their interactions are coupled.

Temperature-dependent flow softening parameters are validated on a set of experimental data using measured cutting forces and chip morphology.

2D Finite Element simulations are validated with experimental results at two different rake angle, three different undeformed chip thickness values and two different cutting speeds. The results

reveal that material flow stress and finite element formulation greatly affects not only chip formation mechanism but also forces and temperatures predicted. Chip formation process for adiabatic shearing in machining Ti-6Al-4V alloys is successfully simulated using finite element models without using damage models. It is also shown that Finite element simulations are reliable if the material properties and friction are defined properly in the chip formation process models.

The following are specific conclusions can be drawn for this study:

The cutting forces increase with increasing cutting speed and thrust forces decrease with decreasing rake angle.

The degree of serration decreases while pitch of the serrated chips increases with decreasing cutting speed and increasing undeformed chip thickness and decreasing tool rake angle.

TiAlN coated tools resulted in higher temperatures and higher cutting and thrust forces due to the larger edge radius.

Flow softening is most effective between 300-700 °C and causes adiabatic shearing in the deformation zone during machining of Ti-6Al-4V alloy much lower than allotropic phase transformation ( $\beta$ -transus) temperature.

Flow softening increases the degree of chip serration chip but produce more curved chips since strain-hardening effect weakens.

In additions, 3D FE simulations on turning Ti-6Al-4V alloy with uncoated, TiAlN coated, and TiAlN+cBN coated single and multi-layer coated tungsten carbide inserts have been conducted. 3D FE simulations are utilized to predict chip formation, forces, temperatures and tool wear on these inserts. In these studies, the modified material model for Ti-6Al-4V titanium alloy that was developed where strain (flow) softening, strain hardening and thermal softening effects are coupled has been used.

The simulation predictions are compared with experimental results. Although cBN and TiAlN+cBN coated WC/Co inserts exhibit largest cutting forces at higher cutting speeds, they reveal favorable wear development. Tool wear zone measurements and predictions show that cBN coated WC/Co inserts depict smallest wear zone. Consequently, cBN coatings may lead to reduction in tool wear dry machining of titanium alloyed Ti-6Al-4V material. It is also concluded that the temperature distributions and tool wear contours demonstrate some advantages of coated insert designs.

### **3. MACHINING EXPERIMENTS**

### 3.1. Introduction

In machining processes, experimental results are required, however, due to expensive experimental set-up and time consuming conduct experimentation, selected experiments ought to be considered. For this purpose, 2D orthogonal cutting experiments for machining Ti-6Al-4V titanium alloy have been designed and conducted in order to understand the basic chip formation mechanism and generation of cutting and thrust forces in response to different tool rake angles, feed rate, cutting speed and tool material and coating.

On the other hand, industrial machining operations involve 3D cutting processes such as straight turning. Therefore, the physical performance of cutting tools (tool wear, tool life and reliability) can be only explored under 3-D cutting configurations and conditions.

In order to reduce the machining process to 2D, the interaction of the tool-work piece is modeled symmetrical in one of the Cartesian coordinates in the orthogonal cutting tests (see Figure 3.1). So the process of the chip formation is modeled in a plane; whereas the third dimension (i.e., the cutting force) is considered insignificant and unimportant. Although orthogonal cutting is not applied in the industry, force measurements obtained from such experimental tests are useful for calibrating and validating finite element simulation.

As mentioned, experimental work on 3D machining processes such as straight turning is necessary due to industrial practices. However, in 3D modeling, mechanics of chip formation is so complicated which results in more complex FE process simulations and take more computational effort.

In all machining experiments, cutting forces are measured using Kistler force dynamometer that is attached to the cutting tool holder. Chips are collected for further measurements of the geometry and morphology of serrated chips. Moreover, in the straight turning experiments, cutting tools with

different coating types (single and multi-layer) and edge micro-geometry are used to investigate tool wear, tool life and tool reliability effects.

It is essential to provide the chemical composition of the titanium-based alloy Ti-6Al-4V as given in Table 3.1 together with mechanical and thermal properties of this alloy as given in Table 3.2.

Table 3.1. Chemical composition of Ti-6Al-4V titanium-based alloy (Ulutun, 2013)

Element	Ti	Al	V	Fe	O	C	N	H	Others
%	Balance	6	4	0.25	0.13	0.08	0.03	0.01	0.4

Table 3.2. Mechanical and thermal properties of Ti-6Al-4V titanium-based alloy (Ulutun, 2013)

Property	Unit	Ti-64
Ultimate Strength	MPa	896
Yield Strength (0.2%)	MPa	827
Hardness	HRC	36
Thermal Expansion	$K^{-1}$	$9 \cdot 10^{-6}$
Density	$kg \cdot m^{-3}$	4430
Melting Point	K	1604
Elastic Modulus	GPa	42
Thermal Conductivity	$W \cdot m^{-1} \cdot K^{-1}$	6.6
Specific Heat Capacity	$J \cdot kg^{-1} \cdot K^{-1}$	565

## 3.2. Experimental Analysis

### 3.2.1. 2-D Orthogonal Machining Experiments

Orthogonal cutting provides chip formation during a coupled motion of the tool and workpiece in a 2D plane formed by cutting velocity and a normal to the velocity vector. (See Figure 3.1). Chip formation into the third dimension is not significantly when a width of cut is large enough. In this configuration, the uncut chip thickness ( $t_u$ ) is equivalent to the feed rate, and the tool or workpiece motion is in that direction. Cutting velocity or speed ( $V_c$ ) is a resultant surface velocity of rotating workpiece. The force component along cutting velocity direction is known as the cutting force ( $F_c$ ), whereas the force along the feed direction is known as feed or thrust force ( $F_t$ ).

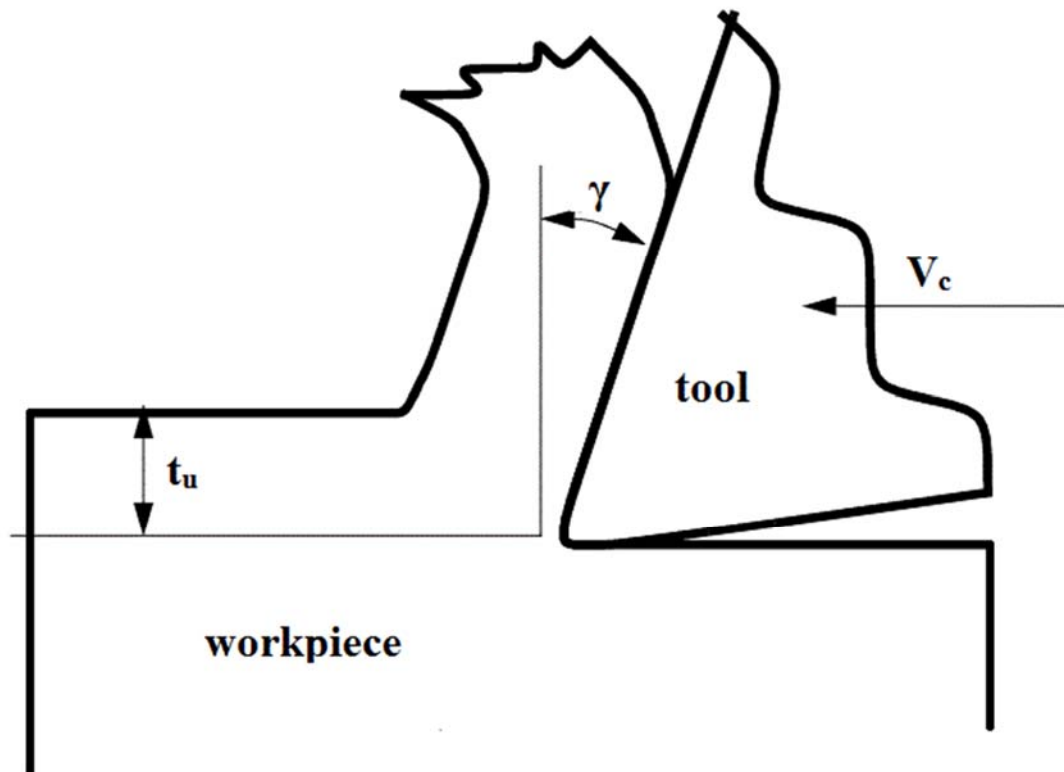


Figure 3.1. Illustration of orthogonal cutting

The orthogonal cutting of titanium-based alloy Ti-6Al-4V were conducted at two cutting speed levels ( $V_c = 121.9$  and  $240.8$  m/min) using orthogonal turning of Ti-6Al-4V titanium alloy tubes

(50.8 mm diameter and 3.175 mm thick) and uncoated tungsten carbide (WC/Co) cutting tools with sharp edges (around 5  $\mu\text{m}$  edge radius) and TiAlN coated carbide inserts (WC/Co) along with toolholders that provided rake angles of  $\gamma = 0^\circ$  and  $5^\circ$  and relief angles of  $11^\circ$  and  $6^\circ$  and five different feeds ( $t_u = 0.0254, 0.0508, 0.0762, 0.1016, 0.127$  mm/rev). All experiments have been performed at dry orthogonal turning conditions and replicated at least twice at each condition in a rigid CNC turning center at TechSolve Inc. This experimental set-up has created the orthogonal cutting condition illustrated in Figure 3.2. The cutting forces were measured with a Kistler force dynamometer and high-speed data acquisition devices (Özel et al. 2009). For all sets of experiment, to avoid the effects of tool wear, fresh (unworn) tools were used for each experiment.

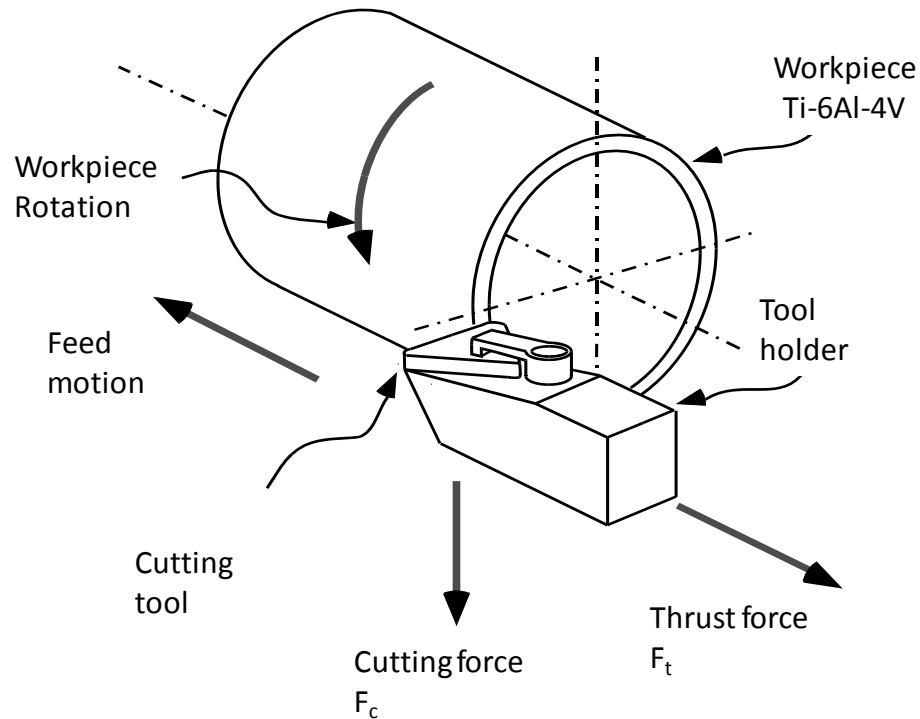


Figure 3.2. Orthogonal cutting of Ti-6Al-4V workpiece specimens (Özel et al. 2009)

### 3.2.2. Straight bar turning (Three-dimensional) experiments

In straight bar turning experiments, the tool and workpiece engagement creates a three-dimensional cutting where the edge of the tool cutting edge is no longer orthogonal to the cutting velocity. Thus, the tool forces in all three directions (i.e. cutting, feed, and thrust) are all significant compared to orthogonal cutting. The straight bar turning configuration is shown in Figure 3.3.

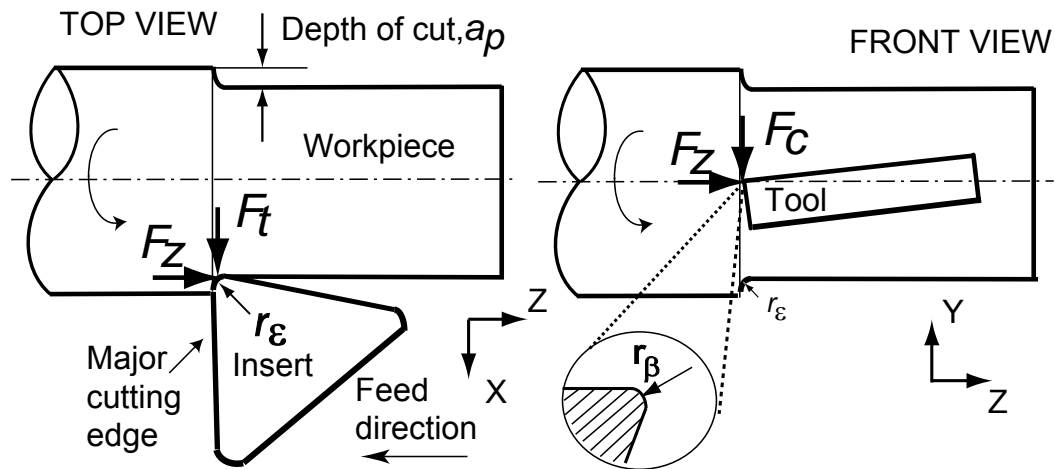


Figure 3.3. Straight bar turning of Ti-6Al-4V Titanium Alloy (Özel et al. 2010)

In this figure, the depth of cut is denoted with  $a_p$ , which can be seen. As it is shown in the same figure,  $F_c$ ,  $F_z$ , and  $F_t$  are the cutting, feed, and thrust forces, whereas  $r_\epsilon$  is the nose radius and  $r_\beta$  is the cutting edge radius of the tool.

In order to study the effect of coating and multiple coated tools on the measured forces and tool wear four different sets of coated tools has been tested at the same cutting condition; uncoated/unalloyed tungsten carbide (WC/Co), tungsten carbide (WC/Co) PVD coated with TiAlN, tungsten carbide (WC/Co) PVD coated with cBN, tungsten carbide multi-layer PVD coated with cBN over TiAlN coating. Tungsten carbide (WC/Co) and PVD coated WC/Co with TiAlN inserts are coated with cBN by magnetron sputtering PVD system as mono and multi-layer coatings at National Boron Research Institute (BOREN) in Turkey at a deposition pressure of  $3 \times 10^{-3}$  Torr

and heater temperature of 100 °C. Applied magnetron power is fixed at 900 W and argon to nitrogen gas ratio is adjusted to 5/1 and run at the lowest possible bias voltage to obtain uniform cBN coating as explained in Özel et al. (2010b).

In this experimental configuration, straight turning of annealed Ti-6Al-4V titanium alloy bars (90 mm in diameter, 100 mm in length) was performed by using TPG432 type insert geometry (insert nose radius of  $r_e = 0.8$  mm and relief angle of  $\alpha = 11^\circ$ ) in a rigid Bridgeport CNC turning centre under dry machining conditions at Rutgers University Manufacturing Automation Research Laboratory. The inserts were used with a tool holder that provided  $0^\circ$  lead,  $-5^\circ$  side rake, and  $-5^\circ$  back rake angles. The cutting forces were measured with a Kistler force dynamometer mounted on the turret disk of the Bridgeport CNC turning centre. A constant depth of cut ( $a_p = 2$  mm) and feed ( $f = 0.1$  and  $0.2$  mm/rev) were selected as cutting conditions.

### **3.3. Results and Discussion**

The results of machining experiments on Ti-6Al-4V titanium alloy using uncoated and coated tools in orthogonal cutting (2D) and straight turning (3D) include measured forces, measured chip morphology, and measure tool wear (flank and crater wear).

#### **3.3.1. Orthogonal cutting experiments**

Cutting forces measured in orthogonal turning tests of Ti-6Al-4V titanium alloy tubes have been presented in Figure 3.4. The cutting forces were generally lower at the positive rake angle ( $\gamma = 5^\circ$ ) and at the lower cutting speed ( $V_c = 121.9$  m/min). The thrust forces were much lower when using a positive rake angle ( $\gamma = 5^\circ$ ) toolholder with TiAlN coated carbide inserts at the higher cutting speed ( $V_c = 240.8$  m/min).

There was a significant increase in thrust force with an increase in cutting speed however this increase becomes small at increased feeds ( $> 0.076$  mm/rev) and at the lower cutting speed.

It is reported in literature that the relationship between thrust force and cutting speed in machining Ti-6Al-4V is mainly affected by the interfacial conditions at the tool rake face. As the temperatures increase titanium alloy tends to weld itself to the rake face and creates higher thrust forces (Arrazola et al. 2009 & Cotterell and Byrne 2008).

However, at the same cutting conditions, TiAlN coated carbide tools resulted always higher cutting and thrust forces. It is believed that the effect of larger edge radius ( $r_\beta$ ) due to added layer of coating (TiAlN) becomes the dominant mechanism on increased forces.

The larger edge radius in coated tools hinders their potential benefits in tool life, hence results insignificantly higher forces especially when cutting speed is increased from  $V_c = 121.9$  m/min to  $V_c = 240.8$  m/min. Hence, it may be beneficial to modify edge preparation of the coated tools (TiAlN) to lower the effects of increasing cutting edge radius.

In order to take measurements on the chip cross-sections, chips were embedded into black-epoxy, polished and etched. The images of micro-chip geometries were captured with optical digital microscopy at Rutgers University facilities. In Figure 3.5, serrated chips obtained under different cutting conditions are shown.

It is observed that degree of serration increase with increasing feed or uncut chip thickness and increasing cutting speed. There were no significant effects of rake angle and tool coating on the degree of serration. In Table 3.3, minimum and maximum serrated chip thickness and serration pitch with measurements under different cutting conditions is given.

The chips produced at lower cutting speeds and feeds as shown in Figure 3.5 are fairly uniform along their thickness with less similar to “saw-tooth” shapes. Whereas, the chips at high feeds at both cutting speeds show a clear periodic “saw-tooth” shape formation with mostly uniform size segments after a single large segment and then same pattern is repeated (Sima & Özel, 2010).

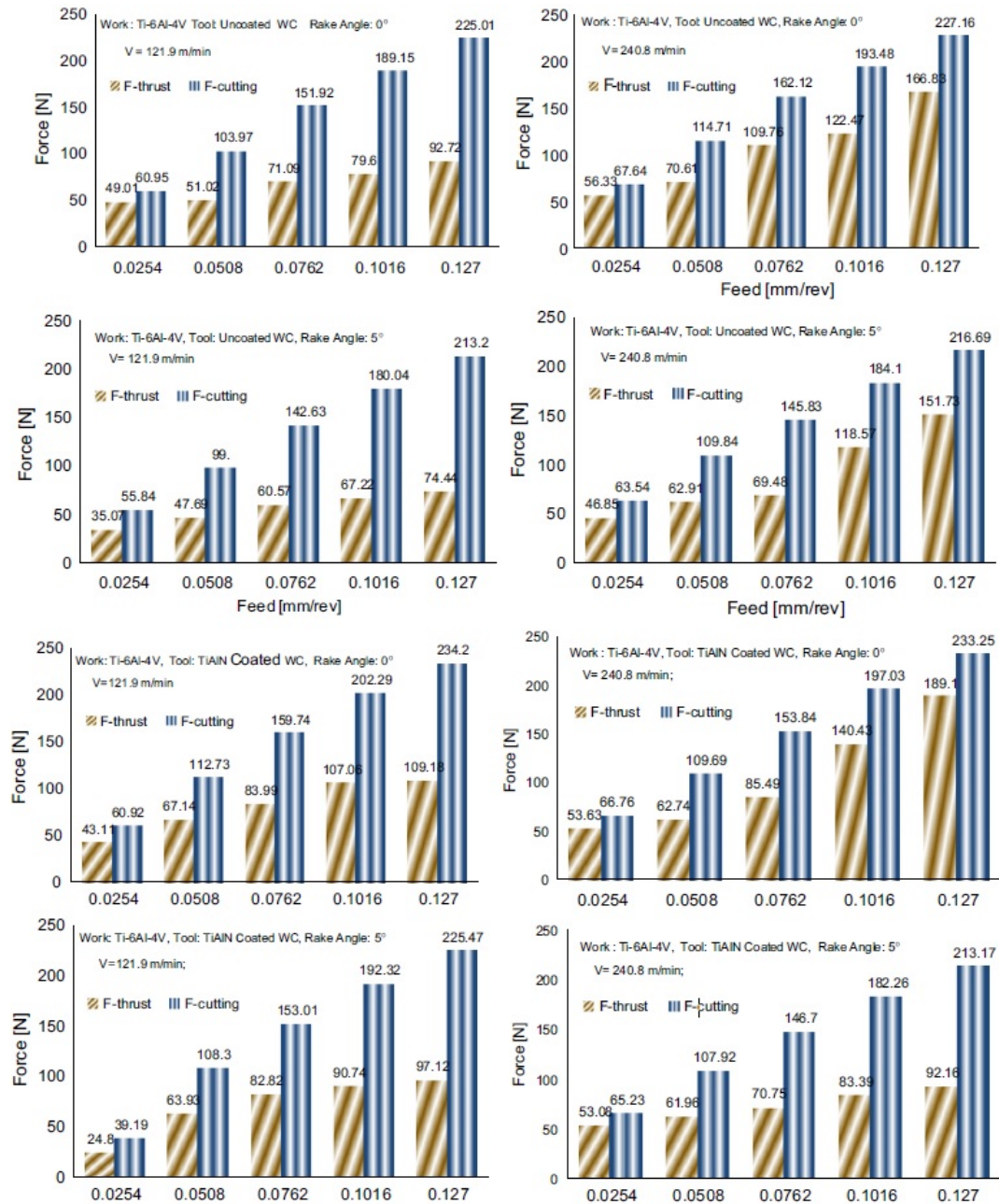


Figure 3.4. Cutting and thrust forces in orthogonal cutting test of Ti-6Al-4V (Sima & Özel, 2010)

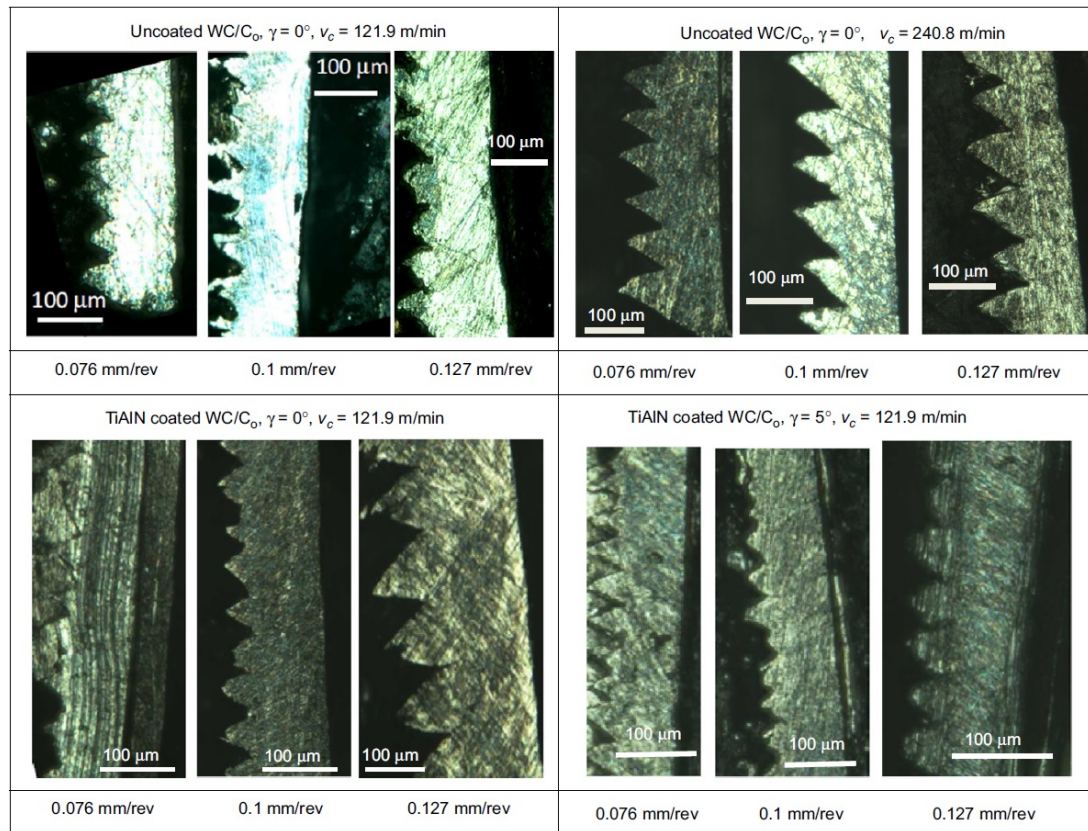


Figure 3.5. Images of serrated chips at different cutting conditions (Sima & Özel, 2010)

Table 3.3. Serrated chip dimensions under certain orthogonal cutting conditions (Sima &amp; Özel, 2010)

Tool	Rake angle, $\gamma$ [°]	$V_c$ [m/min]	$t_u$ [mm]	Experimental		
				$t_{c\_min}$	$t_{c\_max}$	$p$
Uncoated WC/Co	0	121.9	0.075	0.095	0.133	0.05
Uncoated WC/Co	0	121.9	0.1	0.13	0.192	0.07
Uncoated WC/Co	0	121.9	0.127	0.104	0.177	0.9
Uncoated WC/Co	0	240.8	0.1	0.087	0.16	0.08
Uncoated WC/Co	0	240.8	0.127	0.102	0.186	0.095
TiAlN coated WC/Co	0	121.9	0.1	0.137	0.182	0.075
TiAlN coated WC/Co	0	121.9	0.127	0.14	0.216	0.1
TiAlN coated WC/Co	5	121.9	0.1	0.102	0.158	0.073
TiAlN coated WC/Co	5	121.9	0.127	0.12	0.208	0.080
Uncoated WC/Co	5	121.9	0.127	0.156	0.23	0.089

### 3.3.2. Straight bar turning experiments

#### 3.3.2.1 Force measurements

In order to observe the performance of coatings at different cutting speeds, two sets of tests are done at cutting speeds of  $V_c = 50$  and  $100$  m/min respectively. All force components are measured as shown in Figure 3.6. Thrust force was the lowest since inserts use  $11^\circ$  relief angle; hence flank contact area is very small. According to force measurements, cBN and cBN+TiAlN coated inserts exhibit lowest cutting forces at  $50$  m/min cutting speed but the highest at  $100$  m/min cutting speed. Moreover, the highest thrust force is seen in cBN coated WC/Co inserts at high cutting speed. The advantage of cBN coatings on forces is apparent for the lower cutting speed. Adding cBN coating over TiAlN coating decreases forces. As cutting speed increases, the effect of larger edge radius

( $r_\beta$ ) due to added layer of coatings (cBN and TiAlN) becomes the dominant mechanism on forces. This larger edge radius in multi-layer coated tools hinders the potential benefits of coatings, hence results in higher forces especially when cutting speed is doubled. Hence, it may be beneficial to modify edge preparation of the coated tools (TiAlN and cBN) to lower the cutting edge radius.

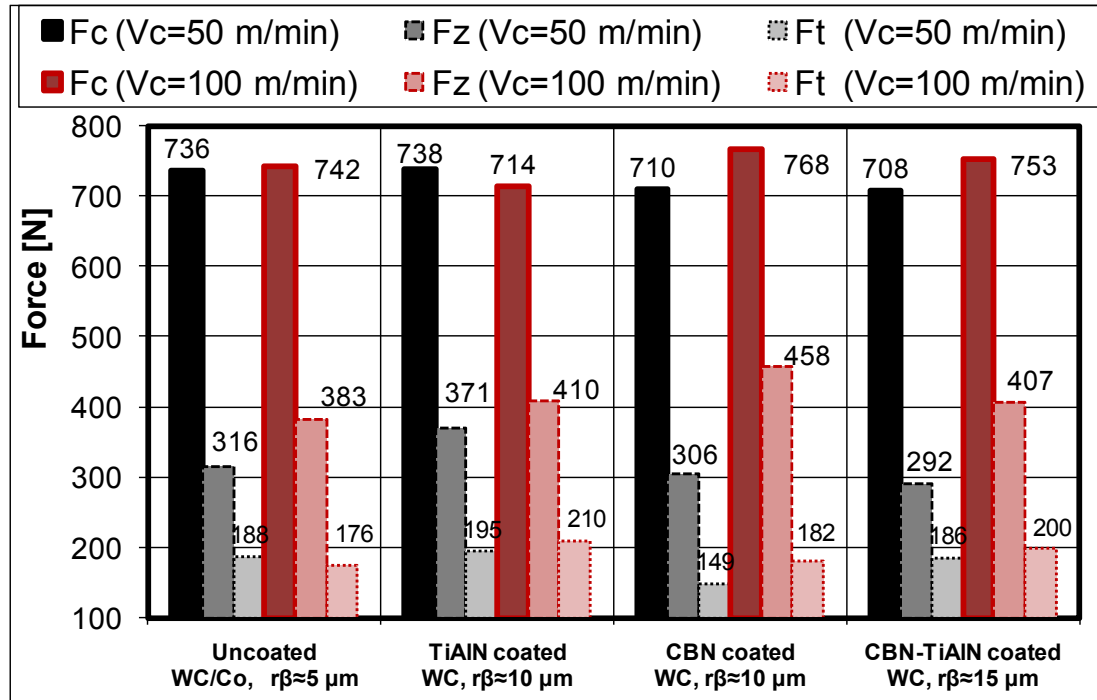


Figure 3.6. Forces in straight turning of Ti-6Al-4V titanium alloy using uncoated, TiAlN and cBN coated inserts ( $a_p = 2 \text{ mm}$ ,  $f = 0.1 \text{ mm/rev}$ ) (Özel et al., 2010)

In order to observe the performance of coatings at different cutting speeds, two sets of tests are done at cutting speeds of  $V_c = 50$  and  $100 \text{ m/min}$  respectively. Thrust force was the lowest since inserts use  $11^\circ$  relief angle; hence flank contact area is very small. According to force measurements, cBN and cBN+TiAlN coated inserts exhibit lowest cutting forces at  $50 \text{ m/min}$  cutting speed but the highest at  $100 \text{ m/min}$  cutting speed. Moreover, the highest thrust force is seen in cBN coated WC/Co inserts at high cutting speed.

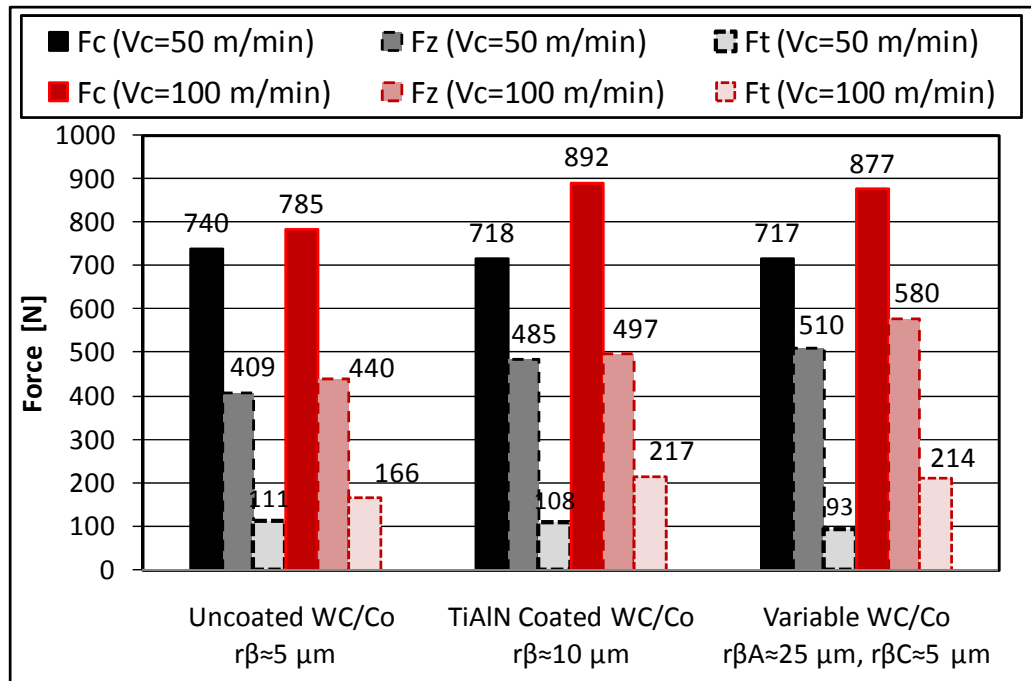


Figure 3.7. Measured forces in turning of Ti-6Al-4V titanium alloy using TiAlN coated and variable micro-geometry inserts ( $a_p = 2 \text{ mm}$ ,  $f = 0.1 \text{ mm/rev}$ ) (Özel et al., 2010)

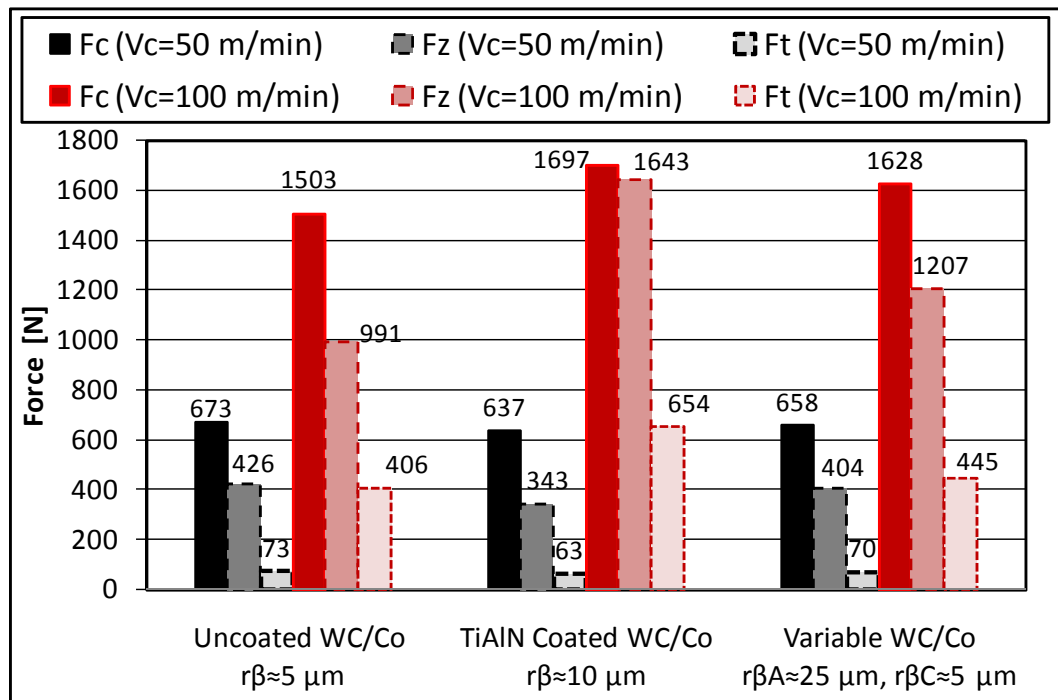


Figure 3.8. Measured forces in turning of Ti-6Al-4V titanium alloy using TiAlN coated and variable micro-geometry inserts ( $a_p = 2 \text{ mm}$ ,  $f = 0.2 \text{ mm/rev}$ ) (Özel et al., 2010)

The advantage of cBN coatings on forces is apparent for the lower cutting speed. Adding cBN coating over TiAlN coating decreases forces. As cutting speed increases, the effect of larger edge radius ( $r_\beta$ ) due to added layer of coatings (cBN and TiAlN) becomes the dominant mechanism on forces. This larger edge radius in multi-layer coated tools hinders the potential benefits of coatings, hence results in higher forces especially when cutting speed is doubled. Hence, it may be beneficial to modify edge preparation of the coated tools (TiAlN and cBN) to lower the cutting edge radius.

### 3.3.2.2 Tool wear measurements

Tool wear is measured by using tool maker's microscope and digital camera at the rake face and flank face as indicated in Fig. 3.9. Measured tool wear values are represented in Figures 3.10, 3.11 and 3.12.

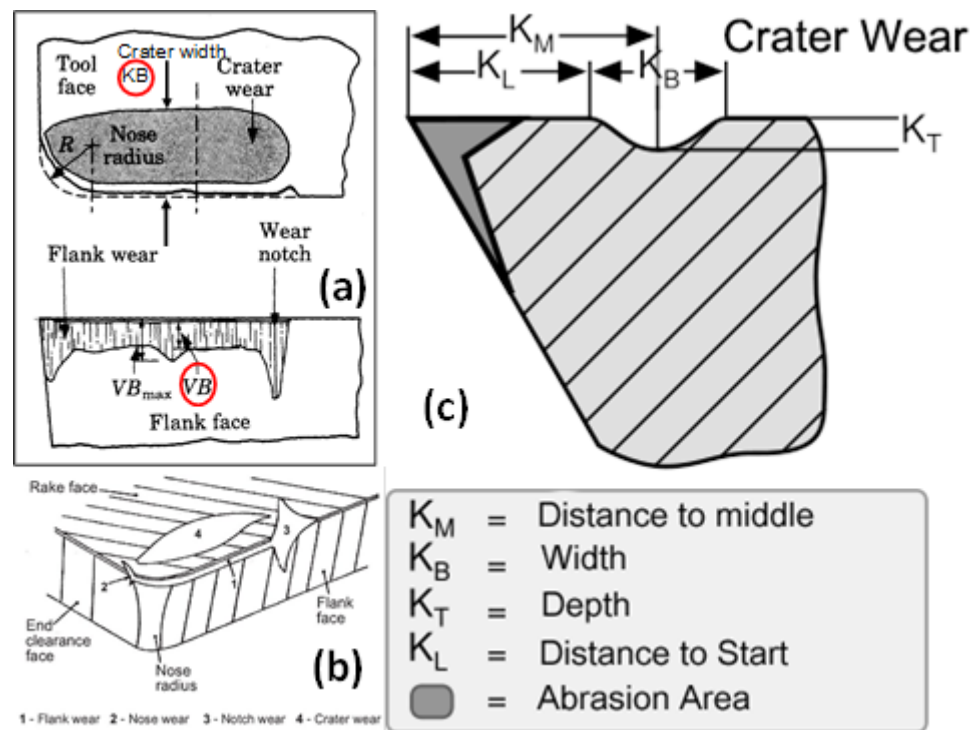


Figure 3.9. a) Schematic drawing of wear patterns (Özel et al., 2010) b) typical tool wear features in titanium machining (Antonialli et al., 2012), c) crater wear indexes (Wikipedia)

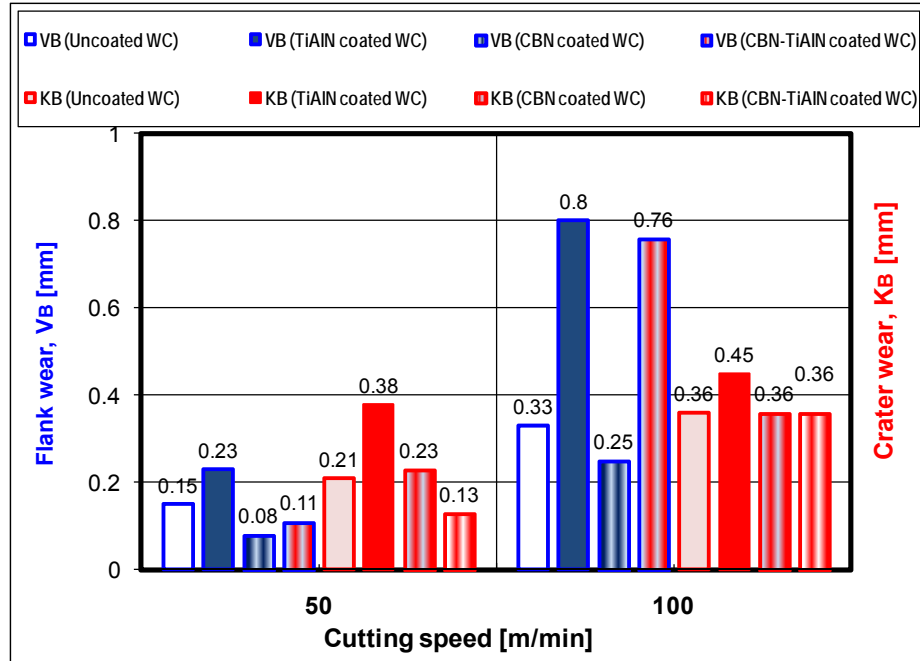


Figure 3.10. Measured tool wear of uncoated, TiAlN and cBN Coated inserts in turning of Ti-6Al-4V titanium alloy ( $a_p = 2$  mm,  $f = 0.1$  mm/rev) (Sima et al., 2011)

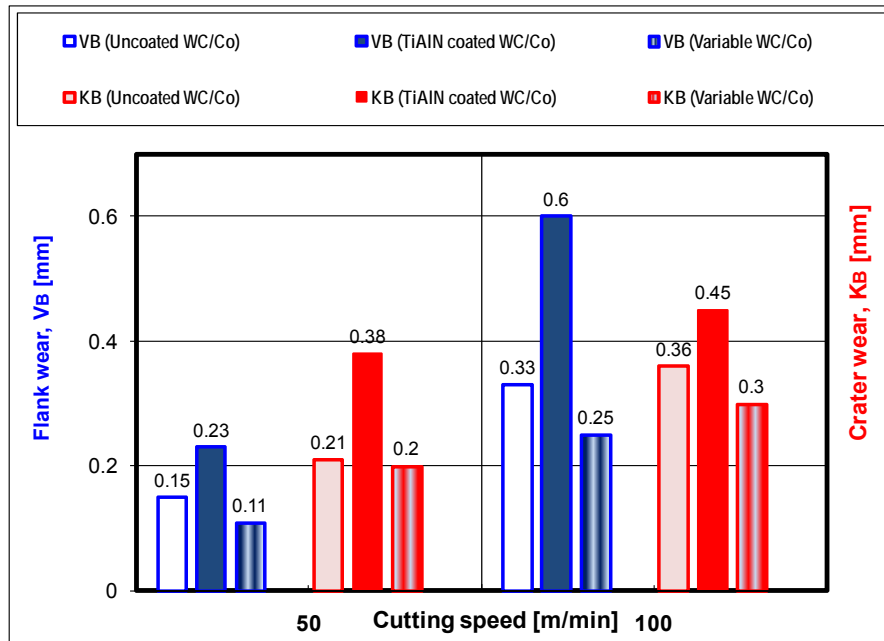


Figure 3.11. Measured tool wear of uniform and variable micro-geometry WC/Co, TiAlN coated inserts in turning of Ti-6Al-4V titanium alloy ( $a_p = 2$  mm,  $f = 0.1$  mm/rev) (Sima et al., 2011)

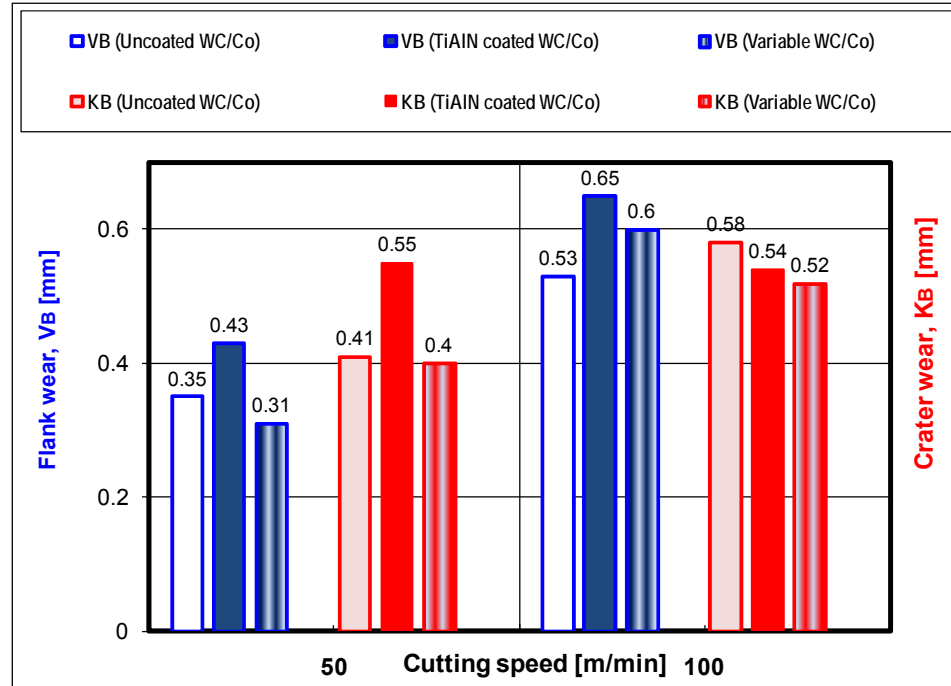


Figure 3.12. Measured tool wear of uniform and variable micro-geometry WC/Co, TiAlN coated inserts in turning of Ti-6Al-4V titanium alloy ( $a_p = 2$  mm,  $f = 0.2$  mm/rev) (Sima et al., 2011)

Figure 3.13 represents the area of worn cutting tools with different coating types during straight bar turning of Ti-6Al-4V. Figure 3.13 represents crater wear zones of five types of cutting tools used in experimental machining test of titanium alloy Ti-6Al-4V. These images are taken under Keyence VH-Z100UR optical microscope. Machining process parameters and cutting times are written on each image. Each row of images represents one type of tool and each column represents one combination of cutting speed and feed. Rows 1 to 5 are assigned to uncoated WC/Co, TiAlN coated WC/Co, cBN coated WC/Co, multi-layered coated WC/Co, and variable edge WC/Co consecutively. Column 1 is for  $V_c = 50$  m/min,  $f = 0.1$  mm/rev, column 2 belongs to  $V_c = 100$  m/min,  $f = 0.1$  mm/rev, column 3 is assigned for  $V_c = 50$  m/min,  $f = 0.2$  mm/rev, and column 4 if for  $V_c = 100$  m/min,  $f = 0.2$  mm/rev.

In Image 1a, even though the cutting speed and feed are in lower level, but since the cutting time is much higher than other conditions, it can be seen that tool is fractured and lost its original

geometry and is in more severe condition than other cutting tools in its row and column. Image 1d seems to be the second highly worn cutting tool due to higher value of cutting speed and feed despite the fact that cutting time is low in this test. Images 1b and 1c seem to be gradually worn considering that Image 1c seems to be more worn than 1b where cutting time in 1c is longer than 1b and feed factor is higher as well but cutting speed factor is higher in 1b. In row 2 where images of TiAlN coated WC/Co are presented, Image 2a despite the long cutting time gradual wear can be seen in the crater wear area while chipping off or tool fracture is visible on the non-cutting edge of the tool. While condition 2c is missing, Images 2b and 2d present harshly worn tools despite not too long cutting time which means less tool life is expected for TiAlN coated WC/Co. cBN coated WC/Co cutting tools in row 3 show normal and less level of wear despite long cutting times. Some areas of grain dislodging is visible in Image 3b where cutting speed is higher than Image 3a. In row 4 where multi-layered coated WC/Co is presented pretty worn tools are presented but not as severe as in row 2. Variable edge radius WC/Co cutting tools in row 5 present normal wear trend except Image 4d where both feed and cutting speed are at higher level, despite short cutting time. Please notice that condition 5a is taken place in shorter cutting time than other tools in this column, therefore less wear is taking place in this condition.

In order to quantify these data and find the proper relationship between cutting speed, feed and type of tool in machining of Ti-6Al-4V, one should measure these wear values and with respect to cutting time and levels of input machining parameters, build a reliability model. In Chapter 4 reliability models based on these experimental data as well as FE physics-based simulations are developed and presented.



Figure 3.13. Experimental crater wear zones in cutting tools

### 3.4. Conclusions

To sum up, two major results can be obtained from the experimental analysis in this study: Orthogonal machining tests and straight bar turning tests. The orthogonal machining test results showed that the increases in feed rate have direct impacts on the increasing in cutting and feed forces; On the other hand, the rake angle, cutting edge radius, and cutting speed have also slightly affected the cutting forces. In addition, it was concluded that the increase in cutting speed increased forces in cutting Ti-6Al-4V. The degree of serration decreases while pitch of the serrated chips

increases with decreasing cutting speed and increasing undeformed chip thickness and decreasing tool rake angle. TiAlN coated tools resulted in higher temperatures and higher cutting and thrust forces due to the larger edge radius.

Straight bar turning tests of Ti-6Al-4V revealed that although increasing cutting speed merely decrease feed forces, increasing feed rate increased all components of forces. Tests observation proved that For Ti6Al4V, the force components can be increased by the aid of using a tool with TiAlN coating. Cutting performance of the coatings were evaluated under turning experiments for uncoated, mono and multi-layer coated WC/Co carbide tools. Although cBN and TiAlN + cBN coated WC/CO inserts exhibit largest cutting forces at higher cutting speeds, they reveal favorable wear development. Tool wear zone measurements and predictions show that cBN coated WC/Co inserts depict smallest wear zone. Consequently, cBN coatings may lead to reduction in tool wear dry machining of titanium alloyed Ti6Al4V material.

Experiments have been conducted with uncoated, variable micro-geometry, single and multi-layer coated WC/Co carbide tools and cutting performance of these cutting tools are evaluated. According to force measurements, cBN and cBN+TiAlN coated inserts exhibit lowest cutting forces at 50 m/min cutting speed but the highest at 100 m/min cutting speed. Moreover, the highest thrust force is seen in cBN coated WC/Co inserts at high cutting speed. Thrust force component of machining forces was the lowest since inserts use  $11^\circ$  relief angle; hence flank contact area is very small. Variable micro-geometry WC/Co inserts provided high axial ( $F_z$ ) and radial ( $F_r$ ) but lower tangential force ( $F_c$ ) force components at the lower feed. This is much more pronounced at the higher cutting speed ( $V_c = 100$  m/min). However, at the higher feed ( $f = 0.2$  mm/rev), the opposite of this trend is observed that lower tangential forces occur. In addition, the average tangential forces fairly consistently increase with increasing cutting speed, which appears to be inconsistent with general expectations that cutting forces decrease with increasing cutting speed. A possible explanation is that the tool was wearing rapidly at the higher cutting speed.

The advantage of cBN coatings on forces is apparent for the lower cutting speed. Adding cBN coating over TiAlN coating decreases forces. As cutting speed increases, the effect of larger edge radius ( $r_{\beta}$ ) due to added layer of coatings (cBN and TiAlN) becomes the dominant mechanism on forces. This larger edge radius in multi-layer coated tools hinders the potential benefits of coatings, hence results in higher forces especially when cutting speed is doubled. Hence, it may be beneficial to modify edge preparation of the coated tools (TiAlN and cBN) to lower the cutting edge radius.

Tool wear zone measurements and predictions show that uncoated WC/Co and cBN coated WC/Co inserts depict smallest wear zone. Consequently, cBN coatings may lead to reduction in tool wear dry machining of titanium alloyed Ti-6Al-4V material. TiAlN coated WC/Co insert showed worst tool wear performance both in low and high cutting speeds. cBN+TiAlN coated WC/Co insert showed low crater wear at the low cutting speed. cBN coated WC/Co showed lowest flank wear at both low and high cutting speeds. Therefore, Tool life is expected to be longer in machining Titanium alloy (Ti-6Al-4V) when using uncoated WC/Co and cBN coated inserts.

Although it is generally true that the experimental studies can significantly help in better understanding the physical nature and mechanics of the machining process, whereas reliability analysis and Finite Element Analysis-based simulations for tool wear modeling are benefitting the results of the experiments, they establish just a direction for analytical simulations. Prediction of the forces and tool wear during machining to estimate the reliability of coated cutting tools is a valuable output from the analytical simulation and modeling.

By using different types of cutting tools under different cutting conditions, experimental and physics-based simulation data of worn cutting tools was available to study cutting tool life in machining of Ti-6Al-4V. Although the experimental tests in this research were not originally designed for this purpose, otherwise the tests should have run in at least three levels of cutting process parameters (cutting speed, feed, and depth of cut) and also cutting time should have controlled more accurately. The tests should have stopped at some predetermined increments of

time and wear measurements should have been taken under microscope for that period of time. Then fresh cutting tools should have been used for cutting up to next defined period of time. By this trend, it is possible to track magnitude of cutting tool wear by time. It is important to use fresh cutting tools each time, since we don't want the tool cool off during taking measurements and unload from machining stresses and again start a new machining test with that already used test.

Even though our experimental sets were not perfectly suit for reliability analysis of cutting tools and therefore cutting tool life, but since we had experimental data for two levels of cutting speed and feed for two types of cutting tool (uncoated WC/Co and TiAlN coated WC/Co) and two levels of cutting speed and one level of feed for the other two types of tool (cBN coated WC/Co and multi-layered coated WC/Co) and we were able to design and run FE simulations for all cutting conditions, even those missing conditions (second level of feed for cBN coated WC/Co and multi-layered coated WC/Co), it is possible to investigate the reliability of these types of cutting tools using the available data and develop a new methodology to investigate wear-based cutting input parameters dependent reliability of cutting tools using experimental and FE simulation data.

In order to develop experimental-based reliability model, precise measurements are taken from worn regions of cutting tools under the Keyence VH-Z100UR optical microscope. In this research, we are focused on crater wear since in experimental machining tests, because of positive tool clearance angle, the dominant wear-based failure was happening in rake face (crater wear) rather flank face (flank wear). Also, no data of flank wear was developed in FE simulations; therefore, it was not possible to develop flank wear related physics-based reliability models. Wear predictions in FE simulations are based on Usui's wear rate model built-in FE software using instantaneous sliding velocity, normal stress and temperatures of cutting tool elements during simulation of machining process.

All simulations are run for same length of time and wear rate data are collected at all affected zone on tool rake face for developing physics-based reliability models in chapter 4. By using the

measurements of the worn regions of cutting tools under Keyence VH-Z100UR optical microscope and recorded cutting times, experimental-based reliability models are generated in chapter 4.

# **4. RELIABILITY MODELING OF ADVANCED CUTTING TOOLS IN MACHINING TI-6AL-4V**

## 4.1. Introduction

In most machining operations, tool life is considered to be the most important factor. Especially, most of the mathematical models for the machining operation rely, to a greater or lesser extent, on the tool life equation predetermined by experimental methods or others. Aside from the problem of experimentally determining the parameters in the tool life equation, there is always the difficulty of the stochastic nature of the machining operation which are the inherent variations in tool life for a certain set of machining conditions.

In this chapter the reliability of cutting tools under the machining conditions of Ti-6Al-4V titanium alloy is formulated and evaluated. Experimental-based reliability modeling is performed based on experimental tests results while physics-based reliability models are driven using finite element simulations of the machining processes.

For this purpose, four types of cutting tools have been tested under the conditions explained in chapter 3; a) Uncoated Tungsten Carbide (WC/Co), b) Tungsten Carbide (WC/Co) coated with Titanium Aluminum Nitride (TiAlN), c) Tungsten Carbide coated with cubic Boron Nitride (cBN) and, d) Tungsten Carbide multi-layered coated with cBN and TiAlN. It should be noted that, ideally, full factorial experiments with three levels of cutting speed and feed for each tool type would be preferable to provide balanced data sets to use statistically-based reliability analysis model. However, the experiments were not originally designed for reliability modeling, and it is necessary to exploit the available data to the maximum extent. Although not the ideal situation, it is not unusual in advanced engineering research to have less data than would be desirable. Experiments are performed in two levels of cutting speed ( $V_c$ ), 50 m/min and 100 m/min for all cutting tool types and, two levels of feed ( $f$ ), 0.1 mm/rev and 0.2 mm/rev for two tool types, WC/Co and TiAlN coated WC/Co. Only one level of feed, 0.1 mm/rev has been applied during machining with cBN coated WC/Co and multi-layered coated WC/Co.

Therefore, 12 sets of experimental tests have been designed and conducted; however some of the tests have replications. The reason of running the experiments in different levels of cutting speeds and feeds is to investigate the effect of these parameters for each tool type separately and also to explore cutting tool reliability modeling.

Table 4.1. FE simulations utilized in physics-based reliability modeling

Simulation	Cutting Tool	Cutting Speed $V_c$ (mm/min)	Feed F(mm/rev)	Depth of Cut $a_p$ (mm)
1	Uncoated WC/Co	50	0.1	2
2	Uncoated WC/Co	100	0.1	2
3	Uncoated WC/Co	50	0.2	2
4	Uncoated WC/Co	100	0.2	2
5	TiAlN coated WC/Co	50	0.1	2
6	TiAlN coated WC/Co	100	0.1	2
7	TiAlN coated WC/Co	50	0.2	2
8	TiAlN coated WC/Co	100	0.2	2
9	cBN coated WC/Co	50	0.1	2
10	cBN coated WC/Co	100	0.1	2
11	cBN coated WC/Co	50	0.2	2
12	cBN coated WC/Co	100	0.2	2
13	Multi-layered (cBN+TiAlN) coated WC/Co	50	0.1	2
14	Multi-layered (cBN+TiAlN) coated WC/Co	100	0.1	2
15	Multi-layered (cBN+TiAlN) coated WC/Co	50	0.2	2
16	Multi-layered (cBN+TiAlN) coated WC/Co	100	0.2	2

In FE simulation runs for all four aforementioned types of tools, two levels of cutting speed and feed have been applied, meaning that 16 set of FE simulations have been designed and run, 4 simulations for each tool type as shown in Table 4.1.

Duration of cut varies in each experiment in order to identify the effect of time as it affects increasing wear amount during the machining process and also consider the stochastic nature of the machining process. While finite element simulations are performed in a constant period of time, 500 steps equals 0.9 milliseconds, since there is no stochasticity involved in finite element simulations.

## 4.2. Reliability Modeling of Cutting Tools

Reliability of tool type  $i$  at zone  $j$  with assumption of Weibull distribution of tool wear rate is formulated as follows. A two parameter Weibull distribution is assumed for the wear rate in this research since it is a general distribution and based on selection of shape parameter  $\beta$ , it can approximate other types of distributions, such as normal, lognormal and exponential. In other researchers' work who studied reliability of cutting tools, Weibull distribution has been utilized before (Aramesh et al., 2014, Mazzuchi & Soyer, 1998, Klim et al., 1996, and Shaban et al., 2014). In general it is known with certainty that a normal or lognormal distribution is most appropriate, and then it is logical to make that assumption. However, if there is some uncertainty about the distribution shape, then a Weibull distribution is more appropriate. For example, a normal distribution always pertains to a symmetrical distribution with the familiar shape. Alternatively, the Weibull distribution can be symmetrical or asymmetrical based on the shape parameter ( $\beta$ ).

The wear rate for tool type  $i$  at zone  $j$  is distributed as a two parameter Weibull distribution, but the scale parameter  $\eta_{ij}(f, V_c)$  is a function of feed ( $f$ ) and cutting speed ( $V_c$ ). Thus, there is a different and unique distribution for each combination of  $f$  and  $V_c$ ,

$$\frac{dW_{ij}}{dt} \sim Weibull(\beta_{ij}, \eta_{ij}(f, V_c)) \quad (4.1)$$

Assuming a tool has a linear wear with time, tool type  $i$  wear distribution at zone  $j$  at time  $t$  follows a Weibull distribution as well:

$$W_{ij} \sim Weibull(\beta_{ij}, \eta_{ij}(f, V_c)t) \quad (4.2)$$

where in equations 4.1 and 4.2,  $\beta$  is the shape parameter of the Weibull distribution and  $\eta$  is the scale parameter of the distribution which its

elf is a function of cutting speed and feed.

Reliability of tool type  $i$  at zone  $j$  by time  $t$  is calculated from Equation 4.3 as follows:

$$\begin{aligned} R_{ij}(t) &= \Pr\{W_{ij} < H_j\} = F_{W_{ij}(t)}(H_j) \\ &= 1 - \exp\left\{-\left(\frac{H_j}{\eta(f, V_c)t}\right)^\beta\right\} \end{aligned} \quad (4.3)$$

where  $H_j$  is the failure threshold at zone  $j$ . The failure threshold represents the amount of wear where the tool type can no longer produce satisfactory. It needs to be specified based on the intended application and knowledge of tool capability.

Therefore the mean or expected value of crater wear by time  $t$ , since wear is following Weibull distribution is calculated by Equation 4.4. In the equation,  $K_B$  is crater wear width value which is the failure mechanism of interest in this investigation.

$$E[K_B] = \eta(f, V_c) t \Gamma\left(1 + \frac{1}{\beta}\right) \quad (4.4)$$

For typical values of  $\beta$ , the gamma function,  $\Gamma\left(1 + \frac{1}{\beta}\right)$ , would be approximately one. A general log-linear equation form was used to model the effects of  $f$  and  $V_c$ . The general log-linear form is desirable because it is always non-negative (even when exponential) and by taking logarithm or inverse transformation, it can assume many different forms. In this analysis,  $\ln(f)$  and  $\ln(V_c)$  are used as covariates in the log-linear model. Therefore using general log-linear model for the relationship of feed, cutting speed and time to crater wear is in the form of Equation 4.5:

$$\begin{aligned} E[K_B] &= \eta(f, V_c) t \Gamma\left(1 + \frac{1}{\beta}\right) = \left(e^{\alpha_0 + \alpha_1 \ln f + \alpha_2 \ln V_c} t\right) \Gamma\left(1 + \frac{1}{\beta}\right) \\ &= C f^{\alpha_1} V_c^{\alpha_2} t^1 \end{aligned} \quad (4.5)$$

where  $C = e^{\alpha_0} \Gamma\left(1 + \frac{1}{\beta}\right)$ , this form of relationship between expected wear amount and machining input parameters is suggested by Hitomi et al. (1979).

Therefore, by having a wear rate distribution of each cutting region on the rake face, tip trailing, nose radius and cutting edge as represented in Figure 4.1, we are able to model the reliability of that region for a specific tool type. In essence, the tool fails if the wear amount of any one of these regions reaches the specified threshold of that region. This is the definition of a competing risk model. A competing risk model means that in a system consisting of different types of components or a single component with different failure mechanisms and each one of the are subject to failure, if failure of any one of these components or mechanisms results in failure of the system or component, i.e., they are “competing” to cause a failure. Cutting tool wear during

the machining process is a continuous process and stress and temperature (two major causes of tool wear) are distributed on the tool continuously. All of these wear regions affect each other. It is not necessarily logical to assume independence of effects for these regions. However, to provide an approximation they are assumed independent of each other. In reliability analysis, it is common to assume independence for complex problems can be efficiently analyzed. To consider dependence, it would require a multivariable joint distribution function which is not available or practical. The independence assumption provides a conservative or pessimistic approximation, i.e., often predict reliability to be slightly lower.

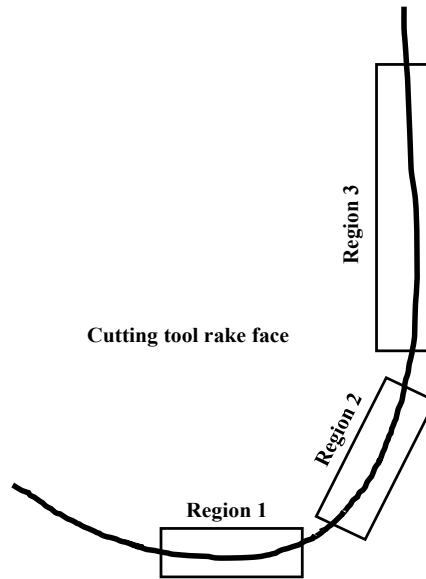


Figure 4.1. Illustration of proposed regions on rake face of cutting tool. (Region 1: Tool tip trailing, Region 2: Tool nose radius, and Region 3: Tool cutting edge)

By assuming an independent relationship between these regions, meaning that failure or wear of one zone does not have any influence on the adjacent or the other zone, the reliability formulation of cutting tool is in the form of Equation 4.6:

$$\begin{aligned}
R_i(t) &= \Pr\{W_{i1} < H_1 \cap W_{i2} < H_2 \cap W_{i3} < H_3\} \\
&= \prod_{j=1}^3 \Pr\{W_{ij} < H_j\} \\
&= \prod_{j=1}^3 \left( 1 - \exp\left\{ -\left( \frac{H_j}{\eta(f, V_c)t} \right)^\beta \right\} \right)
\end{aligned} \tag{4.6}$$

### 4.3. Experimental-Based Reliability Evaluation

The machining experiments presented in Chapter 3 are utilized in this section. Measured crater wear values at each region together with experimental conditions are listed in Table 4.2.

Using KEYENCE optical microscope, model VH-Z100UR located at Rutgers, Materials Science and Engineering Department, high quality images of the worn tools are captured at 50 times magnification. Since the major failure cause for cutting tools during machining titanium alloy Ti-6Al-4V is tool crater wear ( $K_B$ ) occurring on the rake surface of the cutting tool, this investigation is focused on reliability modeling of cutting tools susceptible to crater wear failure.

In order to quantify the crater tool wear amount, perpendicular lines are drawn on the captured images of tool worn region as shown in Figure 4.2. In Figure 4.2 some samples of the captured figures with measuring lines are shown for different cutting conditions and tool types.

Table 4.2. FE Experimental setup for machining test for the purpose of tool wear measurement and reliability modeling

No.	Tool	$V_c$ (m/min)	$a_p$ (mm)	$f$ (mm/rev)	Cutting time (s)	$K_B$ Region 1 (mm)	$K_B$ Region 2 (mm)	$K_B$ Region 3 (mm)
1a	Uncoated WC/Co	50	2.0	0.1	443	0.130	0.291	0.349
1b	Uncoated WC/Co (rep 2)	50	2.0	0.1	211	0.107	0.227	0.287
1c	Uncoated WC/Co (rep 3)	50	2.0	0.1	163	0.078	0.172	0.137
2a	TiALN coating-WC/Co	50	2.0	0.1	412	0.143	0.304	0.489
2b	TiALN coating-WC/Co (rep 2)	50	2.0	0.1	195	0.064	0.284	0.304
3	CBN coating-WC/Co	50	2.0	0.1	427	0.121	0.266	0.355
4	(CBN-TiALN) coating-WC/Co	50	2.0	0.1	420	0.03	0.167	0.189
5a	Uncoated WC/Co	100	2.0	0.1	175	0.24	0.491	0.471
5b	Uncoated WC/Co (rep 2)	100	2.0	0.1	162	0.227	0.398	0.255
6	TiALN coating-WC/Co	100	2.0	0.1	198	0.194	0.41	0.585
6a	TiALN coating-WC/Co (rep 2)	100	2.0	0.1	154	0.103	0.25	0.259
7	CBN coating-WC/Co	100	2.0	0.1	183	0.276	0.519	0.462
8	(CBN-TiALN) coating-WC/Co	100	2.0	0.1	191	0.078	0.261	0.258
9	Uncoated WC/Co	50	2.0	0.2	216	0.176	0.485	0.439
10	TiALN coating-WC/Co	50	2.0	0.2	208	No data	No data	No data
11	Uncoated WC/Co	100	2.0	0.2	65	0.47	0.621	0.737
12	TiALN coating –WC/Co	100	2.0	0.2	61	0.52	1.037	0.694 0

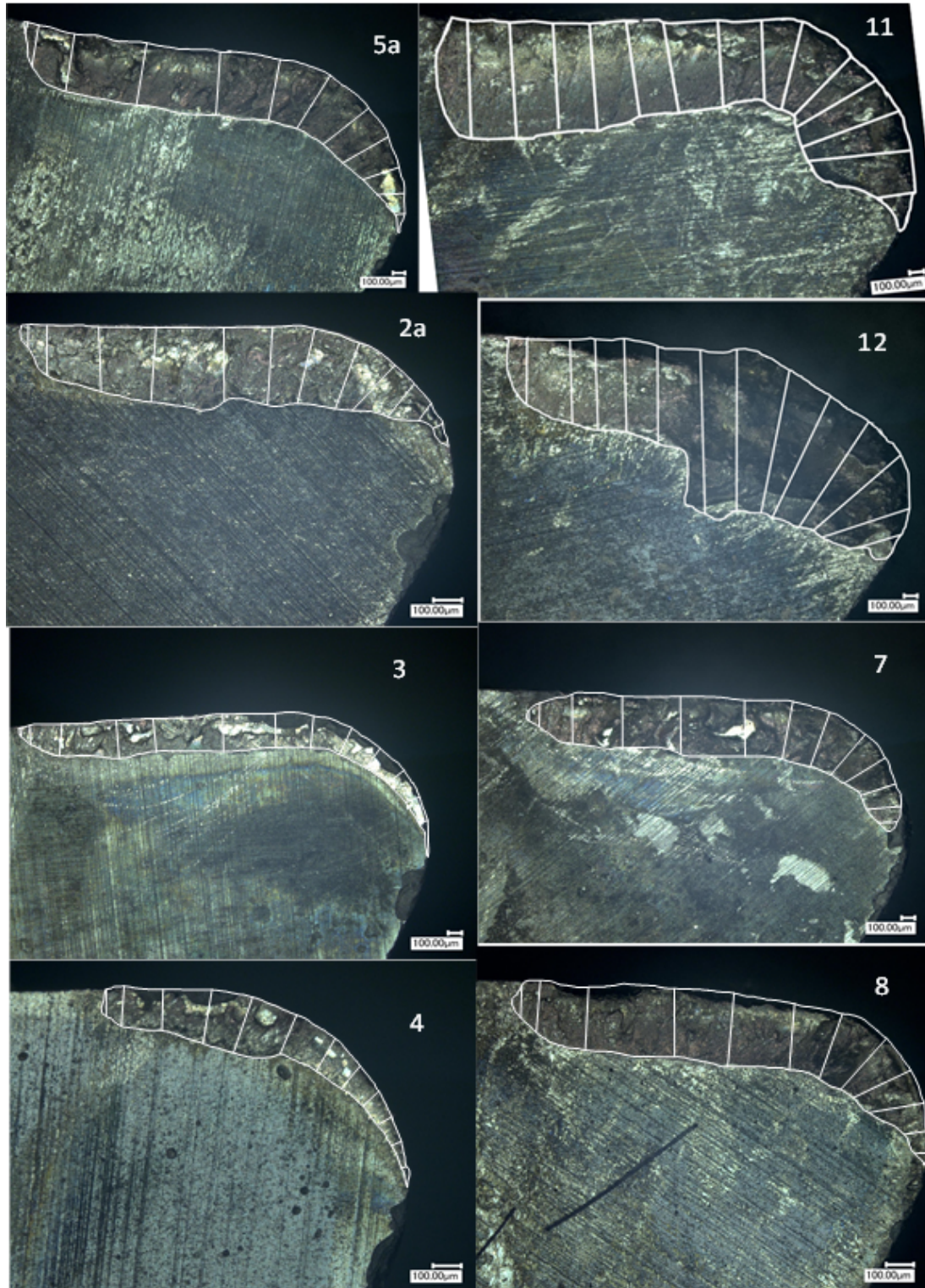


Figure 4.2. Sample images of worn tools from machining tests with measurement lines for the purpose of quantifying crater wear

As it can be seen in Figure 4.2, there is no certain or consistent wear pattern in either one of the three defined worn zones. Uncertainty and stochasticity of the process can show itself in form of unpredictable chipping off or spalling which can occur anywhere along the worn area. Since wear is not consistent, it is modeled as random variable with an associated probability of failure. Reliability is the probability of not failing in a specific time.

As can be seen from Figure 4.2, the wear amount is smaller in the tool tip trailing region and tends to increase by entering the tool nose radius region and then the cutting edge region. The tool is considered to be failed if wear amount exceeds a certain threshold value. It is less meaningful to compare magnitude of wear in these three zones with only one threshold value, since in the majority of cases, the value of wear and resistance to wear in the cutting edge zone is greater than tool nose radius and that is greater than the wear amount in the tool tip trailing region. Therefore, there should be a threshold value defined associated with each region. Assuming the threshold value for tool tip trailing is defined by  $H_t$ , for tool nose radius by  $H_r$  and for tool cutting edge by  $H_e$ , therefore

$$H_e > H_r > H_t \quad (4.7)$$

This relationship is based on mechanics of machining in turning. As illustrated in figures 4.2 and 4.3, uncut chip thickness has its maximum value in the tool cutting edge region which is equal to the feed, and its minimum value is located at the tool tip trailing region. Uncut chip thickness in the tool nose radius is between minimum chip thickness and maximum chip thickness as a transition value. The material removal mechanism at tool tip trailing region is by plowing the material from workpiece, while at the cutting edge region, it is by shearing the material. In the tool nose radius region both mechanisms are effective and basically it is a transient region from one to the other. To have a better insight of these three regions, they are classified with respect to angular distance from tool tip as depicted in Figure 4.3. Tool tip trailing

region falls in between  $0^\circ < \phi < 30^\circ$ , tool nose radius is considered in between  $30^\circ < \phi < 90^\circ$ . Tool cutting region is considered after the tool nose radius up to the end of depth of cut length.

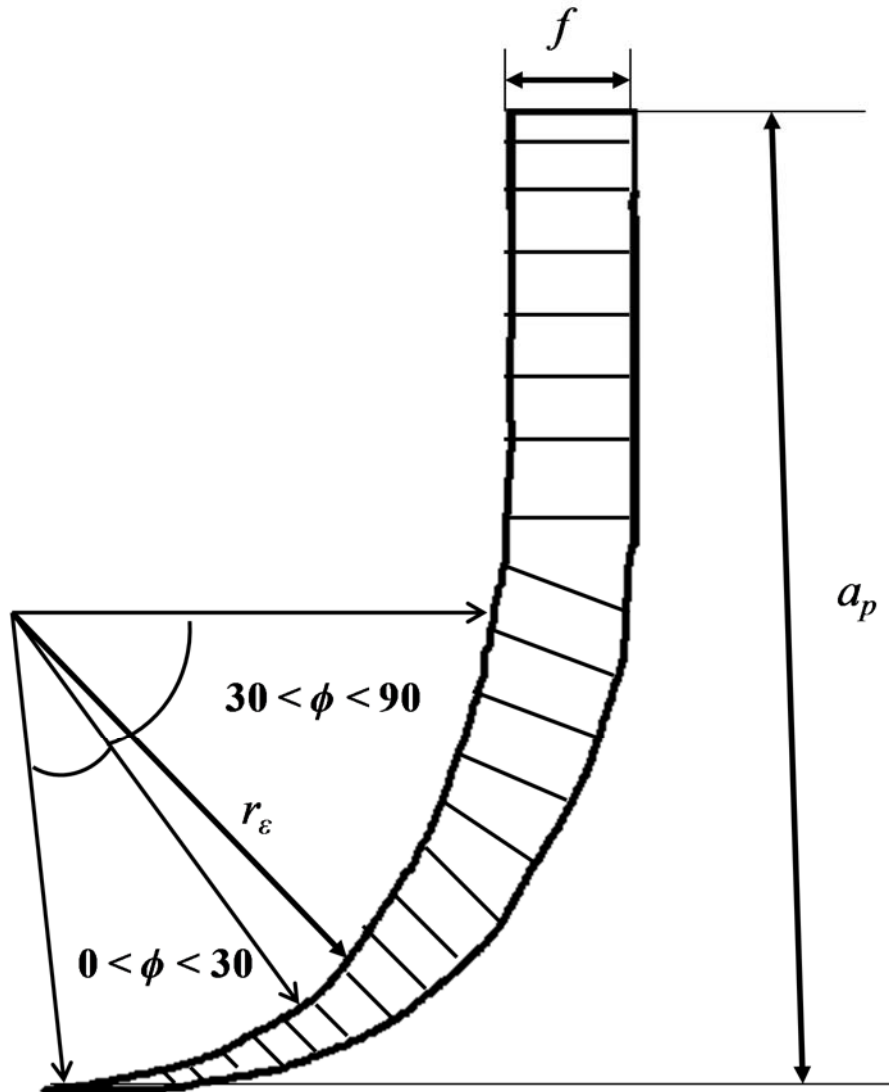


Figure 4.3. Schematic view of uncut chip thickness in turning and its relation with crater wear region classification

Figure 4.4 demonstrates aforementioned classification of worn zones of the crater wear, tip trailing zone (Region 1), nose radius (Region 2) and cutting edge (Region 3).

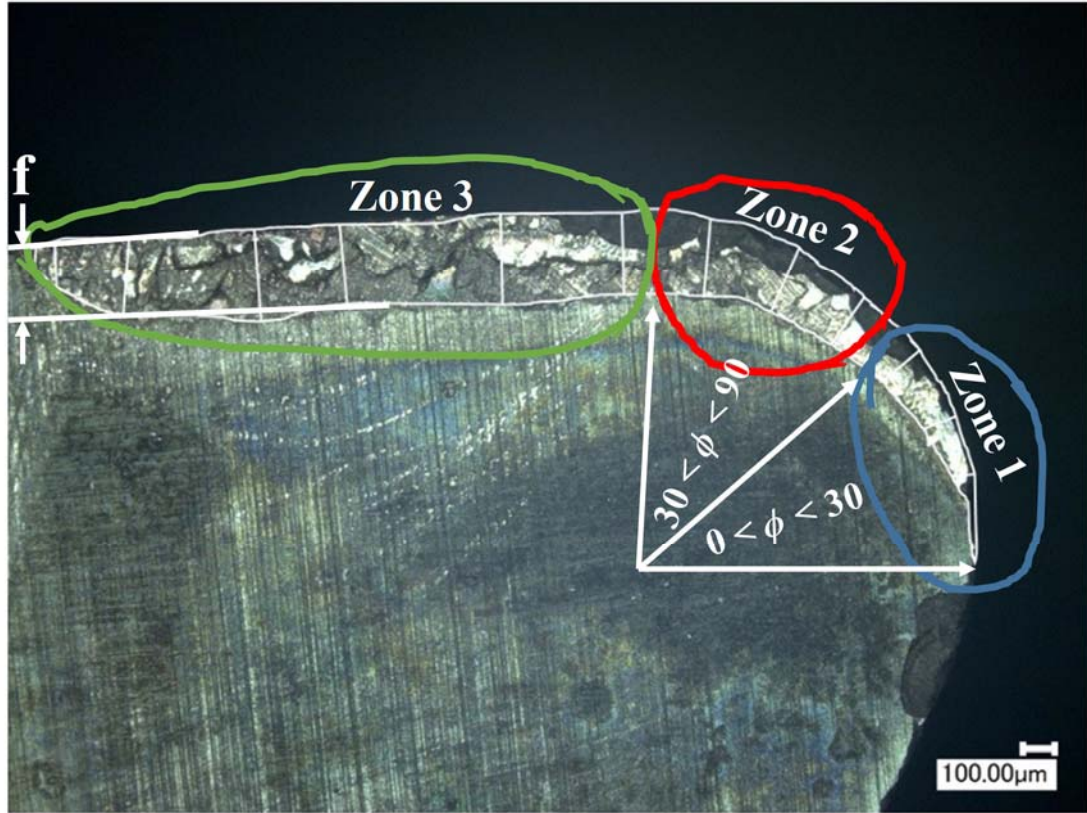


Figure 4.4. Classification of three regions on tool crater face a) tool tip, b) tool radius and, c) tool cutting edge

The experimental data have been clustered according to these three regions and wear rate amount are measured accordingly as shown in Table 4.2. The reason for such classification is that these regions are subject to different levels of stress and temperature which are the main physical attributes for wear, and hence, there should be different failure criteria considered for these regions respectively. Assuming  $H_t$  is the failure threshold for tool tip region,  $H_r$  for tool radius region and  $H_e$  for cutting edge region. Therefore, this problem is a competing risk reliability problem meaning that the first region with wear that exceeds the associated threshold causes the tool to fail (or the tool is considered failed).

$$R_i(t) = \Pr\{(K_{Bt} < H_t) \cap (K_{Br} < H_r) \cap (K_{Be} < H_e)\} \quad (4.8)$$

For consistency, a general log-linear model is considered for reliability assessment of each zone worn region in each tool type. The general log-linear model is the most general model available for analyzing data with time-independent stresses and can handle data with up to eight stresses. Its flexibility comes from the ability to specify a life-stress relationship for each stress. Each stress can be modeled with an exponential, Arrhenius or power life-stress relationship.

$$L(\mathbf{x}) = \exp\left(\alpha_0 + \sum_{i=1}^m \alpha_i X_i\right) \text{ with } \mathbf{x} = (x_1, x_2) \quad (4.9)$$

where  $x_1 = \ln(V_c)$  and  $x_2 = \ln(f)$  and can be substituted in Equation 4.5.  $L(\mathbf{x})$  is life or scale parameter, and its specific meaning or interpretation differs depending on the distribution selection.

The Weibull distribution is one of the most commonly used distributions in reliability engineering because of the many shapes that it can attain for various values of the shape parameter,  $\beta$ , (slope). It is an all-purpose distribution and can therefore model a variety of data and life characteristics (Aramesh et al., 2014, Mazzuchi & Soyer, 1998, Klim et al., 1996, and Shaban et al., 2014). In ALTA, the scale parameter,  $\eta$ , is used as the life characteristic  $L(\mathbf{x})$  that is a function of stress,  $\mathbf{x}$ .

Reliasoft's ALTA provides the life-stress relationships required to analyze accelerated life test data. ALTA offers the advanced statistical modeling power to analyze data with up to 8 simultaneous stress types and scenarios where stress is constant or varies with time.

Furthermore, in order to find the wear rate distribution associated with each cutting region of each type of tool, for all combinations of cutting conditions that type of tool is tested, wear data are clustered together with respect to the cutting region. Wear rates for each measurement are calculated by dividing the value of measured wear to time duration of cut. The results of the wear rate distributions of experimental tests are shown in Table 4.3 in terms of Weibull distribution and

general log-linear model parameters. These values are generated using ALTA analyzer by defining the general log-linear model and Weibull distribution fit to the input data, which is wear rate value and inputting associated  $\ln(V_c)$  and  $\ln(f)$ .

As it can be seen in Table 4.3, since experiments with cBN coated WC/Co tools and multi-layered (cBN+TiAlN) coated WC/Co tools have been run in only one level of feed, the exponent  $\alpha_2$  associated with feed in the general log-linear model cannot be determined for these two tool types. Due to the fact that enough correlation has been seen between experimental tests and FE simulation wear prediction in Chapter 3, and for the purpose of consistency, we use  $\alpha_2$  parameters calculated via FE simulation results for these conditions in order to model experimental-based reliability of these two types of tool.

In Figure 4.5, distribution fit and shape of the probability density function for some of these cutting tool types and tool regions are presented for illustrating experimental tests. The complete set of these distribution fit figures can be found in Appendix 1.

Therefore, according to aforementioned definition,  $R_{ij}(t)$  represents reliability of tool type  $i$  at region  $j$  with following definitions of  $i$  and  $j$ :

$$\left\{ \begin{array}{ll} i = 1 & \text{uncoated WC/Co} \\ i = 2 & \text{TiAlN coated WC/Co} \\ i = 3 & \text{cBN coated WC/Co} \\ i = 4 & \text{Multi-layered coated WC/Co} \end{array} \right. \left\{ \begin{array}{ll} j = 1 & \text{Tip trailing Region} \\ j = 2 & \text{Nose Radius Region} \\ j = 3 & \text{Cutting Edge Region} \end{array} \right.$$

Associated reliability models for each cutting tool region and tool type based on experimental data are listed in Table 4.4. Please note that  $\alpha_2$  values for tool types  $i = 3$  and 4 are used as the corresponding values from physics-based  $\alpha_2$  values that are listed in Table 4.5.

Table 4.3. Weibull wear rate distribution parameters obtained from experimental results for different tool types at each wear zone

Type of Tool	Cutting Regions	$\beta$	$\alpha_0$	$\alpha_1$	$\alpha_2$
Uncoated WC/Co	tip trailing (Region 1)	1.928973	-11.097698	1.841746	1.589464
	nose radius (Region 2)	4.173234	-8.794619	1.307371	1.247749
	cutting edge (Region 3)	2.692409	-8.909124	1.258331	1.002787
TiAlN coated WC/Co	tip trailing (Region 1)	1.400716	-6.01755	0.044466	0.770914
	nose radius (Region 2)	2.299581	-2.333937	0.621767	2.856087
	cutting edge (Region 3)	2.572315	-6.662554	1.146511	1.731465
cBN coated WC/Co	tip trailing (Region 1)	5.276704	-17.658891	2.444873	(*)
	nose radius (Region 2)	8.410532	-15.437289	2.084517	(*)
	cutting edge (Region 3)	2.885912	-13.983928	1.736207	(*)
cBN+TiAlN coated WC/Co	tip trailing (Region 1)	2.207946	-22.636358	3.366199	(*)
	nose radius (Region 2)	2.019805	-11.679255	0.97325	(*)
	cutting edge (Region 3)	5.038452	-13.909426	1.583552	(*)

Note: (\*) for these tests, associated  $\alpha_2$  values are used from physics-based FE simulation results.

Since the area of the cutting tool tip trailing region is smaller than tool nose radius region, and the tool nose region area is generally smaller than tool cutting edge region, more data are collected in cutting tools cutting edge regions than tool nose regions and also in nose region rather than tool tip trailing region. This number of measurement data may affect the goodness-of-fit to the distributions. However, with respect to Figure 4.5 and Appendix 1 most of the data which diverse from the distributions are in the lower values of wear rate which are not as critical, i.e., relatively far from failure.

Uncoated WC/Co wear measurements seem to be fit well in Regions 1 and 2 but not as good in Region 3. Some sort of trend can be observed in Region 3 data. While TiAlN coated WC/Co tools follow almost the same trend in goodness-of-fit meaning that they show good fitness in Regions 1 and 2, although not as good as uncoated WC/Co, but again Region 3 data does not fit as good. cBN coated WC/Co seem to have the worst fitness of data in Region 3 among all other tools but the other two regions fitness seem to be fine. Finally, unlike the other tool types, Region 3 crater wear data fit well to the distribution, while Region 1 and 2 data follow a satisfactory fitness to the distribution.

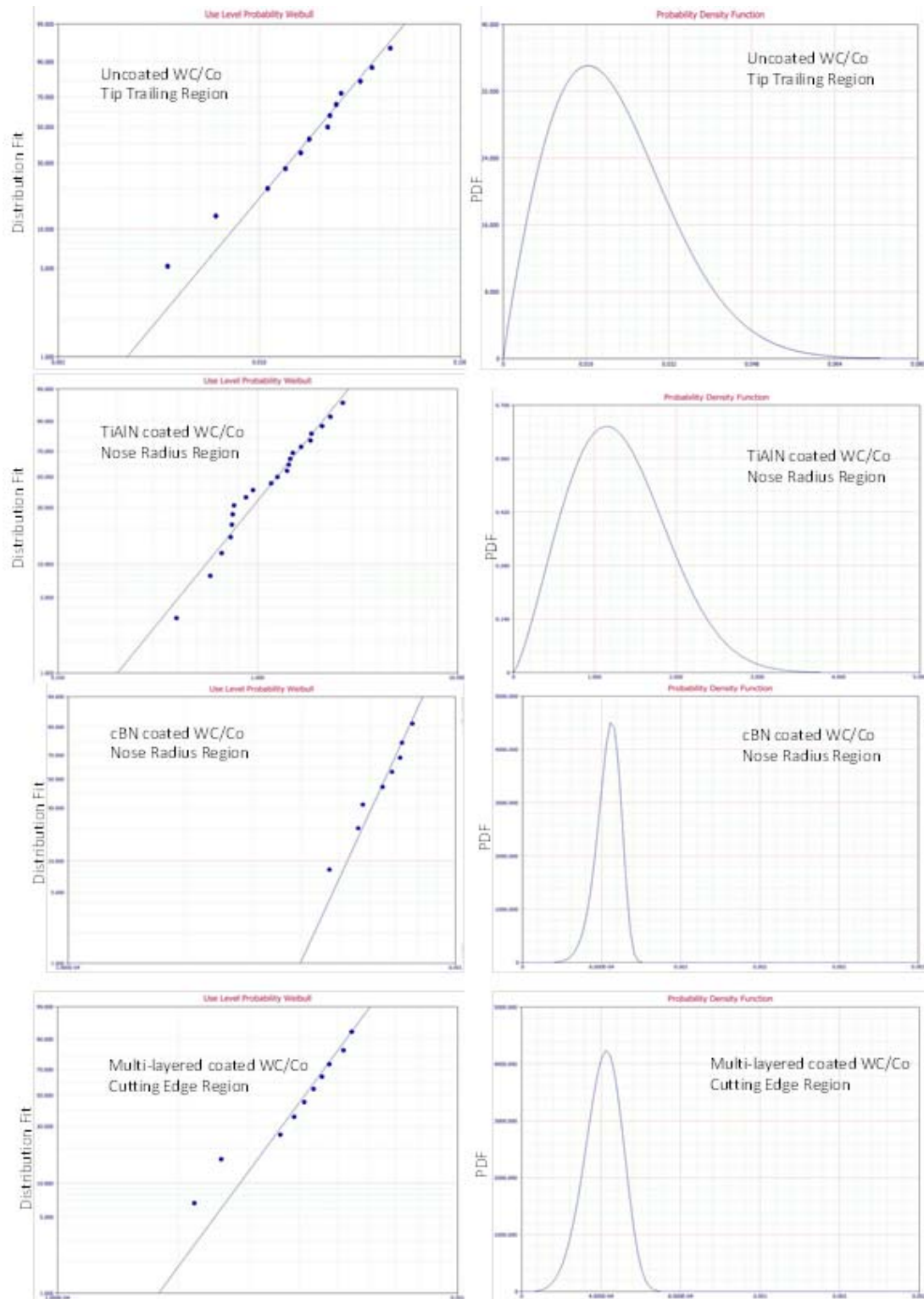


Figure 4.5. Probability distributions and distribution fits of experimental-based wear rate values

Table 4.4. Experimental-based reliability models of cutting tools at crater wear sub-regions

Type of Tool	Cutting Zone	$R_{ij}(t)$	Reliability Models
Uncoated WC/Co	tip trailing (Region 1)	$R_{11}(t)$	$1 - \exp \left\{ - \left( \frac{H_1}{te^{-11.097698+1.841746\ln V_c+1.589464\ln f}} \right)^{1.928973} \right\}$
	nose radius (Region 2)	$R_{12}(t)$	$1 - \exp \left\{ - \left( \frac{H_2}{te^{-8.794619+1.307371\ln V_c+1.247749\ln f}} \right)^{4.173234} \right\}$
	cutting edge (Region 3)	$R_{13}(t)$	$1 - \exp \left\{ - \left( \frac{H_3}{te^{-8.909124+1.258331\ln V_c+1.002787\ln f}} \right)^{2.692409} \right\}$
TiAlN coated WC/Co	tip trailing (Region 1)	$R_{21}(t)$	$1 - \exp \left\{ - \left( \frac{H_1}{te^{-6.01755+0.044466\ln V_c+0.770914\ln f}} \right)^{1.400716} \right\}$
	nose radius (Region 2)	$R_{22}(t)$	$1 - \exp \left\{ - \left( \frac{H_2}{te^{-2.333937+0.621767\ln f+2.856087\ln V_c}} \right)^{2.299581} \right\}$
	cutting edge (Region 3)	$R_{23}(t)$	$1 - \exp \left\{ - \left( \frac{H_3}{te^{-6.662554+1.146511\ln V_c+1.731465\ln f}} \right)^{2.572315} \right\}$
cBN coated WC/Co	tip trailing (Region 1)	$R_{31}(t)$	$1 - \exp \left\{ - \left( \frac{H_1}{te^{-17.658891+2.444873\ln V_c+0.615076\ln f}} \right)^{5.276704} \right\}$
	nose radius (Region 2)	$R_{32}(t)$	$1 - \exp \left\{ - \left( \frac{H_2}{te^{-15.437289+2.084517\ln V_c+0.249892\ln f}} \right)^{8.410532} \right\}$
	cutting edge (Region 3)	$R_{33}(t)$	$1 - \exp \left\{ - \left( \frac{H_3}{te^{-13.983928+1.736207\ln V_c+0.287246\ln f}} \right)^{2.885912} \right\}$
cBN+TiAlN coated WC/Co	tip trailing (Region 1)	$R_{41}(t)$	$1 - \exp \left\{ - \left( \frac{H_1}{te^{-22.636358+3.366199\ln V_c+0.338001\ln f}} \right)^{2.207946} \right\}$
	nose radius (Region 2)	$R_{42}(t)$	$1 - \exp \left\{ - \left( \frac{H_2}{te^{-11.679255+0.97325\ln V_c+0.340659\ln f}} \right)^{2.019805} \right\}$
	cutting edge (Region 3)	$R_{43}(t)$	$1 - \exp \left\{ - \left( \frac{H_3}{te^{-13.909426+1.583552\ln V_c+0.162941\ln f}} \right)^{5.038452} \right\}$

Overall reliability of each cutting tool type can be calculated by multiplication of reliability terms of each cutting tool regions, as following:

Experimental-based reliability of uncoated WC/Co:

$$R_1(t) = R_{11}(t)R_{12}(t)R_{13}(t) \quad (4.10)$$

Experimental-based reliability of TiAlN coated WC/Co:

$$R_2(t) = R_{21}(t)R_{22}(t)R_{23}(t) \quad (4.11)$$

Experimental-based reliability of cBN coated WC/Co:

$$R_3(t) = R_{31}(t)R_{32}(t)R_{33}(t) \quad (4.12)$$

Experimental-based reliability of multi-layered (cBN+TiAlN) coated WC/Co:

$$R_4(t) = R_{41}(t)R_{42}(t)R_{43}(t) \quad (4.13)$$

For comparison purpose and as an illustration, reliability of cutting edge region (Region 3) of TiAlN coated WC/Co tools are shown in Figure 4.6 through 4.8 based on experimental machining test results.

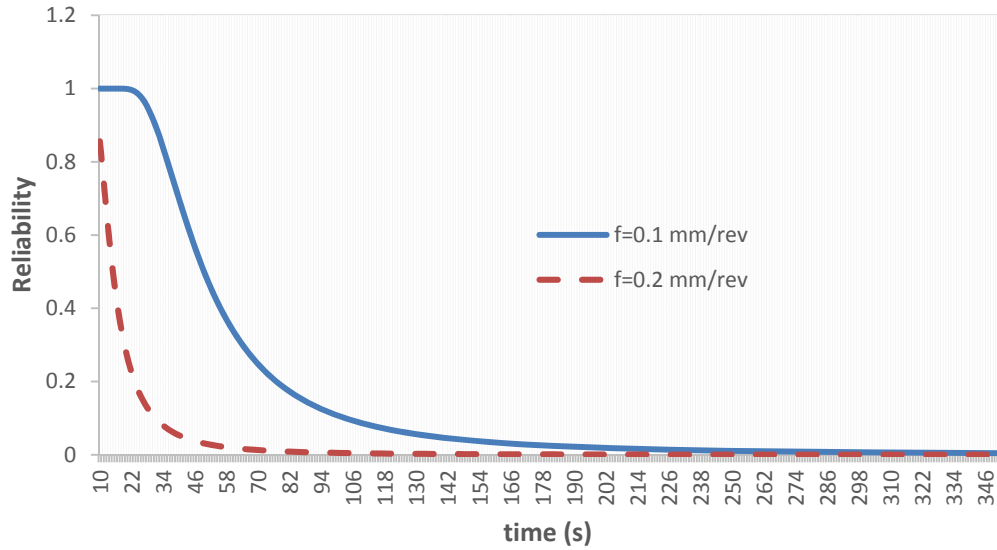


Figure 4.6. Experimental -based reliability of TiAlN coated WC/Co at tool cutting edge region (Region 3) for two levels of feed  $f=0.1$  mm/rev and  $0.2$  mm/rev, cutting speed  $V_c = 100$  m/min, and wear threshold  $H_3 = 0.2$  mm

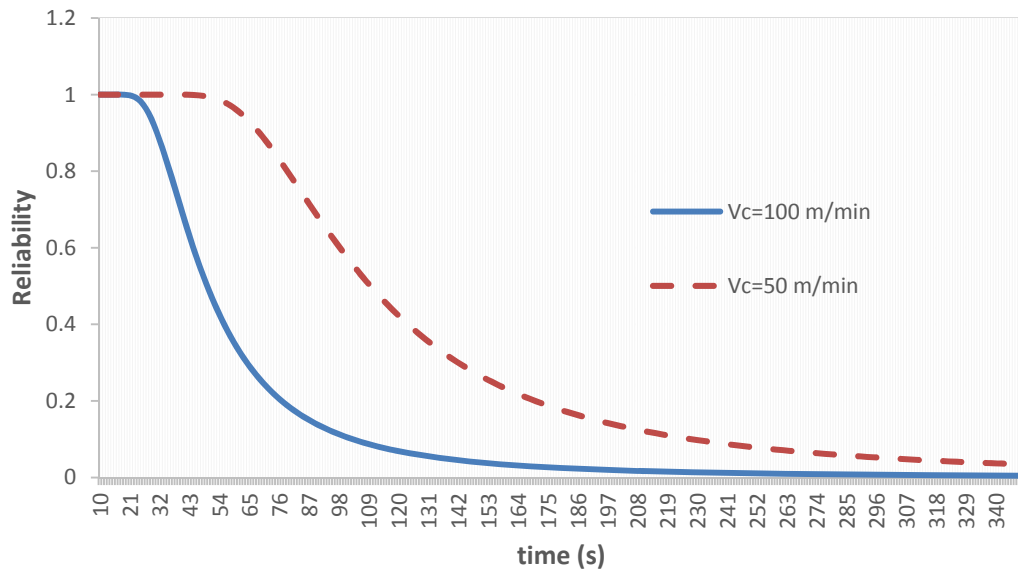


Figure 4.7. Experimental -based reliability of TiAlN coated WC/Co at tool cutting edge region (Region 3) for two levels of cutting speed  $V_c = 100$  m/min and  $50$  m/min, feed  $f=0.1$  mm/rev, and wear threshold  $H_3 = 0.2$  mm

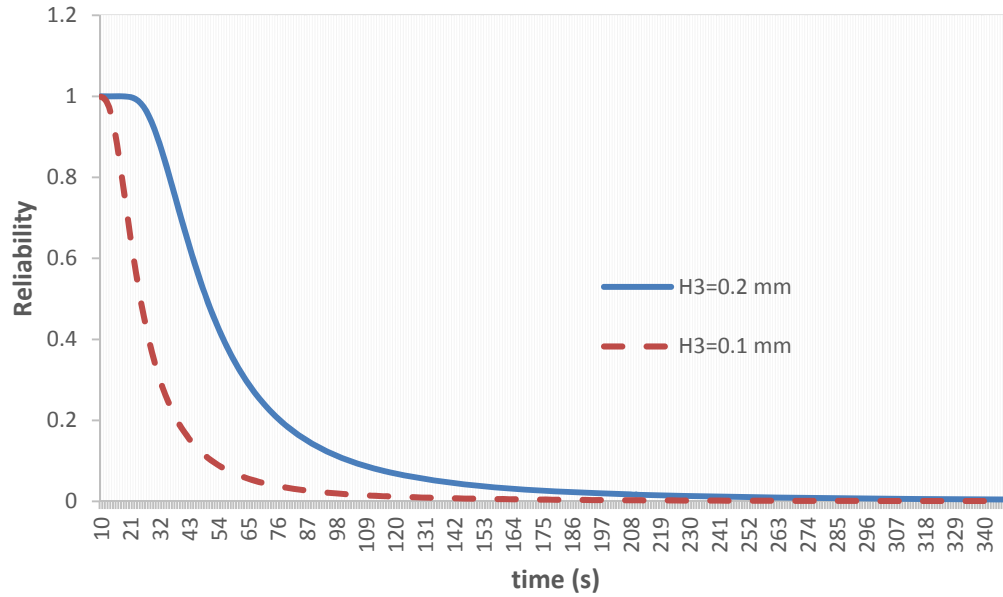


Figure 4.8. Experimental -based reliability of TiAlN coated WC/Co at tool cutting edge region (Region 3) for two levels of wear threshold  $H_3 = 0.2\text{mm}$  and  $H_3 = 0.1\text{mm}$ , cutting speed  $V_c = 100\text{ m/min}$ , and feed  $f = 0.1\text{ mm/rev}$

Figure 4.8 represents the effect of crater wear threshold on the reliability of Region 3. The interpretation of this is either by having a stronger tool type or for those types of operations that surface quality of the machined part is not as critical, wear threshold can be selected slightly bigger and that affects the reliability of the cutting tool.

#### 4.4. Physics-based Reliability Evaluation

The new idea of generating reliability models using FE simulations are developed by extracting wear rate values from elements of the worn regions in FE models as presented in Figure 4.9. As it is shown in Figure 4.9, wear rate values are extracted from each node and presented as a small orange colored dot. All simulations have been run for certain amount of time, i.e., 500 steps equal to 0.9 milliseconds.

Tool wear regions are clustered the same way as experimental images to the three zones, (tool tip trailing, tool nose radius and, tool cutting edge) as represented in figures 4.3 and 4.4. As can

be seen in Figure 4.10, because of the different region sizes, the number of possible points to measure their wear rate is different in each region. More measurements are taken in the tool cutting edge region rather than the other two regions.

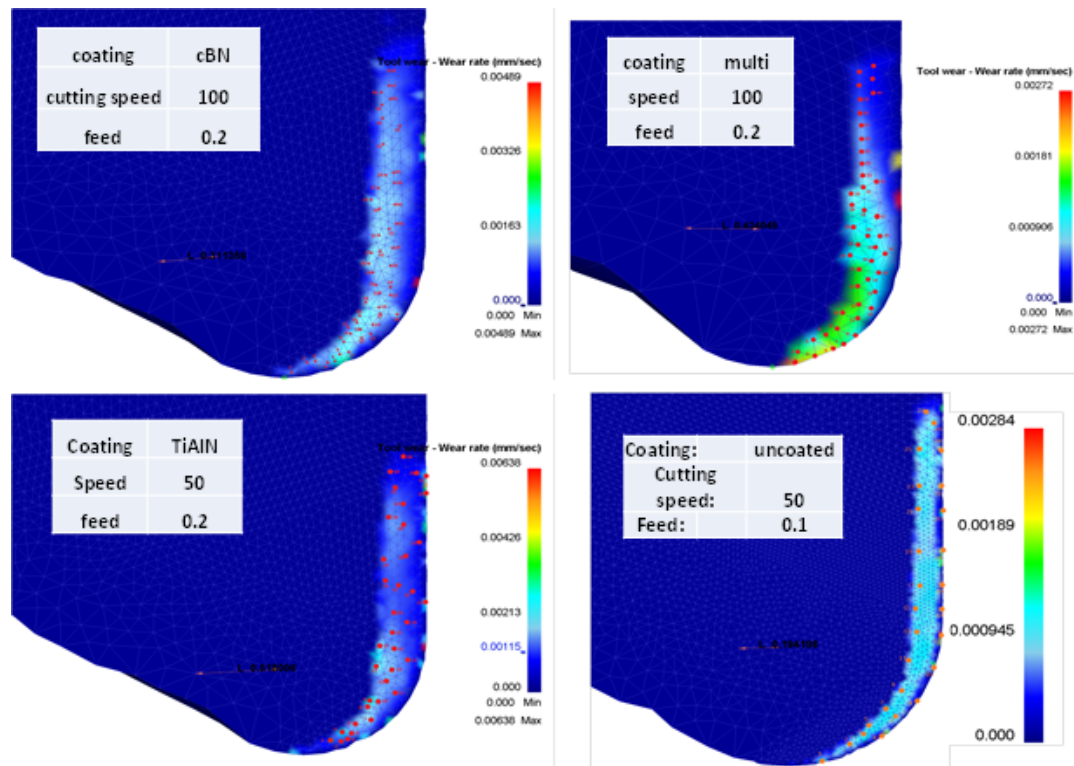


Figure 4.9. Extraction of tool wear rate values from tool rake surfaces for different tool types and cutting conditions in FE simulations of machining Ti-6Al-4V

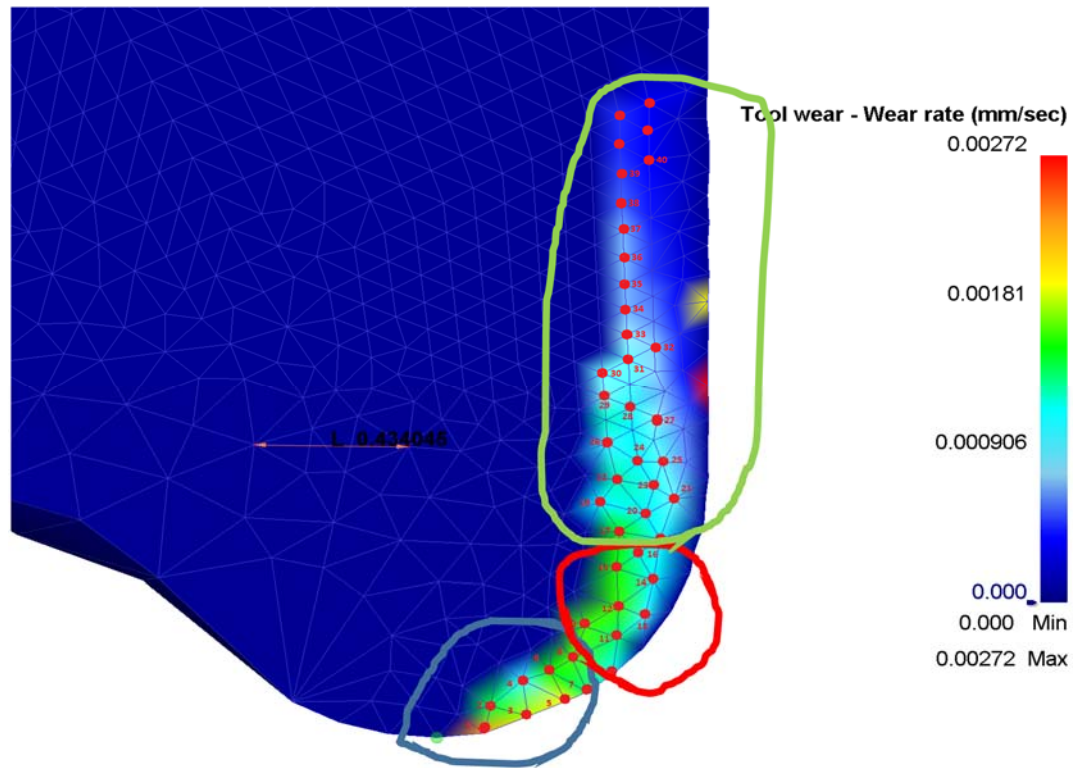


Figure 4.10. Classification of three regions on tool rake face a) tool tip trailing (Region 1), b) tool radius (Region 2) and, c) tool cutting edge (Region 3) in FE simulations

For the comparison purpose, average wear rates that are extracted from FE simulation runs for all cutting conditions are calculated for all tool types at all three wear zones. In order to find out the predicted wear amount using these wear rates from FE simulation runs, these values need to be multiplied to the experimental cutting time for each condition. Figures 4.11 through 4.14 represent these comparisons for all cutting tool types and all regions and at all cutting conditions.

## Uncoated WC/Co

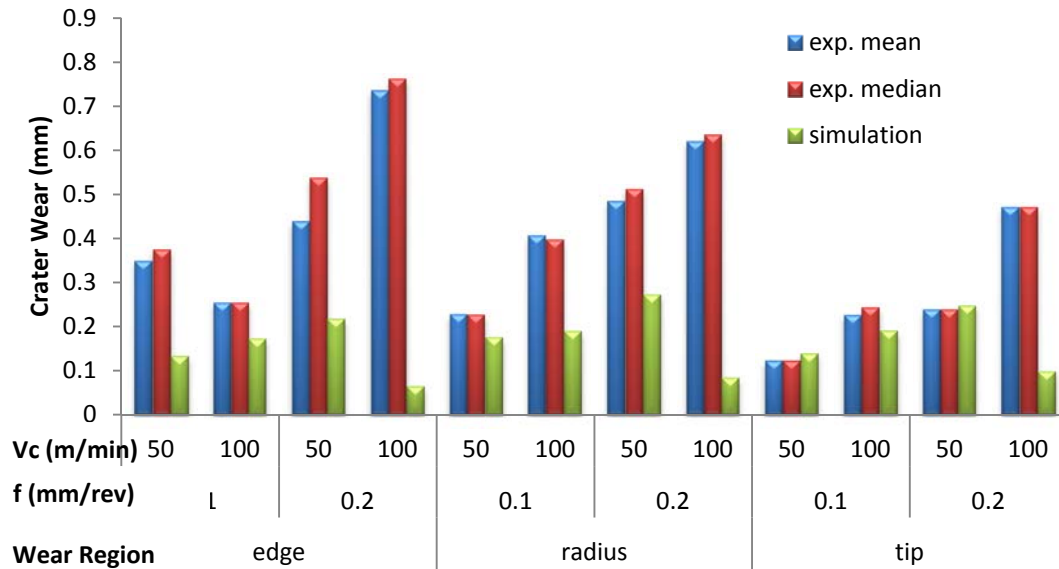


Figure 4.11. Experimentally measured wear amounts vs. FE simulation predictions for uncoated WC/Co cutting tools

## TiAlN coated WC/Co

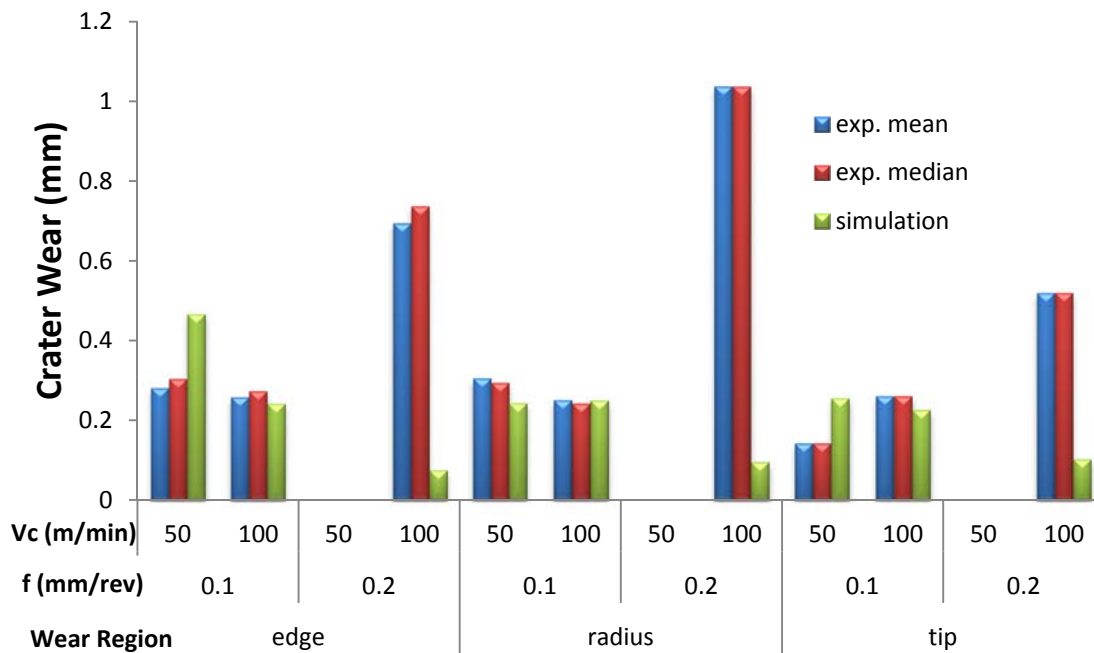


Figure 4.12. Experimentally measured wear amounts vs. FE simulation predictions for TiAlN coated WC/Co cutting tools

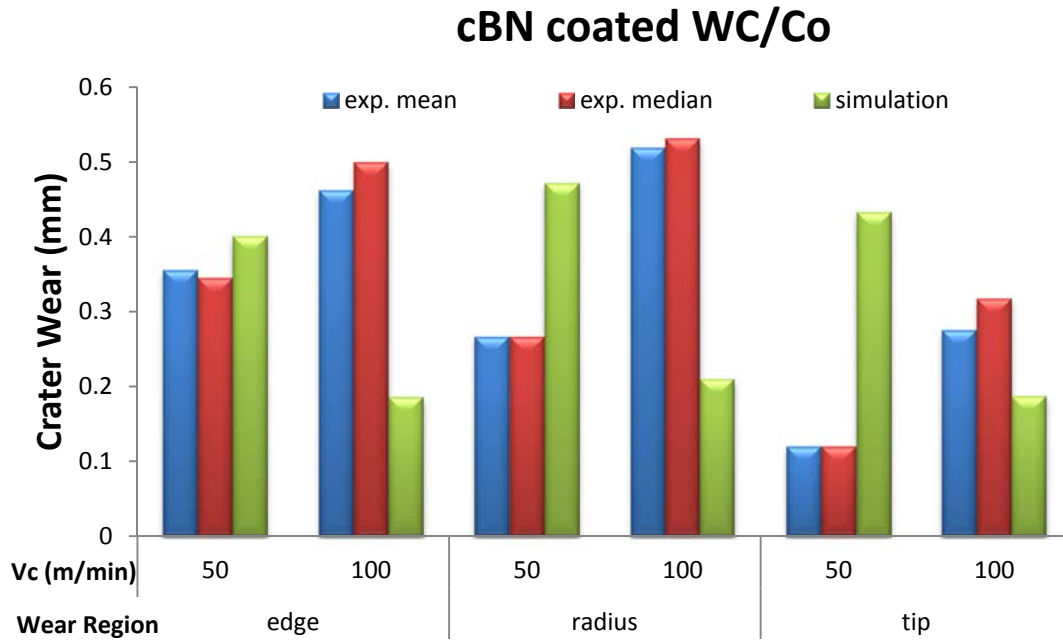


Figure 4.13. Experimentally measured wear amounts vs. FE simulation predictions for cBN coated WC/Co cutting tools

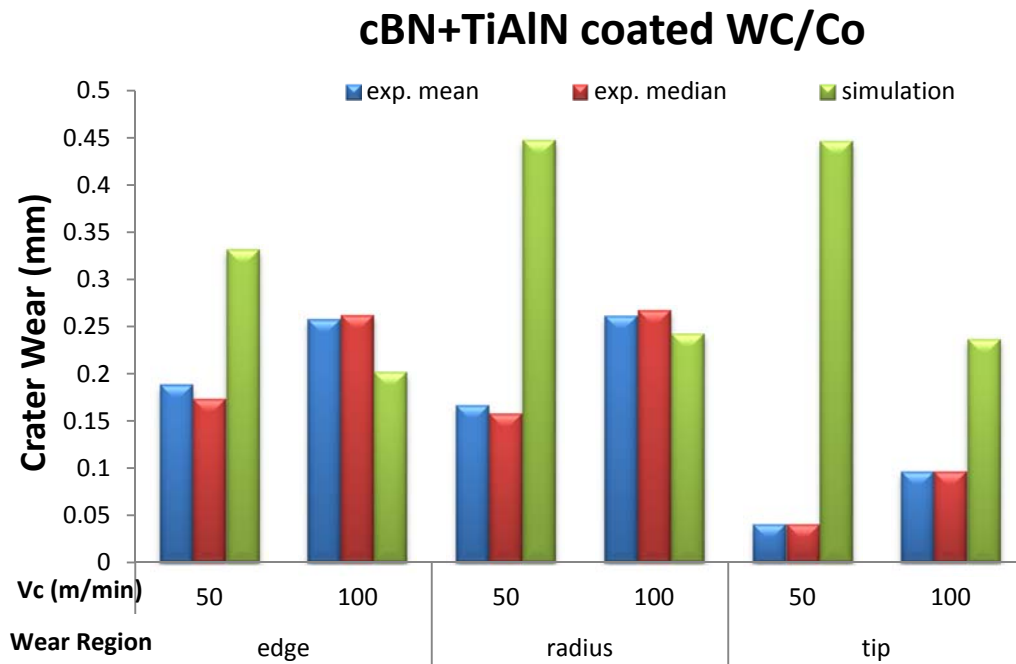


Figure 4.14. Experimentally measured wear amounts vs. FE simulation predictions for multi-layered coated WC/Co cutting tools

Table 4.5. Weibull wear rate distribution parameters for physics-based FE simulation results for different tools types at each wear region

Type of Tool	Regions	$\beta$	$\alpha_0$	$\alpha_1$	$\alpha_2$
Uncoated WC/Co	tip trailing (region 1)	7.282782	-7.492647	0.358043	0.389829
	nose radius (region 2)	9.027744	-6.977422	0.175363	0.219898
	cutting edge (region 3)	7.041446	-7.002633	0.053954	0.049101
TiAlN coated WC/Co	tip trailing (region 1)	7.176807	-6.65104	0.12404	0.170918
	nose radius (region 2)	8.97872	-6.184674	0.046896	0.279891
	cutting edge (region 3)	6.046889	-6.564595	0.012202	0.06488
cBN coated WC/Co	tip trailing (region 1)	5.018721	-5.939155	0.131899	0.615076
	nose radius (region 2)	8.990173	-6.193315	0.008629	0.249892
	cutting edge (region 3)	7.354669	-6.432749	0.056672	0.287246
cBN+TiAlN coated WC/Co	tip trailing (region 1)	4.787515	-6.053544	0.049429	0.338001
	nose radius (region 2)	7.61154	-6.503548	0.134914	0.340659
	cutting edge (region 3)	4.812168	-7.359058	0.203999	0.162941

In Table 4.5 the results for Weibull distribution parameters for wear rate amounts extracted from physics based FE simulations are presented with the associated general log-linear parameters.

In Figure 4.15 distribution fits and shape of the probability density function for some of these wear rate distributions are presented for illustrating finite element simulation based prediction results. The complete set of these distribution fit figures can be found in Appendix 2. As it can be seen in the Figure 4.15 and Appendix 2, since number of collected data in physics-based simulations was higher than measurements of experimental data, generally better fitness of data to the distributions can be observed. However, in cBN region 1 and 3, fitness of data does not show to be as well as other regions in other tool types.

Table 4.6 represents the associated reliability for each crater wear region of the cutting tool types using physics-based FE simulation data.

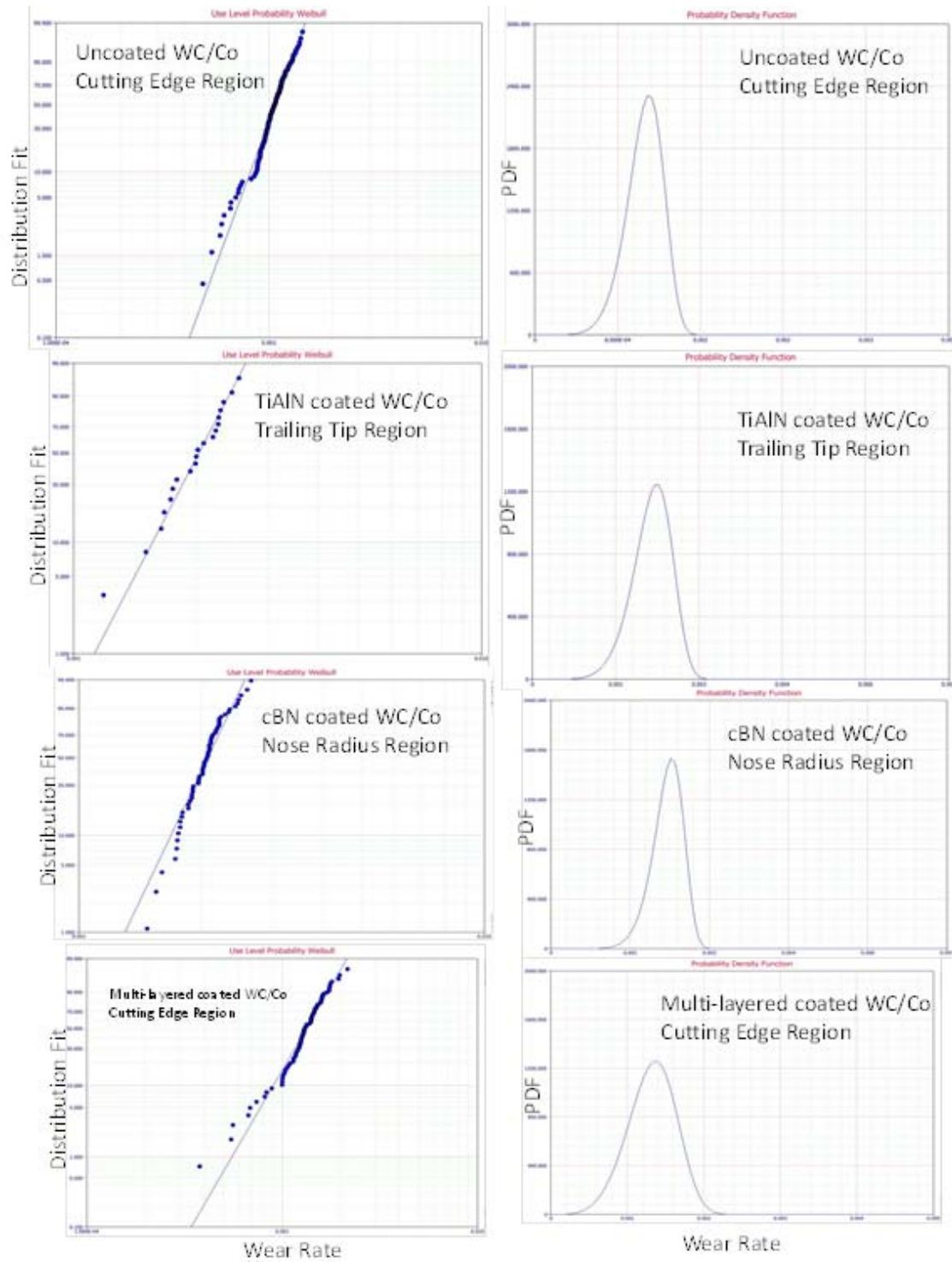


Figure 4.15. Probability distributions and distribution fits of physics-based wear rate values

Table 4.6. Physics-based reliability models of cutting tools at crater wear sub-regions

Type of Tool	Region	$R_{ij}(t)$	Reliability Model
Uncoated WC/Co	tip trailing (region 1)	$R_{11}(t)$	$1 - \exp \left\{ - \left( \frac{H_1}{te^{-7.492647+0.358043 \ln V_c + 0.389829 \ln f}} \right)^{7.282782} \right\}$
	nose radius (region 2)	$R_{12}(t)$	$1 - \exp \left\{ - \left( \frac{H_2}{te^{-6.977422+0.175363 \ln V_c + 0.219898 \ln f}} \right)^{9.027744} \right\}$
	cutting edge (region 3)	$R_{13}(t)$	$1 - \exp \left\{ - \left( \frac{H_3}{te^{-7.002633+0.053954 \ln V_c + 0.049101 \ln f}} \right)^{7.041446} \right\}$
TiAlN coated WC/Co	tip trailing (region 1)	$R_{21}(t)$	$1 - \exp \left\{ - \left( \frac{H_1}{te^{-6.65104+0.12404 \ln V_c + 0.170918 \ln f}} \right)^{7.176807} \right\}$
	nose radius (region 2)	$R_{22}(t)$	$1 - \exp \left\{ - \left( \frac{H_2}{te^{-6.184674+0.046896 \ln V_c + 0.279891 \ln f}} \right)^{8.97872} \right\}$
	cutting edge (region 3)	$R_{23}(t)$	$1 - \exp \left\{ - \left( \frac{H_3}{te^{-6.564595+0.012202 \ln V_c + 0.06488 \ln f}} \right)^{6.046889} \right\}$
cBN coated WC/Co	tip trailing (region 1)	$R_{31}(t)$	$1 - \exp \left\{ - \left( \frac{H_1}{te^{-5.939155+0.131899 \ln V_c + 0.615076 \ln f}} \right)^{5.018721} \right\}$
	nose radius (region 2)	$R_{32}(t)$	$1 - \exp \left\{ - \left( \frac{H_2}{te^{-6.193315+0.008629 \ln V_c + 0.249892 \ln f}} \right)^{8.990173} \right\}$
	cutting edge (region 3)	$R_{33}(t)$	$1 - \exp \left\{ - \left( \frac{H_3}{te^{-6.432749+0.056672 \ln V_c + 0.287246 \ln f}} \right)^{7.354669} \right\}$
cBN+TiAlN coated WC/Co	tip trailing (region 1)	$R_{41}(t)$	$1 - \exp \left\{ - \left( \frac{H_1}{te^{-6.053544+0.049429 \ln V_c + 0.338001 \ln f}} \right)^{4.787515} \right\}$
	nose radius (region 2)	$R_{42}(t)$	$1 - \exp \left\{ - \left( \frac{H_2}{te^{-6.503548+0.134914 \ln V_c + 0.340659 \ln f}} \right)^{7.61154} \right\}$
	cutting edge (region 3)	$R_{43}(t)$	$1 - \exp \left\{ - \left( \frac{H_3}{te^{-7.359058+0.203999 \ln V_c + 0.162941 \ln f}} \right)^{4.812168} \right\}$

For comparison purposes, as an illustration, reliability of tool tip trailing region of uncoated WC/Co tools are shown in figures 4.16 through 4.18 based on experimental test results.

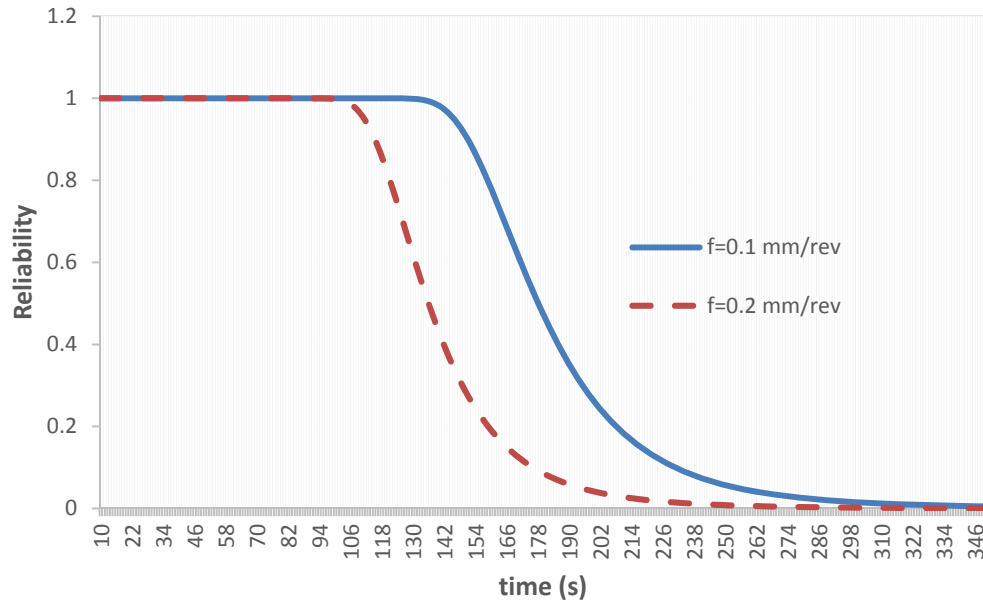


Figure 4.16. Physics-based reliability of uncoated WC/Co tool at tool tip trailing region for two levels of feed ( $f=0.1$  mm/rev and  $0.2$  mm/rev), cutting speed ( $V_c=100$  m/min), wear threshold ( $H_1=0.2$  mm).

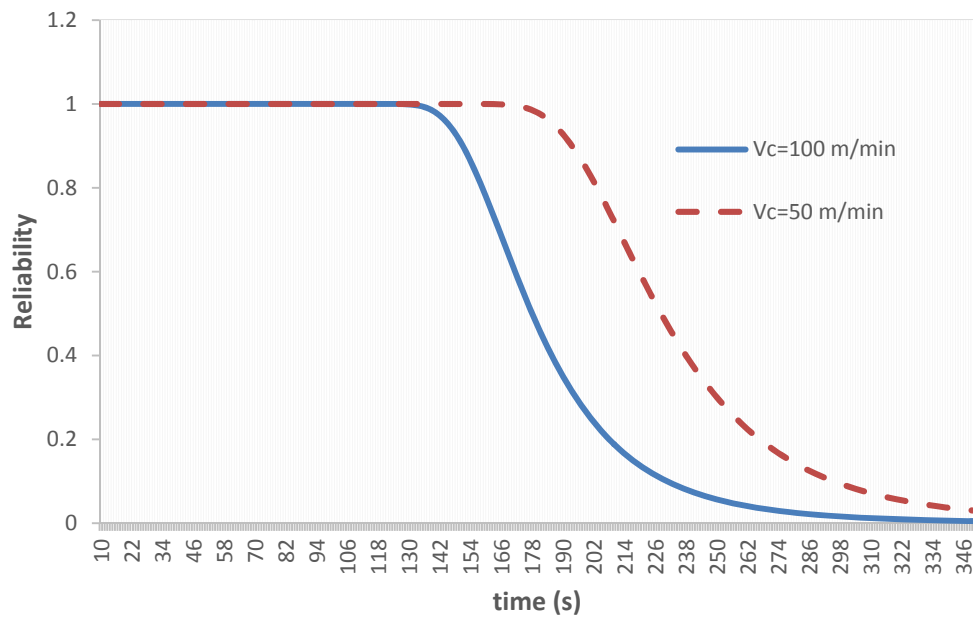


Figure 4.17. Physics-based reliability of uncoated WC/Co tool at tool tip trailing region for two levels of cutting speed ( $V_c=100$  m/min and  $50$  m/min), feed ( $f=0.1$  mm/rev), wear threshold ( $H_1=0.2$  mm).

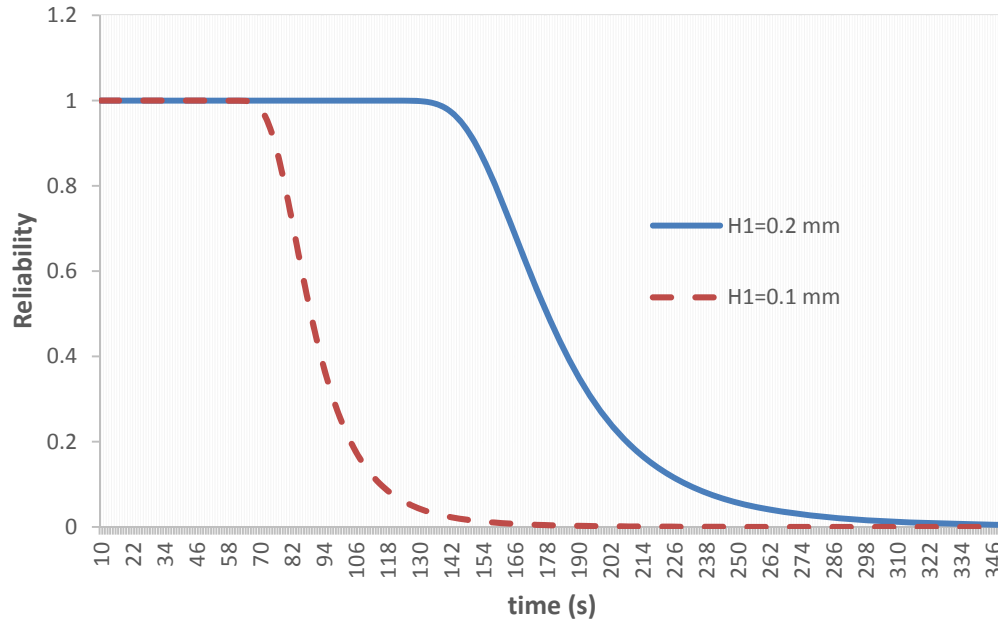


Figure 4.18. Physics-based reliability of uncoated WC/Co tool at tool tip trailing region for two levels of wear threshold ( $H_1 = 0.2\text{mm}$  and  $H_1 = 0.1\text{mm}$ ), cutting speed ( $V_c = 100\text{ m/min}$ ), feed ( $f = 0.1\text{ mm/rev}$ ).

#### 4.5. Usui's Wear Model Coefficient Determination

In order to calibrate the coefficients of Usui's wear model, two tool types are considered, uncoated WC/Co and TiAlN coated WC/Co. For simplicity, only main cutting edge (region 3) is considered. For this purpose, tool crater wear amount (zone 3) of the experimental tests under different cutting conditions for these two tool types are compared with two measurements from FE simulations of the similar cutting conditions and tool types; 1) *predicted worn geometry* 2) *anticipated wear amount* which is equal to the average of the wear rate extracted from the elements nodes multiplied by the actual cutting time of the associated experimental tests. Table 4.7 presents the measurements of the crater wear amounts taken at main cutting edge zone for two types of tool (Uncoated WC/Co and TiAlN coated WC/CO) using experimental tests as well as predicted worn geometries and anticipated wear amounts from FE simulations for the same types of tools at same cutting

conditions and duration of cut. These values are with respect to current coefficients of Usui's wear model which as presented in Equation 2.5,  $c_1 = 7.8 \times 10^{-9}$  and  $c_2 = 2.5 \times 10^3$  for all tool types.

Table 4.7. Experimental crater wear amounts vs. predicted worn geometry and anticipated wear amount for cutting edge region (Zone 3) using non-calibrated Usui's wear model coefficients

Tool Type	Replication	$V_c$ (m/min)	$f$ (mm/rev)	Cutting time (s)	Wear (mm)	Type of Measure
WC/CO	1	50	0.1	211	0.428	Experimental
WC/CO	2	50	0.1	163	0.35	Experimental
WC/CO	1	100	0.1	162	0.628	Experimental
WC/CO	2	100	0.1	175	0.72	Experimental
WC/CO	1	50	0.2	216	0.655	Experimental
WC/CO	1	100	0.2	65	0.932	Experimental
TiAlN	1	50	0.1	195	0.704	Experimental
TiAlN	1	100	0.1	154	0.843	Experimental
TiAlN	1	100	0.2	61	0.84	Experimental
WC/CO	2	50	0.1	163	0.213	Worn Geometry
WC/CO	1	50	0.1	211	0.245	Worn Geometry
WC/CO	1	100	0.1	162	0.215	Worn Geometry
WC/CO	2	100	0.1	175	0.22	Worn Geometry
WC/CO	1	50	0.2	216	0.405	Worn Geometry
WC/CO	1	100	0.2	65	0.31	Worn Geometry
TiAlN	1	50	0.1	195	0.265	Worn Geometry

TiAlN	1	100	0.1	154	0.23	Worn Geometry
TiAlN	1	100	0.2	61	0.306	Worn Geometry
WC/CO	1	50	0.1	211	0.22958206	Anticipated Wear
WC/CO	2	50	0.1	163	0.17735486	Anticipated Wear
WC/CO	1	100	0.1	162	0.17865654	Anticipated Wear
WC/CO	2	100	0.1	175	0.19299318	Anticipated Wear
WC/CO	1	50	0.2	216	0.270216	Anticipated Wear
WC/CO	1	100	0.2	65	0.08005833	Anticipated Wear
TiAlN	1	50	0.1	195	0.27801428	Anticipated Wear
TiAlN	1	100	0.1	154	0.16694883	Anticipated Wear
TiAlN	1	100	0.2	61	0.08129636	Anticipated Wear

These results can be illustrated in column type diagram for better comparison as shown in Figure 4.19.

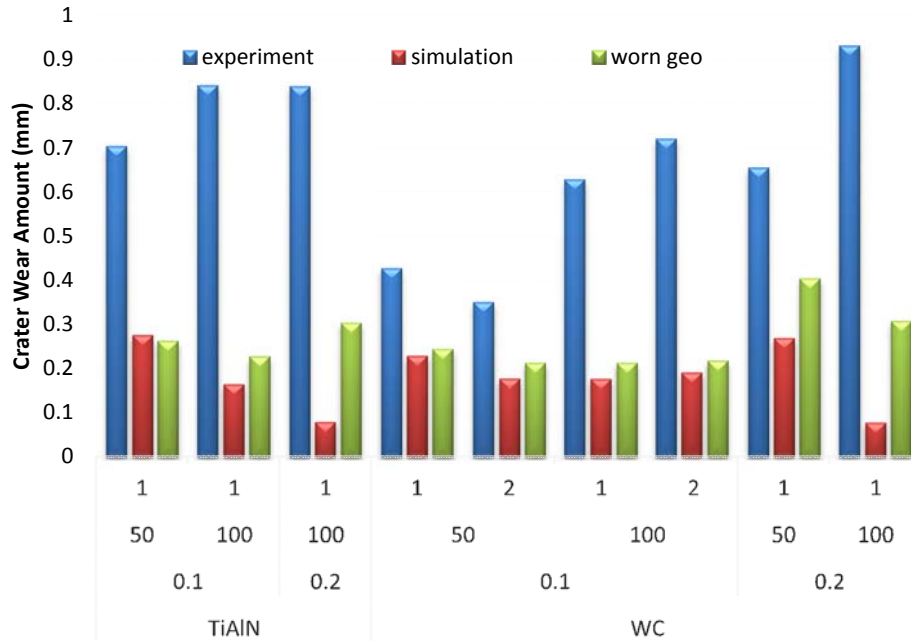


Figure 4.19. Column graph presentation of Table 4.7, cutting edge (region 3) crater wear values, experimental tests, FE worn geometries and FE anticipated wear values using non-calibrated Usui's wear coefficients for uncoated WC/Co and TiAlN coated WC/Co at different cutting conditions

In order to calibrate coefficients of Usui's wear model for these tool types for machining of Ti-6Al-4V using current data, an optimization problem was conducted to minimize the summation of distances between experimental values of wear amount and FE anticipated wear values at all cutting condition for each tool type separately. Therefore, the required physical attributes of Usui's wear model, that is wear rate, sliding velocity, normal stress and temperature, are extracted for each node from cutting edge zone for different cutting conditions as presented in Figure 4.20 in which wear rate data extraction is illustrated at the dotted nodes in cutting edge region, Figure 4.20 is an illustration for an uncoated WC/Co cutting tool under machining condition of  $V_c = 100$  m/min and  $f = 0.2$  mm/rev. Sliding velocity,  $V_s$ , Temperature,  $T$ , and normal stress  $\sigma_n$  associated with these nodes are extracted as well. In Figure 4.21, FE predicted worn geometry with non-calibrated Usui's wear model is shown for uncoated WC/Co tool  $V_c = 50$  m/min,  $f = 0.2$  mm/rev and cutting time of  $t = 216$ s.

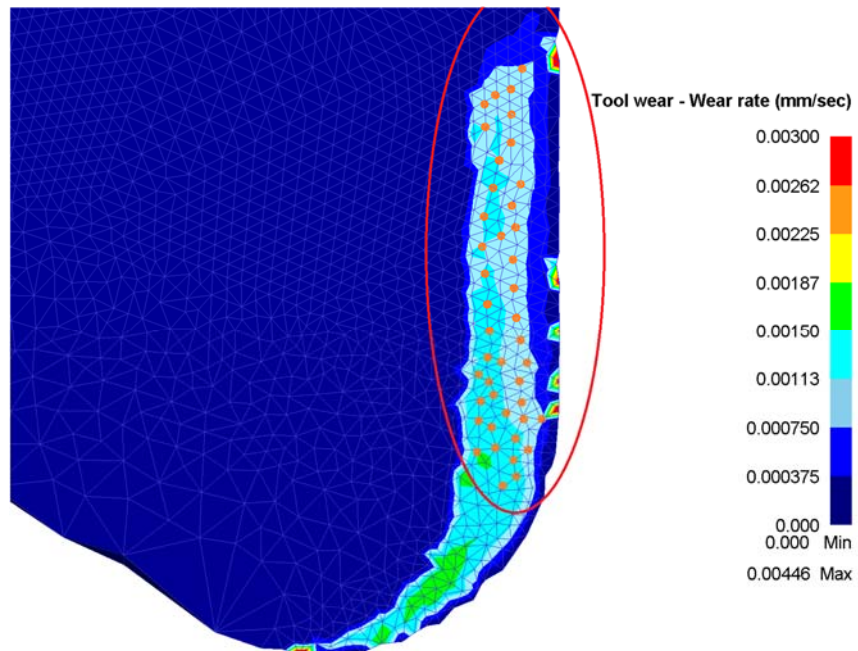


Figure 4.20. Crater wear rate extraction from cutting edge zone (Uncoated WC/Co,  $V_c = 100$  m/min and  $f = 0.2$  mm/rev)

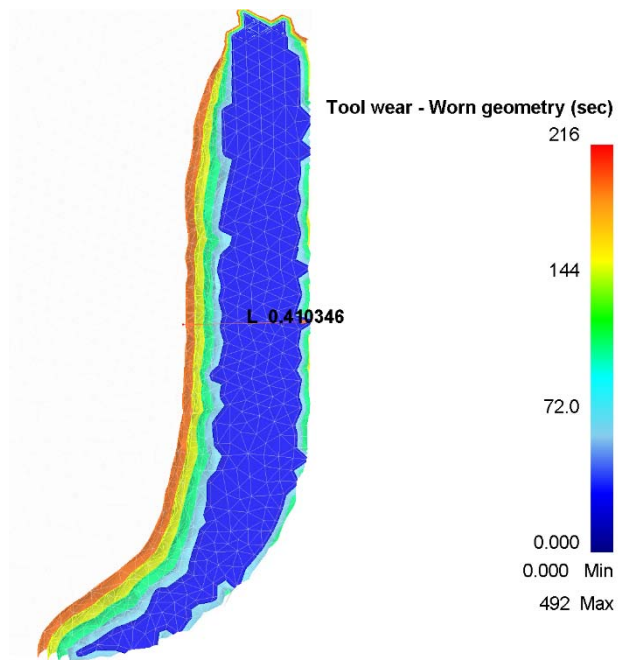


Figure 4.21. FE predicted worn geometry illustration with non-calibrated Usui's wear model coefficients for uncoated WC/Co,  $V_c = 50$  m/min,  $f = 0.2$  mm/rev and cutting time of  $t = 216$  s

The average values of  $V_s$ ,  $T$ , and  $\sigma_n$  are calculated for each cutting condition and been used in solving the optimization problem as follows in Equation 4.14.

$$\begin{aligned} & \text{Min} \sqrt{\sum_{i=1}^4 \sum_{j=1}^2 (K_{BEij} - K_{BSij})^2} \\ & \text{S.T.} \\ & K_{BEij} > K_{BSij} \\ & K_{BEij}, K_{BSij} > 0 \end{aligned} \tag{4.14}$$

where in Equation 4.14,  $K_{BEij}$  is the experimental value of crater wear measured at cutting edge zone at cutting condition  $i$  and replication  $j$ . Four types of cutting conditions are as follows:

$i = 1$ :  $V_c = 50$  m/min,  $f = 0.1$  mm/rev,  $i = 2$ :  $V_c = 100$  m/min,  $f = 0.1$  mm/rev,  $i = 3$ :  $V_c = 50$  m/min,  $f = 0.2$  mm/rev, and  $i = 4$ :  $V_c = 100$  m/min,  $f = 0.2$  mm/rev.

$K_{BSij}$  is the FE predicted crater wear amount at cutting edge zone, for cutting condition  $i$  and replication  $j$  and is calculated by Equation 4.15.

$$K_{BSij} = c_1 \bar{\sigma}_{n_i} \bar{v}_{s_i} \exp\left(\frac{-c_2}{\bar{T}_i}\right) t_{ij} \tag{4.15}$$

Where in Equation (4.15),  $c_1$  and  $c_2$  are Usui's wear model coefficients which basically are the decision variables of the optimization problem of Equation (4.14).  $\bar{\sigma}_{n_i}$ ,  $\bar{v}_{s_i}$  and,  $\bar{T}_i$  are nodes average normal stress, sliding velocity and temperatures of the values extracted from nodes on

cutting edge region for simulation of cutting condition  $i$ .  $t_{ij}$  is time of machining for experimental test of condition  $i$  and replication  $j$ .

After solving this optimization problem for two tool types uncoated WC/Co and TiAlN coated WC/Co separately, following coefficients for Usui's wear model are found out as optimized values.

$$\text{Uncoated WC/Co: } c_1 = 8 \times 10^{-8}, c_2 = 0.8604$$

$$\text{TiAlN coated WC/Co: } c_1 = 6.525 \times 10^{-4}, c_2 = 11496.598$$

Running same sets of simulations using new coefficients of Usui's wear model, resulted in the following set of data as presented in Figure 4.22 in the form of column graph comparing three values of experimental wear amount, predicted worn geometry and anticipated wear values for the same cutting conditions at tool cutting edge region.

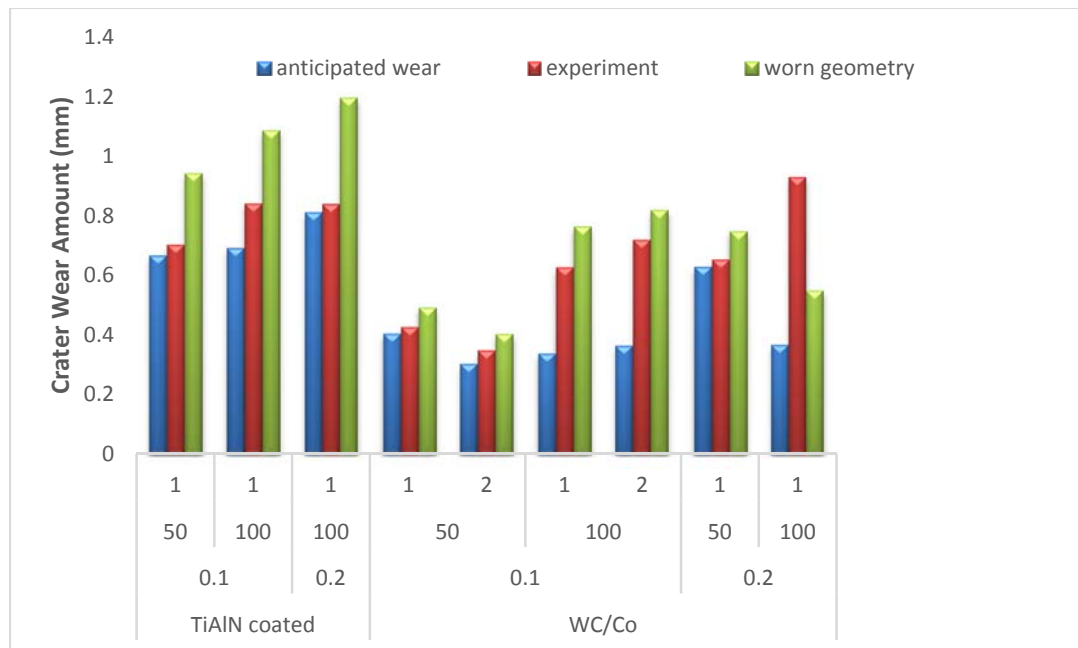


Figure 4.22. Column graph presentation of cutting edge (region 3) crater wear values, experimental tests, FE worn geometries and FE anticipated wear values using calibrated Usui's wear coefficients for uncoated WC/Co and TiAlN coated WC/Co at different cutting conditions

Predicted worn geometries with the calibrated wear coefficients are presented in Figure 4.23 and Figure 4.24 for different replications of cutting conditions and two types of tools. As it can be seen in Figure 4.22 comparing with Figure 4.19, the FE anticipated wear values are much closer to experimental values, as well as predicted worn geometries. It can be seen in Figure 4.22 that all FE anticipated wear values are smaller than experimental values because of the defined constraint in optimization Equation (4.14). The difference between experimental and FE anticipated wear values are non-significant in most of the cases except uncoated WC/Co,  $V_c = 100$  m/min for both levels of feed. FE predicted worn geometries in all cases are greater than FE anticipated worn geometries. FE predicted worn geometries are much closer to the experimental wear values comparing to non-calibrated graph in Figure (4.19), they are all slightly higher than experimental wear values except uncoated WC/Co,  $V_c = 100$  m/min and  $f = 0.2$  mm/rev.

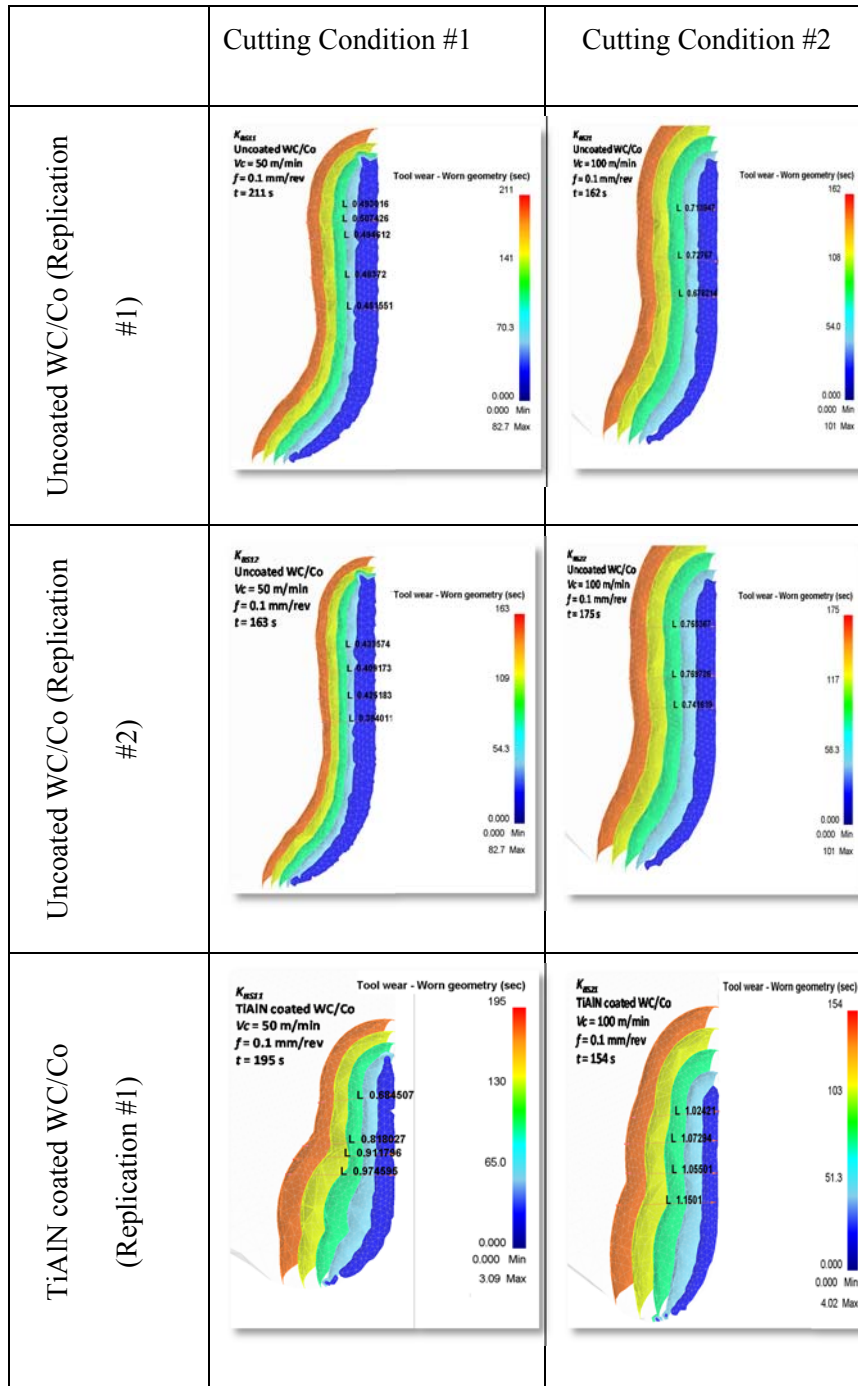


Figure 4.23. FE predicted crated worn geometries at cutting edge regions for two tool types, uncoated WC/Co and TiAlN coated WC/Co using calibrated Usui's wear model coefficients (Cutting condition 1&2)

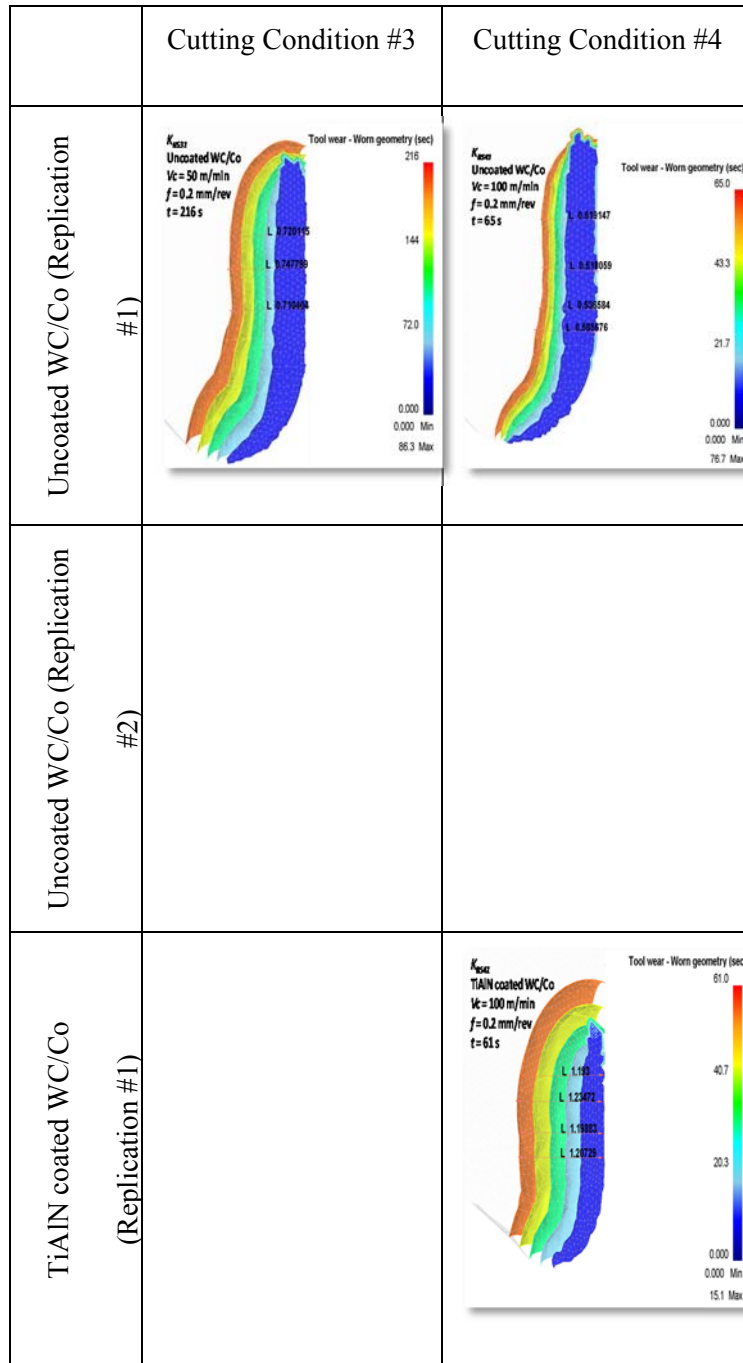


Figure 4.24. FE predicted cratered worn geometries at cutting edge regions for two tool types, uncoated WC/Co and TiAlN coated WC/Co using calibrated Usui's wear model coefficients (Cutting condition 3&4)

## 4.6. Results and Discussions

As it can be seen in figures 4.25 and 4.26, experimental-based reliabilities of the cutting tools are generally lower than physics-based reliabilities. This is due to the fact that in physics-based reliability analysis, the only reason of tool failure is gradual wear and also in this research we are not considering cutting tools failures due to cutting tool flank wear. But in reality, there are other failure mechanisms involved in tool failure such as chipping off, spalling, chemical reaction, etc. Therefore tool tends to wear out, and hence, fail earlier in reality which means lower reliability than physics-based reliability is predicted. As it can be seen in the figures, all the selected input parameters (tool type, cutting speed and feed) affect the reliability of cutting tools in that way, i.e., higher values of cutting speed and feed result in lower reliability respectively but reliability is more sensitive to feed than cutting speed.

Reliability models are very sensitive and dependent on threshold values  $H_j$ . For simplicity and for the purpose of illustration, physics-based reliability of cutting tools under  $V_c = 100$  m/min,  $H_1 = 0.1$  mm,  $H_2 = 0.15$  mm and  $H_3 = 0.2$  mm under two levels of feed  $f = 0.1$  &  $0.2$  mm/rev is represented in Figure 4.25.

On the other hand, cBN coated WC/Co and uncoated WC/Co carbide tools predict the highest levels of reliability at  $f = 0.1$  mm/rev and TiAlN coated WC/Co tools show lowest level of reliability at  $f = 0.1$  mm/rev. Reliabilities are lower in higher level of feed at fixed other conditions, at  $f = 0.2$  mm/rev, highest level of reliability is predicted for uncoated WC/Co tool and the lowest one for TiAlN coated WC/CO tools again.

Reliability of same conditions is modeled using the experimental-based data. Since experimental tests are run only in one level of feed for cBN and multi-layered coated WC/Co tools, it is not possible to find  $\alpha_2$  values for these types of cutting tools. Hence for the purpose of consistency, we used  $\alpha_2$  values from physics-based results of the same types of cutting tools

which resulted in enhancement of reliability values associated with cBN and multi-layered coated WC/Co tools as presented in Figure 4.26.

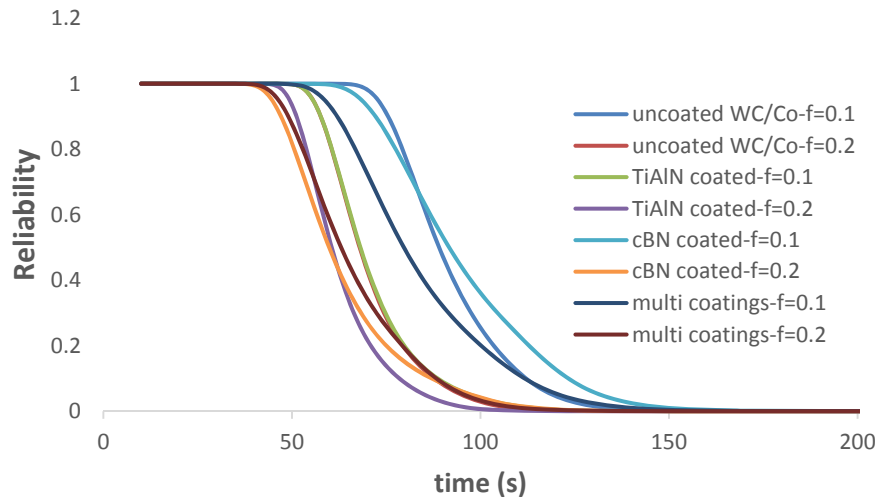


Figure 4.25. Physics-based reliability of cutting tools at  $V_c = 100$  m/min and two levels of feed  $f = 0.1$  and  $0.2$  mm/rev in machining of Ti6Al4V titanium alloy

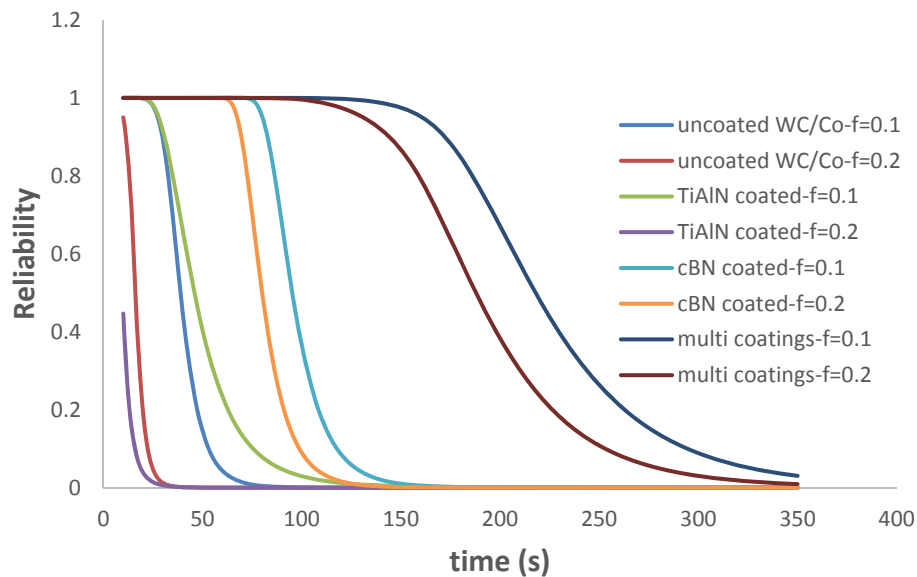


Figure 4.26. Experimental-based reliability of cutting tools at  $V_c = 100$  m/min and two levels of feed  $f = 0.1$  and  $0.2$  mm/rev

As it can be seen in Figure 4.26 experimental-based reliability of multi-layered coated WC/Co cutting tools are predicting higher values than other types of tools, i.e., higher than cBN coated WC/Co. Uncoated WC/Co tools consistently show higher values of reliability and TiAlN coated tools again show the lowest values of reliability, which is the same as the results of physics-based models.

As it is presented in Figures 4.6 through 4.8 and Figures 4.16 through 4.18 and Figures 4.25 and 4.26, reliability of cutting tools whether experimental-based or physics-based are very dependent on machining input parameters, type of tool and also deterministic value of crater wear thresholds. Therefore it is particularly useful and informative to perform an optimization study to help select optimum values for these input parameters for longer tool life, smaller probability of failure for a given period of time and higher MRR.

## **4.7. Conclusion**

In this chapter, reliability of coated and uncoated tungsten carbide WC/Co tools are modeled based on experimental tool wear measurements and physics-based finite element simulation results for crater wear failure criteria. A new concept of dividing the worn cutting tool regions into three sub-regions (tip trailing, nose radius and cutting edge regions) are defined and then, overall reliability of cutting tool is evaluated by considering independent competing risk reliability of these sub-regions.

Physics-based reliabilities, in general, predict higher reliabilities than experimental-based reliabilities because they do not consider the stochastic nature of cutting tool failure in machining process. Cutting tool experiences different types of failure mechanisms in reality while in physics-based simulations only gradual wear with deterministic wear constant values is taken into consideration. However the experimental tests performed in this research were not originally intended for reliability modeling and tool wear estimation purposes. Otherwise the

tool wear tests for machining Ti-6Al-4V should have been designed and conducted in more consistent way at equal cutting times in each case.

Reliabilities are sensitive to machining input process parameters (i.e., cutting speed and feed), type of cutting tool and coating and also very sensitive to value of failure threshold associated with each worn sub-region  $H_j$ , in a way that higher values of  $H_j$  result in reliabilities close to 1 for a majority of conditions and smaller values tend to result in 0 values for reliability very fast. Therefore, the necessity of multi-objective optimization with an objective other than maximization of reliability becomes clear.

# **5. MULTI-OBJECTIVE OPTIMIZATION**

## 5.1. Introduction

This chapter is focused on multi-objective optimization of machining input parameters which are the selection of type of cutting tool, cutting speed and feed. After conducting experimental tests on different types of cutting tools under different cutting conditions, and analyzing the crater worn regions on the cutting tools and derivation of experimental-based reliability models, finite element simulations of machining processes using the same types of cutting tools and process parameters are designed and run for every machining condition. Wear prediction using finite element simulations are then validated with experimental results. After validation, physics-based reliability of cutting tools using finite element simulation results are modeled. The main objective of this chapter is to optimize these results in terms of multiple objective functions. Since FE simulations, as described in previous chapters, are validated with experimental findings, the main focus of this chapter is to generate optimization results based on finite element simulation predictions.

In different applications, objective functions may vary based on the nature of the process. In all machining processes, Material Removal Rate (MRR) is a good measure for efficiency of the process and increasing this rate is desirable (Karpap & Özel, 2007 and Ulutan & Özel, 2013). On the other hand, cutting tools tend to wear out fast during machining and need to be replaced, especially in machining of difficult-to-machine alloys such as titanium and nickel alloys, which is very costly and time consuming and reduces the rate. Therefore it is important to design new advanced cutting tools with higher reliability and longer tool life.

Based on the requirements of the process, many other objective functions can be defined for a machining process, such as minimization of cutting force, minimization of surface roughness, minimization of residual stresses, and minimization of process uncertainties, etc. All of these objective functions are important in different aspects of the machining process (Thepsonthi &

Özel, 2012 and Ciurana et al., 2009). To this purpose, this chapter focuses on multi-objective optimization rather than a single objective optimization. In order to handle this multi-objective optimization, the fast Non-dominated Sorting Genetic Algorithm (NSGA-II) was employed in order to optimize process parameters. NSGA-II demonstrates the ability to identify a set of optimal solutions (Pareto front), which provides the decision maker with a complete picture of the optimal solution space. After finding the Pareto front, a procedure is used to select the best solution from the Pareto front. Objectives are solved for maximizing the predicted reliability of cutting tools and maximizing the material removal rate (MRR). Decision variables in this research are selection of one type of tool out of four different types of uncoated and coated (TiAlN, cBN, and multi-layered) tools, feed and cutting speed. The optimum values in terms of objective functions and decision values are further presented in objective function space and decision variable space.

## 5.2. Multi-Objective Optimization Problem Formulation

Two objectives of this research are: a) Maximization of Reliability of Cutting Tools, and b) Maximization of Material Removal Rate. Decision variables are tool type, feed, and cutting speed.

The selection of tool type should be considered in the problem formulation, which makes an integer programming added to the problem formulation. Then the formulation of the problem becomes as follows:

$$\begin{aligned}
 &Max \sum_{i=1}^{m=4} x_i R_i(V_c, f), Max MRR(V_c, f) \\
 &st \sum_{i=1}^{m=4} x_i = 1
 \end{aligned}
 \tag{5.1}$$

$$25 \text{ m/min} < V_c < 250 \text{ m/min}$$

$$0.05 \text{ mm/rev} < f < 0.5 \text{ mm/rev}$$

$$x_i \in \{0,1\}$$

where  $R_i$  is reliability of tool type  $i$  which is been calculated by Equation 4.10.  $x_i$  represents which tool type is being selected as the optimized tool in terms of reliability and material removal rate.  $x_i = 1$  is for tool type uncoated WC/Co,  $x_i = 2$  is for TiAlN coated WC/Co,  $x_i = 3$  is for cBN coated WC/Co, and  $x_i = 4$  is for multi-layered (cBN+TiAlN) coated WC/CO.  $V_c$  and  $f$  are cutting speed and feed respectively.  $MRR$  is material removal rate which is calculated by Equation 5.2 in turning operations as follows:

$$MRR = a_p f V_c \quad (5.2)$$

where  $a_p$  is depth of cut in turning operation which in this research  $a_p = 2$  mm.

We initially analyzed the reliability of cutting tools as well as reliability of each one of the cutting tool worn regions. Therefore the purpose was finding optimum values of decision variables (cutting speed, feed and selection of cutting tool type). Figures 5.1 and 5.2 presents the reliability change in uncoated WC/Co tool at tip trailing region as wear threshold  $H_1$  and cutting time  $t$  changes respectively. In practice,  $H_1$  is fixed based on failure mechanisms and the tool type intended usage. However, Figure 5.1 shows how results change for different thresholds.

Please notice the shift in the shape of the reliability surface in 3D as the wear threshold at tool tip trailing Region 1 is increased. This indicates that reliability of the cutting tool remains high at the wider ranges of cutting speeds and feeds employed in machining. When  $H_1 = 0.1$ mm crater wear threshold is selected, the reliability rating is only high at the lowest cutting speed and feed conditions and immediately decays when cutting speed or feed is increased.

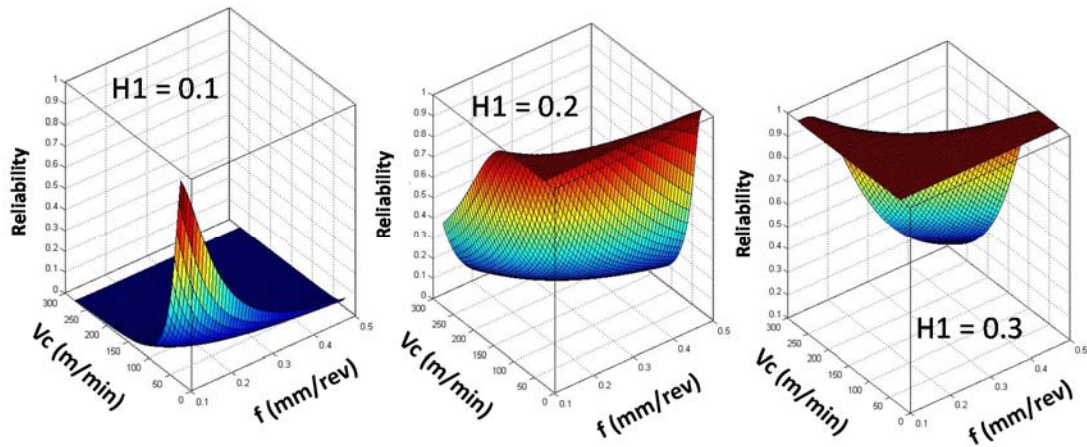


Figure 5.1. Dependency of physics-based reliability of tip trailing region of uncoated WC/Co on failure threshold  $H_1$  at  $t = 100$  s

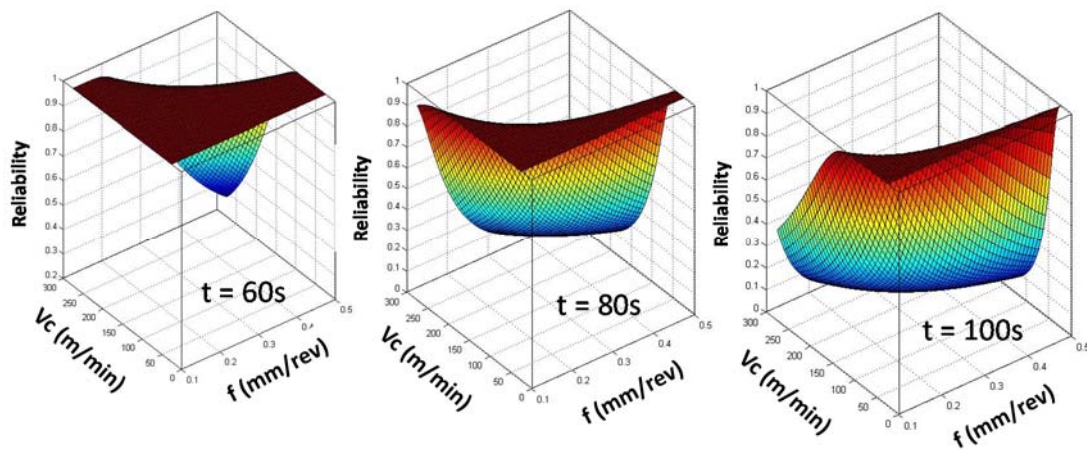


Figure 5.2. Dependency of physics-based reliability of tip trailing region of uncoated WC/Co on cutting time at failure threshold  $H_1 = 100$  mm

Figure 5.3 presents in three dimensional plot how the reliability of the uncoated cutting tools is very sensitive to selection of crater wear thresholds,  $H_j$  at constant cutting time  $t = 50$  s. As it can be seen in this figure by selecting relatively higher values of crater wear threshold (Figure 5.3 in right), in a wide range of cutting speed and feed selection, the reliability of cutting tool

remains high. The 3D graph shows intermediate values of crater threshold values and the ranges of cutting speed and feed in which cutting speed maintains high reliability and then decreases. While in the 3D plot on the left side of the Figure 5.3, reliability of same cutting tool (uncoated WC/CO) at the same cutting time  $t = 50$ s but with lower values of crater wear threshold is illustrated. Reliability values drops very fast as cutting speed or feed values increase from lower values to higher values. Figure 5.4 illustrates the trend of reliability decrease as time increases at fixed threshold values of  $H_1 = 0.05$  mm,  $H_2 = 0.15$  mm and  $H_3 = 0.2$  mm. In practice, failure threshold is fixed.

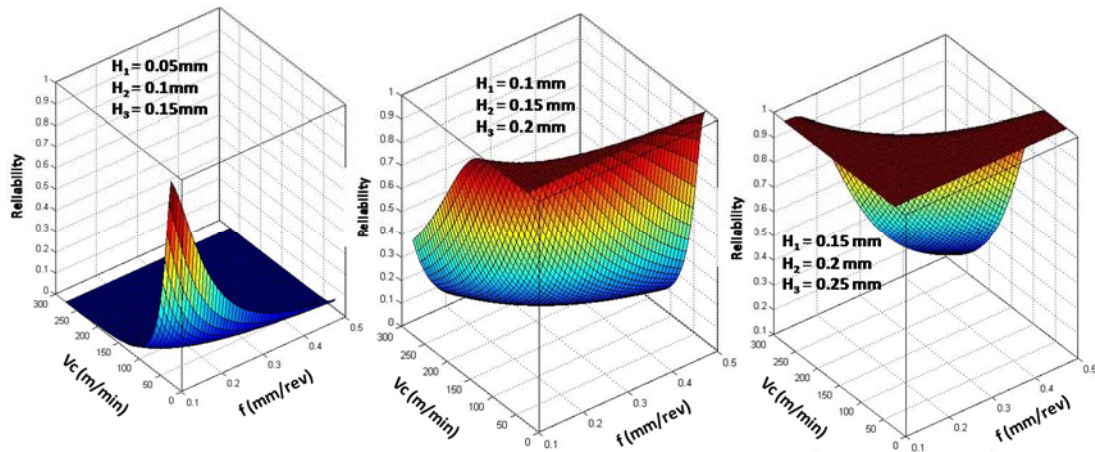


Figure 5.3. Illustration of dependency of physics-based reliability of cutting tool to values of thresholds  $H_j$  (Uncoated WC/Co, cutting time  $t = 50$  s)

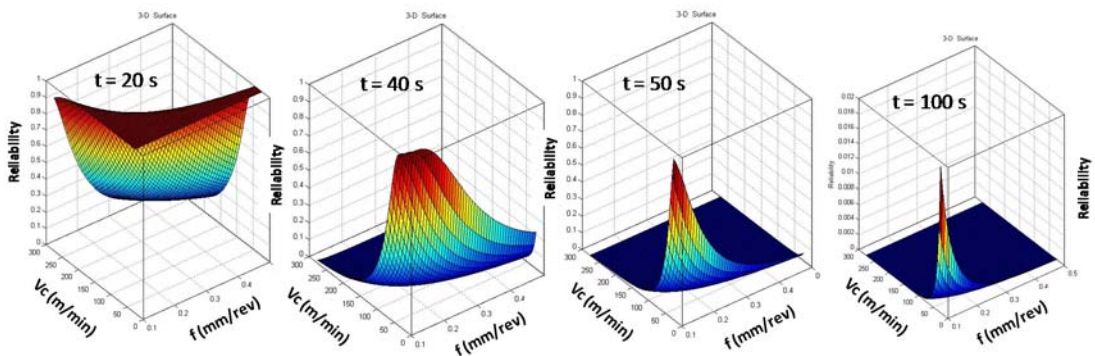


Figure 5.4. Illustration of dependency of physics-based reliability of cutting tool to cutting time (Uncoated WC/Co,  $H_1 = 0.05$  mm,  $H_2 = 0.15$  mm and  $H_3 = 0.2$  mm)

The fact of dependency of reliability on the values of the crater wear threshold and with respect to the Figure 5.3, second and third figure, it is shown that in many solution spaces the reliability values are equivalent. Therefore there should be other criteria available for selection of best combination of input parameters apart from maximization of reliability. Hence, the necessity of formulating a multi-objective optimization problem becomes clearer. In machining and manufacturing processes, maximization of rate of production is always desirable in order to reduce production time and consequently costs. A good metric for measurement of machining efficiency is material removal rate (MRR) which is defined in Equation 5.2.

### **5.3. Fast Non-dominated Sorting Genetic Algorithm (NSGA-II)**

In multi-objective problems, the main purpose is to reach to a representative and favorable Pareto frontier of solutions. Jones et al. (Jones et al. 2002) reported that more than 90% of the proposed methodologies to solve multi-objective problems are aimed to find a good approximation of the Pareto frontier.

During the last decade, many techniques are proposed for solution of multi-objective problems which were based on Genetic Algorithm (GA). Some of the most efficient ones are: Vector Evaluated Genetic Algorithm (VEGA), Weight Based Genetic Algorithm (WBGA), Random Weight Genetic Algorithm (RWGA), Strength Pareto Evolutionary Algorithm (SPEA), Rank-Density based Genetic Algorithm (RDGA), Non-dominated Sorting Genetic Algorithm (NSGA) and, fast Non-dominated Sorting Genetic Algorithm (NSGA-II) (Coit & Smith, 1996, Konak et al., 2006, and Branke et al. 2008).

Generally, multi-objective genetic algorithms differ based on their fitness assignment procedure, elitism, or diversification approaches. NSGA-II is one of the GA-based algorithms which were developed by Deb et al. (2002). According to literature in multi-objective

optimization of systems reliability, NSGA-II is one of the most powerful Evolutionary Algorithms (EA) for solving these types of problems. Therefore, in this dissertation NSGA II is employed to solve nonlinear programming problems.

NSGA-II uses a fast non-dominated sorting procedure with the time complexity of  $O(MN^2)$  to assign the ranks of individuals in the population with size  $N$ , where the problem has  $M$  objective functions. The ranking method emphasizes the good solutions and tries to create a population of such points throughout the procedure. NSGA-II maintains its diversity by an index which is called the crowding distance. The crowding distance is defined for the solutions with the same rank. A lower crowding distance, demonstrates that the area of the solution is more crowded; and vice versa. So, among two solutions with the same rank, the one with a higher crowding distance is preferable. Using the crowding distance index, prevents focusing on certain regions of the solution space, and explores different regions in the Pareto front. Hence, NSGA-II is highly efficient in obtaining good Pareto optimal fronts (Tillman 1980, Levitin 2006 and Reeves 1995). The pseudo-code of NSGA-II is presented below. Figure 5.5 shows the flowchart for NSGA-II algorithm.

1. Set the fitness function, the crossover and mutation procedure, the population size ( $N$ ), the generation index ( $g=0$ ) and maximum number of generation ( $Max\ Gen$ ).
2. Initialize first population ( $P_0$ ) randomly and set  $evolution=0$ .
3. evaluate population,  $evolution++$
4. while  $evolution < Max\ Gen$ , do
  - { $evolution++$
  - 4.1. Offspring ( $Og$ )= mutation (crossover (selection (population))).
  - 4.2. Evaluate offspring and combine them with their parents,  $Cg=Pg \cup Og$ .
  - 4.3. Sort all combined population ( $Cg$ ) to obtain all non-dominated fronts ( $F$ ).
  - 4.4. Set  $Pg+1=\phi$  and  $i=1$
  - 4.5. While the parent population size  $|Pg+1|+|Fi|<N$  do
    - 4.5.1. calculate crowding-distance of front  $i$  ( $Fi$ )
    - 4.5.2. add the  $i$ th non-dominated front  $Fi$  to the parent pop  $Pg+1$
    - 4.5.3.  $i=i+1$
  - End while
  - 4.6. Sort the  $Fi$  according to the crowding distance.
  - 4.7. Fill the parent pop  $Pg+1$  with the first  $N-|Pg+1|$  elements of  $Fi$ .
  - 4.8. Set  $g=g+1$ .
- End while
5. The population in vector  $P$  are the non-dominated solutions.

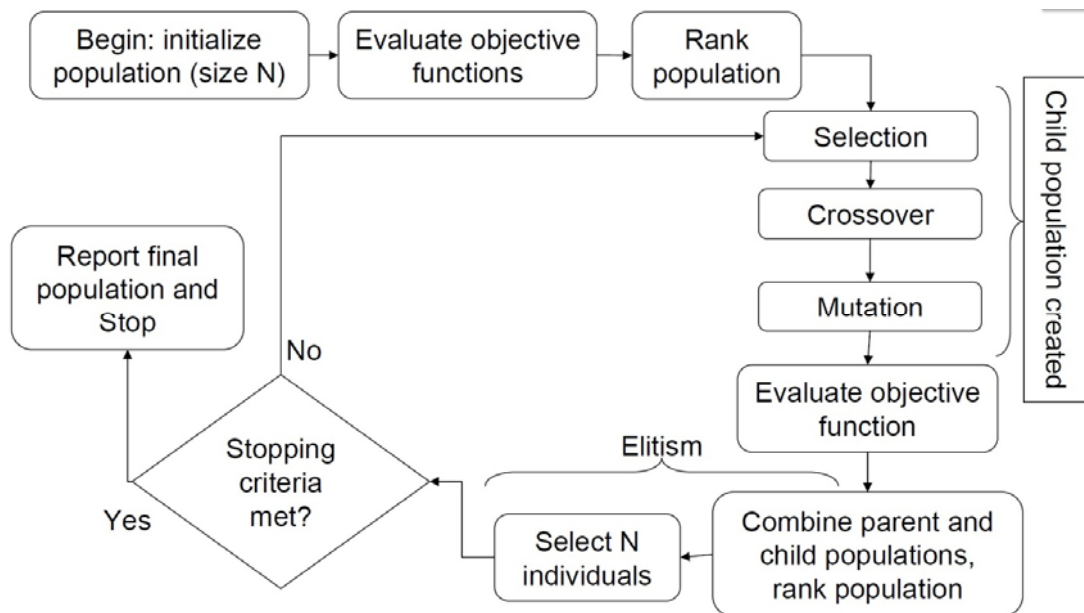


Figure 5.5. NSGA-II algorithm flowchart (Ardakan et al., 2014)

### 5.3.1. Chromosome definition

In the NSGA-II algorithm employed in this research, chromosomes are in form of 1x3 matrixes. The first column of the matrix is assigned to cutting speed,  $V_c$ , second column is assigned for feed,  $f$ , and third column to type of cutting tool which can have integer numbers 1 to 4 because of four types of tool. Figure 5.6 shows a sample of the chromosomes:

$V_c$	$f$	$X$
30	0.2	3

Figure 5.6. Sample shape of NSGA-II chromosome used in this research

### 5.3.2. Fitness function

One of the main issues in evolutionary computation is how to guide the search towards the feasible region in the presence of constraints. The existing approaches can be classified in the following groups: a) penalty techniques, b) repair techniques, c) separation techniques and, d) hybrid techniques. In this research, penalization technique is utilized. One fitness function should be defined corresponding with each objective function of the problem. For this research, the first fitness function which is associated with the first objective function (maximizing reliability of cutting tool), is amount of reliability subtracted by penalty of violating the constraints. Similarly, the second fitness function associated with the second objective function (MRR) is defined as subtracting the penalty of violating the constraints from MRR. In other words, the constraints are combined with the objectives of the problem in a way that the added penalty to the solution causes that solution to be excluded from solution space. As stated earlier, the penalization results in two important features of the algorithm; first, not finding infeasible solutions in final iterations of the algorithm, and second, searching within the infeasible space during initial iterations which itself results in diversity in solutions.

### 5.3.3. Initial population

In order to generate the initial population,  $PoP$  numbers of chromosomes are generated randomly considering the constraints of the problem. For solving this multi-objective optimization problem, the initial considered population is above hundred chromosomes. As indicated in previous researchers' work (Li & Haines, 1992 and Tillman, 1980), in case of large solution spaces, the selected number of initial solutions should be greater or equal to 100. Population size in this research is equal to 100.

### 5.3.4. Selection

In order to select chromosomes for crossover and mutation operators, one of the selection methods should be utilized. In this research, tournament method is being applied which is explained in Step 3 in the pseudo-code.

### 5.3.5. Crossover breeding operator

Crossover operators are defined with a pre-determined rate  $r_c$ , in this research after trial-and-error,  $r_c = 0.2$  is selected. Each crossover operator produces selects two parents solution and produces two new solutions (children or offspring) from them. Therefore, by using two or three types of crossover operators, 4 or 6 offspring chromosomes can be produced from a pair of parent chromosomes. Then, among two parents chromosomes combining with 4 or 6 children chromosomes, the two best ones in terms of objective functions are selected to transfer to the next generation. Therefore after completion of crossover operation, again  $PoP$  numbers of new chromosomes are in the next generation.

Three crossover operators are being applied for this research, double point crossover, single point crossover operator, and a new defined crossover operator. These three types of crossovers are explained in detailed here:

a) Double point crossover operator: One of the most widely used crossover operators in GA is double point crossover operator. In this operator, two chromosomes are selected randomly, and then two random points are picked at these chromosomes and genes that fall between two points (or in some cases outside of two points) are exchanged together. For a better illustration of double point crossover Figure 5.7 represents it between two 3x14 chromosome types and then a sample of double point crossover in the chromosomes of this research is presented in Figure 5.8.

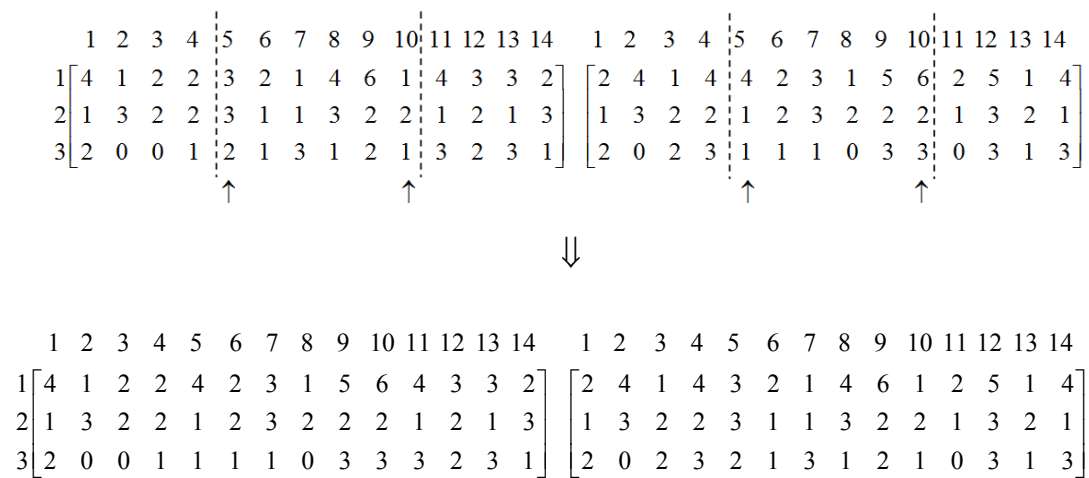


Figure 5.7. Double point crossover on a 3x14 matrix

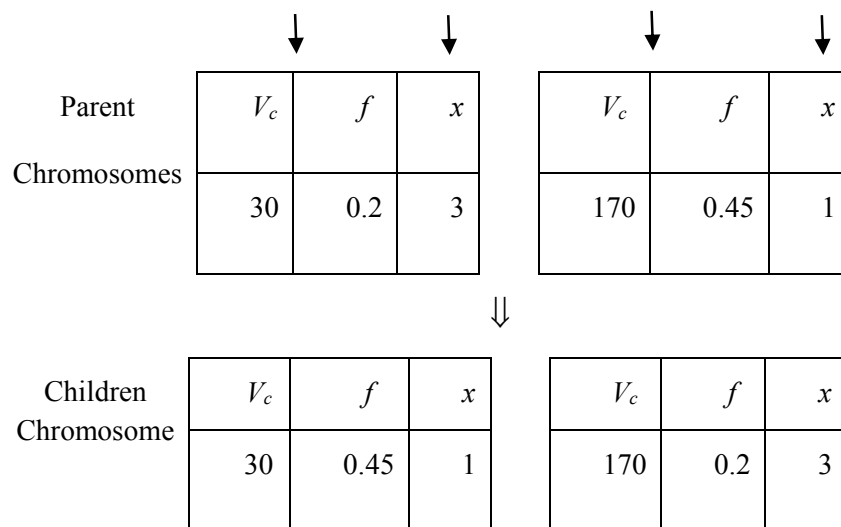


Figure 5.8. Sample representation of a crossover operation on two parent chromosomes and achieved children chromosomes

b) Single point crossover operator: The functionality of single point crossover is exactly like double point but they only differ in number of selected points. In single point crossover only one random point of two random parent chromosomes are selected and then according to the algorithm, the genes on the right side or left side of the selected point are exchanged between parent chromosomes. In Figure 5.9 single operator crossover is presented with change in the left hand side genes.

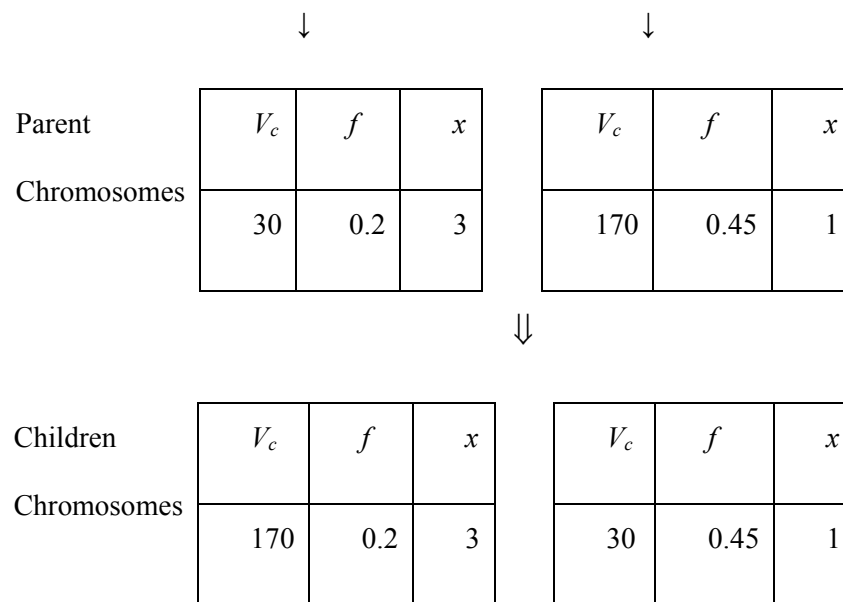


Figure 5.9. Sample single point crossover operation with a left-handed genes exchange

c) New crossover operator: New developed crossover operator is employed in this research, to describe this operator assume a current generation chromosome defined as  $x^p$ , and  $x_i^p$  represents the  $i^{\text{th}}$  gene of  $x^p$ . Assume  $x^{Best}$  as the best solution (chromosome) of the current generation among other solutions and  $x_i^{Best}$  represents the  $i^{\text{th}}$  gene of this solution. The new chromosome is defined as follows using the new crossover operator:

$$x_i^{new} = x_i^P + rand.(x_i^{Best} - x_i^P); \quad \forall i \quad (5.3)$$

In Equation 5.3, *rand* is a uniformly distributed random number between zero and one. This operator generates a new chromosome in which at the random point (gene), a random value between the current chromosome and the best chromosome is replaced. In addition, it is possible to use the best solution among all generations instead of the best solution of current generation.

### 5.3.6. Mutation operator

The mutation operator performs random perturbations to the selected solutions. Each value within the solution matrix is altered at random with a predefined mutation rate of  $r_M$  which in this research  $r_M = 0.2$  is selected. The main reason for using this operator is to increase diversity in the solutions and get rid of local optimal solutions. In order to perform mutation operation,  $r_M$  percent of parents are selected randomly and their genes are exchanged with the rate of  $p_m$  which in this research  $p_m = 0.1$ . Then, after fitness functions are calculated for mutated chromosomes and in case of higher fitness function values than original chromosome, the original chromosome is replaced by mutated chromosome. Otherwise, the parent chromosome is selected. In this research another type of mutation operator is applied, called Mask Operator. This is how mask mutation operator works:

a) Mask Operator: In this operator a mask matrix of the parent chromosome is made out of random numbers between zero and one. Then those entities in the mask matrix which have a value of less than  $r_M$ , their corresponding genes in the chromosome are randomly altered. Mask Operator is shown in Figure 5.10.

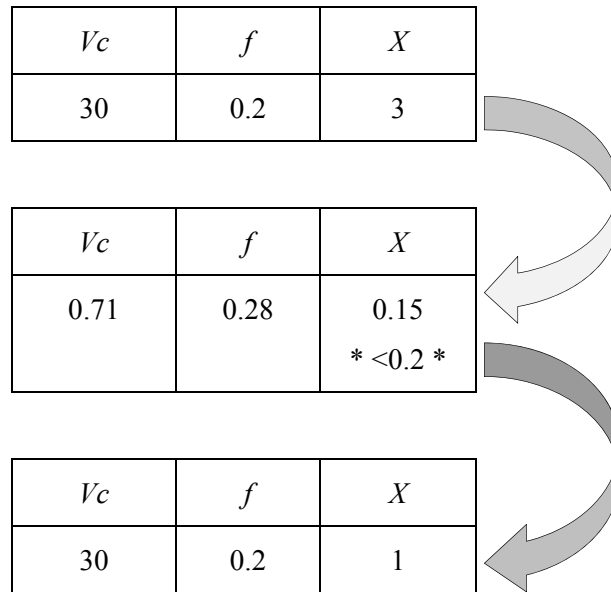


Figure 5.10. Example of Mask Operator

### 5.3.7. Stopping condition

NSGA-II terminates either after a preselected number of generations. 500 is selected as the termination number or not change in the best solution set after 10 consecutive iterations, whichever happens earlier. The number of 500 is decided after initial tests of the algorithm.

## 5.4. Optimization Results

In single objective optimization, at mission cutting time of  $t = 60$  s, and crater wear threshold values of  $H_1 = 0.05$  mm,  $H_2 = 0.1$  mm and  $H_3 = 0.15$  mm, the search space is  $f = [0.025 \text{ mm/rev} - 0.5 \text{ mm/rev}]$ ,  $V_c = [25 \text{ mm/rev} - 250 \text{ mm/rev}]$  and types of tool [ $x_i = 1$  means uncoated WC/Co,  $x_i = 2$  means TiAlN coated WC/Co,  $x_i = 3$  means cBN coated WC/Co,  $x_i = 4$  means multi-layered coated WC/Co]. The problem was first solved to maximize reliability at time

$t = 0$ . The best achievable reliabilities and optimum values of decision variables are as follows:

Highest Reliability:  $R = 0.946$

Type of tool: 1 = Uncoated WC/Co

Cutting speed:  $V_c = 26$  m/min

Feed:  $f = 0.1005$  mm/rev

After solving the multiple-objective function problem with the same assumptions and conditions, the best solution Pareto frontier is presented at Figure 5.11.

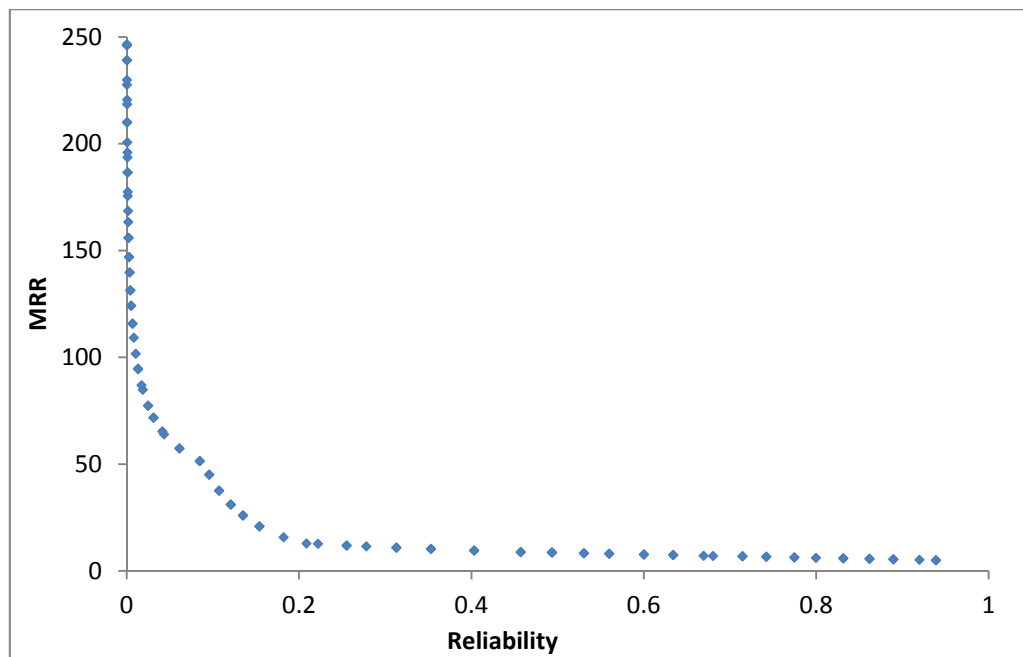


Figure 5.11. Illustration of dependency of physics-based reliability of cutting tool to cutting time (Uncoated WC/Co,  $H_1 = 0.05$  mm,  $H_2 = 0.15$  mm and  $H_3 = 0.2$  mm)

As it is shown in Figure 5.10, these two objectives have conflicts of interest, increasing one result in decreasing the other and vice versa. Figure 5.12 presents the trend of solutions in different generations before reaching to the best solution Pareto frontier. The solution with highest value of reliability is as follows:

Highest Reliability:  $R = 0.9388$

Type of tool: 1 = Uncoated WC/Co

Cutting speed:  $V_c = 25$  m/min

Feed:  $f = 0.1017$  mm/rev

Material Removal Rate:  $MRR = 5.08$  mm<sup>3</sup>/min

While the solution with highest value of material removal rate is:

Material Removal Rate:  $MRR = 245.5$  mm<sup>3</sup>/min

Type of tool: 3 = cBN coated WC/Co

Cutting speed:  $V_c = 249$  m/min

Feed:  $f = 0.495$  mm/rev

Highest Reliability:  $R = 0.0003$

A list of other best solutions is shown in Table a in the Appendix 3. Figure 5.13 represents optimum solution space in different views.

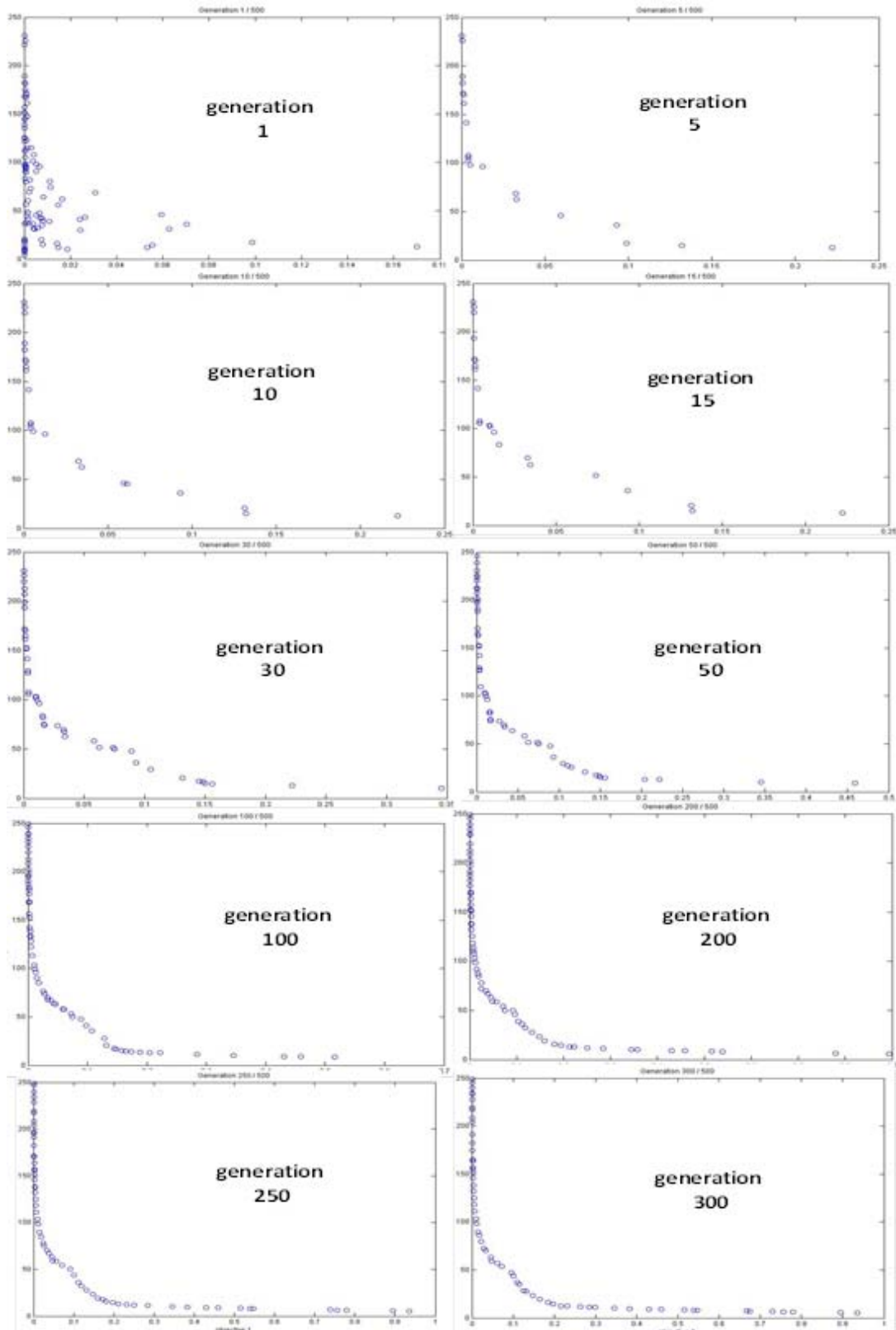


Figure 5.12. Solution space in different generations and how Pareto frontier forms

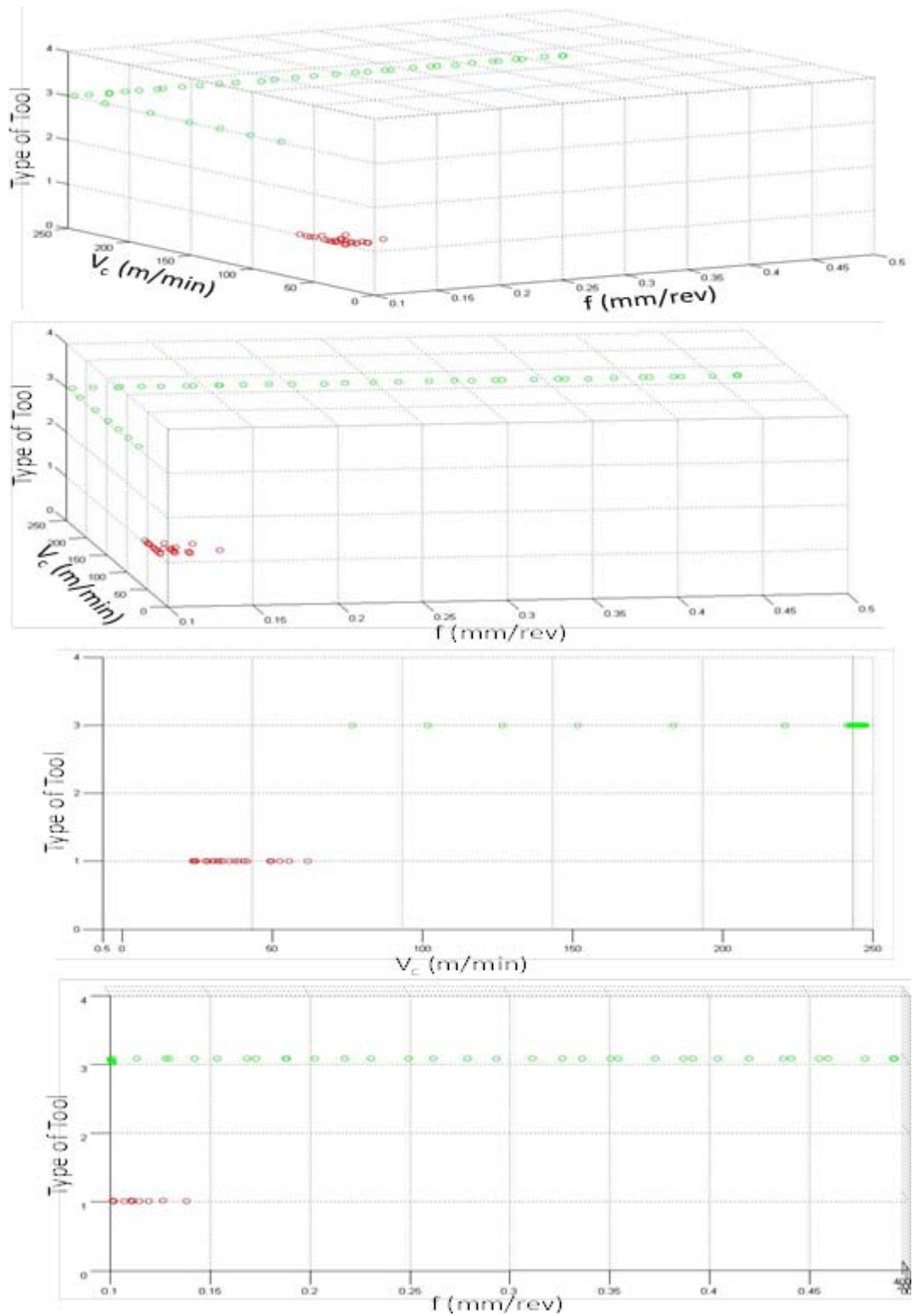


Figure 5.13. Optimum solution space in different views

## 5.5. Validation of Results

In order to validate the optimization results, same multi-objective optimization problem is solved only with single tool type being considered. Therefore, two tool types, uncoated WC/Co and TiAlN coated WC/Co are selected and optimization problem are solved considering only one tool at a time. The mission time for uncoated WC/Co tool is selected to be one minute and since reliability ratings for TiAlN coated WC/Co was low in mission time of one minute, the problem has been solved for mission times of 30 and 40 seconds for this tool type. The Pareto frontiers associated with each one of these cases are shown in Figures 5.14 and 5.15. One set of cutting condition is selected for each tool type with similar reliability ratings to run experimental tests to validate the survival rates of these cutting tools under these cutting conditions. The experimental test for TiAlN coated tool is selected from 40 seconds mission time. Therefore, the complete tables of optimized results for single tool types of uncoated WC/Co, mission time 60 seconds and TiAlN coated WC/Co, mission time 40 seconds are provided in Appendixes 4 and 5. The selected condition for uncoated WC/Co is condition #37 in Appendix 4, in which cutting speed,  $V_c = 50$  m/min, and feed  $f = 0.11$  mm/rev. The estimated reliability rating for 60 seconds mission time is about 0.3, meaning that the survival probability of uncoated WC/Co under this cutting condition is 30%. Similar cutting condition from TiAlN coated tools in terms of reliability rating is being selected which is condition #25 in Appendix 5 in which tool type is TiAlN coated WC/Co, cutting speed,  $V_c = 56$  m/min, and feed  $f = 0.1$  mm/rev. Estimated value of reliability at mission time 40 seconds for this case is also 0.31 or 31%.

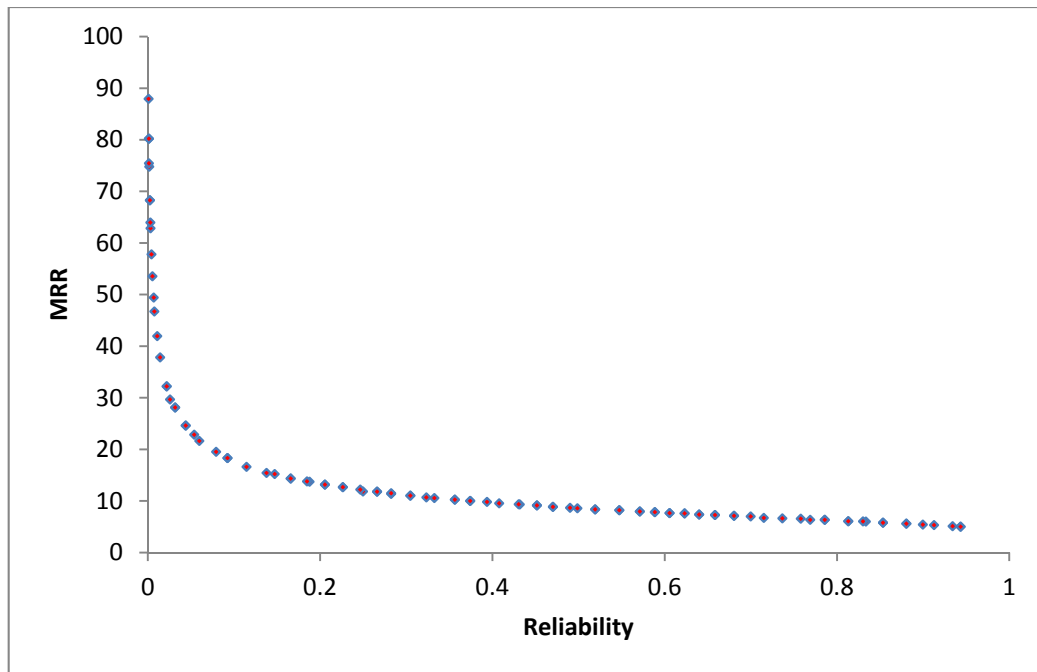


Figure 5.14. Pareto frontier considering only uncoated WC/Co tool type for cutting time  $t = 60s$

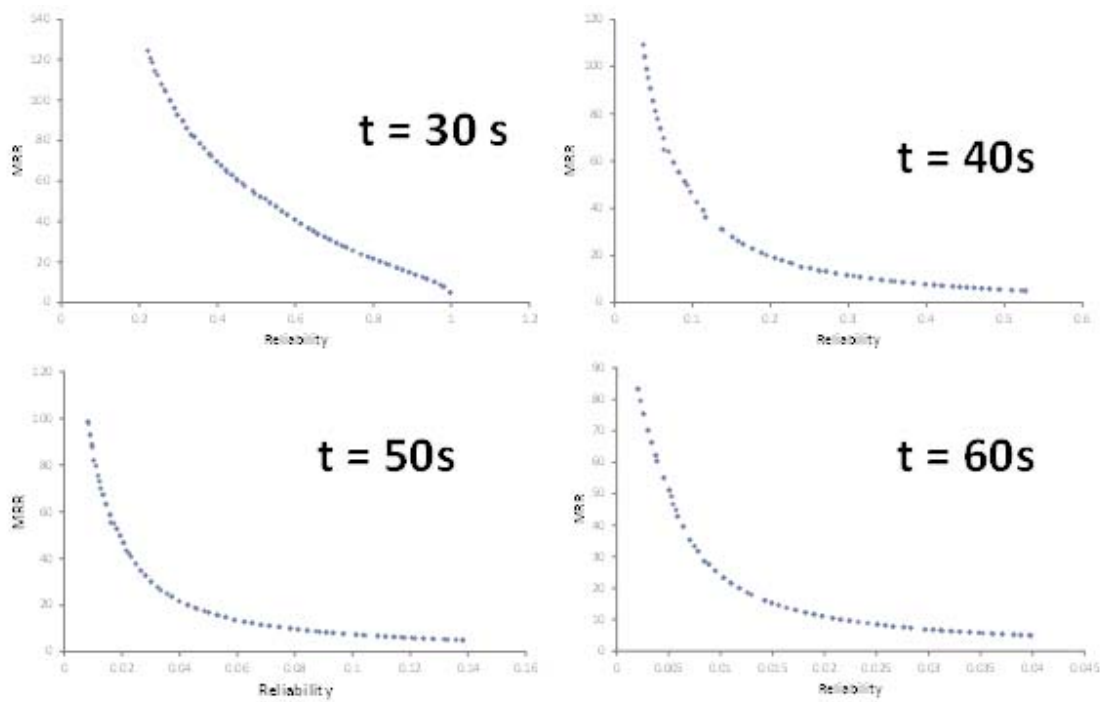


Figure 5.15. Pareto frontiers considering only TiAlN coated WC/Co tool type for cuttings time  $t = 30s, 40s, 50s$  and  $60s$

9 replications of both cutting conditions have been experimentally tested in dry machining conditions. Cutting inserts are numbered and the rake faces of the used tools are looked at under optical microscope for investigation of crater wear and probable failures with respect to defined failure criteria.

Figure 5.16 represent 9 sets of cutting edges that are used in machining Ti-6Al-4V under cutting condition #37 from Appendix 4.

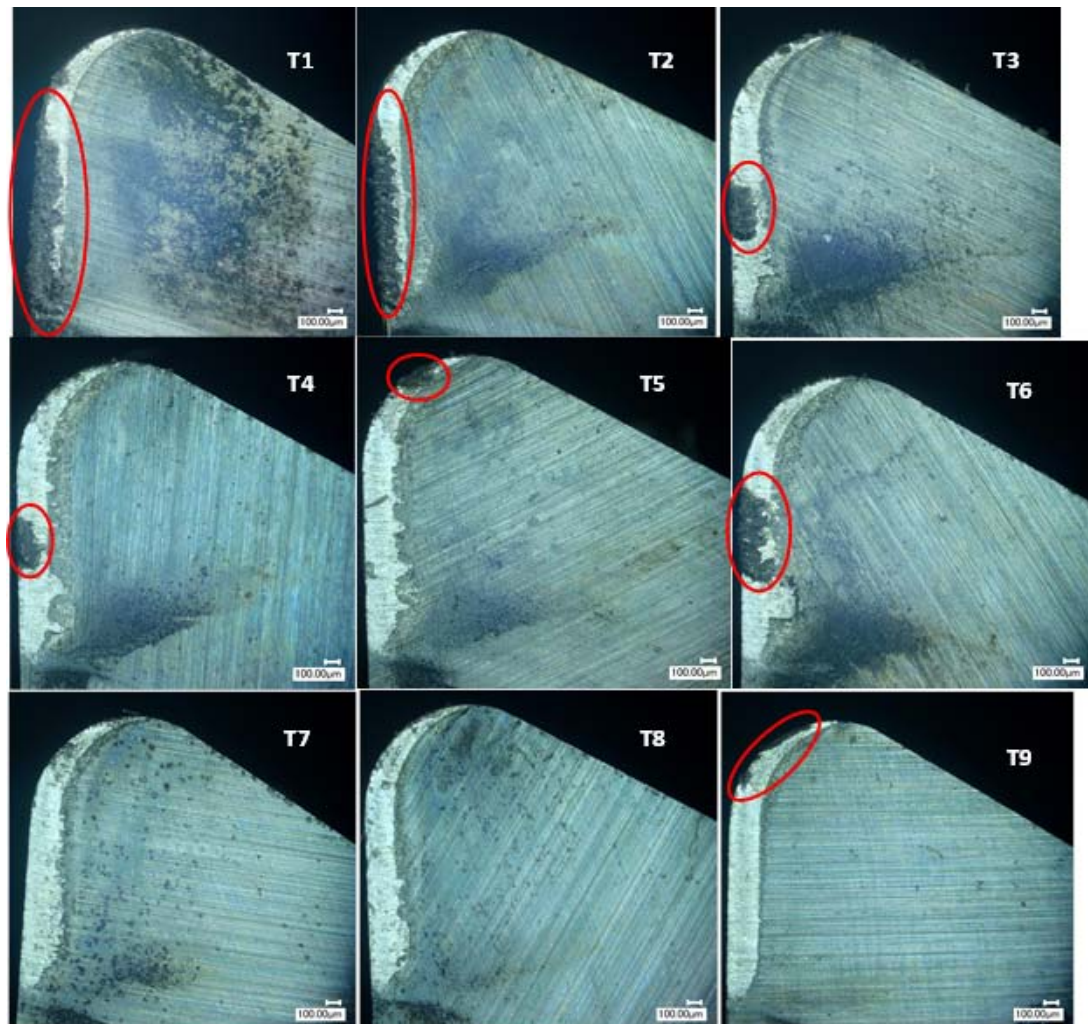


Figure 5.16. Wear conditions of 9 uncoated WC/Co inserts replication of condition #37 in Appendix 4

As it can be seen in Figure 5.16, T1 and T2 are failed because of gradual wear failure happened in cutting edge region (Zone 3) where the failure threshold is  $H_3 = 0.2$  mm. Since in the case of T1 wear amount is measured as 0.32 mm and in the case of T2 wear amount is measured as 0.263 mm, these two cases are considered as failed due to the gradual wear failure mechanism. In the cases of T3 through T6, indications of chipping off or premature failure is visible. In T5, chipping off happened in tool nose radius region (Zone 2) with magnitude of 0.185 mm which exceeds the defined failure threshold in Zone 2 which is  $H_2 = 0.15$  mm. Magnitudes of chipping off in Zone 3 of cases T3, T4 and T5 are measured to be 0.27 mm, 0.22 mm and, 0.32 mm. All of these values are greater than  $H_3 = 0.2$  mm, therefore tool are considered failed in the cases of T3 though T6 because of premature chipping off failure mechanism. In cases T7 and T8, no significant edge geometry loss is observed and therefore, in these two cases, tool is considered survived and not failed. In the case of T9, despite the fact that gradual wear in tool tip region (Zone 1) is observed which extends until tool nose radius region (Zone 2), since the maximum magnitude of wear is measured to be 0.072 mm and is smaller than both Zone 1 and Zone 2 thresholds ( $H_1 = 0.1$  mm and  $H_2 = 0.15$  mm), the T9 case is considered as survival. In summary, 3 cases out of 9 cases are survived which is close agreement with predicted reliability of 0.3 (30%).

Figure 5.17 represents the conditions of 9 replications of experimentally tested TiAlN coated WC/Co inserts under machining condition #25 in Appendix 5.

As it can be seen, no indication of premature failure can be observed in these sets of experiments and all inserts experience gradual wear mechanism. The magnitude of gradual failure is pretty consistent in all cases from nose radius region (Zone 2) to cutting edge region (Zone 3), only in the cases of T16 and T18, more severe wear amount can be seen in the cutting edge region (Zone 3) rather than the nose radius (Zone 2). In these two cases, the magnitudes of crater wear in cutting region (Zone 3) are measured as 0.24 mm and 0.26 mm. Since both are greater than defined wear threshold for Zone 3 ( $H_3 = 0.2$  mm), these cases are considered as failed. In other cases, considering

the possible uncertainties in measurements and machining operation, all cases are either failed or close to a failure. In the case of T10, crater wear amount in both Zone 2 and Zone 3 is measured as 0.158 mm. In the case of T11, wear amount is measured in both regions as 0.163 mm. Therefore, both cases of T10 and T11 are considered to be failed because of exceeding the wear threshold in Zone 2 ( $H_2 = 0.15$  mm).

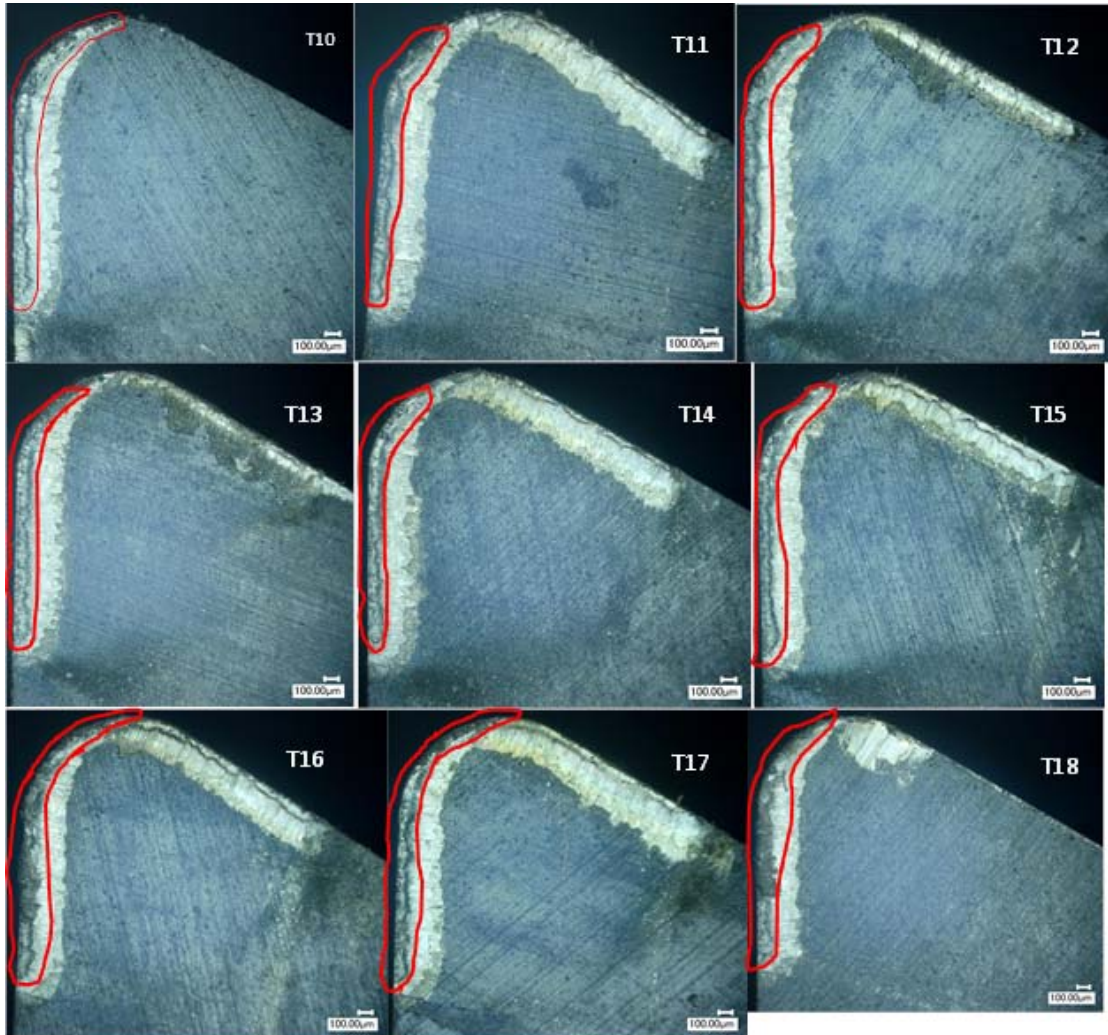


Figure 5.17. Wear conditions of 9 uncoated WC/Co inserts replication of condition #25 in Appendix 5

In the case of T12, crater wear amount is measured as 0.147 mm in Zone 3 and no significant wear in the nose radius region is observed. Therefore, since the wear amount

of 0.147 mm is smaller than  $H_3 = 0.2$  mm, T12 is considered survived. T13 is considered failure because of 0.18 mm measured failure in Zone 2 which exceeds  $H_2 = 0.15$  mm. T14 is survived as no considerable amount of wear is observed in Zone 2 and wear amount in Zone 3 is 0.175 mm which is smaller than Zone 3 wear threshold ( $H_3 = 0.2$  mm). Cases 15 and 17 are also considered failure because of 0.163 mm and 0.155 mm wear amount in nose radius region which is greater than defined wear threshold in Zone 2 ( $H_2 = 0.15$  mm).

In summary, 2 out of 9 cases are considered to be survived which results in 0.22 (22%) survival rate. Considering all uncertainties involved in the process and measurements, this amount of deviation from the predicted reliability value sounds reasonable.

## 5.6. Conclusion

As it is shown in the single objective problem with unique objective of reliability optimization of cutting tools, uncoated WC/Co is selected as the preferred tool with higher reliability. Material removal rate, a popular objective in machining problems is also defined. NSGA-II is employed to solve the multiple objective problems. The benefit of this technique is not using weight factors to the objective and instead applies non-dominated sorting methodology. For consistency, from TiAlN coated tool also a condition has been selected with reliability around 30%. Therefore, from Appendix 5 Two types of tools are selected with multi-objective problem, uncoated WC/Co and cBN coated WC/Co. Tool number 1, uncoated WC/Co, is selected for higher values of reliability but lower values of MRR, these solutions are concentrated at feed values of between 0.1 mm/rev to 0.15 mm/rev and cutting speed value of 25 m/min to 63 m/min. On the other hand, tool number 3, cBN coated WC/Co is selected for higher values of MRR but lower values of reliability, the solutions with tool number 3 cover a wider range of cutting speed and feed; feed ranges in between

0.1 mm/rev to 0.495 mm/rev in the solution space and cutting speed ranges in between 78 m/min to 249 m/min.

By these results, designers and industry have a choice to select from the possible alternatives, based on their system requirement and budget, whether they want to satisfy MRR for higher tool reliability or vice versa. It should be noted that one needs to validate these optimum decision variable, etc. (tool type, cutting speed, and feed) for machining Ti6Al4V with the actual cutting tool tests and resultant tool wear measurements. This remains as a future test of this research work.

## **6. CONTRIBUTIONS AND FUTURE WORK**

The motivation and overall content of this dissertation focuses on the investigation of machining process of titanium alloy Ti-6Al-4V, better understanding of the material constitutive model, two and three dimensional physics-based simulation of the process, cutting tool material, coatings and micro-geometry, tool wear prediction, experimental and physics-based reliability modeling of cutting tools and finally process optimization. Although the main focus of this study was on titanium alloy Ti6Al4V, the results and achievements of this study can be expanded to other materials as well. The main objectives of this study were understanding of the physical material removal process under shear-localization and cyclical serrated chip formation conditions for machining titanium alloys, establish the effect of cutting tool material, coatings, single versus multi-layer coatings, micro-geometry and variable edge preparation on machining of titanium alloy with experimental tests data and using three dimensional finite element simulations. In addition, wear measurements of worn tools of different types coming out of experimental test at different machining conditions set the ground for experimental-based reliability modeling as well as physics-based simulations led to physics-based reliability models of cutting tools and at the end by using those physics-based reliability models, a multi-objective optimization problem is solved using fast Non-dominated Sorting Genetic Algorithm (NSGA-II) and optimum selections of types of tools and cutting conditions are presented with the predicted levels of reliability and material removal rate. Main contributions of this research towards these objectives are listed as follows.

1. Development of a New Temperature-Dependent Flow Softening-Based Modified Constitutive Material Model for Titanium Alloy Ti-6Al-4V (Chapter 2)
  - Flow stress in form of a constitutive material model is a key input to the physics-based finite element simulations to introduce the material behavior under different physical, mechanical and environmental conditions. Machining is of those conditions that material goes under severe temperature, strain and strain rates and a comprehensive material model should capture material behavior at these elevated conditions in reality and turn it to a

mathematical model of flow stress. After studying different constitutive material models for Ti-6Al-4V alloy, such as original Johnson-Cook model, different modifications of Johnson-Cook model, micro-mechanical model and, etc., a new developed modification to Johnson-Cook material model is proposed, tested and validated with experimental test results. This model takes flow softening of the material at elevated strains using temperature-dependent parameters. This model represents the dynamic behavior of material very well and hence, this material model is utilized for two dimensional and three dimensional finite element simulations in this research. The parameters of this model are determined by comparing the force and serrated chip morphology coming out of experimental tests and simulations (Sima & Özel 2010).

## 2. 2D and 3D Physics-Based Finite Element Simulation and Analysis of Machining Process (Chapter 2)

- Analytical thermal modeling and finite element analysis modeling of machining with uniform and variable edge micro-geometry tools and 2D/3D process simulation have been established in a systematic fashion. The physics-based modeling techniques studied in this research not only predicted cutting forces but also related strain, stress and temperature fields which leads to predict the tool wear rate and to optimize the cutting process parameters, tool geometry and multi-layer coatings for a more productive manufacturing environment.

In the FE Simulations, broad range of concepts are studied, such as formulation a material constitutive model of Ti-6Al-4V for the simulation purpose, effects of tool type and coatings in machining, Tool wear modeling, Stress, temperature, strain prediction during machining and last but not least prediction of residual and surface integrity of the machined part. All these achievements happened using both 2D and 3D finite element simulation,

updated Lagrangian software DEFORM. Several FE simulations of machining process of titanium alloys has been run for different purposes which some are listed below:

- a) Better understanding of physics of material removal process under shear-localization and cyclical serrated chip formation conditions for machining titanium alloys using cutting tools with micro-geometry design.
- b) Established and validated a physics-based wear model that relates temperature, shear localization, stresses, and other contact conditions to tool wear mechanisms, when machining Titanium alloy using 3-D simulation modeling (Özel & Sima et al., 2010 and Sima et al., 2011).
- c) Established the effect of the cutting edge angles, micro-geometry and variable edge preparation on machining of titanium alloy with experimental data and using 3-D simulations (Özel & Sima et al., 201 and Sima et al., 2011).

### 3. Experimental Analysis of 3D Machining and Tool Wear Measurement(Chapter 3)

- Chapter 3 was focused on studying different aspects of machining Ti6Al4V, experimentally. Some limited conditions of the machining process with different types of uncoated and coated tools, single layer versus multi-layer coatings and different types of coating material, as well as variable edge design tools are utilized at two levels of cutting speeds and feed for validation and verification purpose of simulation results. Cutting forces are measured during machining process using a Kistler dynamometer attached to the Bridgeport CNC turning machine. Serrated chips produced during machining of each cutting condition are collected, mounted in epoxy resin, and then observed under the Keyence VH-Z100UR optical microscope and the dimensions and sized are recorded (Sima

& Özel 2010, Özel, Sima & Srivastava 2010, Özel, Sima, Srivastava & Kaftanoglu 2010, Sima et al. 2011).

- Various types of advanced cutting tools that are used for machining of Ti-64 bar turning tests, are then closely studied under Keyence VH-Z100UR optical microscope and size and dimensions of worn areas are measured as well as studying the dominant wear mechanism in that tool (Özel & Sima et al., 2010 and Sima et al., 2011).

#### 4. Reliability Modeling and Analysis of Advanced Cutting Tools (Chapter 4)

- Experimental-based crater wear reliability models of four types of cutting tools, uncoated WC/Co, TiAlN coated WC/Co, cBN coated WC/Co and, multi-layered (cBN+TiAlN) coated WC/Co are developed using closed tools that went through experimental tests. Then these worn tools are closely looked under the microscope and images of their crater wear area taken. These images are used for taking measurements of the crater wear region. Crater wear sub-region concept is introduced in this section for purpose of accurate failure threshold consideration. These three sub-regions are named: tool tip trailing, tool nose radius and tool cutting edge. Based on experimental results, sub-reliability of each of these regions is investigated separately and reliability of tool is model by competing risk model as failure of each one of these regions results in tool failure.
- Physics-based reliability modeling and investigation is also performed using physics-based finite element simulations ran under different machining conditions with different types of cutting tools. In these simulations, wear rates are collected from each element on the crater wear region and same division of regions as experimental data also took place here. Wear predictions are based on Usui's wear model defined for the software. Similar to experimental-based reliability modeling Weibull distribution is applied to fit to wear rate

data and general log-linear model is utilized to take into account the effect of process input parameters (cutting speed and feed). Competing risk reliability models are evaluated for each tool with respect to reliability of each sub-region of that tool.

5. Multi-Objective Fast Non-Dominated Sorting Genetic Algorithm of Machining Process Parameters and Tool Selection (Chapter 5)
  - Many objectives can be defined in machining processes. These can be minimizing machining forces, production time, cost, tool wear and/or maximizing reliability of tool, surface integrity and tool life. In this study, maximizing tool reliability as well as material removal rate which is the best index of operation's efficiency in machining operations are determined. Decision variables of this multi-objective optimization problem are type of cutting tool, cutting speed and feed. Problem is solved using strong and fast dominated sorting genetic algorithm (NSGA-II) and at the end a Pareto frontier of non-dominated solutions is provided along with the optimal values of the decision variables in the decision space.

Based on aforementioned contributions of this dissertation, possible future directions of research can be listed as follows.

1. Regarding material constitutive model in Chapter 2, it would be worthy of conducting more research to reach to a more accurate match to the Lee-Lin experimental results in smaller values of strain. It is obvious conducting more intelligent trial and error efforts on the parameters along with regression analysis can lead to better alignment between predicted forces and chip morphology and experimental results.
2. Finite element simulations can be designed and run for more machining conditions to be able to perform a more thorough optimization study on the process parameters. 3D finite element simulations can be designed and conducted with elasto-viscoplastic material

assumption for more accurate representation of any metal forming process, conditional to advancement of computational capabilities finite element software (Chapter 2).

3. More research can be conducted to figure out Usui's wear model parameters for different types of coated/uncoated and/or single/multi-layered cutting tool with different materials in order to predict more accurate tool wear (Chapter 2).
4. Experimental analysis given in Chapter 3 can be expanded for more machining set of parameters. Particularly, higher feeds and cutting speeds can be investigated (high speed machining), which would result in increase in the material removal rate. Similarly, different depth/width of cut values can also be studied. Also, different types of tool material, coatings and micro-geometries (angles and radius) can be more investigated for better understanding of their effects on machining outputs.
5. In experimental-based reliability modeling in Chapter 4, it would be beneficial that the tests are designed originally for wear and reliability analysis. All the cutting tools experience same duration of cut, same conditions, the test stop at fixed time increments and wear are measured at that time and then either new tools are used for longer time increment (preferably) or tests are conducted until next increment. Of course running more replications of each condition would decrease the uncertainty of the data.
6. Physics-based reliability modeling would be more comprehensive by considering flank wear-related failures in Chapter 4. By more developed software and computational power capabilities, modeling cutting tool material as elasto-viscoplastic material deformation assumption, complete set of flank wear data could be extracted and used towards flank wear prediction and failures due to flank wear and consider it in reliability modeling.
7. A more detailed research on crater wear sub-regions and their associated thresholds lead to a better and more accurate reliability model as optimization problem in chapters 4 and 5.

More objective functions could be considered to solve such as minimizing the cutting forces, surface roughness etc. as well as more decision variables from input parameters such as depth of cut, type of lubricant etc. in formulating multi-objective optimization problem in chapter 5. It is obvious that having more than 100 populations and more than 500 generation may result in better solutions considering increase in elapsed time in solving the problem.

# References

- Andrade U., Meyers M., Vecchio K., Chokshi A., “Dynamic recrystallization in high-strain, high-strain-rate plastic deformation of copper”, *Acta Metallurgica et Materialia*, Vol. 42 (1994): 3183–3195.
- Anurag S., Guo Y. B., “A modified micromechanical approach to determine flow stress of work materials experiencing complex deformation histories in manufacturing processes”, *International Journal of Mechanical Sciences*, Vol. 49 (7) (2007): 909–918.
- Aramesh M., Shaban Y., Balazinski M., Attia H., Kishawy H. A., Yacout S., “Survival Life Analysis of the Cutting Tools During Turning Titanium Metal Matrix Composites (Ti-MMCs)”, *Procedia CIRP*, Vol. 14 (2014): 605-609.
- Ardakan M. A., Hamadani A. Z., Alinaghian M., “Optimizing bi-Objective Redundancy Allocation Problem with a Mixed Redundancy Strategy”, *ISA Transactions*, article in press, 2014.
- Arrazola P. J., Garay A., Iriarte L. M., Armendia M., Marya S., Le Maitre F., “Machinability of titanium alloys (Ti6Al4V and Ti555.3)”, *Journal of Materials Processing Technology*, Vol. 209(5) (2009): 2223–2230.
- Aurich J. C., Bil H., “3D Finite Element Modelling of Segmented Chip Formation”, *CIRP Annals - Manufacturing Technology*, Vol. 55(1) (2006): 47–50.
- Bammann D. J., Chiesa M. L., Johnson G. C., “Modeling large deformation and failure in manufacturing processes”, *Theoretical and Applied Mechanics*, (1996) 359–376.
- Black J. R., “Electromigration: A Brief Survey and some recent results”, *IEEE Transaction on Electron Devices*, Vol. 16 (1969): 338-347.
- Bouzakis K. D., Gerardis S., Katirtzoglou G., Makrimallakis S., Bouzakis A., Cremer R., Fuss H. G., “Application in Milling of Coated Tools with Rounded Cutting Edges after Film Deposition”, *CIRP Annals – Manufacturing Technology*, Vol. 58(1) (2009): 61–64.
- Branke, J., Deb, K., Miettinen, K., Slowinski, R., “Multi-Objective Optimization, Interactive and Evolutionary approaches” *Lecture Notes in Computer Science*, Vol. 5252: Springer, (2008).
- Byrne G., Dornfeld D., Denkena B., “Advanced Cutting Technology”, *CIRP Annals – Manufacturing Technology*, Vol. 52 (2) (2003): 483–507.

- Calamaz M., Coupard D., Girot F., “A new material model for 2D numerical simulation of serrated chip formation when machining titanium alloy Ti-6Al-4V”, *International Journal of Machine Tools and Manufacture*, Vol. 48 (2008): 275–288.
- Che-Haron C. H. & Jawaid A., “The Effect of Machining on Surface Integrity of Titanium”, *Journal of Materials Processing Technology*, Vol. 166 (2005): 188-192.
- Chen L., El-Wardany T. I., Harris W. C., “Modeling the Effects of Flank Wear Land and Chip Formation on Residual Stresses”, *CIRP Annals – Manufacturing Technology*, Vol. 53 (1) (2004): 95-98.
- Chou Y. K., Evans Ch. J., Barash M. M., “Experimental Investigation on cBN Turning of Hardened AISI 52100 Steel”, *Journal of Material Processing Technology*, Vol. 124, No. 3 (2002): 274-283.
- Ciurana J., Arias G. & Özel T., “Neural Network Modeling and Particle Swarm Optimization (PSO) of Process Parameters in Pulsed Laser Micromachining of Hardened AISI H13 Steel”, *Materials and Manufacturing Processes*, Vol. 24.3 (2009): 358-368.
- Coit D.W., Smith A.E., “Reliability optimization of series-parallel systems using a genetic algorithm”, *Reliability, IEEE Transactions on*, Vol. 45-2 (1996): 254-260, 266.
- Corduan, N., Himbert, T., Poulachon, G., Dessoly, M., Lambertin, M., Vigneau, J., Payoux, B., “Wear Mechanisms of New Tool Materials for Ti6Al4V High Performance Machining,” *CIRP Annals - Manufacturing Technology*, Vol. 52(1) (2003): 73–76.
- Cotterell M., Byrne G., “Dynamics of chip formation during orthogonal cutting of titanium alloy Ti-6Al-4V”, *CIRP Annals - Manufacturing Technology*, Vol. 57(1) (2008): 93–96.
- Deb, K., Pratap, A., Agarwal, S., Meyarivan, T., “A Fast and Elitist Multi Objective Genetic Algorithm: NSGA-II”, *IEEE Transactions on Evolutionary Computations*, Vol. 6(2) (2002): 182-197.
- Engelmaier W., Liao H. T., Wang X. D., “Reliability of Surface Mount Solder Joints: Physics and Statistics of failure”, *National Electronic Packaging and Production West Proceedings*, Ann Arbor, MI: University of Michigan, (1993): 1782.

- Flaherty J. M., "How to Accelerate SMT Attachment Reliability Testing", *Test and Measurement World*, January (1994): 47-54.
- Gahr K. H. Z., "Microstructure and Wear of Materials", Amsterdam, Elsevier Publications, 1987.
- Guo Y. B., Wen Q., Woodbury K. A., "Dynamic material behavior modeling using internal state variable plasticity and its application in hard machining simulations", *ASME Journal of Manufacturing Science and Engineering*, Vol. 128 (2006) 749–756.
- Guo Y.B., Li W., Jawahir I. S., "Surface Integrity Characterization and Prediction in Machining of Hardened and Difficult-to-Machine Alloys; A State-of-the-Art Research Review and Analysis", *Machining Science and Technology*, Vol. 13 (2009): 437-470.
- Hitomi K., Nakamura N. & Inoue S., "Reliability Analysis of Cutting Tools" *Journal of Engineering for Industry* Vol. 101 (1979): 185-190.
- Holmberg K., Matthews A., "Coatings Tribology: Properties, Techniques and Applications in Surface Engineering", *Tribology Series 28*, Elsevier, 2<sup>nd</sup> impression, 1998, printed in Netherlands.
- Jahanmir S., Suh N. P., Abrahamson E. P., "Microscopic Observations of The Wear Sheet Formation by Delamination", *Wear*, Vol. 28 (1974): 235-249.
- Jain V. K., Bahadur S., "Development of a Wear Equation for Polymer - Metal Sliding in Terms of Fatigue and Topography of Sliding Surfaces", *Wear of Materials*, ASME, (1979): 556-562.
- Jawahir I. S., Ghosh R., Fang X. D., Li P. X., "An Investigation of the Effects of Chip Flow on Tool Wear in Machining with Complex Grooved Tools", *Wear*, Vol. 184 (1995): 145-154.
- Jianxin D., Yousheng L., Wenlong S., "Diffusion Wear in Dry Cutting of Ti-6Al-4V with WC/Co Carbide Tools", *Wear*, Vol. 265 (2008): 1776–1783.
- Johnson G. R., Cook W. H., "A constitutive model for metals subjected to large strains, high strain rates and high temperatures", *Proceedings of the Seventh International Symposium on Ballistics*, Hague, Netherlands, Vol. 54 (1983): 1–7.
- Jones, D. F., Mirrazavi, S. K., Tamiz, M., "Multi Objective Meta-Heuristics: An Overview of Current State-of-the-Art", *European Journal of Operation Research*, Vol. 137(1) (2002): 1-9.
- Kagnaya T., Boher C., Lambert L., Lazard M., Cutard T., "Wear Mechanisms of WC-Co Cutting Tools from High-Speed Tribological Tests", *Wear*, Vol. 267 (2009): 890–897.

- Kalpakjian, S. and Schmid, S. *Manufacturing Processes for Engineering Materials (5th Edition)*, (2010) Prentice-Hall.
- Kannatey-Asibu E. Jr., “A Transport-Diffusion Equation in Metal Cutting and its Application to Analysis of the Rate of Flank Wear”, *Journal of Engineering for Industry*, Vol. 107 (1985): 81-89.
- Karpat Y. & Özel T. “Multi-Objective Optimization for Turning Processes Using Neural Network Modeling and Dynamic-Neighborhood Particle Swarm Optimization”, *International Journal of Advanced Manufacturing Technology*, Vol. 35, 3-4 (2007): 234-247.
- Karpat Y., Özel T., “Mechanics of high speed cutting with curvilinear edge tools”, *International Journal of Machine Tools and Manufacture*, Vol. 48(2008): 195–208.
- Kato K., “Wear in Relation to Friction. A Review”, *Wear*, Vol. 241, (2000): 151-157.
- Kay G., “Failure Modelling of Titanium 6Al-4V and Aluminum 2024-T3 with the Johnson-Cook Material Model”, U.S. Lawrence Livermore National Laboratory Report, DOT/FAA/AR-03/57(2003).
- Kitigawa T., Maekawa K., Shirakashi T., Usui, E., “Analytical Prediction of Flank Wear of Carbide Tools in Turning Plain Carbon Steels (Part 1) - characteristic Equation of Flank Wear”, *Bulletin of Japanese Society of Precision Engineering*, Vol. 22, No. 4 (1988): 263 - 269.
- Klim Z., Ennajimi E., Balazinski M., Fortin C., “Cutting Tool Reliability Analysis for Variable Cutting Feed Milling of 17-4PH Stainless Steel”, *Wear*, Vol. 195 (1996): 206-213.
- Komanduri R., Hou Z. B., “On thermoplastic shear instability in the machining of a titanium alloy”, *Metallurgical and Materials Transactions*, Vol. 33A (2002) 2995–3010.
- Konak A., Coit D. W., Smith A. E., “Multi-objective optimization using genetic algorithms: A tutorial”, *Reliability Engineering and System Safety*, Vol. 91, (2006): 992–1007.
- König W., “Fertigungsverfahren / Manufacturing Methods”, In German, VDI - Verlag, Düsseldorf, Germany, Vol. 1 (1984): 372-372.
- Kramer B. M., Judd P. K., “Computational Design of Wear Coatings”, *Journal of Vacuum Science and Technology, A*, Vol. 3, No. 6 (1985): 2439-2444.
- Lee W. S., Lin C. F., “High-temperature deformation behavior of Ti6Al4V alloy evaluated by high strain-rate compression tests”, *Journal of Materials Processing Technology*, Vol. 75 (1998a): 127–136.

- Lee W. S., Lin C. F., "Plastic deformation and fracture behavior of Ti-6Al-4V alloy loaded with high strain rate under various temperatures", *Materials Science and Engineering*, Vol. A241 (1998b): 48-59.
- Levitin, G., "Genetic Algorithms in Reliability Engineering", *Reliability Engineering & System Safety*, Vol. 91(9): (2006): 975-976.
- Li, D., Haimes, Y. Y., "A Decomposition Method for Optimization of Large-System Reliability", *IEEE Transactions on Reliability*"; Vol. 41(2) (1992): 183-188.
- Lim S. C., Lee S. H., Liu Y. B., Seah K. H. W., "Wear Maps for Uncoated High-Speed Steel Cutting Tools", *Wear*, Vol. 170 (1993): 137-144.
- Lin W. S., "The Reliability Analysis of Cutting Tools in the HSM Processes" *International Scientific Journal*" Vol. 30 (2008): 97-100.
- Loladze T. N., "Of the Theory of Diffusion Wear", *Annals of the CIRP*, Vol. 30/1/1981, (1981): 70-76.
- M'Saoubi R., Outeiro J. C., Chandrasekaran H., Dillon Jr. O. W., Jawahir I. S., "A Review of Surface Integrity in Machining and Its Impact on Functional Performance and Life of Machined Products", *International Journal of Sustainable Manufacturing*, Vol. 1.1-2 (2008): 203-236.
- Maekawa K., Kitagawa T., Shirakashi T., Childs T. H., "Finite Element Simulation of Three-Dimensional Continuous Chip Formation Processes", *Proc.8th,ASPE Annual Meeting, Seattle, USA, (1993)*.
- Maekawa K., Kitigawa T., Shirakashi T., Usui, E., "Analytical Prediction of Flank Wear of Carbide Tools in Turning Plain Carbon Steels (Part 2) - Prediction of Flank Wear", *Bulletin of Japanese Society of Precision Engineering*, Vol. 23, No. 2 (1989): 126-133.
- Maekawa K., Ohhata H., Kitigawa T., Childs T. H. C., "Simulation Analysis of Machinability of Leaded Cr-Mo and Mn-B Structural Steels", *Journal of Materials Processing Technology*, Vol. 62 (1996): 363 - 369.
- Maekawa K., Shirakashi T., Usui E., "Flow stress of low carbon steel at high temperature and strain rate (Part 2)", *Bulletin of the Japan Society of Precision Engineering*, Vol. 17 (3) (1983) 167-172.
- Mathew P., "Use of Predicted Cutting Temperatures in Determining Tool Performance", *Int. Journal of Machine Tools and Manufacture*, Vol. 29, No. 4 (1989): 481-497.

- Mazzuchi T. A., Soyer R., "Assessment of Machine Tool Reliability Using a Proportional Hazards Model", *Naval Research Logistics*, Vol. 36, Issue 6 (1998): 765-777.
- McPhersen J. W., "Reliability Physics and Engineering, Time-to-Failure Modeling", Texas, Springer, 2nd Edition, 2013.
- Meyer H. W., Kleponis D. S., "Modeling the high strain rate behavior of titanium undergoing ballistic impact and penetration", *International Journal of Impact Engineering*, Vol. 26 (2001): 509-521.
- Molinari A., Nouari M., "Modeling of tool wear by diffusion in metal cutting," *Wear*, Vol. 252, (2002): 135-149.
- Muthukrishnan N., Davim P., "Influence of Coolant in Machinability of Titanium Alloy (Ti-6Al-4V)", *Journal of Surface Engineered Materials and Advanced Technology*, (2011): 9-14.
- Nemat-Naser S., Guo W. G., Nesterenko V. F., Indrankanti S. S., Gu Y. B., "Dynamic response of conventional and hot isostatically pressed Ti-6Al-4V alloys", *Experiments and Modeling, Mechanics of Materials*, Vol. 33 (2001): 425-439.
- Nemat-Nasser S., Isaacs J. B., "Direct measurement of isothermal flow stress of metals at elevated temperatures and high strain rates with application to Ta and Ta-W alloys", *Acta Materialia*, Vol. 45 (1997) 907-919.
- Nurul-Amin A. K. M., Ismail A. F., Nor Khairusshima M. K., "Effectiveness of Uncoated WC-Co and PCD Inserts in End Milling of Titanium Alloy – Ti-6Al-4V", *Journal of Materials Processing Technology*, Vol. 192-193 (2007): 147-58.
- Oxley, P.L.B., "Mechanics of Machining - An Analytical Approach to Assessing Machinability", Ellis Horwood Series in Mechanical Engineering, Chichester, Ellis Horwood Limited, (1989).
- Özel T., "Computational Modelling of 3-D Turning with Variable Edge Design Tooling: Influence of Micro-Geometry on Forces, Stresses, Friction and Tool Wear", *Journal of Materials Processing Technology*, Vol. 209(11) (2009): 5167-5177.
- Özel T., "Influence of friction models on finite element simulations of machining", *International Journal of Machine Tools and Manufacture*, Vol. 46(5) (2006): 518-530.
- Özel T., Karpuz Y., Srivastava A. K., "Hard turning with variable micro-geometry PcBN tools", *CIRP Annals-Manufacturing Technology*, Vol. 57(1) (2008): 73-76.

- Özel T., Lianos I., Soriano J. & Arrazola P.J. “3D Finite Element Modelling of Chip Formation Process for Machining Inconel 718: Comparison of FE Software Predictions”, *Machining Science and Technology*, Vol. 15.1 (2011): 21-46.
- Özel T., Sima M., Srivastava A. K., “Finite element simulation of high speed machining Ti–6Al–4V alloy using modified material models”, *Transactions of the NAMRI/SME*, Vol. 38(2010a): 49–56.
- Özel T., Sima M., Srivastava A. K., Kaftanoglu B., “Investigations on the effects of multi-layered coated inserts in machining Ti–6Al–4V alloy with experiments and finite element simulations”, *CIRP Annals—Manufacturing Technology*, Vol. 59 (1) (2010b): 77–82.
- Özel T., Zeren E., “Finite Element Modeling the Influence of Edge Roundness on the Stress and Temperature Fields Induced by High-Speed Machining” *International Journal of Advanced Manufacturing Technology*, Vol. 35 (2007): 255-267.
- Peterson M. B., Gabel M. K., Devine M. J., *ASTM Standardization News*, (1974).
- Rabinowicz E., “Friction and Wear of Materials”, New York, John Wiley and Sons Inc., 1964.
- Reeves, C. R., “Modern Heuristic Techniques for Combinatorial Problems”, Oxford: Blackwell Scientific, 1995.
- Rhee S. K., “Wear Equation for Polymers Sliding against Metal Surfaces”, *Wear*, Vol. 16 (1970): 431-445.
- Schmidt C., Frank P., Weule H., Schmidt J., Yen Y. C., Altan T., “Tool wear prediction and verification in orthogonal cutting”, *Proceeding of 6th CIRP International Workshop on Modeling of Machining Operations*, Hamilton, Canada, May 20, 2003.
- Seo S., Min O., Yang H., “Constitutive equation for Ti–6Al–4 V at high temperatures measured using the SHPB technique”, *International Journal of Impact Engineering*, Vol. 31 (2005): 735–754.
- Sette Antonialli A. I., Mendes Filho A. A., Sordi V. L., Ferrante M., “The Machinability of Ultrafine-grained Grade 2 Ti Processed by Equal Channel Angular Pressing”, *Journal of Materials Research Technology*, Vol. 1, No. 3 (2012): 148-153.
- Shaban Y., Aramesh M., Yacout S., Balazinski M., “Optimal replacement of tool during turning titanium metal matrix composites”, *Proceedings of the 2014 Industrial and Systems Engineering Research Conference*
- Shatla M., Yen Y. C., Altan T., “Tool-workpiece interface in Orthogonal Cutting Application of FEM Modeling” *Transactions of NAMRI/SME*, Vol. XXVIII, (2000): 173-178.

- Shatla, M., "Prediction of Forces, Stresses, Temperatures and Tool Wear in Metal Cutting", Ph.D. Dissertation, The Ohio State University, 1999.
- Shaw M. C., "Metal Cutting Principles", Oxford, Oxford Science Publications, 1989.
- Sima M., Özel T., "Modified Material Constitutive Models for Serrated Chip Formation Simulation and Experimental Validation in Machining of Titanium Alloy Ti6Al4V", *International Journal of Machine Tools and Manufacture*, Vol. 59 (2010): 943-960.
- Sima M., Ulutan D., Özel T., "Effects of Tool Micro-Geometry and Coatings in Turning of Ti-6Al-4V Titanium Alloy", *Proceedings of the 39th North American Manufacturing Research Conference*, June 13-17, 2011, Oregon State University, Corvallis, Oregon.
- Smithey D. W., Kapoor S. G., DeVor R. E., "A Worn Tool Force Model for Three-Dimensional Cutting Operations," *Int. J. Mach. Tools Manuf.*, Vol. 40 (2000): 1929–1950.
- Strenkowski J. S., Larson W. C., Chern S. Y., "Prediction of Diamond Tool Wear in Precision Machining", Vol. 54/TRIB-Vol. 2, ASME, edited by Attia, M.H., Komanduri, R., (1991): 279-290.
- Suh N. P., "The Delamination Theory of Wear", *Wear*, Vol. 25 (1973): 111-124.
- Sun J., Guo Y.B., "A Comprehensive Experimental Study on Surface Integrity by End Milling Ti-6Al-4V", *Journal of Materials Processing Technology*, Vol. 209 (2009): 4036-4042.
- Sun S., Brandt M., Dargusch M. S., "Characteristics of Cutting Forces and Chip Formation in Machining of Titanium Alloys" *International Journal of Machine Tools and Manufacture*, Vol. 49 (2009): 561-68.
- Takeyama H., Murata R., "Basic Investigation of Tool Wear", *ASME Journal of Engineering for Industry*, Vol. 85 (1963): 33-37.
- Thepsonthi T., Özel T., "Multi-Objective Process Optimization for Micro-end Milling of Ti-6Al-4V Titanium Alloy", *International Journal of Advanced Manufacturing Technology*, Vol. 63.9 (2012): 903-914.
- Thomas M., Turner S., Jackson M., "Microstructural Damage during High-Speed Milling of Titanium Alloys", *Scripta Materialia*, Vol. 62 (2010): 250-253.
- Tillman, F. A., "Optimization of systems reliability", New York: Dekker, 1980.

- Ulutan D., Özel T., “Machining Induced Surface Integrity in Titanium and Nickel Alloys: A Review” *International Journal of Machine Tools and Manufacture*, Vol. 51 (2011): 250-280.
- Ulutan D., Özel T., “Multi-Objective Optimization of Experimental and Simulated Residual Stresses in Turning of Nickel-Alloy IN100”, *Materials and Manufacturing Processes*, Vol. 28. 7 (2013): 835–841.
- Ulutan D., “Predictive Modeling and Multi-Objective Optimization of Machining-Induced Residual Stresses: Investigation of Machining Parameter Effects” PhD Dissertation, Rutgers, The State University of New Jersey, Graduate Program in Industrial and Systems Engineering, 2013.
- Usui E., Shirakashi T., Kitagawa T., “Analytical Prediction of Three Dimensional Cutting Process, Part 3, Cutting Temperature and Crater Wear of Carbide Tool”, *Journal of Engineering for Industry*, Vol. 100, No. 2 (1978): 236.
- Wager J. G., Barash M. M., “Study for Distribution of the Life of HSS Tools”, *ASME Journal of Engineering for Industry*, Vol. 73 (1971): 295-299.
- Wang X., Kwon P. Y., “WC/Co Tool Wear in Dry Turning of Commercially Pure Aluminum”, *Journal of Manufacturing Science and Engineering*, Vol. 136 (2014).
- Wang Z. G., Rahman M., Wong Y. S., “Tool Wear Characteristics of Binderless CBN Tools Used in High-Speed Milling of Titanium Alloys”, *Wear*, Vol. 258 (2005): 752-758.
- Wu Q., “Serrated Chip Formation and Tool-Edge Wear in High-Speed Machining of Advanced Aerospace Materials” Utah State University, Logan, Utah, 2007.
- Yamaguchi Y., “Tribology of Plastic Deformation”, Amsterdam, Elsevier Publications, 1990.
- Yen Y. C., Söhner J., Weule H., Schmidt J., Altan T., “Estimation of Tool Wear of Carbide Tool in Orthogonal Cutting Using FEM Simulation” *Machining Science and Technology*, Vol. 6, No. 3, (2002): 467-486.

Yen Y. C., Söhner J., Lilly B., Altan T., "Estimation of Tool Wear in Orthogonal cutting Using the Finite Element Analysis", *Journal of Materials Processing Technology*, Vol. 146 (2004): 82-91.

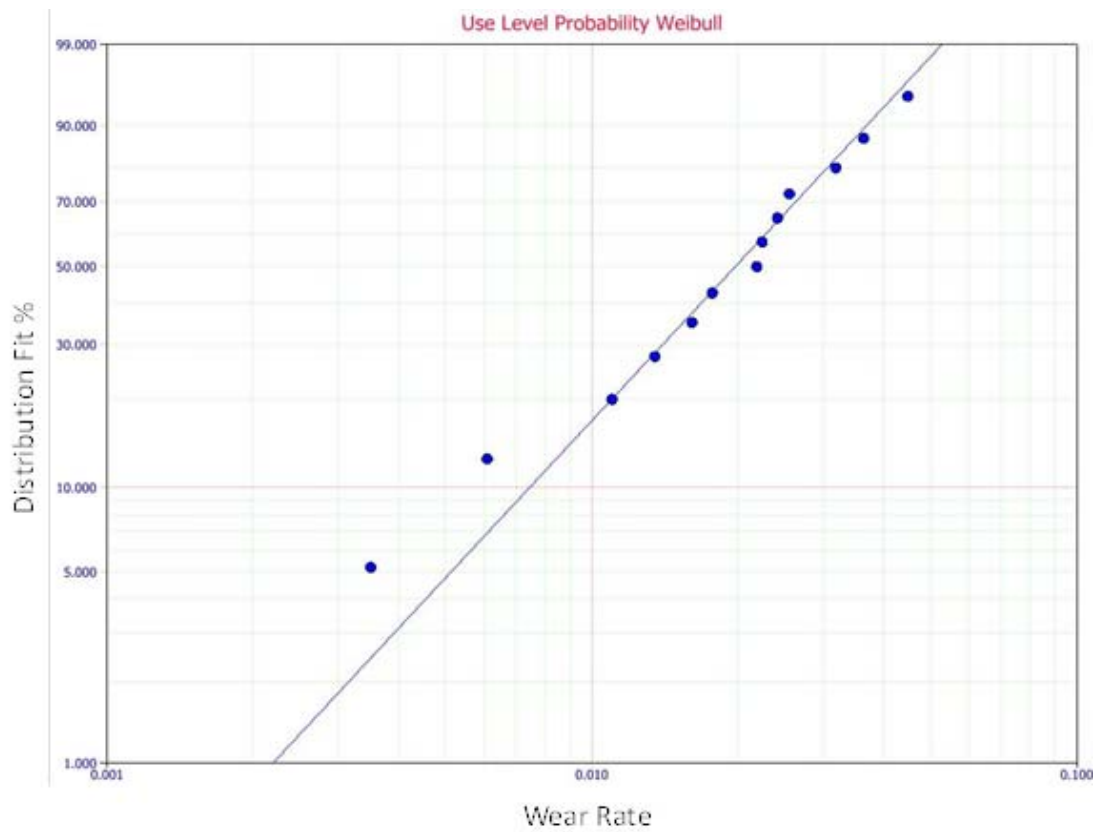
# Appendix

## Appendix 1

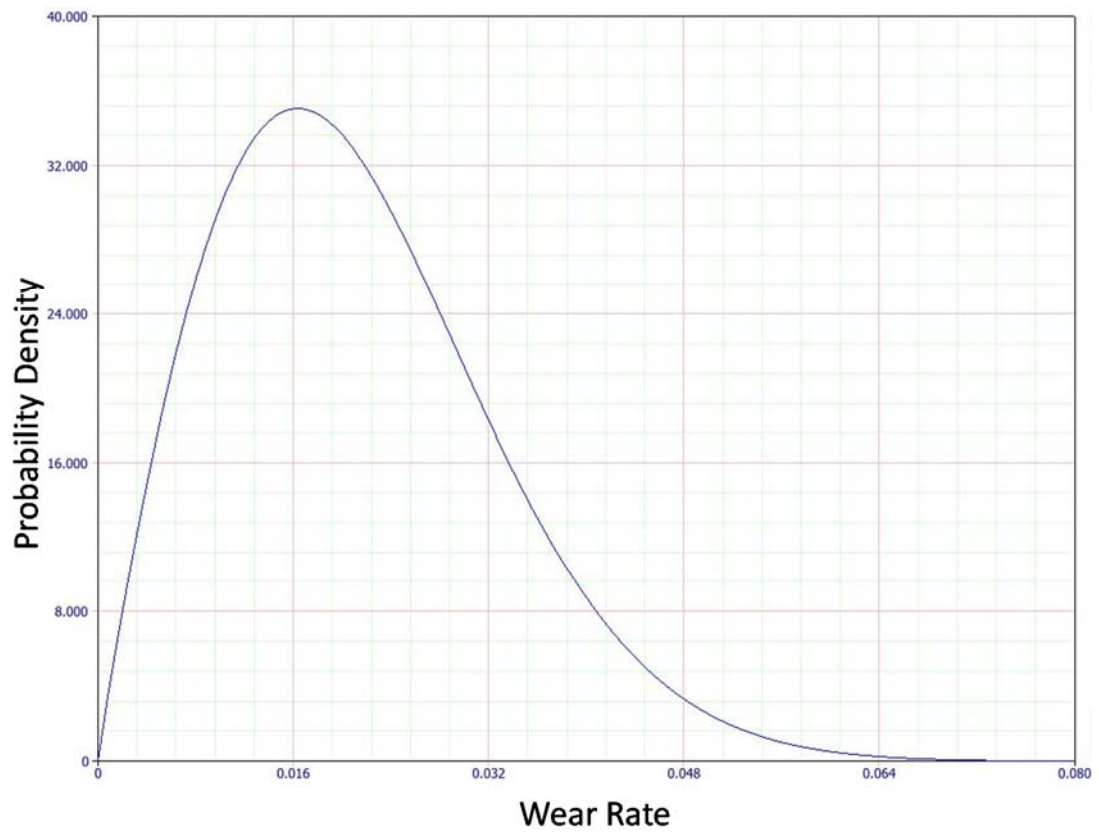
Distribution fits and probability density functions to the experimental data for wear rate of cutting tools at different wear regions.

### 1a) Uncoated WC/Co tool tip trailing zone (Region 1):

Distribution fit plot:

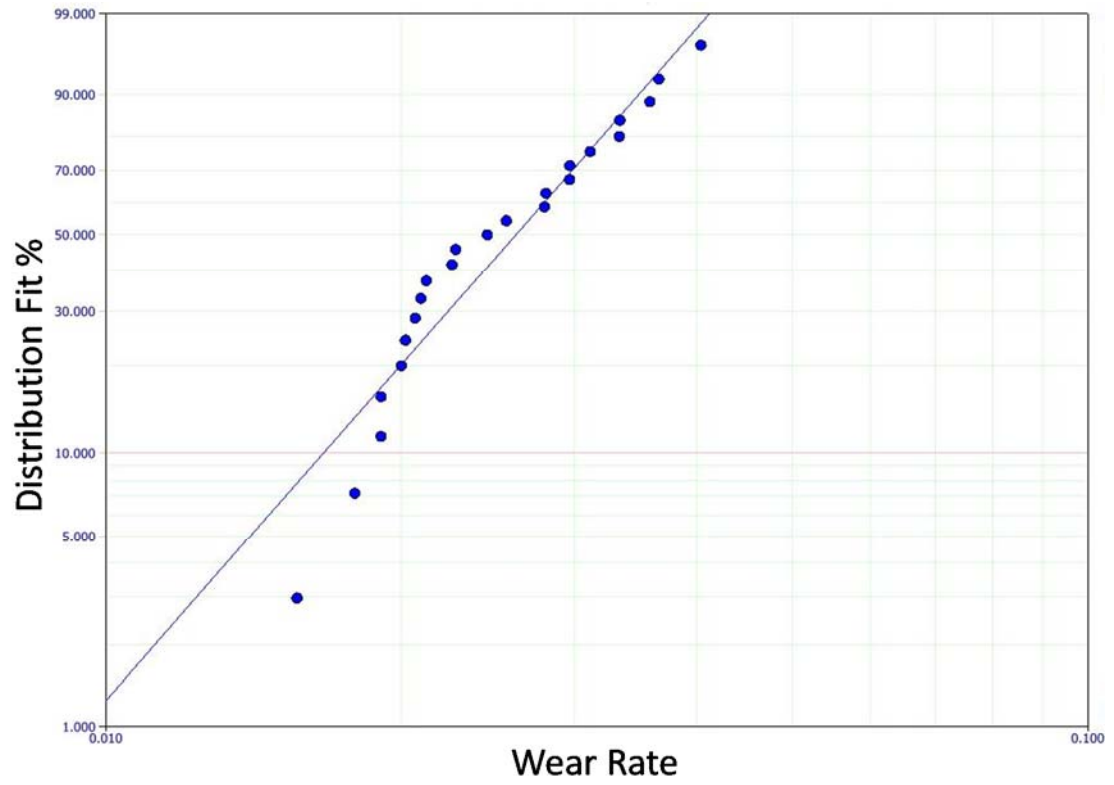


Probability Density Function plot:



**1b) Uncoated WC/Co tool nose radius zone (region 2):**

Distribution fit plot:

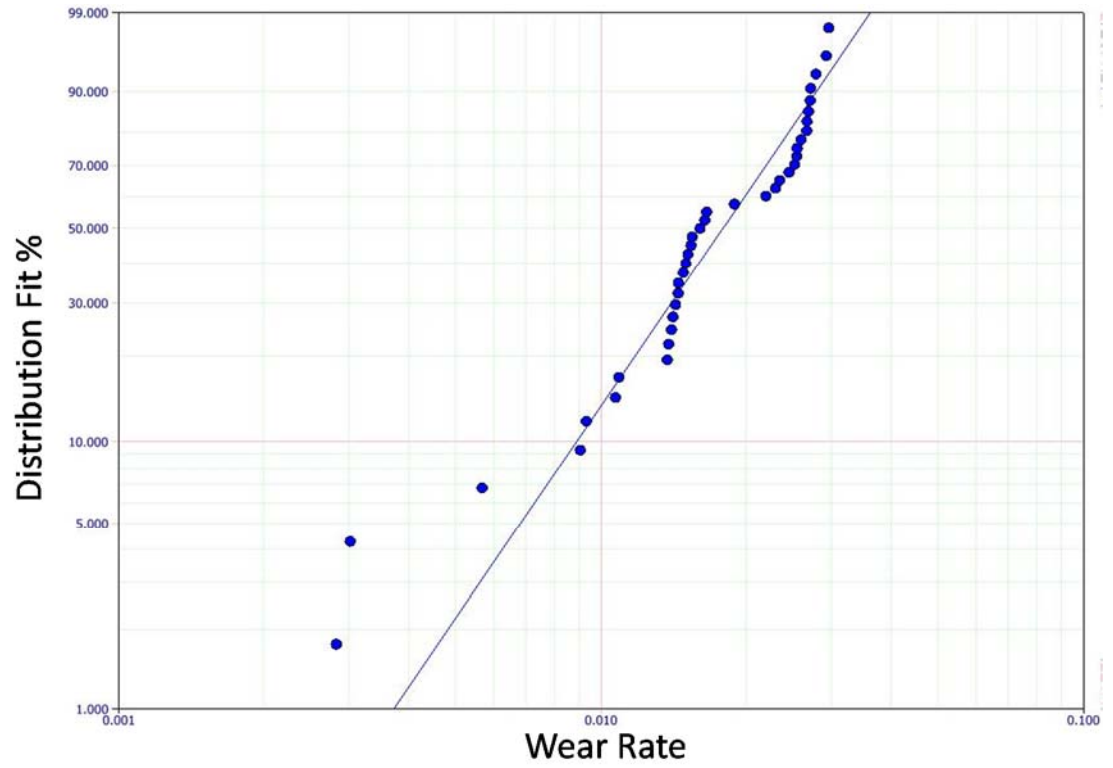


Probability Density Function plot:

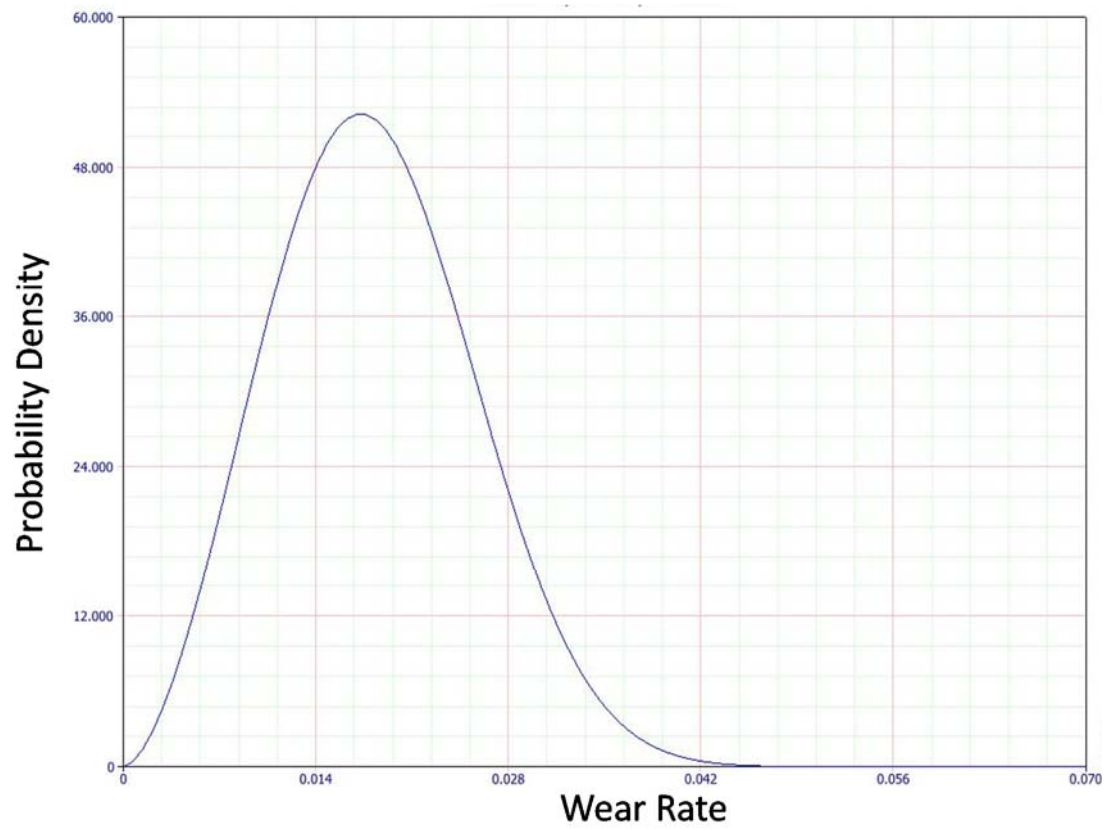


**1c) Uncoated WC/Co tool cutting edge zone (region 3):**

Distribution fit plot:

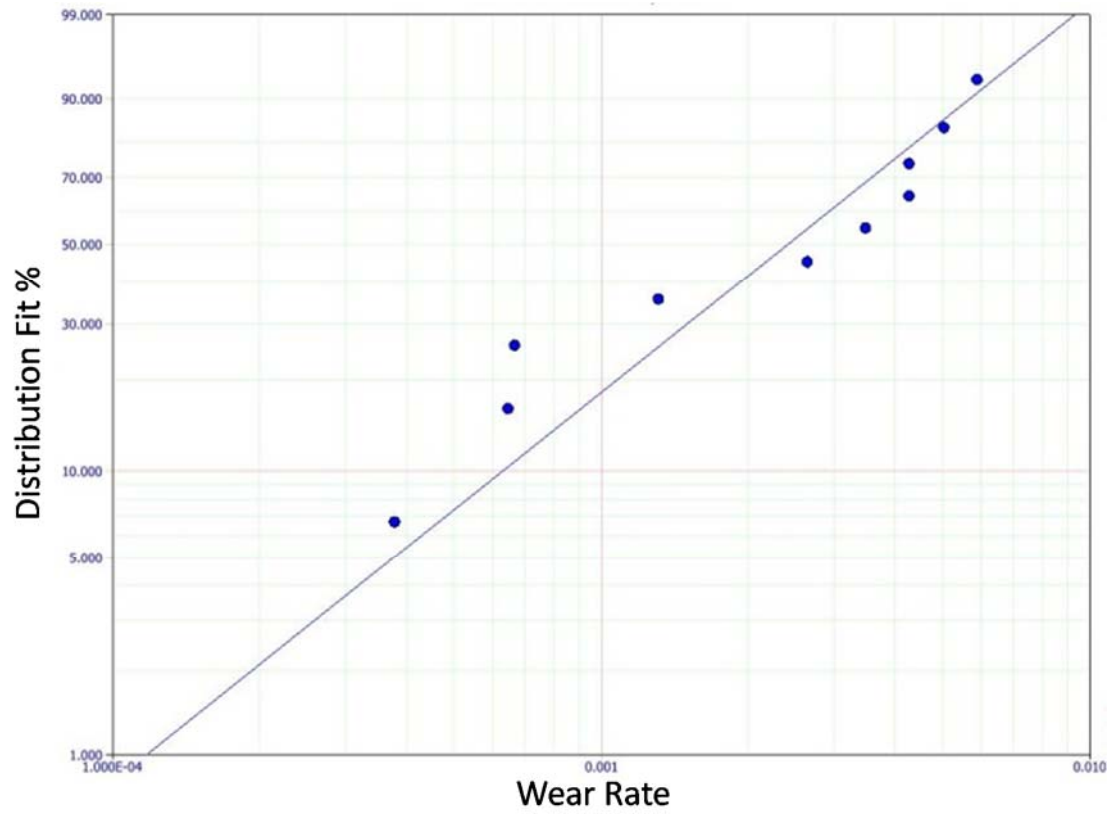


Probability Density Function plot:

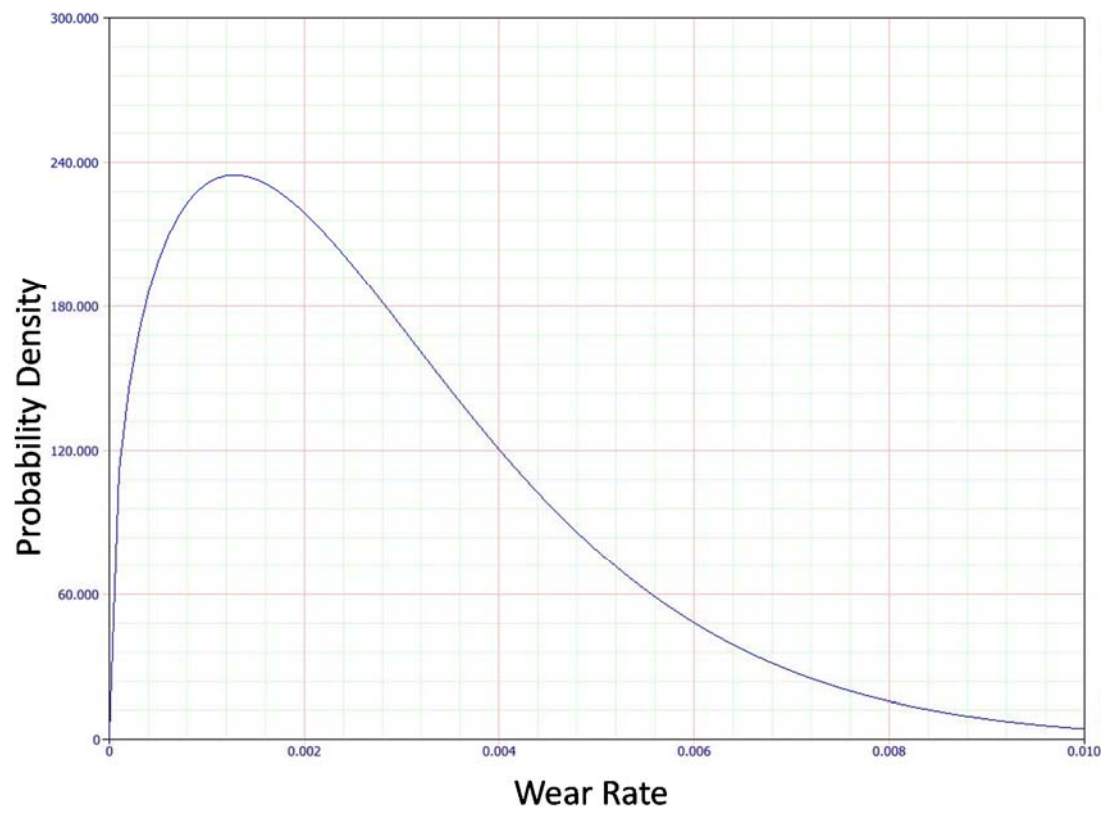


**2a) TiAlN coated WC/Co tool tip trailing zone (region 1):**

Distribution fit plot:

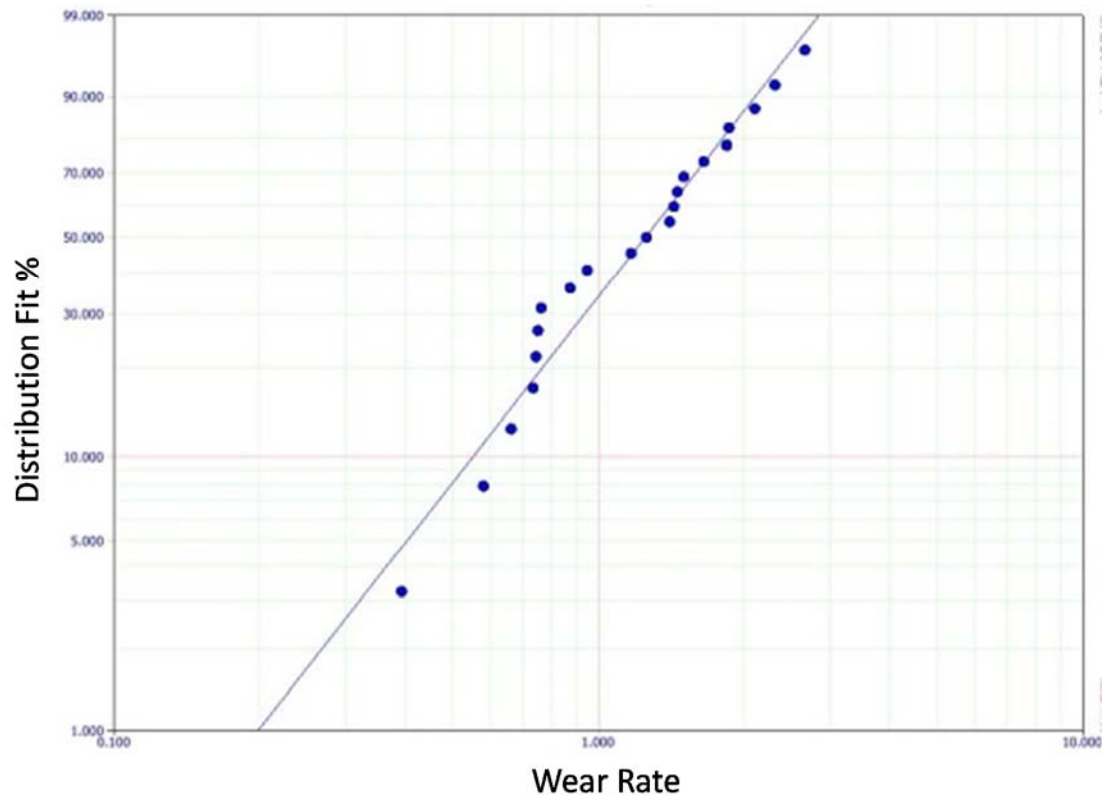


Probability Density Function plot:

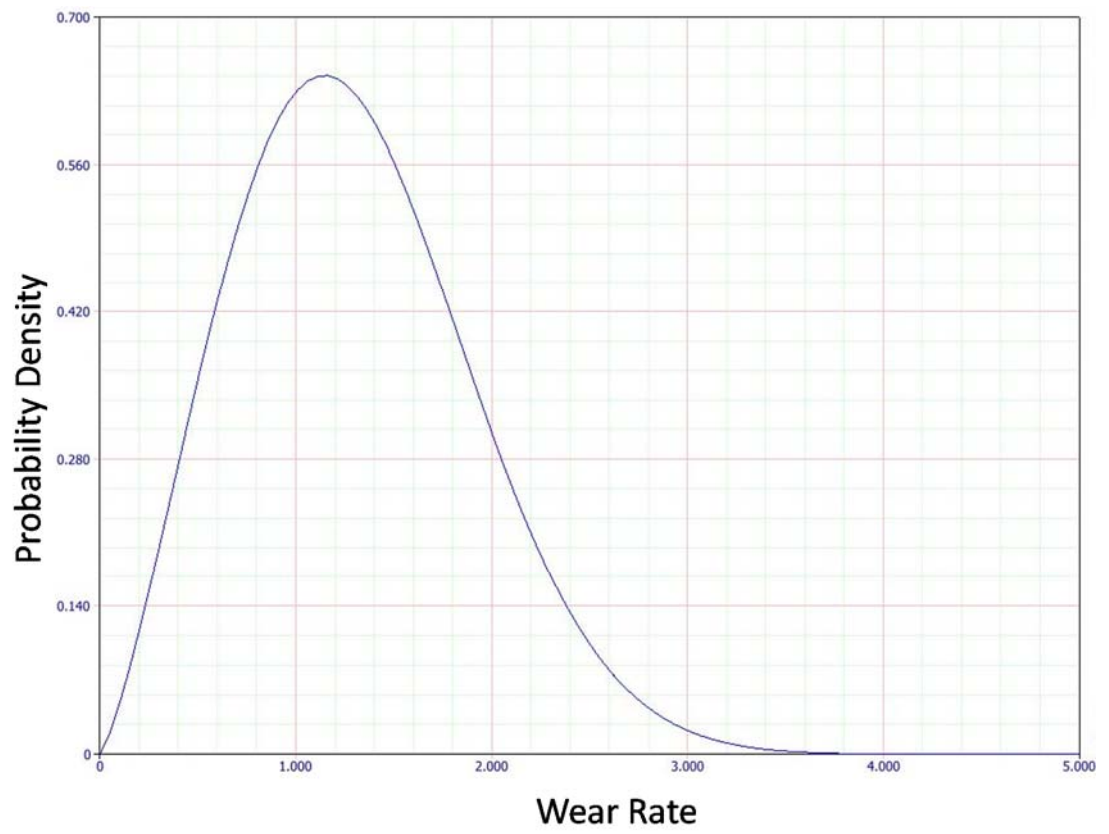


**2b) TiAlN coated WC/Co tool nose radius zone (region 2):**

Distribution fit plot:

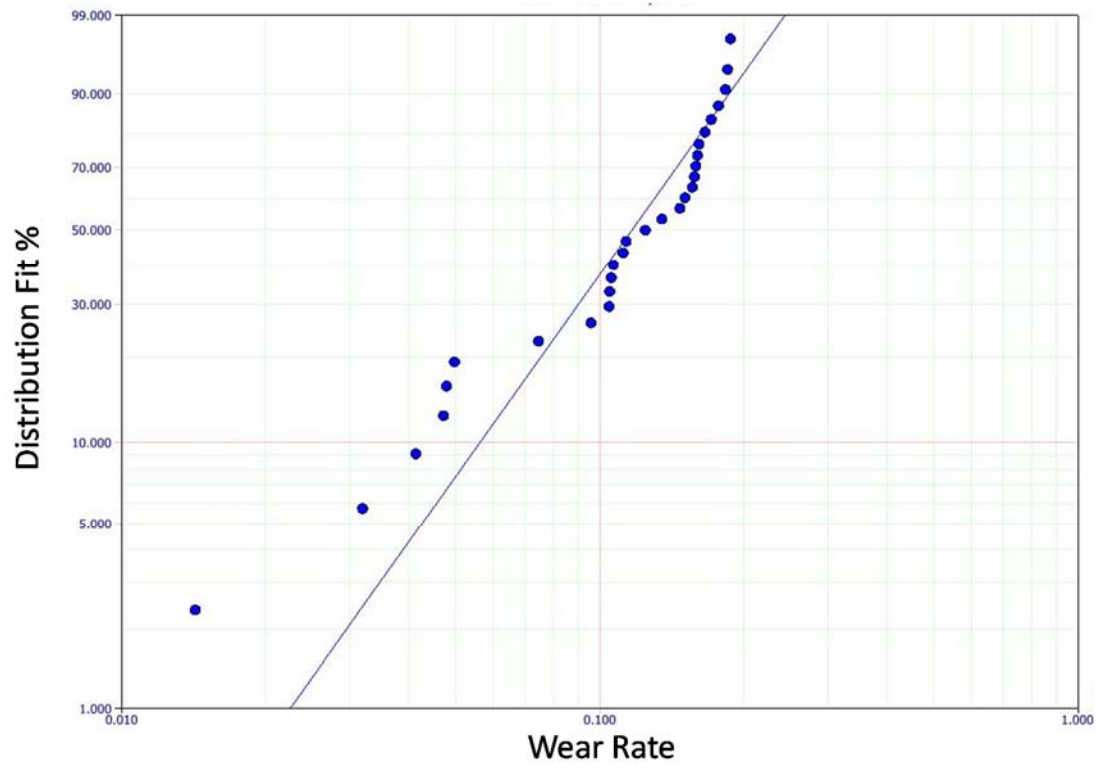


Probability Density Function plot:

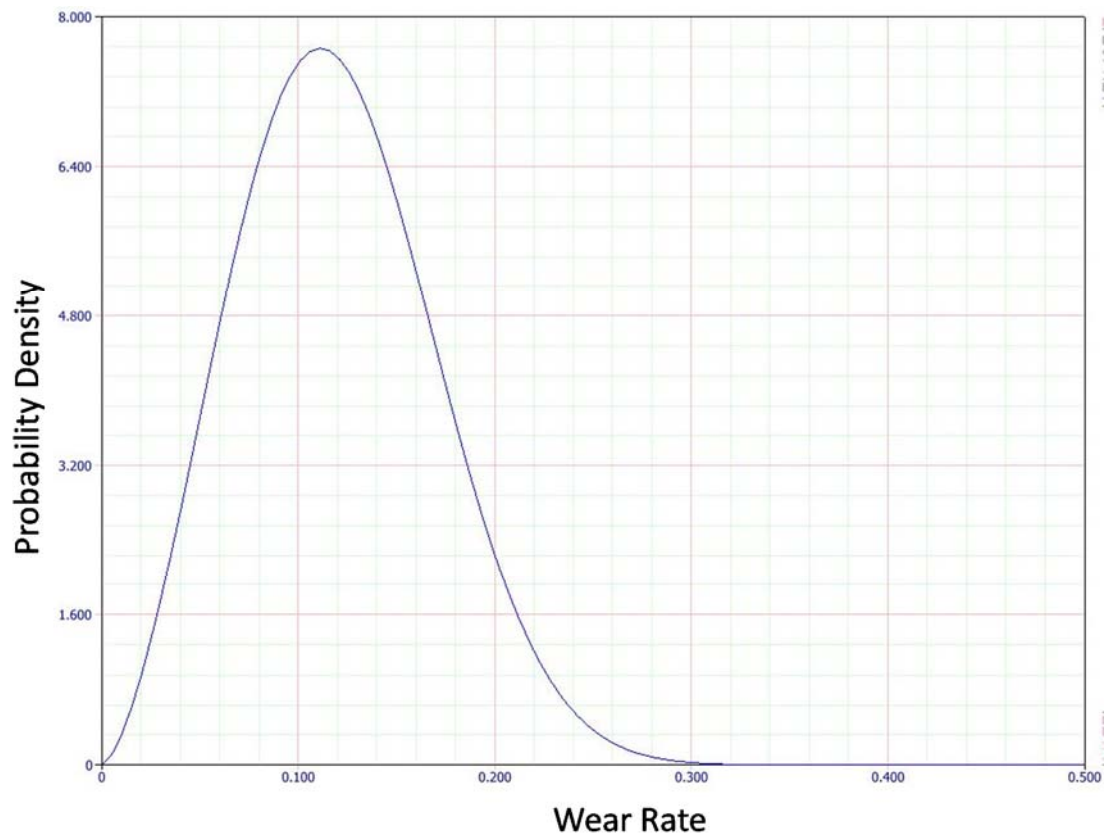


**2c) TiAlN coated WC/Co tool cutting edge zone (region 3):**

Distribution fit plot:

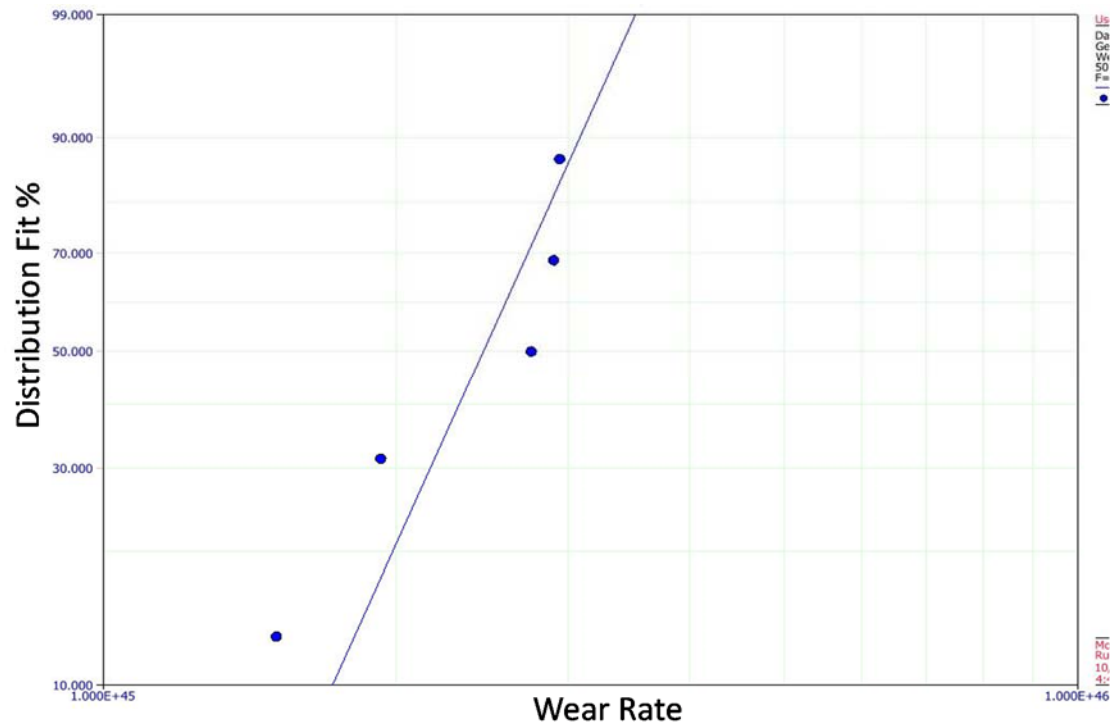


Probability Density Function plot:

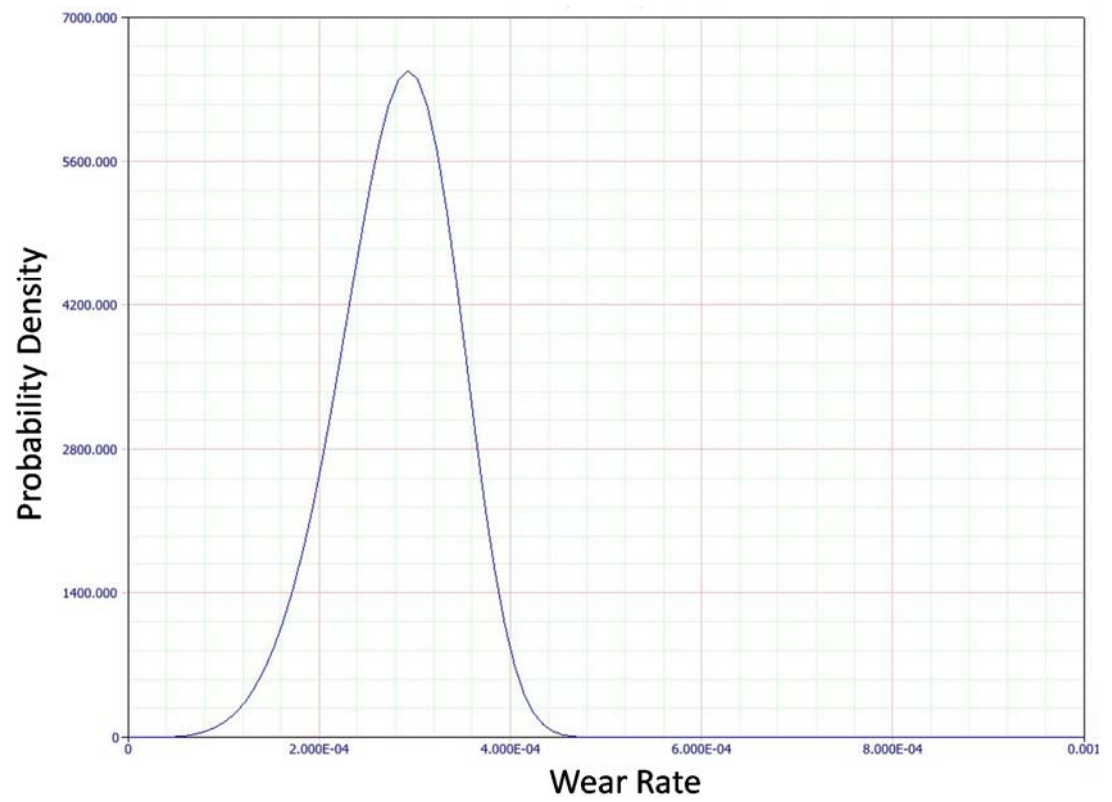


**3a) cBN coated WC/Co tool tip trailing zone (region 1):**

Distribution fit plot:

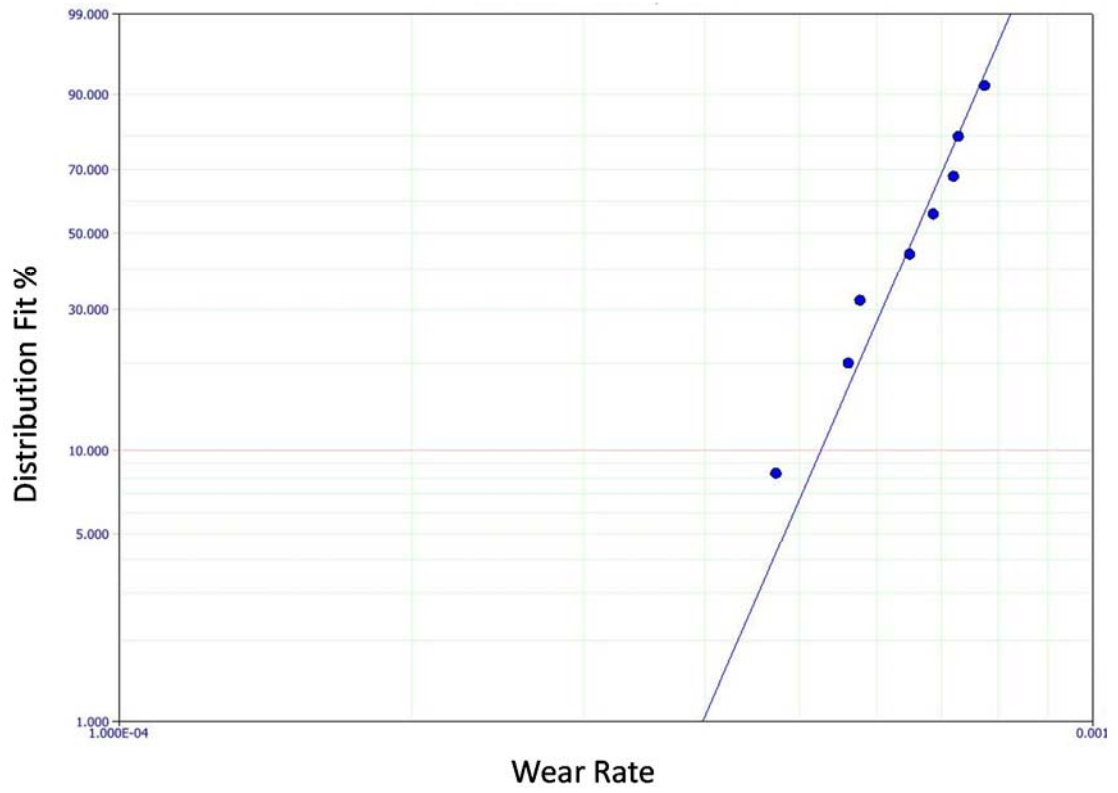


Probability Density Function plot:

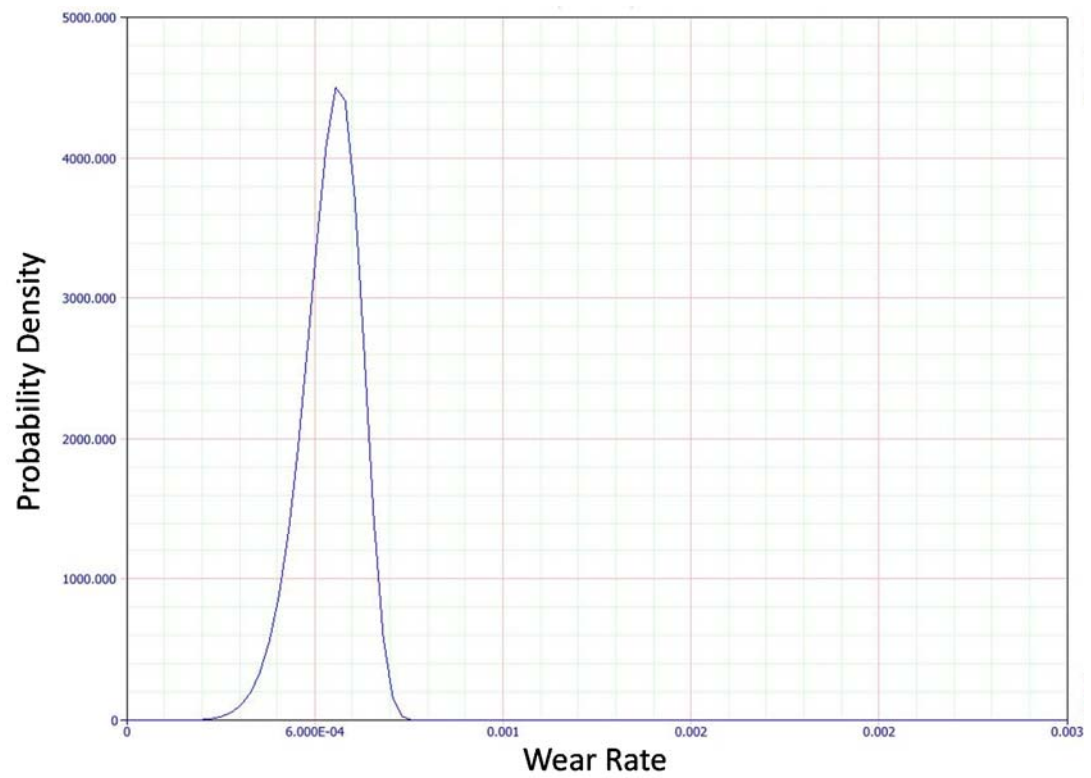


**3b) cBN coated WC/Co tool nose radius zone (region 2):**

Distribution fit plot:

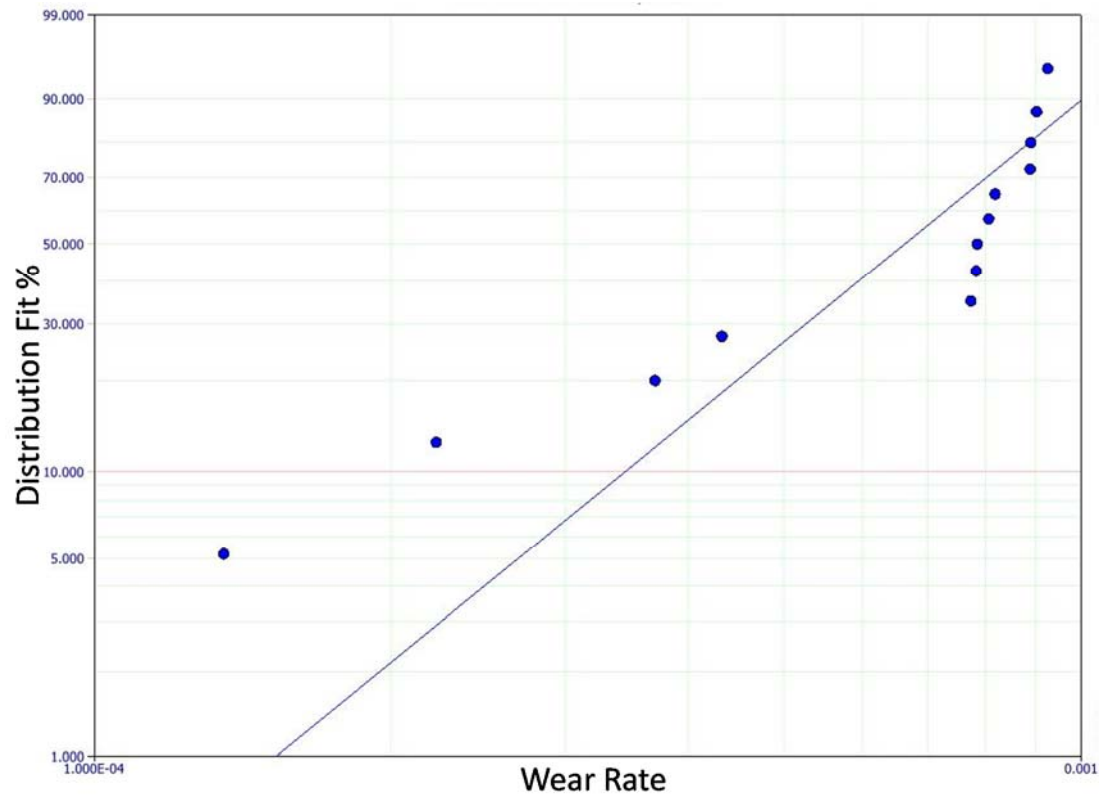


Probability Density Function plot:

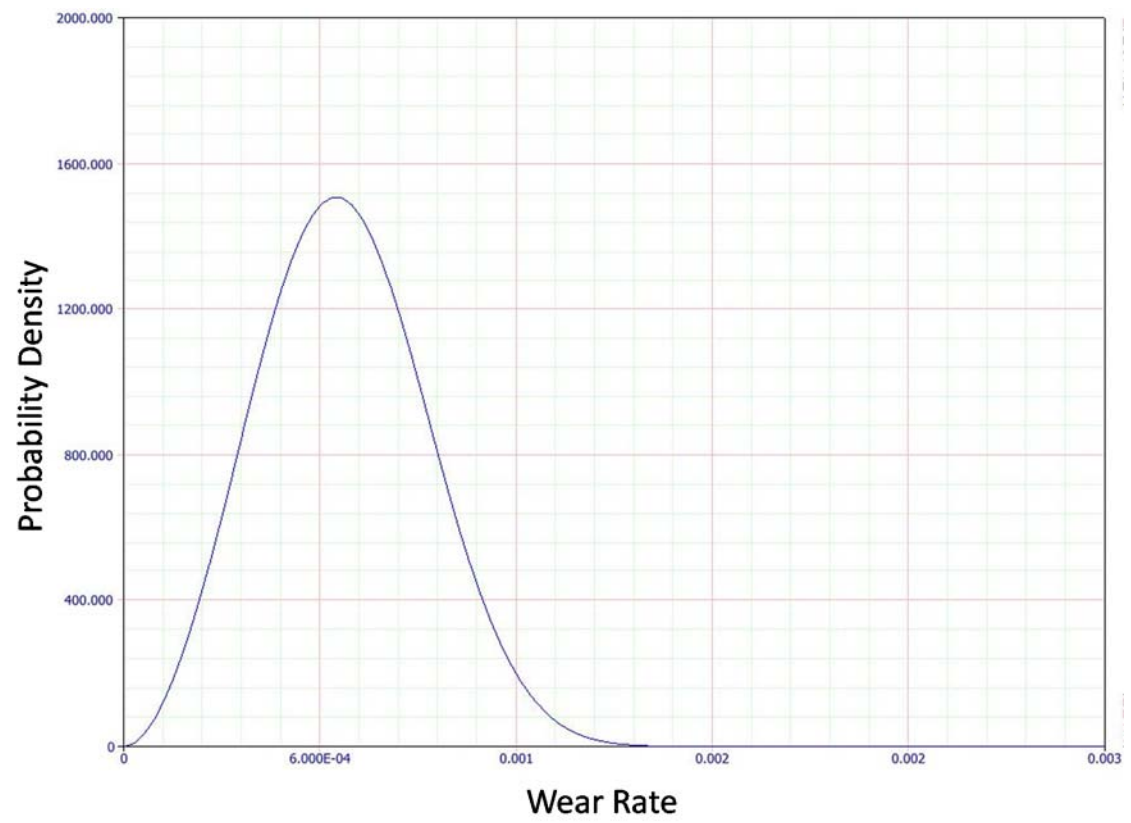


**3c) cBN coated WC/Co tool cutting edge zone (region 3):**

Distribution fit plot:

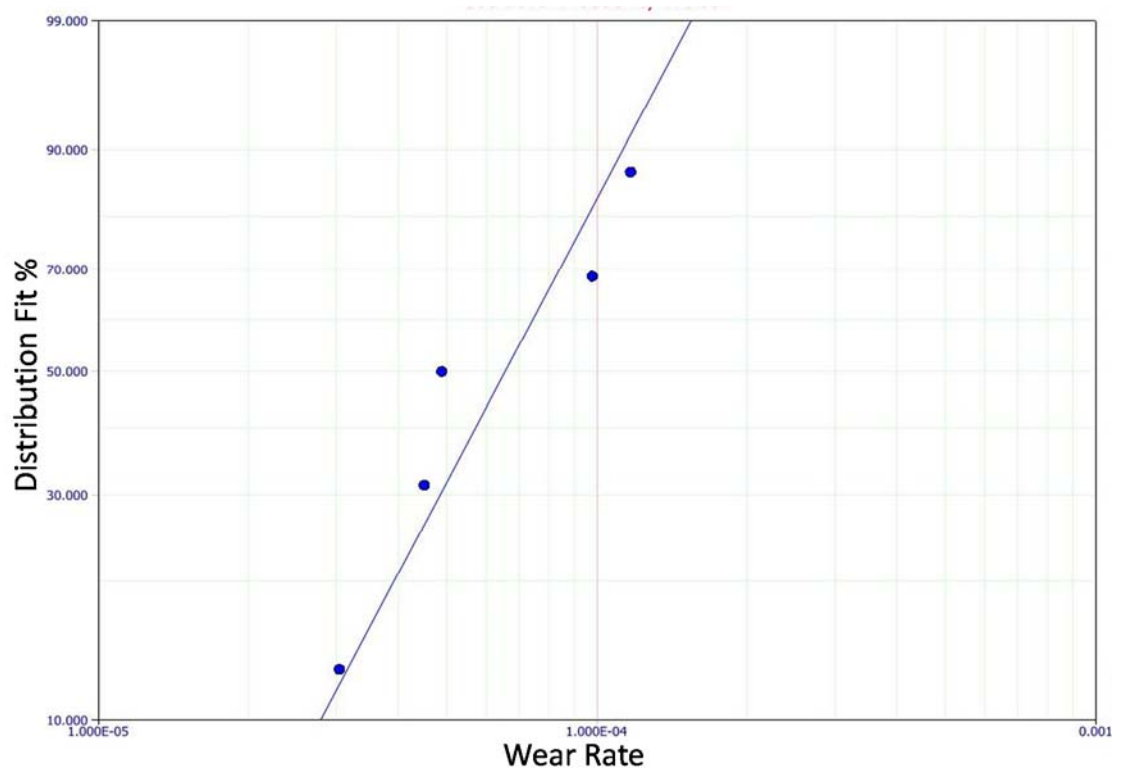


Probability Density Function plot:

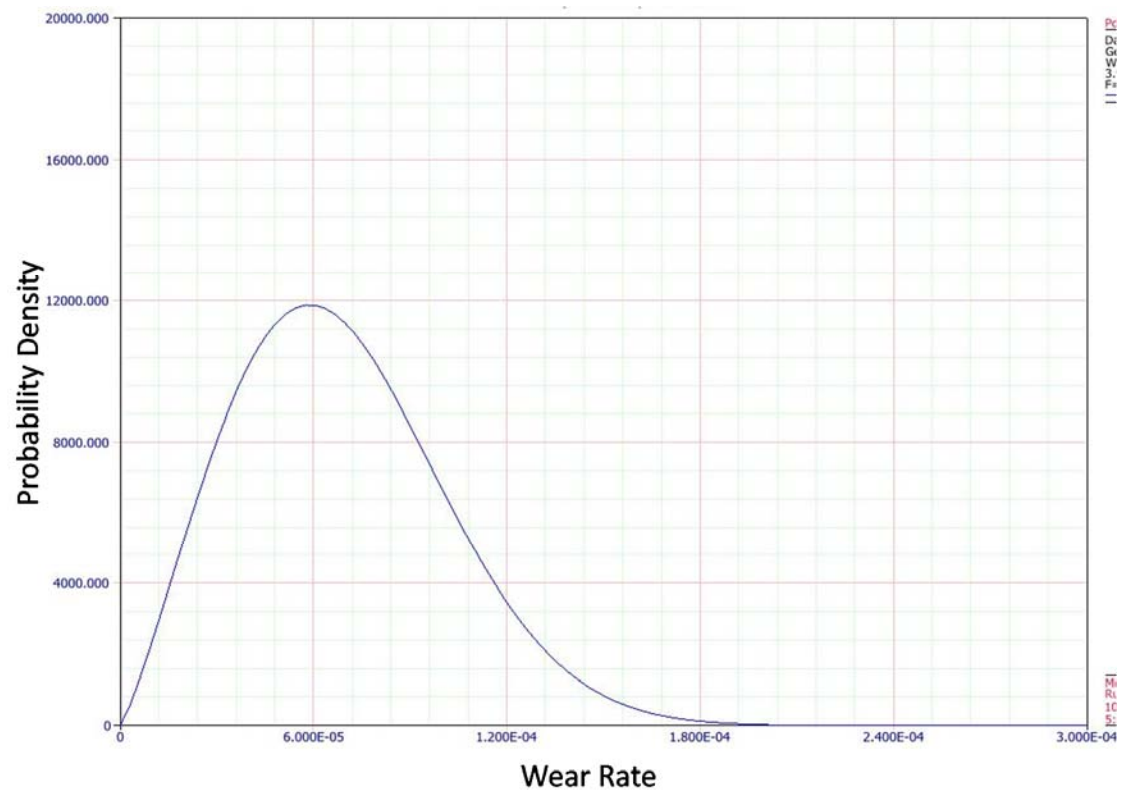


**4a) multi-layered coated WC/Co tool tip trailing zone (region 1):**

Distribution fit plot:

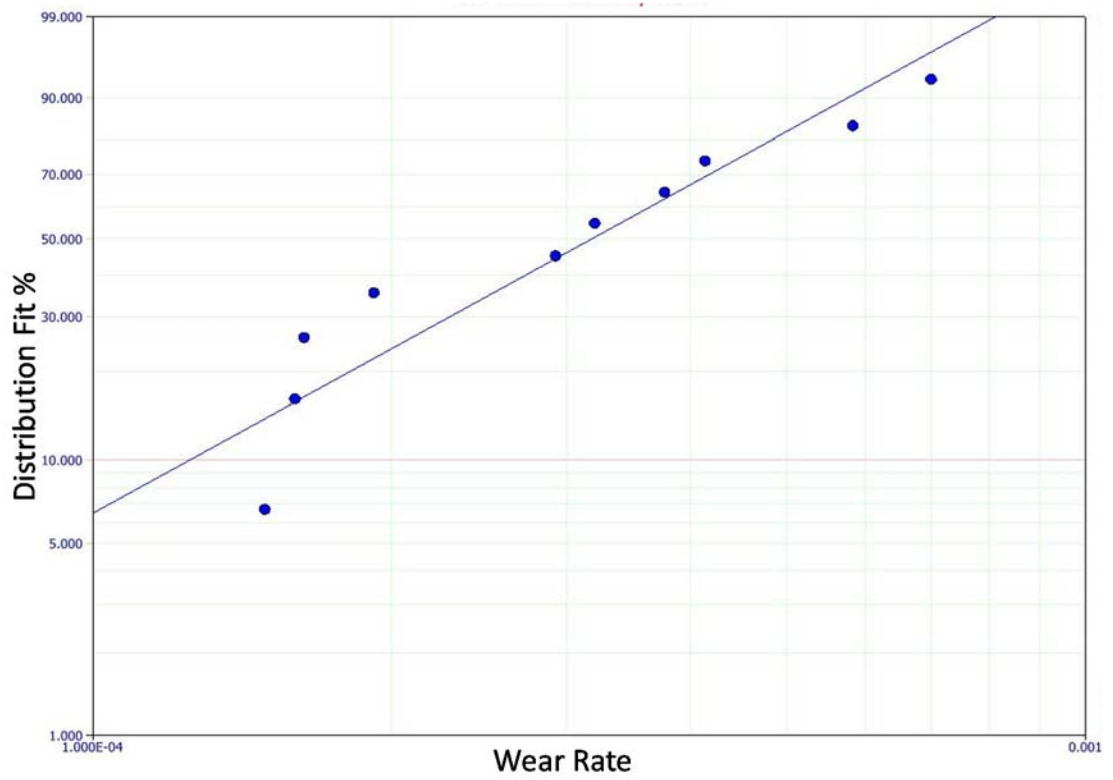


Probability Density Function plot:

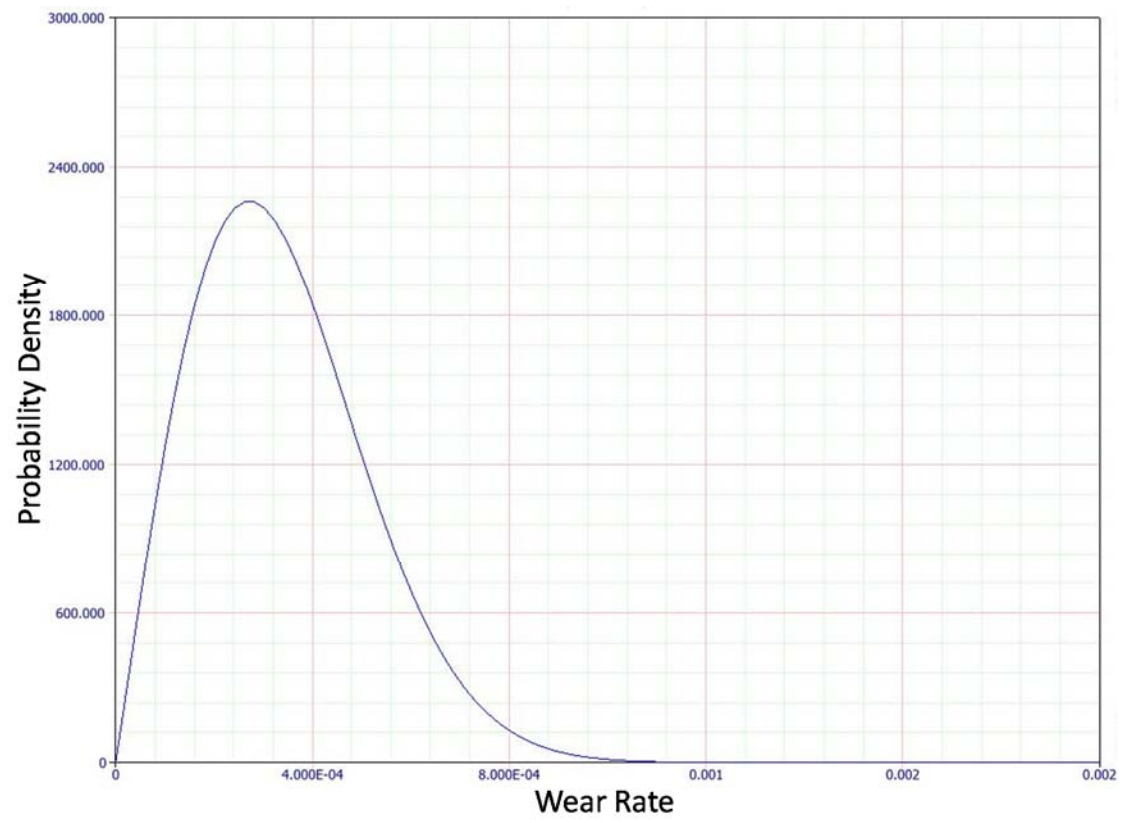


**4b) multi-layered coated WC/Co tool nose radius zone (region 2):**

Distribution fit plot:

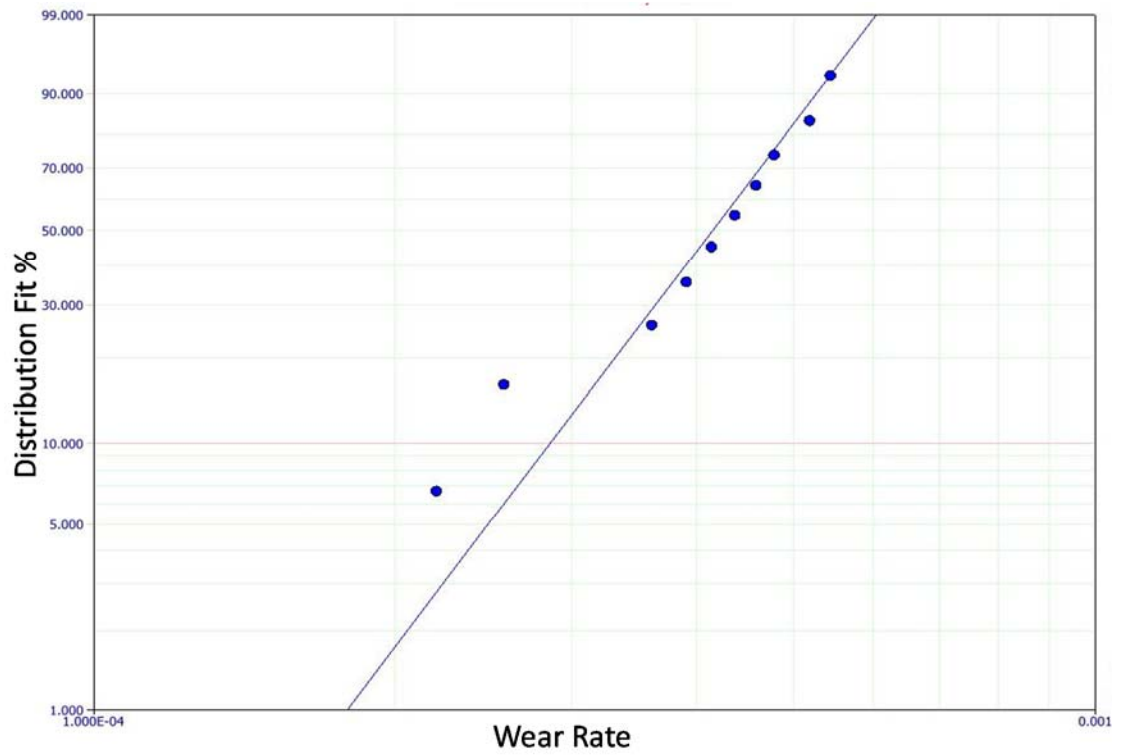


Probability Density Function plot:

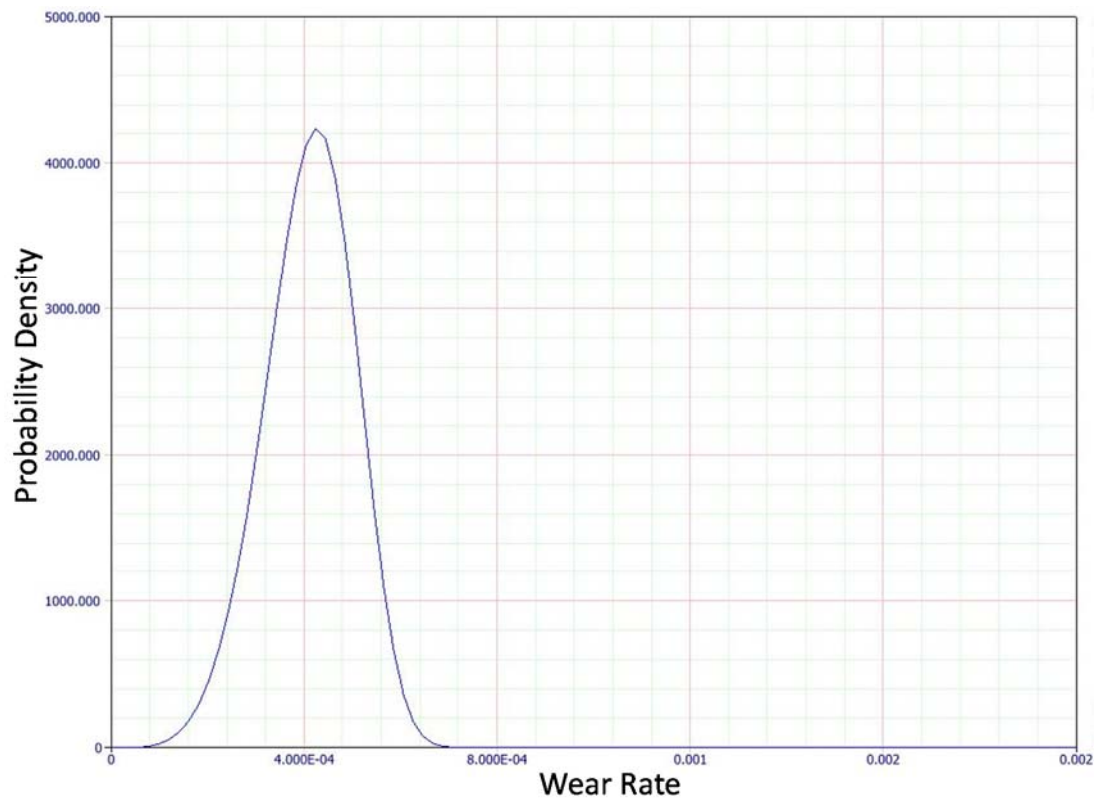


**4c) multi-layered coated WC/Co tool cutting edge zone (region 3):**

Distribution fit plot:



Probability Density Function plot:

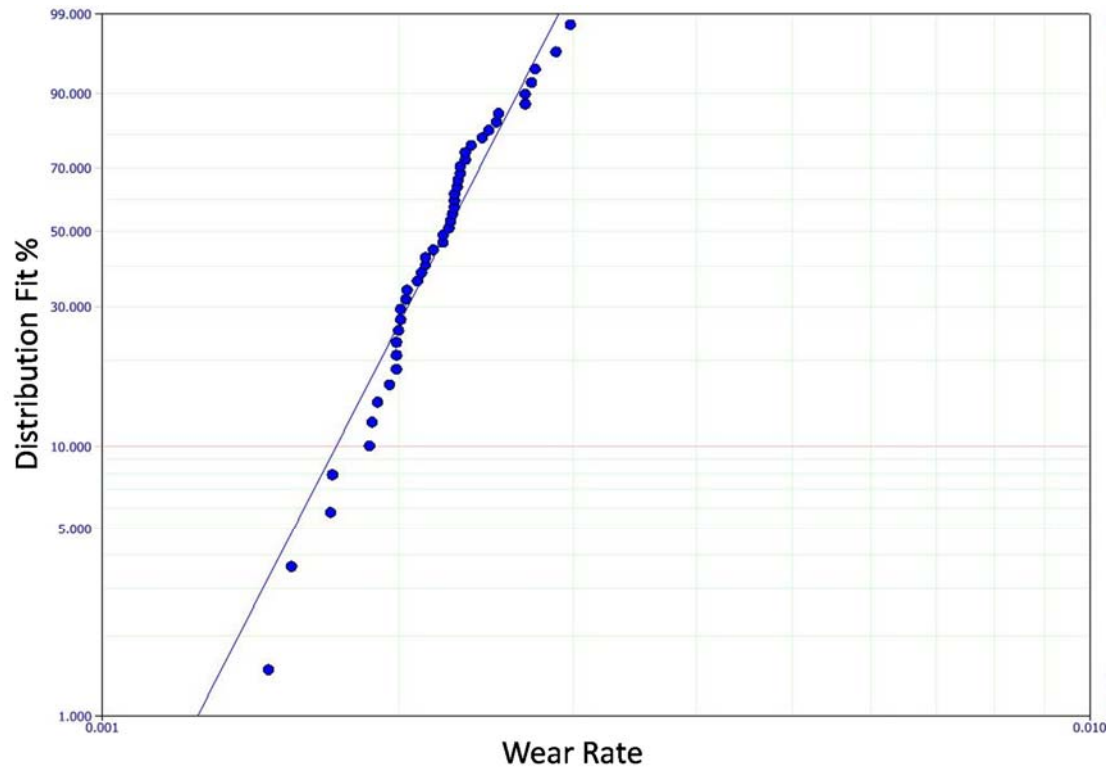


## Appendix 2

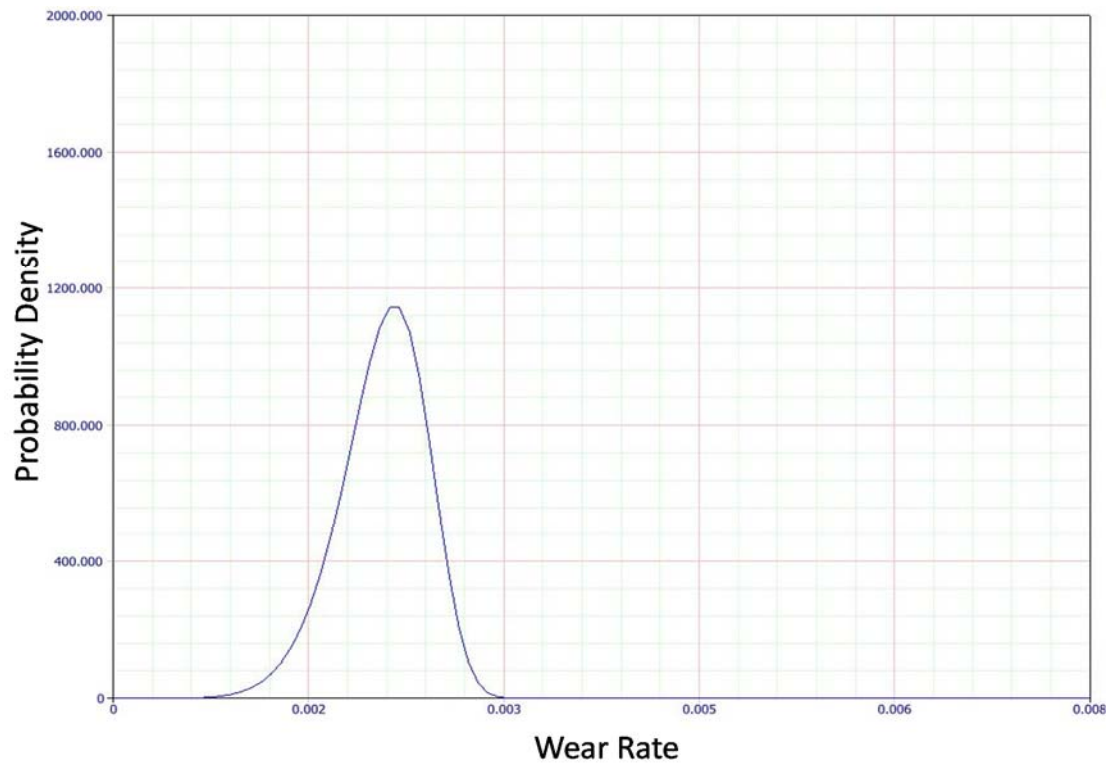
Distribution fits and probability density functions to the physics-based FE simulation data for wear rate of cutting tools at different wear regions.

### 1a) Uncoated WC/Co tool tip trailing zone (Region 1):

Distribution fit plot:

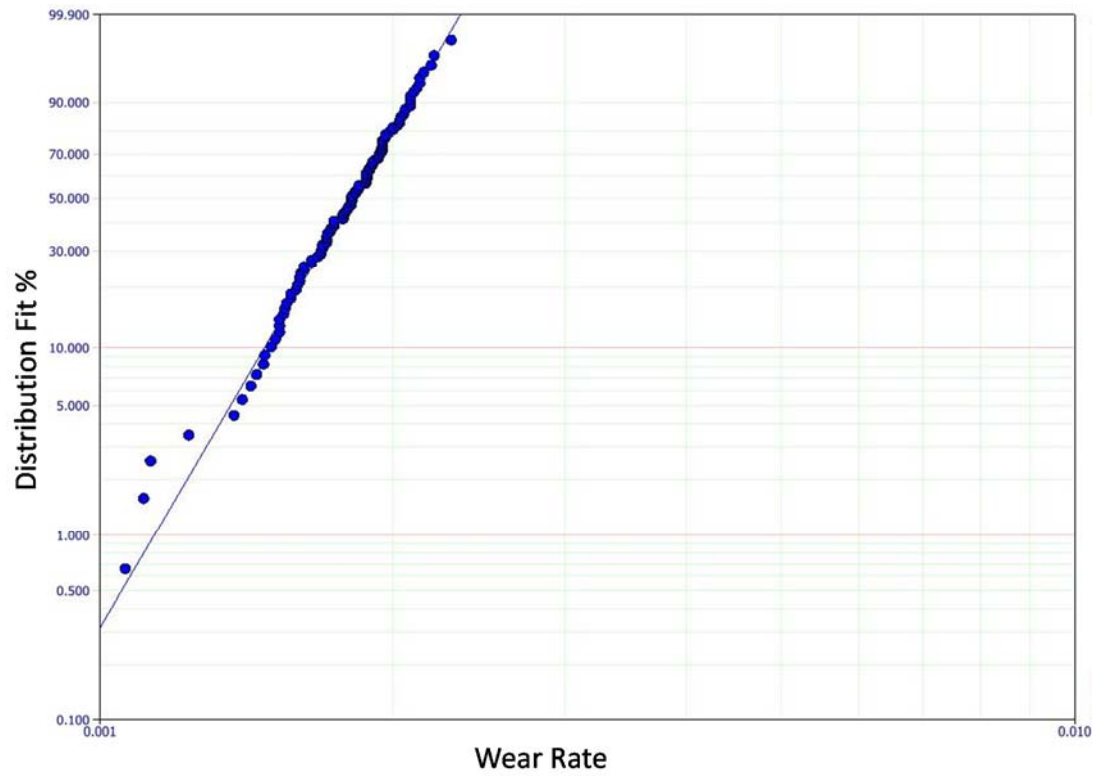


Probability Density Function plot:

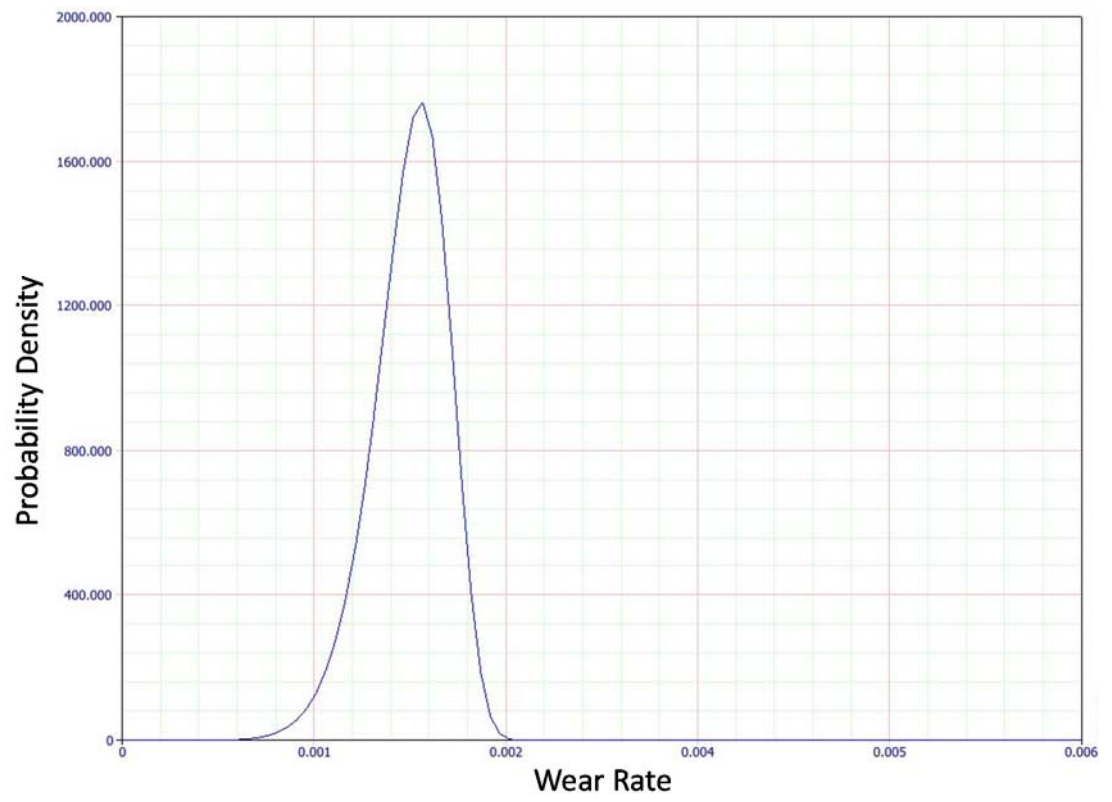


**1b) Uncoated WC/Co tool nose radius zone (region 2):**

Distribution fit plot:

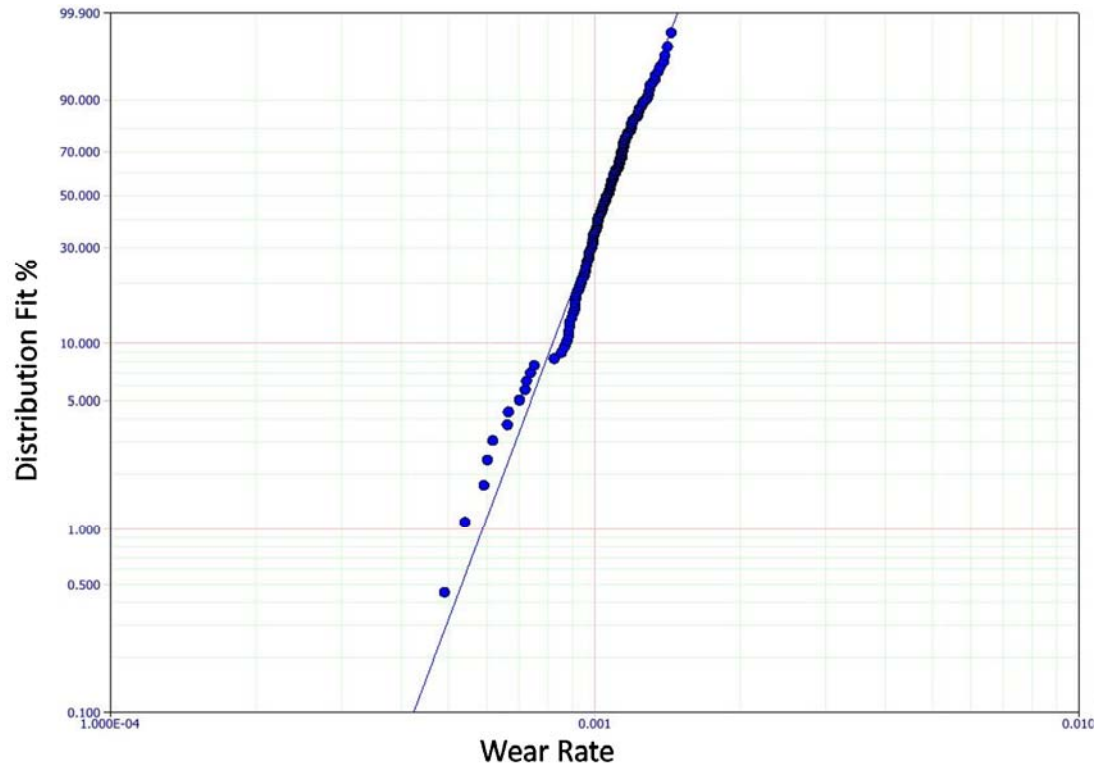


Probability Density Function plot:

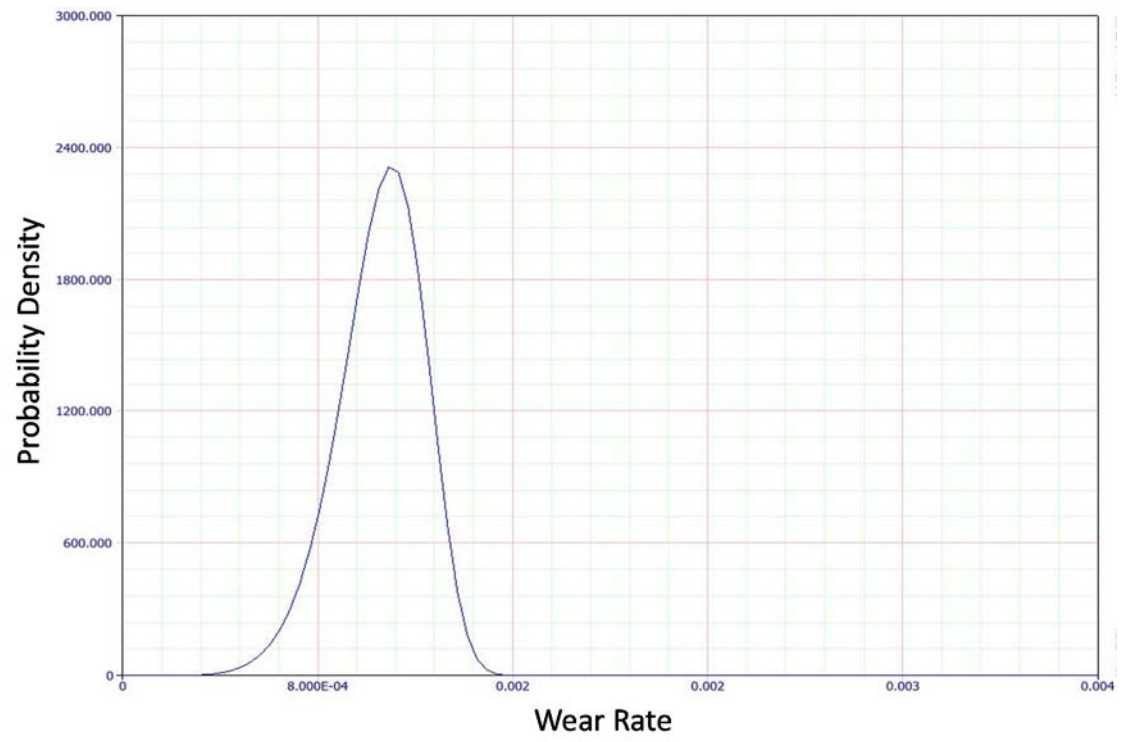


**1c) Uncoated WC/Co tool cutting edge zone (region 3):**

Distribution fit plot:

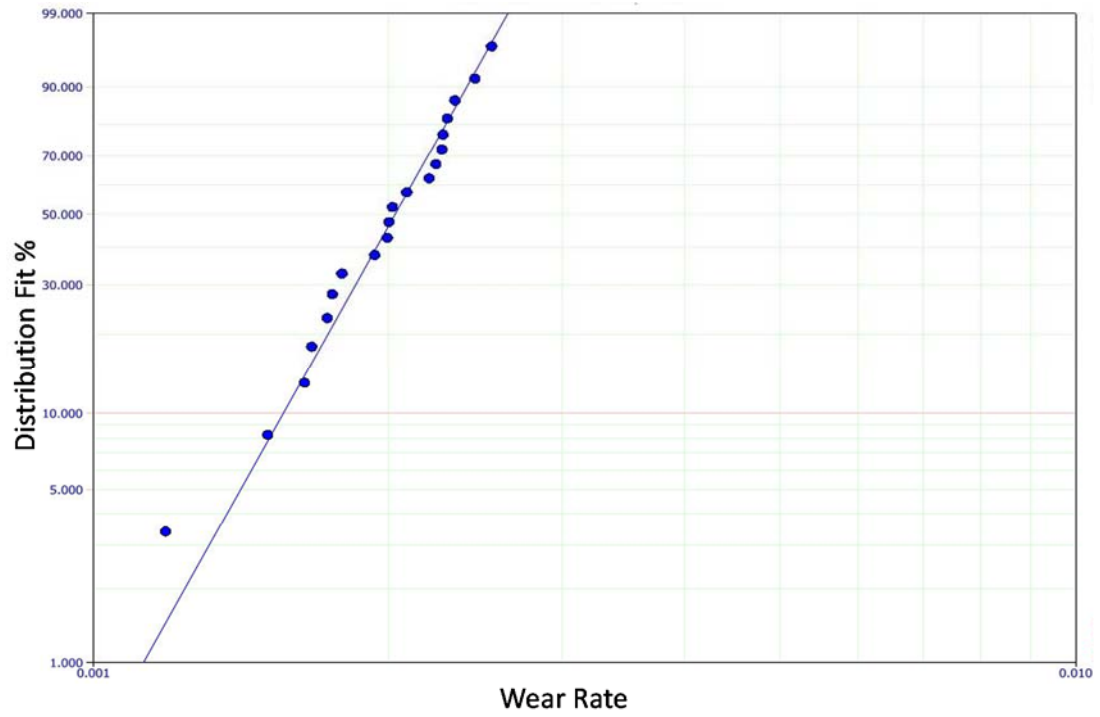


Probability Density Function plot:

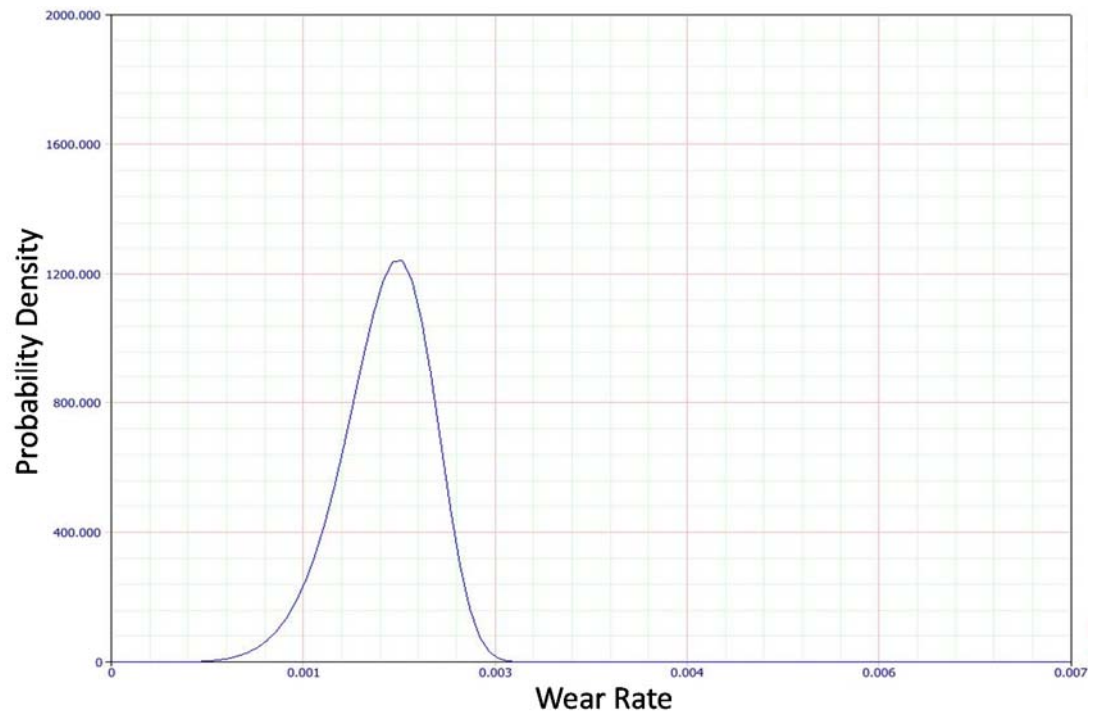


**2a) TiAlN coated WC/Co tool tip trailing zone (region 1):**

Distribution fit plot:

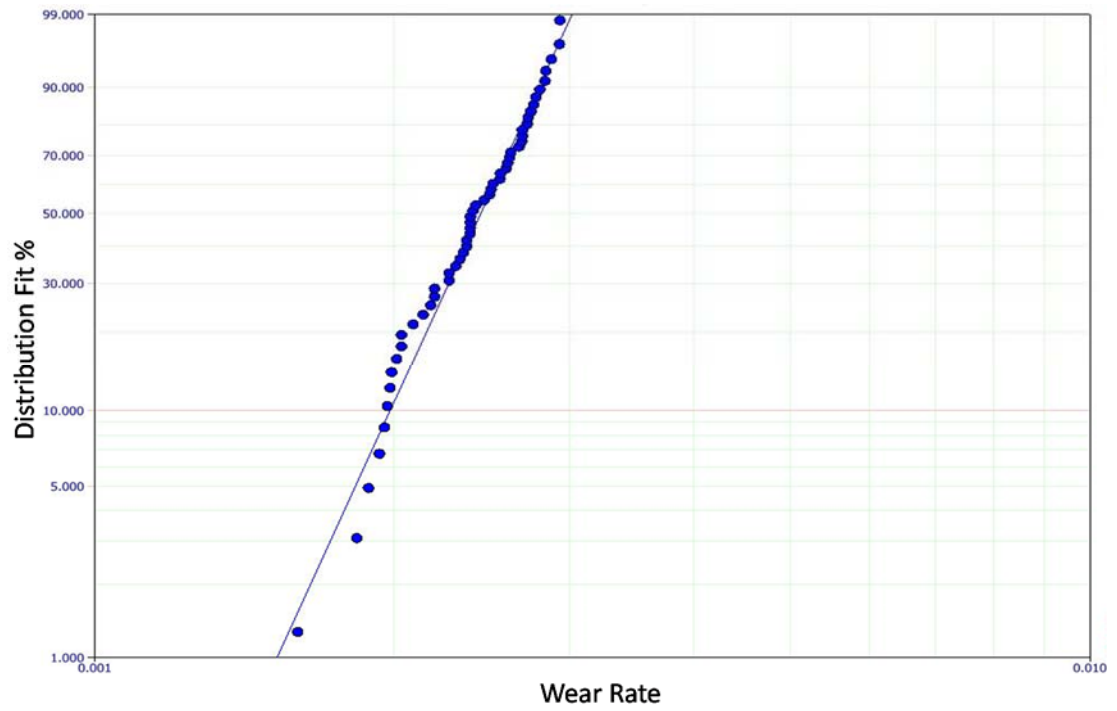


Probability Density Function plot:

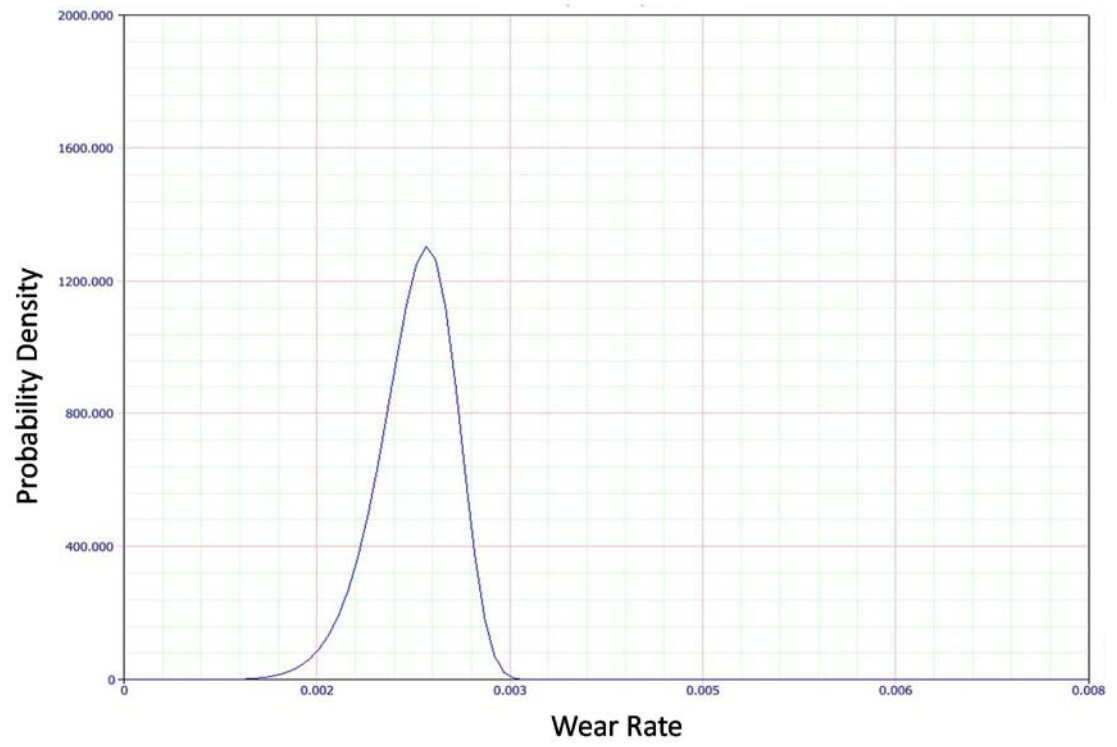


**2b) TiAlN coated WC/Co tool nose radius zone (region 2):**

Distribution fit plot:

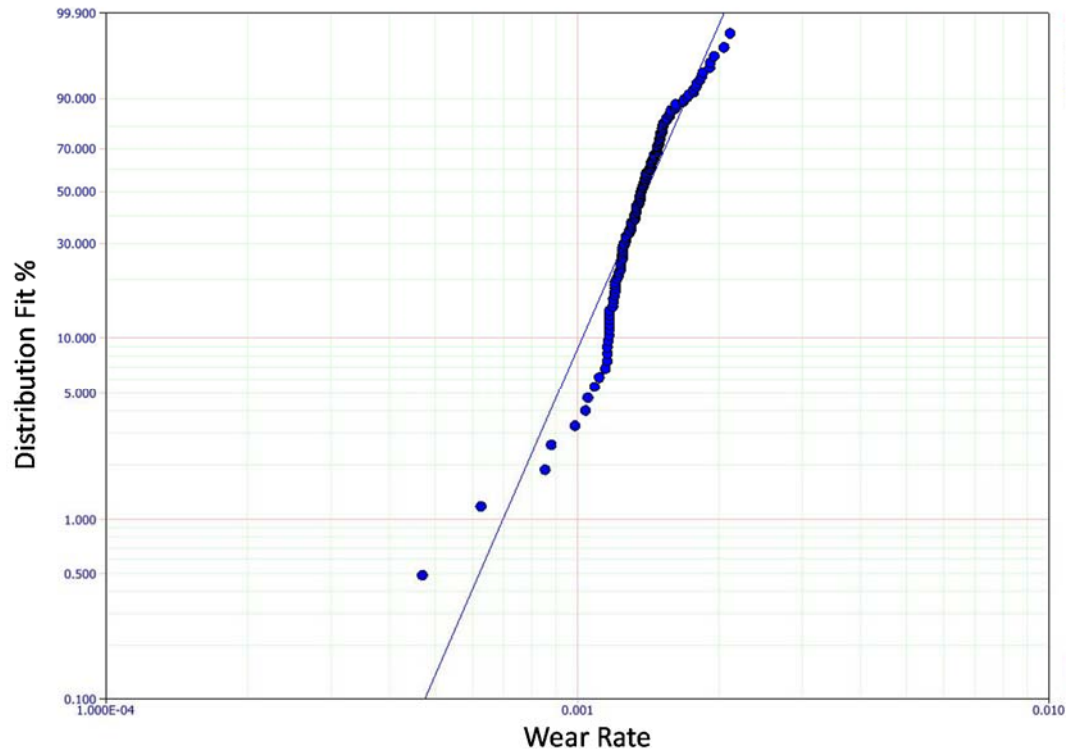


Probability Density Function plot:

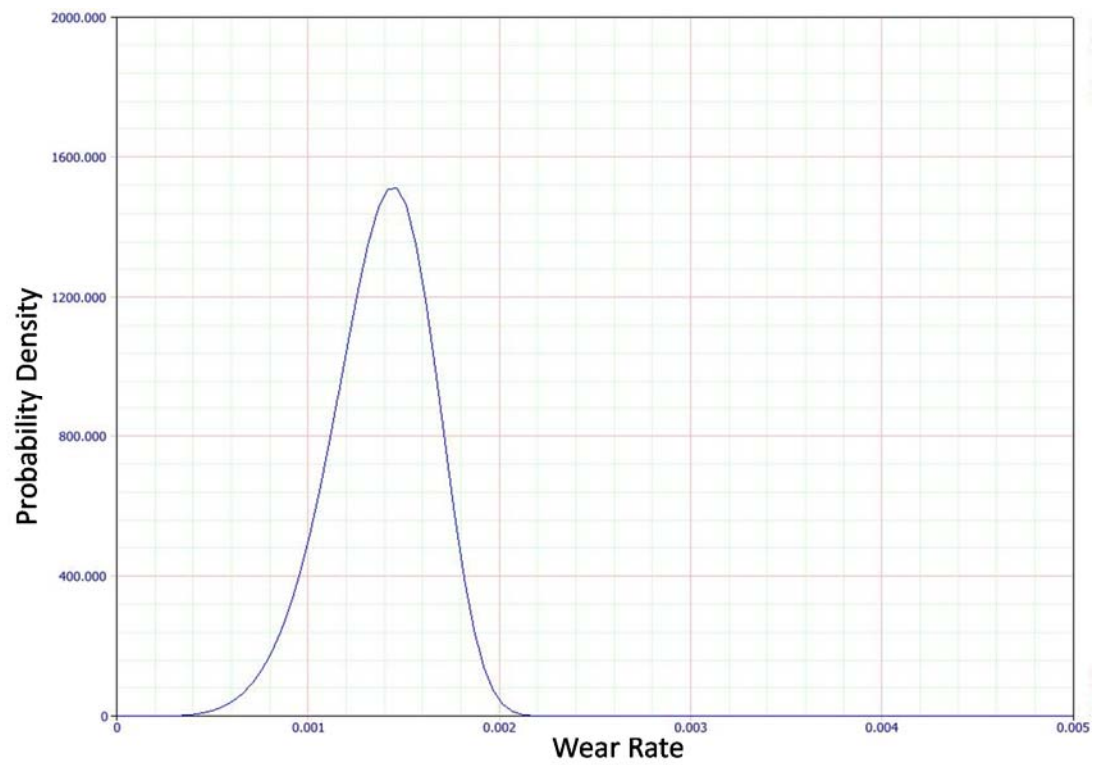


**2c) TiAlN coated WC/Co tool cutting edge zone (region 3):**

Distribution fit plot:

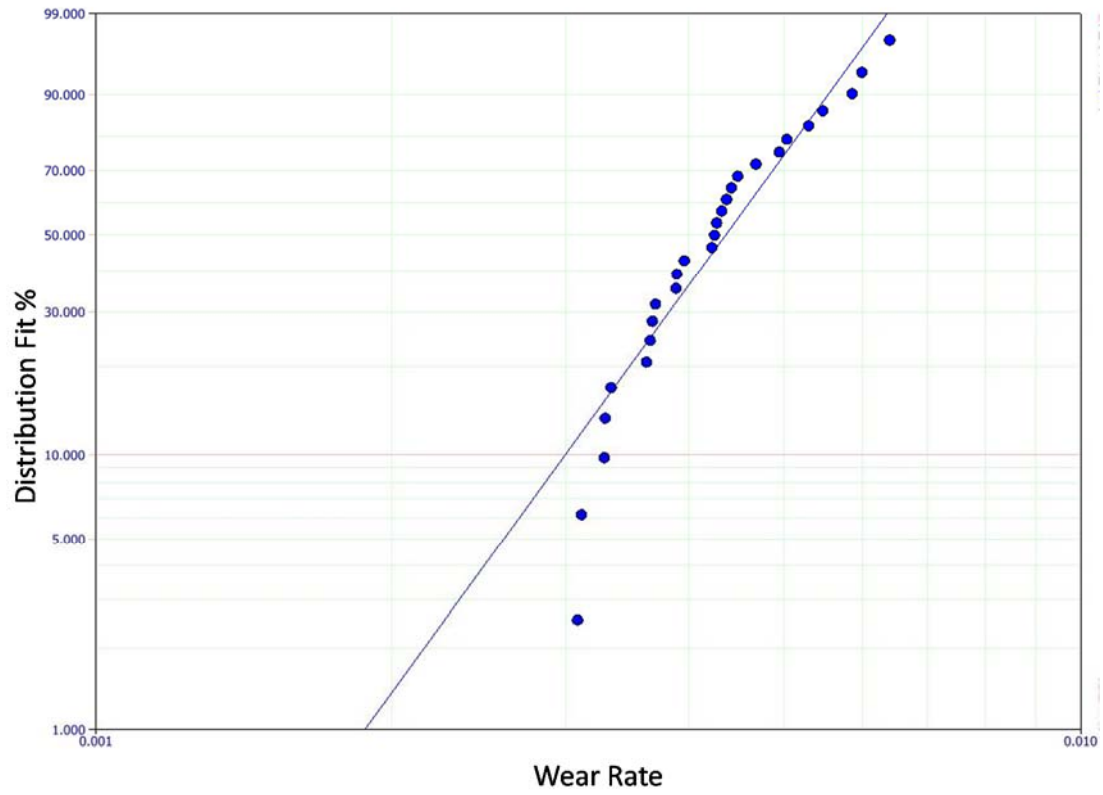


Probability Density Function plot:

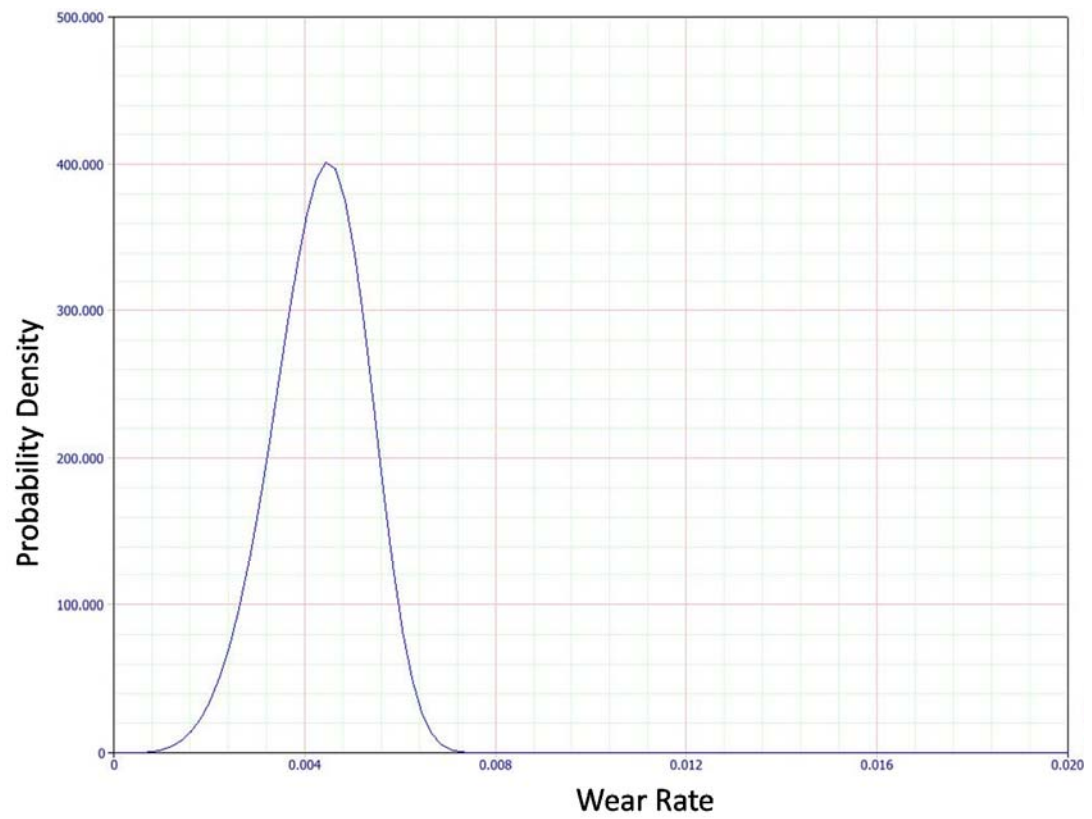


**3a) cBN coated WC/Co tool tip trailing zone (region 1):**

Distribution fit plot:

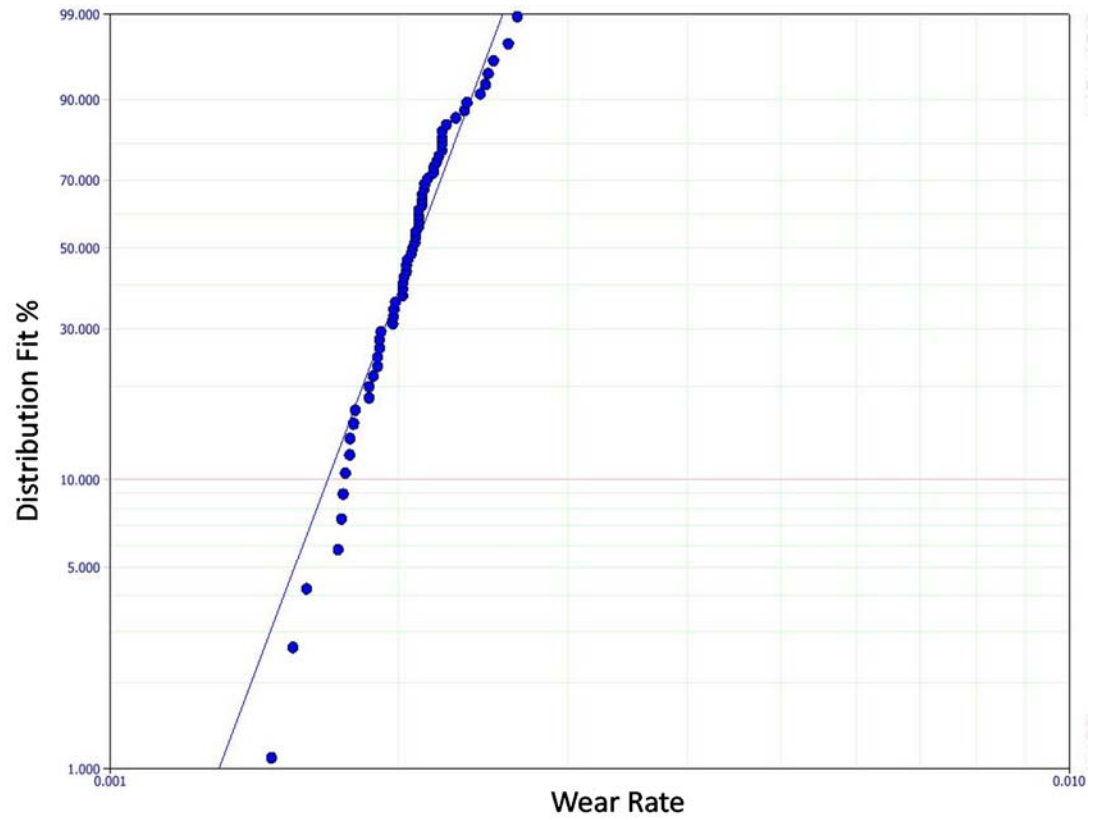


Probability Density Function plot:

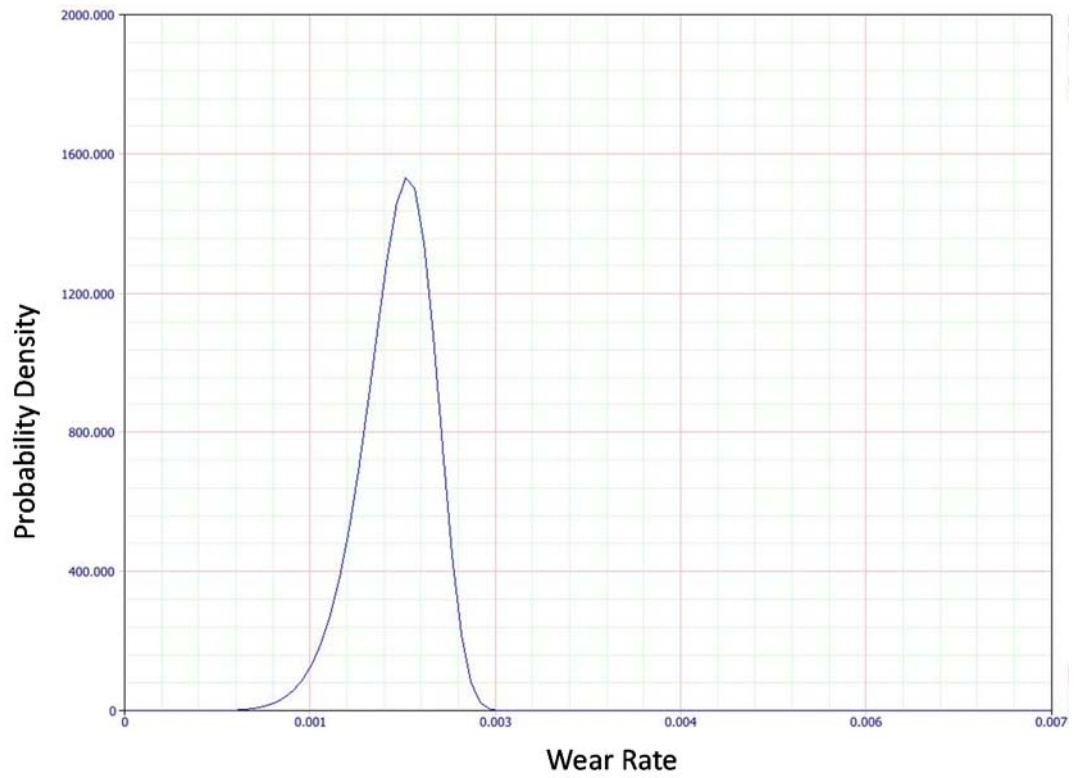


**3b) cBN coated WC/Co tool nose radius zone (region 2):**

Distribution fit plot:

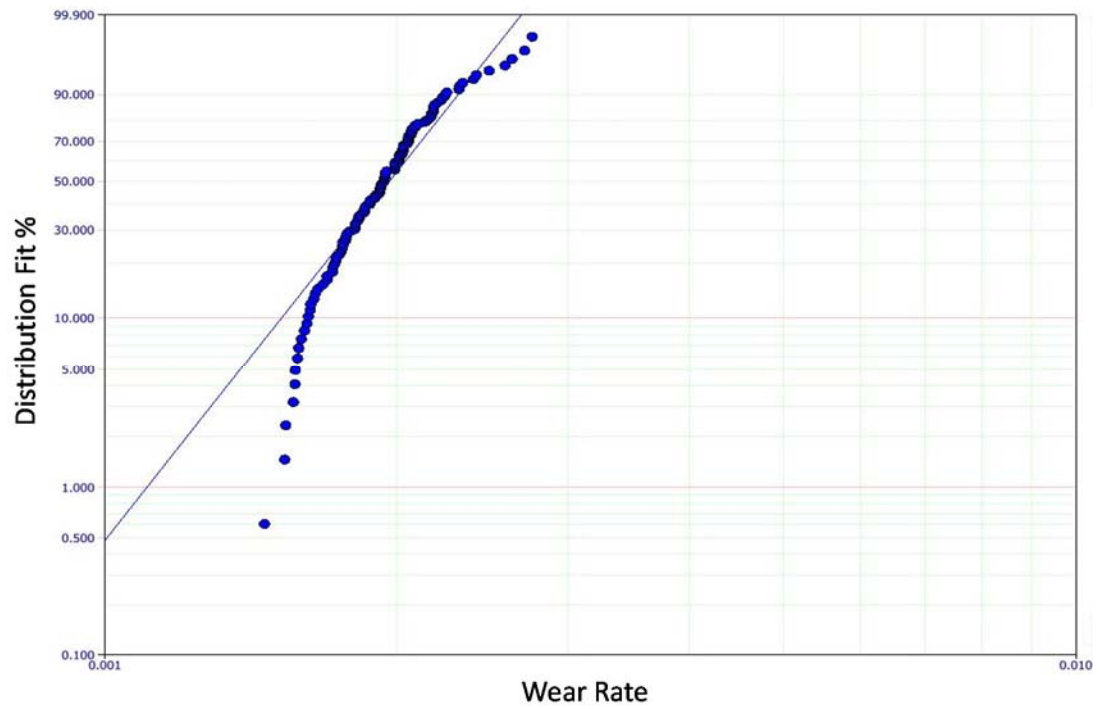


Probability Density Function plot:

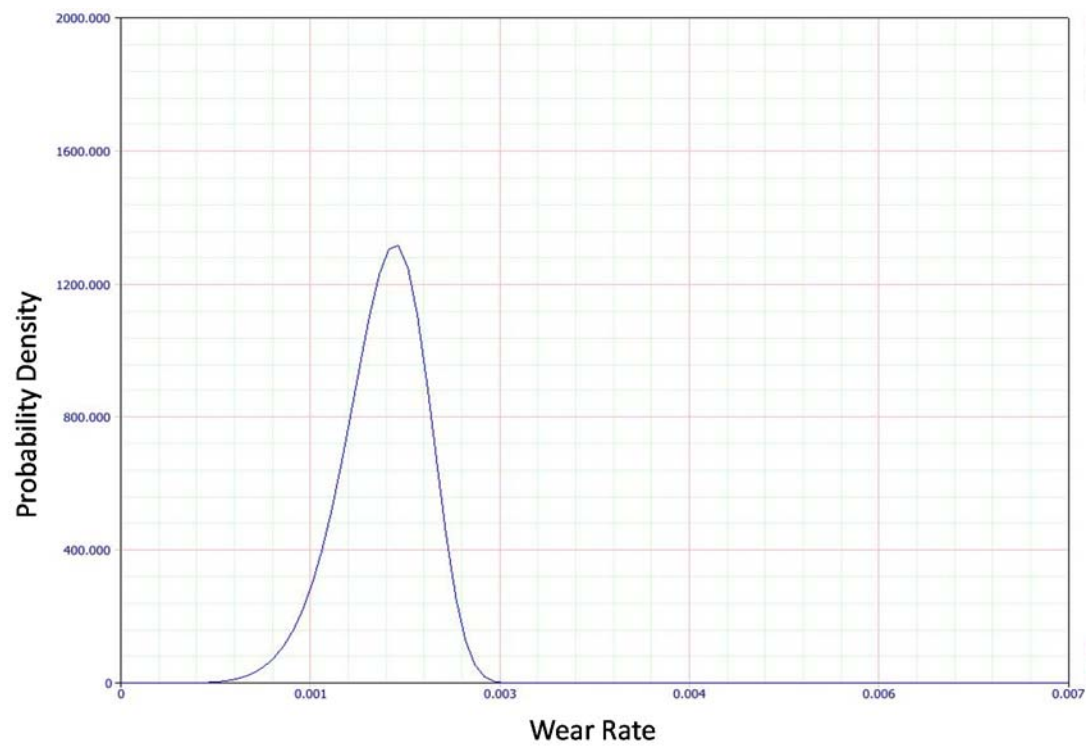


**3c) cBN coated WC/Co tool cutting edge zone (region 3):**

Distribution fit plot:

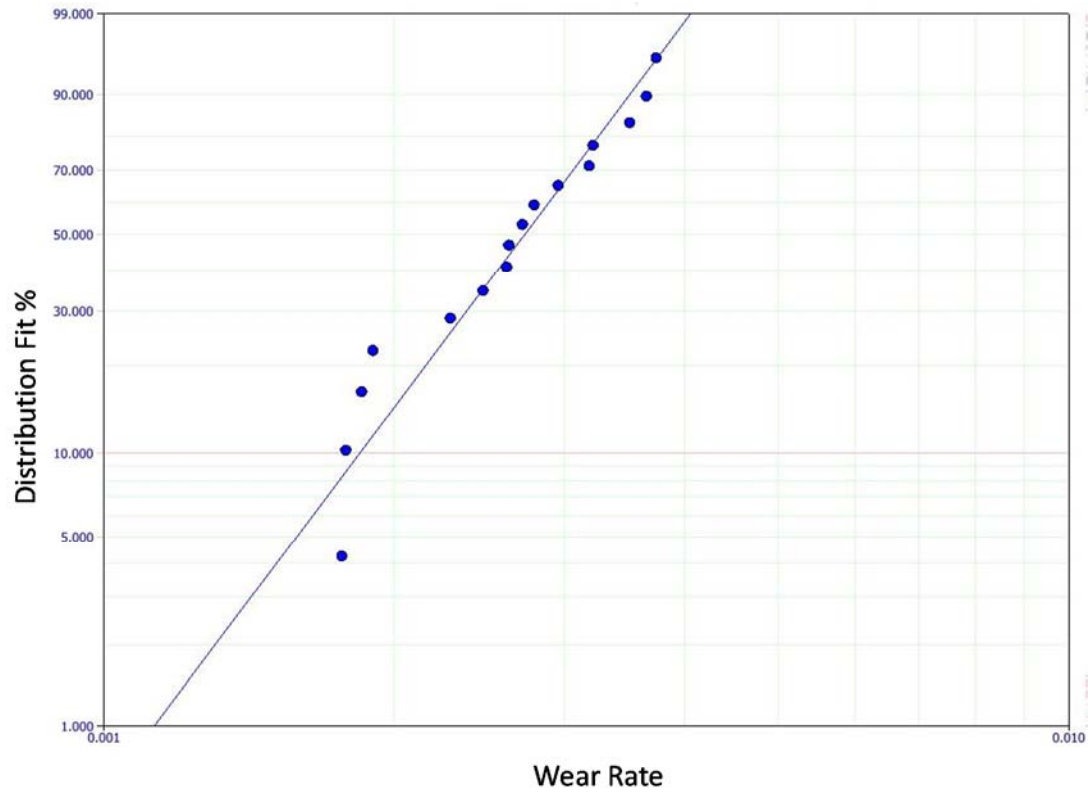


Probability Density Function plot:

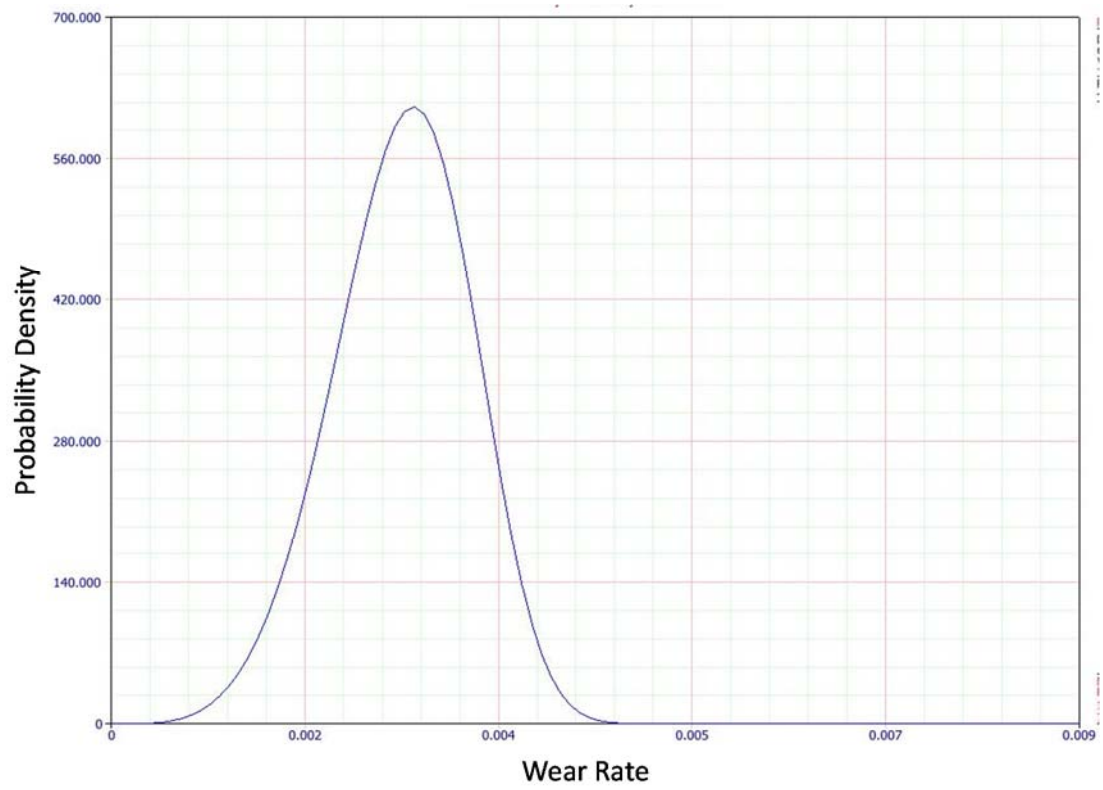


**4a) multi-layered coated WC/Co tool tip trailing zone (region 1):**

Distribution fit plot:

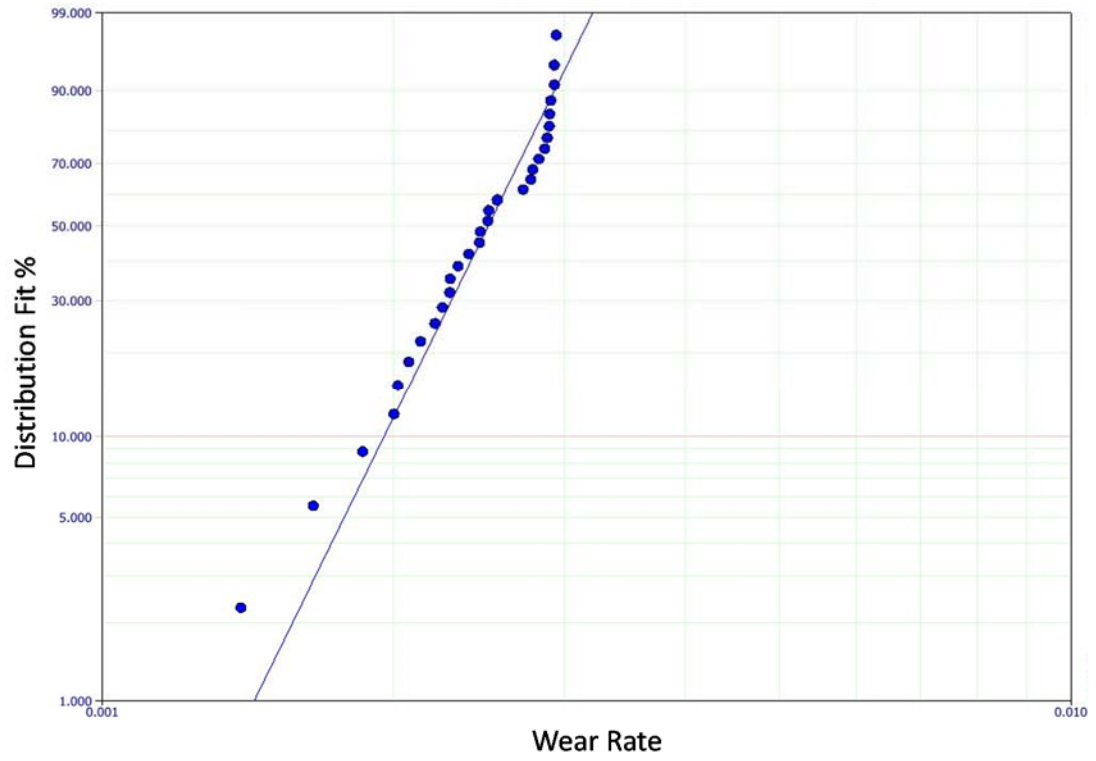


Probability Density Function plot:

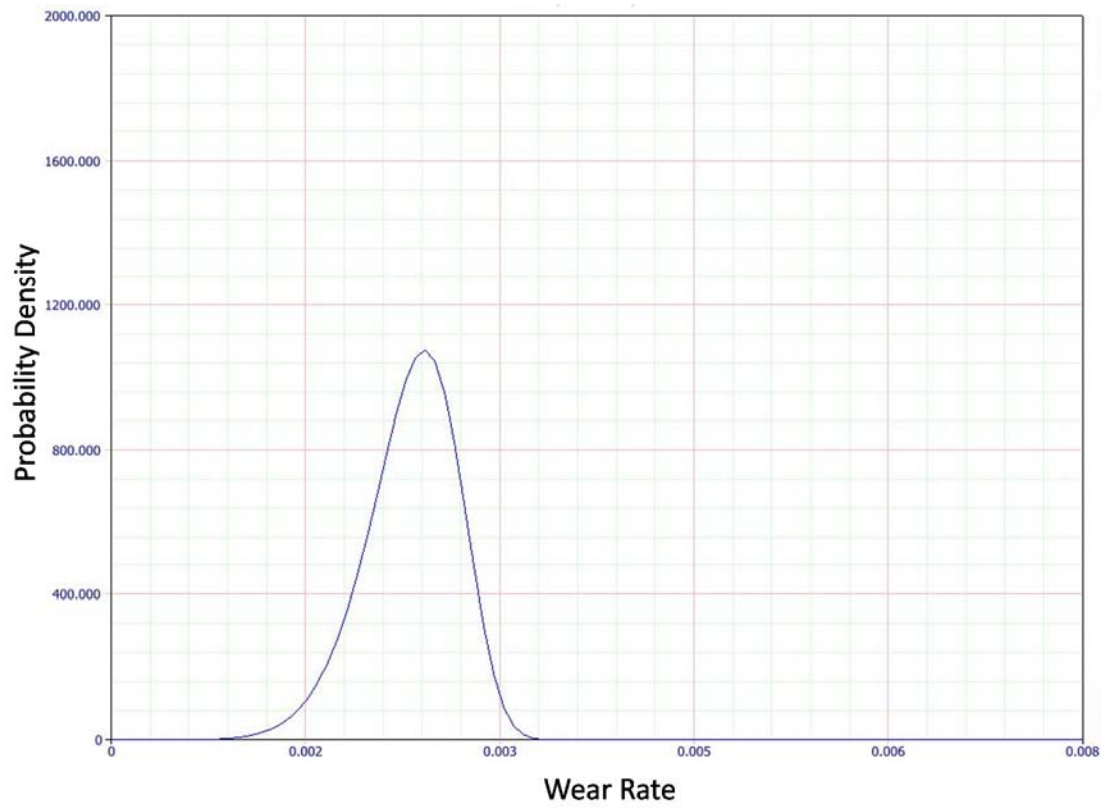


**4b) multi-layered coated WC/Co tool nose radius zone (region 2):**

Distribution fit plot:

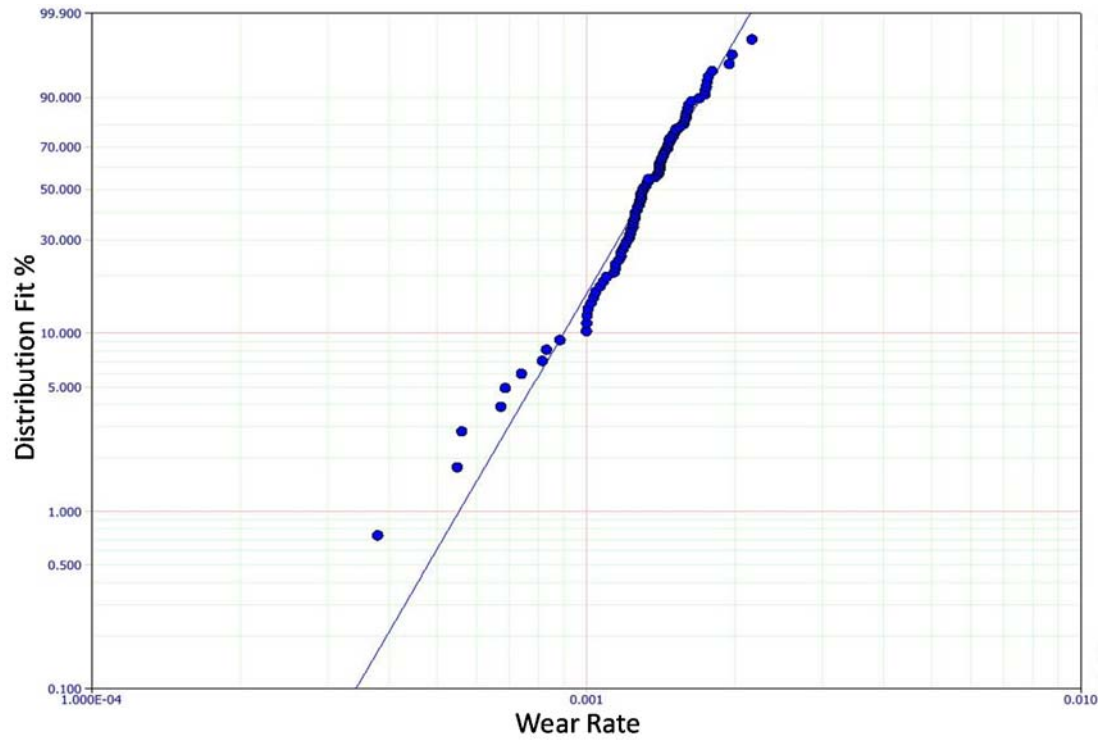


Probability Density Function plot:

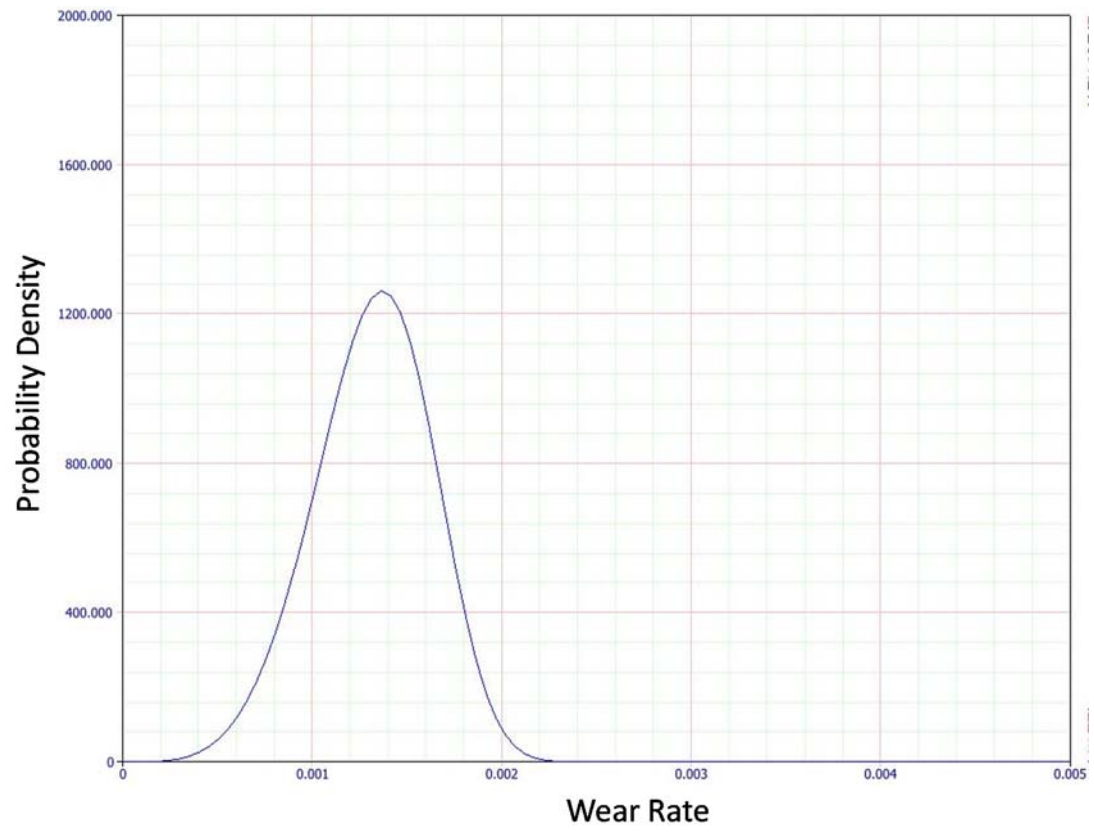


**4c) multi-layered coated WC/Co tool cutting edge zone (region 3):**

Distribution fit plot:



Probability Density Function plot:



### Appendix 3

#### Complete list of optimal solutions for multi-objective optimization using NSGA-II

Solution #	$V_c$ (m/min)	$f$ (mm/rev)	X	Reliability	MRR
1	25	0.101697519	1	0.938878872	5.084875938
2	25	0.101697519	1	0.938878872	5.084875938
3	26	0.101697519	1	0.919796972	5.288270975
4	25	0.110581834	1	0.889576827	5.529091717
5	25	0.110581834	1	0.889576827	5.529091717
6	26	0.110779367	1	0.86181701	5.760527091
7	26	0.110779367	1	0.86181701	5.760527091
8	25	0.119201781	1	0.831452088	5.960089062
9	25	0.119201781	1	0.831452088	5.960089062
10	26	0.119201781	1	0.799600411	6.198492624
11	29	0.11074498	1	0.774641985	6.42320883
12	29	0.11074498	1	0.774641985	6.42320883
13	33	0.101697519	1	0.742072157	6.712036238
14	33	0.101697519	1	0.742072157	6.712036238
15	34	0.101697519	1	0.714522843	6.915431275
16	34	0.101697519	1	0.714522843	6.915431275
17	32	0.11116216	1	0.680337558	7.114378211
18	30	0.119201781	1	0.669395235	7.152106874
19	37	0.101697519	1	0.634153633	7.525616388
20	37	0.101697519	1	0.634153633	7.525616388
21	35	0.110581834	1	0.600026138	7.740728403
22	35	0.110581834	1	0.600026138	7.740728403
23	40	0.101697519	1	0.559817155	8.1358015
24	40	0.101697519	1	0.559817155	8.1358015
25	39	0.107129599	1	0.530542893	8.356108706
26	39	0.107129599	1	0.530542893	8.356108706
27	39	0.11116216	1	0.493824015	8.670648444
28	43	0.101697519	1	0.493149033	8.745986613
29	32	0.138493568	1	0.457191895	8.86358833
30	32	0.138493568	1	0.457191895	8.86358833
31	42	0.114496351	1	0.403134744	9.617693492
32	42	0.114496351	1	0.403134744	9.617693492
33	51	0.101697519	1	0.353060107	10.37314691
34	51	0.101697519	1	0.353060107	10.37314691
35	54	0.101697519	1	0.312847275	10.98333203
36	54	0.101697519	1	0.312847275	10.98333203

37	57	0.101697519	1	0.278094926	11.59351714
38	54	0.11074498	1	0.25514288	11.96045782
39	54	0.11074498	1	0.25514288	11.96045782
40	63	0.101697519	1	0.221986876	12.81388736
41	51	0.126590184	1	0.208557541	12.91219871
42	78	0.101697519	3	0.182118208	15.86481293
43	103	0.101697519	3	0.154006557	20.94968886
44	103	0.101697519	3	0.154006557	20.94968886
45	128	0.101697519	3	0.134836345	26.0345648
46	128	0.101697519	3	0.134836345	26.0345648
47	153	0.101697519	3	0.120764854	31.11944074
48	153	0.101697519	3	0.120764854	31.11944074
49	185	0.101697519	3	0.107294279	37.62808194
50	185	0.101697519	3	0.107294279	37.62808194
51	222	0.101697519	3	0.095700334	45.15369833
52	222	0.101697519	3	0.095700334	45.15369833
53	249	0.103399059	3	0.084769568	51.49273144
54	249	0.103399059	3	0.084769568	51.49273144
55	249	0.115343342	3	0.061252735	57.4409843
56	249	0.115343342	3	0.061252735	57.4409843
57	247	0.129630787	3	0.043345334	64.03760882
58	249	0.131422935	3	0.041367229	65.44862158
59	249	0.14425231	3	0.031185487	71.83765058
60	249	0.14425231	3	0.031185487	71.83765058
61	249	0.155419897	3	0.024835091	77.39910891
62	249	0.155419897	3	0.024835091	77.39910891
63	249	0.170493508	3	0.018668585	84.90576683
64	249	0.174806694	3	0.017271379	87.05373384
65	249	0.189817882	3	0.013318833	94.52930533
66	249	0.190369429	3	0.013195999	94.80397558
67	249	0.204330792	3	0.01049507	101.7567343
68	249	0.219463118	3	0.008271076	109.2926325
69	249	0.23269621	3	0.006762064	115.8827123
70	249	0.23269621	3	0.006762064	115.8827123
71	247	0.251538415	3	0.005149859	124.2599771
72	247	0.251538415	3	0.005149859	124.2599771
73	249	0.263933888	3	0.004287667	131.4390762
74	249	0.263933888	3	0.004287667	131.4390762
75	249	0.280708636	3	0.003390595	139.7929008
76	249	0.280708636	3	0.003390595	139.7929008
77	249	0.295287331	3	0.002779199	147.0530907
78	249	0.295287331	3	0.002779199	147.0530907

79	249	0.313213419	3	0.002190279	155.9802827
80	249	0.313213419	3	0.002190279	155.9802827
81	249	0.328149074	3	0.001805552	163.4182387
82	249	0.338589051	3	0.001581904	168.6173474
83	249	0.352627316	3	0.001328924	175.6084031
84	249	0.356428584	3	0.001268553	177.501435
85	249	0.374751961	3	0.001018002	186.6264767
86	249	0.374751961	3	0.001018002	186.6264767
87	249	0.388975058	3	0.000862096	193.709579
88	249	0.393651663	3	0.000816939	196.0385282
89	247	0.406309594	3	0.000711778	200.7169395
90	249	0.421866829	3	0.000595664	210.0896809
91	249	0.421866829	3	0.000595664	210.0896809
92	249	0.438898869	3	0.000495712	218.5716368
93	249	0.442988904	3	0.000474682	220.608474
94	249	0.457149733	3	0.00040943	227.6605672
95	249	0.461645858	3	0.000390927	229.8996375
96	249	0.480189643	3	0.000324171	239.134442
97	249	0.480189643	3	0.000324171	239.134442
98	249	0.494114507	3	0.000282662	246.0690246
99	249	0.495052784	3	0.000280094	246.5362866
100	249	0.495052784	3	0.000280094	246.5362866

## Appendix 4

Complete list of optimal solutions using tool type 1 (uncoated WC/Co) and  $t = 60s$ , for multi-objective optimization using NSGA-II

Solution #	$V_c$ (m/min)	$f$ (mm/rev)	Reliability	MRR
1	25	0.100722	0.943438113	5.036109203
2	25	0.1027	0.934004738	5.13497656
3	26	0.102957	0.912534743	5.353788528
4	25	0.108958	0.899536195	5.447891765
5	26	0.108066	0.880389637	5.619454416
6	25	0.116096	0.853261129	5.804817849
7	29	0.103773	0.833398216	6.018856881
8	30	0.100985	0.830076663	6.059110899
9	25	0.121755	0.812984515	6.087748912
10	31	0.102957	0.785665846	6.383363245
11	25	0.127686	0.768874214	6.384294877
12	32	0.102957	0.757764604	6.589278188
13	27	0.122977	0.73641528	6.640750162
14	25	0.134837	0.71487634	6.741858156
15	35	0.100471	0.699727017	7.03298202
16	33	0.108066	0.680318205	7.132384451
17	33	0.110384	0.658277028	7.285346987
18	31	0.118988	0.639881083	7.377255672
19	38	0.100296	0.623070853	7.622462341
20	33	0.116096	0.605625714	7.66235956

21	36	0.108958	0.588514627	7.844964142
22	37	0.108066	0.570984517	7.996915899
23	40	0.102957	0.547232194	8.236597736
24	36	0.11662	0.519132574	8.396659458
25	37	0.116096	0.498649378	8.591130416
26	39	0.111593	0.490044741	8.704263178
27	39	0.113904	0.470256111	8.884519657
28	44	0.103993	0.451572587	9.151389572
29	44	0.106253	0.431716923	9.350245641
30	44	0.106409	0.43037971	9.363981244
31	42	0.113904	0.407686013	9.567944246
32	48	0.102394	0.393652467	9.829795981
33	46	0.108958	0.374131759	10.02412085
34	48	0.107078	0.356373635	10.27946621
35	48	0.110384	0.332482825	10.59686835
36	47	0.113904	0.32334349	10.70698523
37	50	0.110384	0.304675561	11.03840453
38	49	0.116096	0.282451038	11.37744298
39	56	0.1027	0.282430409	11.50234749
40	58	0.101933	0.266097066	11.82419192
41	44	0.134848	0.249693683	11.86666576
42	60	0.101933	0.246633489	12.23192267
43	62	0.102394	0.226388805	12.69681981
44	62	0.106409	0.205571244	13.19470084
45	67	0.1027	0.18772729	13.76173718

46	65	0.106253	0.184785015	13.81286288
47	62	0.11576	0.165717574	14.35429671
48	74	0.102957	0.147275783	15.23770581
49	65	0.118988	0.137697896	15.46843931
50	67	0.124065	0.114479393	16.62475242
51	83	0.110384	0.092371499	18.32375151
52	92	0.106253	0.07925988	19.55051361
53	91	0.118988	0.059750097	21.65581504
54	111	0.102957	0.053841525	22.85655872
55	113	0.108958	0.043977349	24.62447078
56	138	0.10191	0.031756076	28.12723596
57	138	0.10191	0.031756076	28.12723596
58	106	0.13997	0.025685684	29.67355176
59	146	0.110384	0.02190025	32.23214122
60	163	0.116096	0.014146449	37.84741237
61	196	0.107078	0.010913935	41.97448701
62	174	0.134294	0.00757967	46.7343313
63	217	0.113904	0.006777252	49.4343786
64	220	0.121755	0.005245121	53.57219042
65	233	0.124065	0.004141763	57.81443753
66	231	0.136056	0.00308773	62.85775877
67	249	0.128478	0.002982439	63.98186976
68	244	0.13997	0.002337683	68.30515688
69	249	0.150231	0.001678586	74.81508887
70	147	0.256658	0.00128556	75.45732242

71	244	0.16443	0.001270336	80.24160125
72	244	0.180248	0.000882099	87.96101369
73	244	0.18892	0.000728804	92.19317768
74	249	0.194265	0.00060362	96.74388975
75	249	0.203343	0.000498942	101.2650114
76	244	0.214884	0.000426208	104.8632055
77	249	0.220346	0.000355041	109.7323016
78	250	0.220049	0.00035176	110.0245585
79	210	0.271923	0.000273029	114.2077281
80	249	0.238222	0.000253598	118.6343937
81	244	0.251387	0.00021671	122.6766259
82	249	0.256658	0.000182969	127.8154645
83	250	0.260028	0.000170074	130.0139895
84	244	0.273318	0.000149833	133.3791175
85	249	0.278809	0.000126705	138.8469042
86	231	0.301917	0.000118998	139.4856319
87	248	0.289827	0.000108206	143.7540328
88	250	0.301917	8.72107E-05	150.9584761
89	249	0.318861	6.91781E-05	158.7929962
90	249	0.318861	6.91781E-05	158.7929962
91	249	0.329206	5.98153E-05	163.9446802
92	211	0.388513	5.43052E-05	163.952511
93	228	0.368635	5.06793E-05	168.0976451
94	244	0.35271	4.73093E-05	172.1226246
95	244	0.355511	4.56226E-05	173.489566

96	244	0.366253	3.97868E-05	178.7317057
97	249	0.36768	3.60214E-05	183.1045257
98	249	0.368635	3.55927E-05	183.5803229
99	249	0.388513	2.79191E-05	193.4795035
100	249	0.405115	2.29912E-05	201.747262
101	249	0.417303	2.00291E-05	207.8166502
102	249	0.42134	1.91503E-05	209.8274429
103	233	0.461383	1.64217E-05	215.0045017
104	233	0.461383	1.64217E-05	215.0045017
105	244	0.45055	1.52086E-05	219.8685199
106	249	0.452984	1.36534E-05	225.585835
107	230	0.498148	1.20913E-05	229.1478505
108	244	0.478443	1.14784E-05	233.480296
109	244	0.487891	1.04714E-05	238.0908871
110	244	0.487891	1.04714E-05	238.0908871
111	249	0.487891	9.6375E-06	242.9697988
112	249	0.491279	0.000009329	244.6568624
113	250	0.498148	8.5967E-06	249.0737505
114	250	0.498148	8.5967E-06	249.0737505

## Appendix 5

Complete list of optimal solutions using tool type 1 (TiAlN coated WC/Co) and  $t = 40s$ , for multi-objective optimization using NSGA-II

Solution #	$V_c$ (m/min)	$f$ (mm/rev)	Reliability	MRR
1	25	0.100652	0.526835414	5.032609163
2	25	0.101901	0.521490247	5.09504868
3	26	0.101901	0.509234014	5.298850627
4	27	0.10269	0.494287333	5.545282228
5	28	0.100473	0.492360952	5.626463121
6	29	0.100652	0.480918519	5.83782663
7	29	0.100794	0.480329411	5.846072312
8	30	0.100652	0.470700837	6.039130996
9	31	0.100652	0.460924296	6.240435363
10	32	0.100652	0.451561445	6.441739729
11	33	0.100652	0.442586958	6.643044096
12	34	0.100794	0.43341992	6.854015814
13	35	0.101901	0.420909953	7.133068152
14	36	0.100473	0.418458855	7.234024013
15	37	0.100794	0.40959167	7.458781915
16	38	0.101901	0.398141042	7.744473993
17	41	0.100473	0.382954067	8.23874957
18	43	0.100652	0.369823989	8.656087761
19	45	0.100381	0.359119715	9.034269755
20	45	0.101901	0.353889481	9.171087623

21	47	0.101901	0.343084216	9.578691518
22	48	0.100794	0.341610265	9.676257619
23	51	0.100381	0.328339104	10.23883906
24	54	0.100473	0.314655016	10.85103602
25	56	0.100381	0.306640626	11.24264681
26	57	0.101901	0.298052383	11.61671099
27	58	0.100652	0.297963712	11.67565326
28	61	0.101901	0.283345722	12.43191878
29	66	0.100473	0.270956824	13.26237736
30	66	0.100473	0.270956824	13.26237736
31	61	0.109613	0.262613808	13.37274749
32	69	0.100652	0.261471971	13.89000129
33	73	0.100473	0.25091176	14.66899314
34	69	0.109613	0.238900446	15.12655044
35	83	0.100381	0.227394901	16.66320866
36	84	0.100652	0.224624094	16.90956679
37	89	0.100794	0.214335838	17.94139434
38	94	0.100652	0.205599502	18.92261045
39	99	0.101901	0.194659853	20.17639277
40	105	0.100652	0.188258674	21.13695849
41	114	0.100381	0.176747807	22.88681671
42	122	0.101901	0.164523005	24.86383756
43	128	0.101901	0.158216139	26.08664924
44	138	0.100381	0.151320442	27.70509392
45	139	0.100381	0.150427834	27.90585547

46	153	0.100652	0.138585131	30.79956808
47	155	0.100652	0.137106728	31.20217681
48	157	0.115066	0.116371147	36.13068269
49	195	0.100473	0.113497009	39.18429674
50	209	0.101901	0.105343539	42.59460696
51	230	0.101901	0.097169797	46.87444785
52	248	0.100381	0.092777729	49.78886443
53	250	0.10269	0.089729785	51.34520581
54	250	0.10269	0.089729785	51.34520581
55	248	0.111309	0.082199953	55.20920343
56	250	0.118726	0.07566956	59.36275107
57	250	0.128084	0.069183467	64.04190893
58	195	0.166113	0.062949978	64.78387602
59	250	0.139396	0.062579849	69.69784735
60	250	0.147577	0.058477428	73.78869878
61	250	0.155751	0.054840224	77.87566911
62	247	0.164392	0.05195869	81.20964016
63	250	0.171207	0.048980797	85.60365171
64	250	0.181604	0.045642964	90.80212004
65	248	0.192081	0.042973513	95.27238005
66	248	0.199526	0.041055836	98.96499025
67	248	0.210062	0.038593572	104.1908381
68	250	0.218471	0.036555788	109.2357015
69	250	0.226992	0.034909479	113.495871
70	248	0.238871	0.033058878	118.4799854

71	250	0.238391	0.032907062	119.1952711
72	250	0.251757	0.030810138	125.8787135
73	248	0.262593	0.029488032	130.2458881
74	250	0.273617	0.027860743	136.8087015
75	247	0.28561	0.026733657	141.0911854
76	225	0.323083	0.024992759	145.387373
77	250	0.304147	0.024511896	152.0736484
78	250	0.315948	0.023406247	157.9738008
79	250	0.32696	0.022452536	163.4801856
80	250	0.33722	0.021624465	168.6100099
81	250	0.347108	0.020875796	173.5539999
82	250	0.358044	0.020098359	179.0218118
83	245	0.366731	0.01986654	179.6979732
84	250	0.371306	0.019218463	185.6532174
85	250	0.381594	0.018577827	190.7967609
86	250	0.381594	0.018577827	190.7967609
87	250	0.390736	0.018035581	195.3679679
88	248	0.403263	0.017453924	200.0182344
89	250	0.409395	0.016997362	204.6975696
90	250	0.419918	0.016446865	209.9588793
91	250	0.431334	0.015874084	215.6668208
92	250	0.437356	0.015581152	218.6781646
93	248	0.444006	0.01537639	220.2267289
94	250	0.452343	0.014877011	226.1716065
95	250	0.46079	0.014494341	230.3948202

96	248	0.477049	0.013886438	236.6161911
97	250	0.477113	0.013780625	238.5564872
98	250	0.48614	0.013399379	243.0699412
99	250	0.499543	0.012849617	249.7715289